LASER ENGINE SIMULATION USING PRESSURE BASED NAVIER-STOKES SOLVER

by

Hazim S. Youssef

Dissertation submitted to the Faculty of the

Virginia Polytechnic Institute and State University

in partial fulfillment of the requirements for the degree of

Doctor of Philosophy

in

Aerospace Engineering

APPROVED:

Antoni K. Jakubowski, Chairman

Joseph A. Schetz

Saad R. Ragab

Robert W. Walters

Charlie L. Yates

February, 1994

Blacksburg, Virginia

C.2

LASER ENGINE SIMULATION USING PRESSURE BASED NAVIER-STOKES SOLVER

by

Hazim S. Youssef

Antoni K. Jakubowski, Chairman

Aerospace Engineering

(ABSTRACT)

Analysis of the flow field in a laser engine represents a difficult computational problem involving combinations of complex physical and gasdynamical processes. Following a brief discussion of these processes a calculation procedure using primitive variables formulation on a non-staggered grid system is introduced. Based on this procedure, a Pressure Based Navier-Stokes Solver (PBNS) is developed using a generalized curvilinear coordinate system. The solver is first tested in application to a subsonic compressible flow over an insulated flat plate and to a flow in an axisymmetric converging-diverging nozzle. Next, the PBNS code is used to analyze the flowfield and performance of a laser thruster. The physical/numerical model includes the geometric ray tracing for the laser beam, beam power absorption, plasma radiation losses, and plasma thermophysical and optical properties. Equilibrium hydrogen is used as a flowing gas and its properties are calculated using the Hydrogen Properties Calculation (HPC) based on the the methods of statistical thermodynamics. Two thruster configurations, two laser types (CO_2 and iodide), various laser power levels, and various injection conditions are tested. The results

of these tests include the temperature, pressure, velocity and Mach nubmer contours, as well as table of the laser beam power absorbed, radiation losses to the thruster walls, thrust level and specific impulse. The maximum specific impulse obtained in these tests is 1537 sec for a CO_2 laser thruster and 827 sec for an iodide laser thruster. Up to 100% power absorption can be achieved, however, the radiation losses from the hot plasma are quite high disallowing a full conversion of the absorbed power into the thermal energy of the propellant. The PBNS code can be used to study the effects of various design parameters on the performance of a laser thruster and provide guidelines for the preliminary design of a laser engine.

Acknowledgements

All glory and gratitude are due to All-Mighty GOD for what HE has given me in this life.

I would like to express my deep appreciation to Dr. A. K. Jakubowski, committee chairman, for providing the opportunity to participate in NASA/USRA program, his continuous support, advice, and his careful review of this dissertation.

I am also very grateful to Dr. Saad Ragab for his interest and his valuable assistances that were provided several times. My appreciation goes to Dr. Robert Walters for providing me with helpful advice and suggestions. I would like to express my deep thanks to Dr. Joseph Schetz for encouraging me. Thanks, also goes to Dr. Charlie Yates for participating on the advisory committee.

I would like to thank Dr. Brenard Grossman, department chairman, for his interest in this research and advice. Also, I would like to thank Dr. Douglas Nelson (Virginia Tech), Dr. Suhas Patankar (University of Minnesota), and Dr. C.M. Rhie (Pratt & Whitney) for their helpful discussions.

I would like to thank all the staff of NASA/USRA Advanced Design Program, especially Dr. Vicki Johnson, for funding this research without their continuous financial support it would have been impossible to finish this study.

Deep gratitude to my parents and my family for their encouragement, trust and understanding.

Table of Contents

List of Tables

List of Figures

Acronyms

LEO	Low earth orbit
GEO	Geosynchronous earth orbit
LLO	Low lunar orbit
OTV	Orbit transfer vehicle
SEP	Solar-electric propulsion
NEP	Nuclear-electric propulsion
LOTV	Laser orbit transfer vehicle
LSD	Laser supported detonation
LSC	Laser supported combustion
CW	Continuous wave laser
RP	Repetitively-pulsed laser
IB	Inverse Bremsstrahlung
PBNS	Pressure based Navier-Stokes Solver
HPC	Hydrogen properties calculation

Chapter I

INTRODUCTION

1.1 Background

After Space Station Freedom becomes operational, the next century will observe a variety of new challenges for the space program. These challenges will include missions such as the transportation of cargos from low earth orbit (LEO) to geosynchronous earth orbit (GEO), or to low lunar orbit (LLO). There will be also missions to intermediate high earth orbit and trans-geosynchronous orbits as well as missions involving interplanetary spacecraft.

An orbit transfer vehicle (OTV) may serve as the key element in completing these missions successfully and economically. This has been pointed out in several NASA studies [10, 16, 18, 47, 59]. Several powering schemes may be utilized for providing the required thrust for the future OTV. These could include chemical , solar-electric (SEP), nuclear-electric (NEP) and laser propulsion systems.

Chemical OTV can provide high thrust but a relatively low specific impulse limited to about 490 sec. This shortens the mission time, but at the cost of using large quantities of propellant. SEP or NEP OTV's operate at high specific impulses (2000 - 9000 sec) allowing significant reduction of the required propellant. However, they are low thrust systems which implies long propulsive maneuvers and trip times. In addition, nuclear waste from NEP may be considered an environmental hazard for missions near LEO.

Laser OTV (LOTV) represents a midpoint between these two systems. LOTV can achieve a relatively high specific impulse of 1000 to about 1500 sec [36, 18, 10], yet it can provide medium thrust, whose magnitude depends on the laser power available. LOTV has high payload-to-weight ratio, because the power source (laser) is not carried on the spacecraft. Because of the relatively high specific impulse that can be produced, LOVT may be well suited to high ΔV orbital transfer missions. In addition, because the thrust level is relatively high compared to electric propulsion, LOTV offers shorter orbital transfer times than either SEP or NEP systems. Further economical and technical comparison between the above systems is discussed in many studies [16, 59, 10].

1.2 Laser Propulsion Classification

The fundamental concept of laser propulsion is based on converting the energy from high-power laser beam into thermal or kinetic energy of a propellant (typically hydrogen). Figure 1.1 illustrates this idea for an OTV using a space-based laser source to produce the laser power. The laser beam is aimed at the OTV which will utilize the beam power and produce the required thrust.

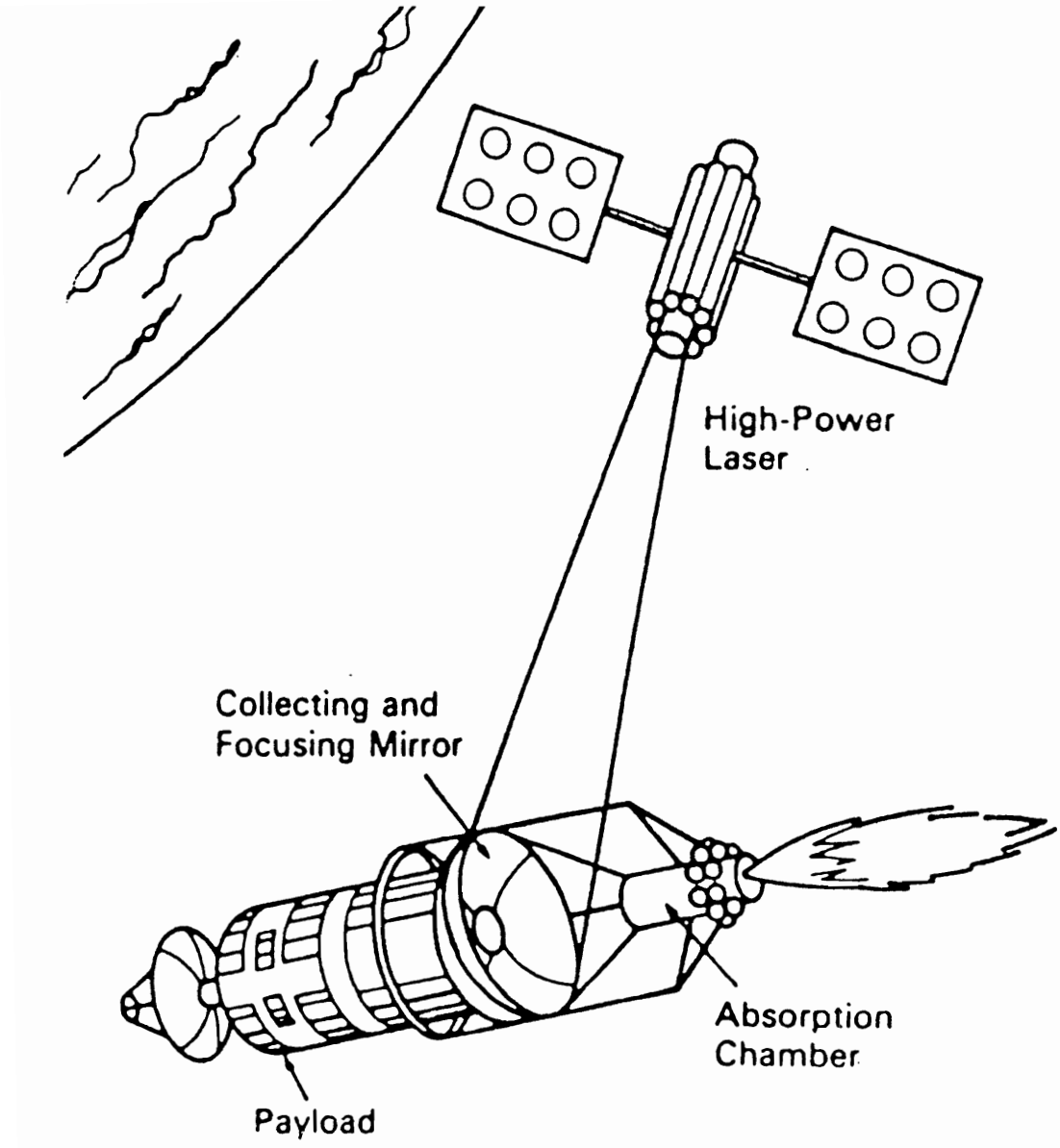

Figure 1.1. Schematic diagram of LOTV elements (ref. 17).

Two different schemes are available for the production of the thrust in LOTV. These are a continuous wave laser (CW) and a repetitively-pulsed laser (RP) systems.

In a CW laser concept, Fig. 1.2(a), a remote high-power laser which can be based either on the earth or in space is aimed at an OTV, which collects the laser beam and focuses it into the absorption chamber. There, it is absorbed by the flowing propellant. The propellant is heated through the absorption process to a temperature as high as 20,000 K. The hot core, which is in plasma state, is mixed with the cold flow of the propellant thereby increasing its thermal energy. The thermal energy is then converted into the kinetic energy by expanding the flow through a conventional nozzle to produce the thrust.

The RP laser, schematically illustrated in Fig. 1.2(b) is based on producing high-frequency pulses of an intense laser beam. The beam is fired into the nozzle where it is focused. This produces high intensity radiation field, which causes the electrical breakdown of a solid propellant, initiating a high-pressure plasma blast wave. This wave, called a " laser-supported detonation" or " LSD wave ", propagates up the laser beam. To keep the high-pressure gas in the vicinity of the nozzle wall, the pulse time should be minimized [10, 18].

This study deals with the CW laser propulsion field. Feasibility studies indicate that the CW laser is most likely to be adapted for the future LOTV [47, 59].

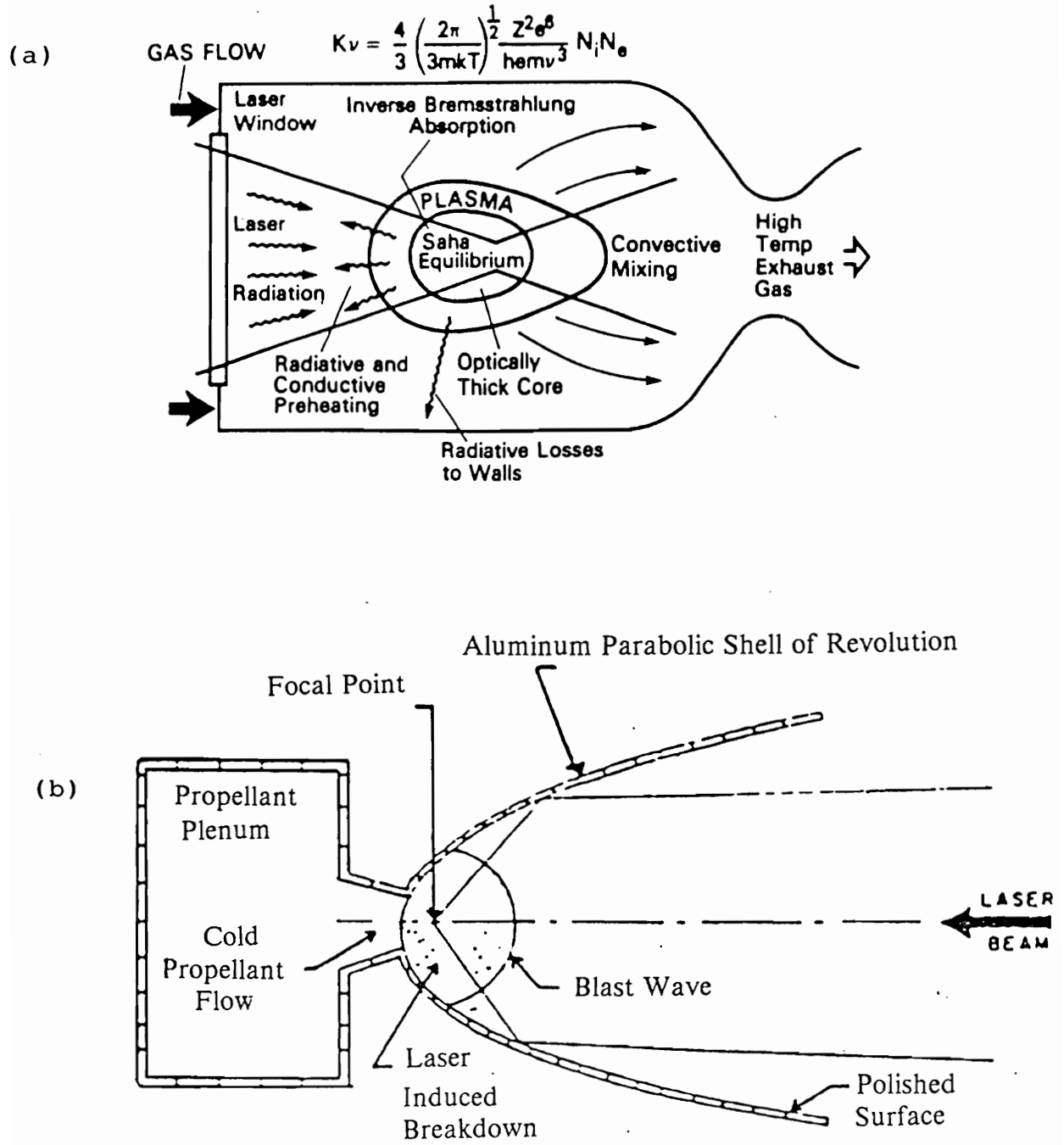

Figure 1.2. Typical representation of (a) Continuous wave laser engine (ref. 31), (b) Repetitive-pulse laser engine (ref. 9).

1.3 CW Laser Propulsion

A successful simulation of the CW laser propulsion should include both the physical model and technological features of the laser-supported propulsion system. The physical model includes an absorption mechanism of the laser power, plasma radiation losses, heat transfer and fluid dynamics. The technological problems include laser-power level, laser type, and lens and windows used for focusing the beam. All these mechanisms and aspects will affect the the laser-engine performance such as specific impulse, thrust level and thermal efficiency of the engine.

1.3.1 Specific Impulse

Specific impulse is one of the most important parameters in rocket propulsion, since it affects the payload and the propellant requirement of OTV. The specific impulse I_{sp} may be written

$$I_{sp} = \frac{F}{\dot{W}_p} = \frac{V_{ex}}{g} = \frac{\sqrt{\frac{2g\gamma}{\gamma-1}\ \frac{\hat{R}}{M}\ T_c[1-(\frac{P_{ex}}{P_c})^{\frac{\gamma-1}{\gamma}}]}}{g} \tag{1.1}$$

where F is the thrust and $\dot{W}_P$ is the rate of propellant weight consumed, V_{ex} is the exit velocity, g is the acceleration of gravity, $\hat{R}$ is the universal gas constant, T_c is the chamber temperature, P_c is the chamber pressure, and M is the molecular weight of the exhaust gas. Since, the specific impulse is inversely proportional to the square of molecular weight of the exhaust gas, hydrogen which becomes fully dissociated at high temperatures, is an excellent candidate propellant for laser propulsion. A specific impulse of 700-1500 sec has been

reported experimentally in small model tests performed by NASA [10], Lockheed [47] and others [38, 39, 49]. Based on these studies, hydrogen is selected as a propellant for this study.

1.3.2 Efficiency and Thrust Level

Thermal efficiency is used to relate the level of laser power to the propulsive energy of the propellant, and is given by

$$\eta = \frac{F I_{sp} g}{2P} = \frac{F V_{ex}}{2P} \tag{1.2}$$

where $F = \dot{m} V_{ex}$ is the thrust, P is the laser power, and $\dot{m}$ is the mass flow rate of the propellant. Equation (1.2) demonstrates that increasing the specific impulse will reduce the thrust level for a given power level. To improve the performance of the system, laser power or efficiency must be maximized.

For a thruster design to be of a practical use, an efficiency of 70% or higher should be obtained. The recent experimental results by Mazumder et al [49] showed that it is possible to absorb 100% of the incident laser power, but only 60% was converted into useful kinetic energy of the propellant. The remaining energy was radiated to the nozzle wall and was considered as loss. However, the radiation to the nozzle wall may be used to heat the incoming propellant. Jeng et al reported an efficiency of 67% [34]. It is believed that 90% efficiency may be achievable for an optimum system design [18].

The thrust level that can be expected for laser engine ranges from 10-20000 N [37]. Obviously, the thrust level increases if the thermal efficiency is improved, which stresses the importance of having a good mathematical model for designing

and studying the effects of various design parameters. The effective mathematical model must incorporate the real physics involved in the CW laser thruster. One of the most important phenomena to be considered is the absorption mechanism which allows the energy to be transferred from the laser beam to the flowing fluid.

1.3.3 Laser Power Selection

The feasibility of using laser propulsion for OTV relies heavily on the ability of the industry to produce a high-power lasers on the order of megawatts [37, 18]. Rapid progress in the development of high-power laser indicates that this would be possible by the year 2020. Unclassified reports show that a 1 MW design already exists [8].

Both theoretical and experimental studies of laser propulsion suggest the use of a CO_2 laser with 10.6 μm wave length. Also, the promising characteristics of a solar-pumped iodide laser make it a strong candidate for space missions. An iodide laser beam has the ability of traveling long distance with minimum scattering, because of its shorter wave length. Also, iodide laser may be economically suitable for high power level and space application. A cost analysis and design for such a system may be found in Young et al [80]. However, compared with CO_2, an iodide laser with a wave length of 1.315 μm will reduce the absorption coefficient of hydrogen as discussed later in Appendix B . In this study, both iodide and CO_2 lasers are tested as propellants for laser propulsion. The best arrangement for the laser source is a space-based laser system which includes several relays in LEO. This will reduce the distortion and the scattering

of the laser beam caused by both the turbulence in the atmosphere and the refraction caused by the inadvertent heating of the air in the beam path known as thermal blooming. These drawbacks will be expected if a ground-space system were selected for LOTV.

1.3.4 Absorption Processes

The success of laser propulsion depends on successful coupling of laser energy to the propellant (hydrogen). In practice, two methods are available to accomplish such coupling: inverse Bremsstrahlung and molecular resonance.

In molecular resonance, the molecules absorb the photons of the laser beam during their transitions from one state to another . This method suffers from the need of matching the frequency of the laser to the frequency of the transition. Also, at a higher temperature, the absorption coefficient drops due to the dissociation of the molecules. Since hydrogen has zero absorption at temperatures below 10000 K, this method is of little use for laser propulsion.

In inverse Bremsstrahlung (IB), the free electron in a partially ionized gas can be made to oscillate in a varying electric field caused by the transmitted electromagnetic beam generated by the laser photons. The electrons then enter inelastic collisions with other particles such as neutral atoms (neutral-electron absorption) , or with ions (ion-electron absorption). The collisions will transfer the energy from the beam to the propellant, resulting in formation of additional free electrons and increasing the absorption. Actual experiments have indicated that IB is the highly recommended method to insure the absorption of the photons in hydrogen flow [41, 38]

One of the factors that will increase the absorption coefficient of hydrogen is the chamber pressure (see Appendix B). However, this pressure is restricted by the strength of the chamber windows. A pressure value above 30 atm. is not considered practical for the projected technology in the next century.

1.3.5 Plasma Initiation and Stability

The drawback of IB absorption mechanism is its inefficiency at temperatures below 10000 K in hydrogen flow. Thus, hydrogen is transparent to a laser beam unless heated to high temperatures. Three different approaches have been suggested to overcome this drawback.

One approach is to seed the hydrogen flow with molecules of other gases (such as H_2O or NH_3) that have the desired resonance-transition. These resonances should match the laser frequency. This will boost the absorption ability of hydrogen, but at the cost of reducing the specific impulse, due to increased molecular weight of the exhaust gases.

The second approach is the artificial injection of a large number of free electrons into the hydrogen. This may be accomplished by focusing the laser beam into a small area and jumping an electric arc through it. This process creates a large number of free electrons at the focal point, increasing the IB absorption. Another alternative for creating free electrons is the use of a second high power laser pulse near the focal point instead of the electric arc.

The third approach involves the use of small particles suspended in the hydrogen. These particles absorb incident laser energy, reach a high temperature rapidly, and then transfer the heat to the propellant through radiation and

conduction. These particles should have high boiling point to survive the high temperature. The problem with this method is that these particles have a tendency to scatter the incoming beam. Also, special care must be used to maintain particle suspension in the hydrogen. Some researchers have demonstrated the ability of using carbon, tungsten, cesium and some ceramics as a seedant in hydrogen [10].

Once the hydrogen begins to absorb the laser beam, additional free electrons are produced, and the plasma begins to form near the focal point of the beam. Heat is transferred to the cold hydrogen through conduction and radiation, and hydrogen becomes more opaque to the laser. Then, the plasma starts to propagate itself downstream of the laser beam. Cold hydrogen must be injected in the opposite direction of plasma propagation to maintain a steady plasma core and stabilize the flow. In this way, if any upstream perturbations occur the plasma will move into the region of less laser intensity that can be created by tightly focusing the beam. There, the plasma will not be able to sustain itself and will return back to its original position. The phenomenon known as the laser sustained plasma (LSP) is one of the key features of laser propulsion. In depth analysis for LSP is found in [49, 42, 38, 67] .

1.4 Flow Field of a Laser Engine

In summary, the cold hydrogen is injected into a chamber in which the laser beam is focused to create a plasma core which will heat the incoming propellant to a high enthalpy level. The propellant is expanded through a nozzle to produce thrust. A typical engine configuration is shown in Fig. 1.2(a). A mathematical

model of the flow field is essential for optimal laser engine design and for analyzing the main parameters of the laser engine before any full scale engines can be produced. The flow field within the laser absorption chamber is very complex and features large energy absorption, energy loss from the hot core plasma via radiation and conduction, laser power conservation, mixing of the hot plasma and cold propellant, high temperature and density gradients in both axial and radial directions, flow regimes ranging from subsonic in the absorption chamber to supersonic at the nozzle exit, and equilibrium thermodynamics with a possibly nonequilibruim flow in the supersonic region. A realistic model should include all of the above elements.

1.4.1 Current Modeling Status

Several models for laser engines have been proposed to analyze the mechanism by which the plasma propagates in a flow field. This mechanism is sometimes called the laser supported combustion (LSC) wave. The models range from a simple one dimensional energy equation to axisymmetric Navier-Stokes equations. Raizer [67] introduced the LSC wave model, assuming one dimensional flow at constant pressure which reduced the governing equation to the energy equation with the temperature as the only unknown. Heat conduction was the principal heat transfer mechanism. The plasma was considered optically thin and in thermal equilibrium, and the Saha equation was used to calculate the electron density. IB absorption was assumed as the absorption mechanism. The heat loss by radiation was given as a function of pressure and temperature. Further, it was assumed that the ratio of specific heat to thermal conduction and

the absorption coefficient are constants. Raizer obtained an integral solution of the energy equation for air flow. His model predicted smaller plasma size than obtained in experiments.

Jackson et al [30] provided another model for LSC wave. They used the same assumptions as Raizer, but with different treatment of the radiation losses. They included radiation losses occurring in 19 frequency groups, with the flux of each calculated from the temperature of each discrete cell along the LSC wave axis. They calculated the LSC structure and the propagation velocity of the wave for various laser intensities. They compared their results with experimental data and produced clear evidence of radial flow, rendering the problem two-dimensional. The calculated velocity of the LSC wave did not agree with experiment.

Batteh and Keefer [6] used a quasi two-dimensional model in their analysis, assuming a uniform flow field in a constant pressure duct and an axisymmetric temperature field. They retained Razier's assumption of thermal conduction as the principal heat transfer mechanism. Plasma radiation served as the only loss mechanism. The absorption coefficient was assumed to be piecewise constant with a zero value in the front of the LSC wave. An analytical solution in terms of Bessel functions was introduced. The model predicted the maximum temperature and the propagation speed of the LSC wave. The calculated propagation speed of the LSC wave was an order of magnitude less than experimental data. A need to include the thermal radiation in the heat transfer mechanism was pointed out.

Kemp and Root [41] included the radiation in a one-dimensional numerical model. They assumed a constant pressure and a constant area duct, used variable thermodynamic and transport properties of equilibrium hydrogen, and integrated the energy equation numerically. Their solution showed that a certain mass flux value can yield a physically reasonable temperature distribution in the LSC wave. They conceded that the one-dimensional model presents serious limitations to the validity of the results. They also pointed out that the laser beam convergence requires a higher flow rate than a collimated beam of the same initial intensity. This was due to the higher intensity that exists in the converged beam near the focal point.

Jeng and Keefer [32, 33, 34] developed several models for the simulation of laser engine flow. Their first model [32] assumed incompressible, steady state, axisymmetric Navier-Stokes equations. They neglected the viscous dissipation in the energy equation, and provided results for hydrogen and argon as propellants. They further assumed local thermodynamic equilibrium and used real ray tracing of the laser beam together with actual transport properties. Their results showed that the previous one and quasi-two dimensional model were insufficient for providing accurate temperature and flow fields. The position of the plasma and its size were in good agreement with the experimental data for argon and were strongly affected by flow configuration and optical arrangement. Their model used a 10.6 μm CO_2 laser, with a low laser power level on order of kilowatts. They used a SIMPLE algorithm with primitive variables solver and staggered grid. Recently, Jeng improved his model to include the compressible, steady state

Navier-Stokes equations as well [35]. The numerical scheme was an extension of the SIMPLE algorithm to compressible flow as developed by Rhie [70] on a non-staggered grid. The treatment of the cell velocity yields a flow field which depends on the relaxation factor and slows the convergence of the continuity equation. Their results are limited to low laser power (30 kW), which would not be sufficient to produce the required thrust for OTV. The convergence history was not reported.

Merkel et al [56] developed a two-dimensional model for the laser thruster. Their model assumed equilibrium hydrogen seeded with 1% cesium, rather than pure hydrogen. This allows high absorption of the laser beam energy at relatively low temperatures. The mixture yields a strongly absorbing plasma at a temperature of 6000 K and results in computational advantages such as reduced temperature gradients, reduced necessity of using a fine grid, and reduced numerical instability problems. The authors used an Euler implicit algorithm with a factorization scheme. In a previous work, Merkel [55] tried both the MacCormack and Beam Warming schemes with strong heat additions. He reported difficulty for converging these schemes with strong heat addition fields. Merkel et al neglected the radiation loss, which can be justified at a low temperature plasma but not for a high temperature plasma. The results indicated that a stable plasma occurred downstream of the focal point with subsonic flow field, but at a relatively low temperature.

All the above mentioned models used a CO_2 laser because of its availability for high power levels.

Review of the literature on the laser engine flow field reveals that the numerical solution of LSC hydrogen thruster represents a formidable computational problem that taxes the ability of the most robust algorithm. The problem involves complex and diverse physics that incorporate absorption of the laser beam energy, energy conversion, plasma radiation, and thermodynamic and transport properties of the high temperature propellant. Specific computational challenges involve a strong energy source term which tends to destabilize the algorithm, steep temperature gradients requiring fine grids, plasma initiation and stability, a very high temperature field, low Mach number flow in the absorption chamber which is nevertheless compressible because of the heat addition which contributes to stiffness in the conversion of the solution, and the existence of different flow regimes (subsonic, transonic, and supersonic) in the different regions of the laser engine. Furthermore, initial guesses with enough accuracy may be required to initiate development of the plasma. Failure of a solution to converge may indicate numerical difficulties or simply the absence of a solution for the initial conditions.

1.5 Objective of this Study

The general objective of this research is to develop a computational model that can be used as a conceptual design tool for the laser engine.

As a first step, a full Navier-Stokes computational model for compressible, axisymmetric hydrogen flow within a thruster has been developed. The model have the ability to predict the flow for a stiff nozzle in which the flow ranges from subsonic to supersonic. Equilibrium thermodynamic and transport properties for

the hydrogen are used. Next, the laser beam and its effects have been integrated in the model. This has involved real ray analysis along the beam light grid, the radiation properties of the hot core plasma, plasma initiation and development, the energy source term treatment, and finally the calculations of thrust level and specific impulse are performed. All the calculations for the laser engine have been done for hydrogen as a propellant and for both CO_2 and iodide lasers. The selection of an iodide laser has been motivated by the choice of this laser (approved by NASA Langley) for a conceptual design of a spaced-based LOTV developed at Virginia Tech 1989/1990.

This study represents the first numerical simulation of a laser engine using high power level of laser beam with pure hydrogen as a propellant. It analyzes the effects of the different design parameters of the laser engine such as power level, engine configuration, and laser type on the engine performance. The study shows the ability of using an iodide laser for propulsion. The study also demonstrates the ability of the pressure-based Navier Stokes solver to handle curvilinear 2-D, or axisymmetric flow problems over a wide range of Mach number.

Chapter II

COMPUTATIONAL MODEL FOR LASER ROCKET ENGINES

2.1 Introduction

The fast development of computer technology in the last decade has had a great impact on the use of computational methodology for solving complex problems in the fields of fluid mechanics and heat transfer. The science known as computational fluid dynamics (CFD) has gained credibility for resolving complex problems that would otherwise be considered impractical or extremely difficult. Certainly, a flow in laser engine belongs such problems. The governing equations for the flow within a laser engine can be analyzed as the full Navier-Stokes equations in axisymmetric form, with both radiation loss and laser absorption heat source included in the energy equation.

Two main computational methods are available for solving Navier-Stokes equations. These are "density-based method " and "pressure-based method ". The effectiveness of these two methods has long been debated, [57, 37, 70].

In "density-based" algorithms, density is chosen as a primary variable, and pressure is then specified using the equation of state. The algorithm has been used mainly for compressible flows, but has been extended to incompressible flows [11, 57] . At low Mach numbers, the pressure and the density become weakly related, and the density depends on temperature alone. Round-off error and computer accuracy can cause the solution to be totally inaccurate [37] . To remedy this problem, Steger et al [57] suggested the use of artificial compressibility. A fictitious density is added to the time derivative term in the continuity equation. However, a problem arises when both compressible and incompressible flows exist in the same computational domain.

A "pressure-based" method, in which the pressure is used as a primary variable, does not suffer from the above problems. This method, known as primitive variables formulation, was originally used [61, 62] for incompressible flows at low Reynolds numbers, and later was extended to compressible flows at high Reynolds numbers [37, 44]. The original algorithm uses an uncoupled and sequential solution of Navier-Stokes equations. Several additions have been made to the original method, such as SIMPLE, [61] (semi-implicit pressure linked equation), SIMPLEX, and SIMPLER, to improve the convergence characteristics of the solution [1, 5, 12, 17, 21, 23, 24, 28, 79]. Recently, Kari et

al, Rhie, and Kobayashi et al [37, 70, 44] have extended the method to compressible flows in complex configurations.

This study will utilize the pressure-based method to resolve the flow within a laser engine. The method is robust, easy to program, requires less user intervention, and provides a solution that is applicable for a wide range of Mach numbers. Also, in real gas flows, the flow properties are usually expressed in terms of pressure rather than density, which is the case for the hydrogen properties calculations code (HPC) developed for this study. Thus, the selection of the pressure as the primary variable facilitates the use of the HPC code.

2.2 Governing Equations

Navier-Stokes equations are the governing equations for flow problems . They include the conservation of mass, momentum, and energy. In order to close these system of equations it is necessary to establish a relationship between the thermodynamic variables: pressure, temperature, enthalpy, and density (p,T,h, ρ) respectively. The transport properties of the flow: viscosity and thermal conduction coefficients (μ,k) must also be related to these thermodynamic variables. These relationships are given in Appendix A for equilibrium hydrogen. The code Hydrogen Properties Calculations (HPC) was developed to evaluate these relations and was used as a subroutine in the main code for the Pressure Based Navier-Stokes Solver (PBNS).

The governing equations for axisymmetric or two-dimensional flow can be written in the following compact form

$$\frac{\partial Q}{\partial t} + \frac{\partial F}{\partial x} + \frac{1}{r^j}\frac{\partial r^j G}{\partial r} = j\frac{H}{r^j} \tag{2.1}$$

where

$$Q = \begin{bmatrix} \rho \\ \rho u \\ \rho v \\ \rho e \end{bmatrix} \qquad F = \begin{bmatrix} \rho u \\ \rho u^2 - \sigma_{xx} \\ \rho uv - \tau_{xr} \\ \rho ue + q_x - u\sigma_{xx} - v\tau_{xr} \end{bmatrix} \tag{2.1a, b}$$

$$G = \begin{bmatrix} \rho v \\ \rho uv - \tau_{xr} \\ \rho v^2 - \sigma_{rr} \\ \rho ve + q_r - u\tau_{xr} - v\sigma_{rr} \end{bmatrix} \qquad H = \begin{bmatrix} 0 \\ 0 \\ -\sigma_H \\ -q_{\text{rad}} + \sum \alpha' I_i \end{bmatrix} \tag{2.1c, d}$$

where

$$\sigma_{xx} = -p - \frac{2}{3}\mu \nabla \cdot \vec{V} + 2\mu \frac{\partial u}{\partial x} \tag{2.2a}$$

$$\sigma_{rr} = -p - \frac{2}{3}\mu \nabla \cdot \vec{V} + 2\mu \frac{\partial v}{\partial r} \tag{2.2b}$$

$$\sigma_H = -p - \frac{2}{3}\mu \nabla \cdot \vec{V} + \frac{2\mu v}{r} \tag{2.2c}$$

$$\tau_{xr} = \mu \left(\frac{\partial u}{\partial r} + \frac{\partial v}{\partial x} \right) \tag{2.2d}$$

$$q_x = -k_{eff} \frac{\partial T}{\partial x} \tag{2.2e}$$

$$q_r = -k_{eff} \frac{\partial T}{\partial r} \tag{2.2f}$$

$$\nabla \cdot \vec{V} = \frac{\partial u}{\partial x} + \frac{\partial v}{\partial r} + j\frac{v}{r} \tag{2.2g}$$

In the above equations $j = 1, 0$ for axisymmetric and two-dimensional flows, respectively.

2.3 Theoretical Model of a Laser Engine

The above Navier-Stokes equations may now be written for laser engine flow assuming that the flow is steady, axisymmetric and laminar. It is assumed that the pressure is relatively high, so that local thermodynamic equilibrium may produce a satisfactory solution [33, 38, 42]. Radiative transfer influences the hot hydrogen plasma in two ways. Hydrogen plasma emits radiation over a wide range of the frequency spectrum. A portion of that radiation escapes from the plasma and therefore corresponds to an energy loss term in the Navier-Stokes equations. In addition, some of the radiation is transported into the cold gas and is absorbed there. Following the Kemp model [41], the radiation is divided into an optically thin part (long wave length), which includes all radiation escaping from the plasma, and an optically thick part, which can be considered as a diffusion process [32]. Detailed discussion of the radiation model is given in Appendix C. The calculations of thermodynamic and transport properties are

explained in Appendices A, B, and D. The axisymmetric form of the Navier-Stokes equations will be used here. They may be written as

$$\frac{\partial(\rho u)}{\partial x}+\frac{1}{r}\frac{\partial(r\rho v)}{\partial r} = 0 \tag{2.3a}$$

$$\begin{aligned}\frac{\partial(\rho uu)}{\partial x}+\frac{1}{r}\frac{\partial(r\rho uv)}{\partial r} &= -\frac{\partial p}{\partial x}+\frac{\partial}{\partial x}(\mu\frac{\partial u}{\partial x})+\frac{1}{r}\frac{\partial}{\partial r}(\mu r\frac{\partial u}{\partial r})\\ &+\frac{\partial}{\partial x}(\mu\frac{\partial u}{\partial x})+\frac{1}{r}\frac{\partial}{\partial r}(\mu r\frac{\partial v}{\partial x})-\frac{2}{3}\frac{\partial}{\partial x}[\mu(\frac{\partial u}{\partial x}+\frac{1}{r}\frac{\partial(vr)}{\partial r})]\end{aligned} \tag{2.3b}$$

$$\begin{aligned}\frac{\partial(\rho uv)}{\partial x}+\frac{1}{r}\frac{\partial(r\rho vv)}{\partial r} &= -\frac{\partial p}{\partial r}+\frac{\partial}{\partial x}(\mu\frac{\partial v}{\partial x})+\frac{1}{r}\frac{\partial}{\partial r}(\mu r\frac{\partial v}{\partial r})\\ &+\frac{\partial}{r\partial r}(\mu r\frac{\partial v}{\partial r})+\frac{\partial}{\partial x}(\mu\frac{\partial u}{\partial r})-\frac{2\mu v}{r^2}\\ &-\frac{2}{3}\frac{\partial}{r\partial r}[\mu r(\frac{\partial u}{\partial x}+\frac{1}{r}\frac{\partial(vr)}{\partial r})]+\frac{2}{3}\frac{\mu}{r}(\frac{\partial u}{\partial x}+\frac{1}{r}\frac{\partial(vr)}{\partial r})\end{aligned} \tag{2.3c}$$

$$\begin{aligned}\frac{\partial(\rho uh)}{\partial x}+\frac{1}{r}\frac{\partial(r\rho vh)}{\partial r} &= \frac{\partial}{\partial x}(\frac{k_{eff}}{c_p}\frac{\partial h}{\partial x})+\frac{1}{r}\frac{\partial}{\partial r}(\frac{rk_{eff}}{c_p}\frac{\partial h}{\partial r})\\ &+u\frac{\partial p}{\partial x}+v\frac{\partial p}{\partial r}+\Phi+\alpha'\sum_i I_i-q_{\text{rad}}\end{aligned} \tag{2.3e}$$

where Φ is the viscous dissipation term given by

$$\begin{aligned}\Phi=\frac{4}{3}\mu[(\frac{\partial v}{\partial r})^2+(\frac{\partial u}{\partial x})^2]+\mu[(\frac{\partial v}{\partial x})^2+(\frac{\partial u}{\partial r})^2]+2\mu(\frac{\partial u}{\partial r})(\frac{\partial v}{\partial x})\\ -\frac{4}{3}\mu(\frac{\partial v}{\partial r})(\frac{\partial u}{\partial x})+\frac{4}{3}\frac{\mu}{r}[\frac{v^2}{r}-v(\frac{\partial u}{\partial x}+\frac{\partial v}{\partial r})]\end{aligned} \tag{2.3f}$$

Here, α' is the absorption coefficient that been calculated based on inverse Bremsstrahlung (Appendix B), q_{rad} is the radiation loss (estimated in detail in

Appendix C), and k_{eff} is the effective thermal conductivity including the radiation conduction term (discussed in Appendix C). The transport properties of hydrogen are given in Appendix D.

The conservation of laser beam energy is given by [56]

$$\frac{\partial P_i}{\partial s} = -\alpha' P_i \tag{2.4}$$

where P_i is the laser power of the ray "i" and "s" is the distance along the ray.

2.4 Nondimensional Compact Form of the Equations

The governing equations are put into nondimensional form. This enables the flow characteristics such as Mach number, Reynolds number, Prandtl number, etc. to vary independently [4]. The previous equations are nondimensionalized using the density value at the stagnation condition, ρ_0, the nozzle length, L, a reference velocity, U_0, the viscosity at inlet, μ_0, the value of thermal conductivity at inlet, k_0, the stagnation temperature at inlet, T_0 and the value of specific heat at inlet, c_{p0} . These parameters are used for nozzle flow problems.

The following definitions for the flow characteristics are adapted

$$Re = \frac{\rho_0 U_0 L}{\mu_0} \qquad Pr = \frac{c_{p0}}{k_0}\mu_0 \qquad Q_{ref} = \frac{\rho_0 U_0^3}{L} \tag{2.5a,b,c}$$

After some manipulation, the governing equation may be written in the following conservative transport form (see Table 2.1)

$$\frac{\partial(r\rho u\phi)}{\partial x} + \frac{\partial(r\rho v\phi)}{\partial r} = \frac{\partial}{\partial x}\left(r\Gamma^{\phi}\frac{\partial \phi}{\partial x}\right) + \frac{\partial}{\partial r}\left(r\Gamma^{\phi}\frac{\partial \phi}{\partial r}\right) + R^{\phi}(x,r) \tag{2.6}$$

Table 2.1. Transported governing equations for the flow field.

equation	ϕ	Γ^{ϕ}	S^{ϕ}
continuity	1	0	0
Axial momentum	u	$\frac{\mu}{R_e}$	$-r\frac{\partial p}{\partial x}+\frac{1}{R_e}\left(\frac{\partial}{\partial x}\left(\mu r\frac{\partial u}{\partial x}\right)+\frac{\partial}{\partial r}\left(\mu r\frac{\partial v}{\partial x}\right)\right.$ $\left.-\frac{2}{3}\frac{\partial}{\partial x}\left[\mu r\left(\frac{\partial u}{\partial x}+\frac{1}{r}\frac{\partial (vr)}{\partial r}\right)\right]\right)$
Radial momentum	v	$\frac{\mu}{R_e}$	$r-\frac{\partial p}{\partial r}+\frac{1}{R_e}\left(+\frac{\partial}{\partial r}\left(\mu r\frac{\partial v}{\partial r}\right)+\frac{\partial}{\partial x}\left(\mu r\frac{\partial u}{\partial r}\right)-\frac{2\mu v}{r}\right.$ $\left.-\frac{2}{3}r\frac{\partial}{\partial r}\left[\mu\left(\frac{\partial u}{\partial x}+\frac{1}{r}\frac{\partial (vr)}{\partial r}\right)\right]\right)$
Energy	h	$\frac{K_{eff}}{C_p R_e Pr}$	$ru\frac{\partial p}{\partial x}+rv\frac{\partial p}{\partial r}+\frac{r\Phi}{R_e}+r\sum_i \alpha_i I_i - rq_{\text{rad}}$

where Φ is the viscous dissipation term given by:

$$\Phi=\frac{4}{3}\mu\left[\left(\frac{\partial v}{\partial r}\right)^2+\left(\frac{\partial u}{\partial x}\right)^2\right]+\mu\left[\left(\frac{\partial v}{\partial x}\right)^2+\left(\frac{\partial u}{\partial r}\right)^2\right]+2\mu\left(\frac{\partial u}{\partial r}\right)\left(\frac{\partial v}{\partial x}\right)-\frac{4}{3}\mu\left(\frac{\partial v}{\partial r}\right)\left(\frac{\partial u}{\partial x}\right)+\frac{4}{3}\frac{\mu}{r}\left[\frac{v^2}{r}-v\left(\frac{\partial u}{\partial x}+\frac{\partial v}{\partial r}\right)\right]$$

2.5 Finite Volume Formulation

2.5.1 Transformation to Curvilinear Coordinates

A more accurate description of the boundary may be obtained by utilizing curvilinear coordinates. Thus, a transformation of the physical domain into a computational domain is necessary to resolve the transport equations . Appendix E gives a more detailed account of the grid generation used in this study. The grid lines divide the flow field into small control volumes, with scalar grid points located at their centers as shown in Fig. (2.1).

Two methodologies may be used to resolve the flow by the finite volume method. In the first, the conservative equations are transformed to the computational domain using one-to-one mapping. There, they are integrated over the computational domain. In the second method, the conservative equations are integrated directly in the physical domain, and the relations between the computational domain and the physical domain can be introduced through the matrix coefficients.

In the present study, the first methodology was selected. The non-staggered grid, in which all the variables are located at the cell center, was also used. The non-staggered method allows for the use of Cartesian components of velocity rather than the oriented covariant or contravariant components in a staggered grid [43, 46, 64, 58, 52, 1, 2, 69]. One control volume in the non-staggered grid reduces the algebraic complexity involved in the number of metric terms that must be stored. Also, the non-staggered grid can be extended to a multigrid system

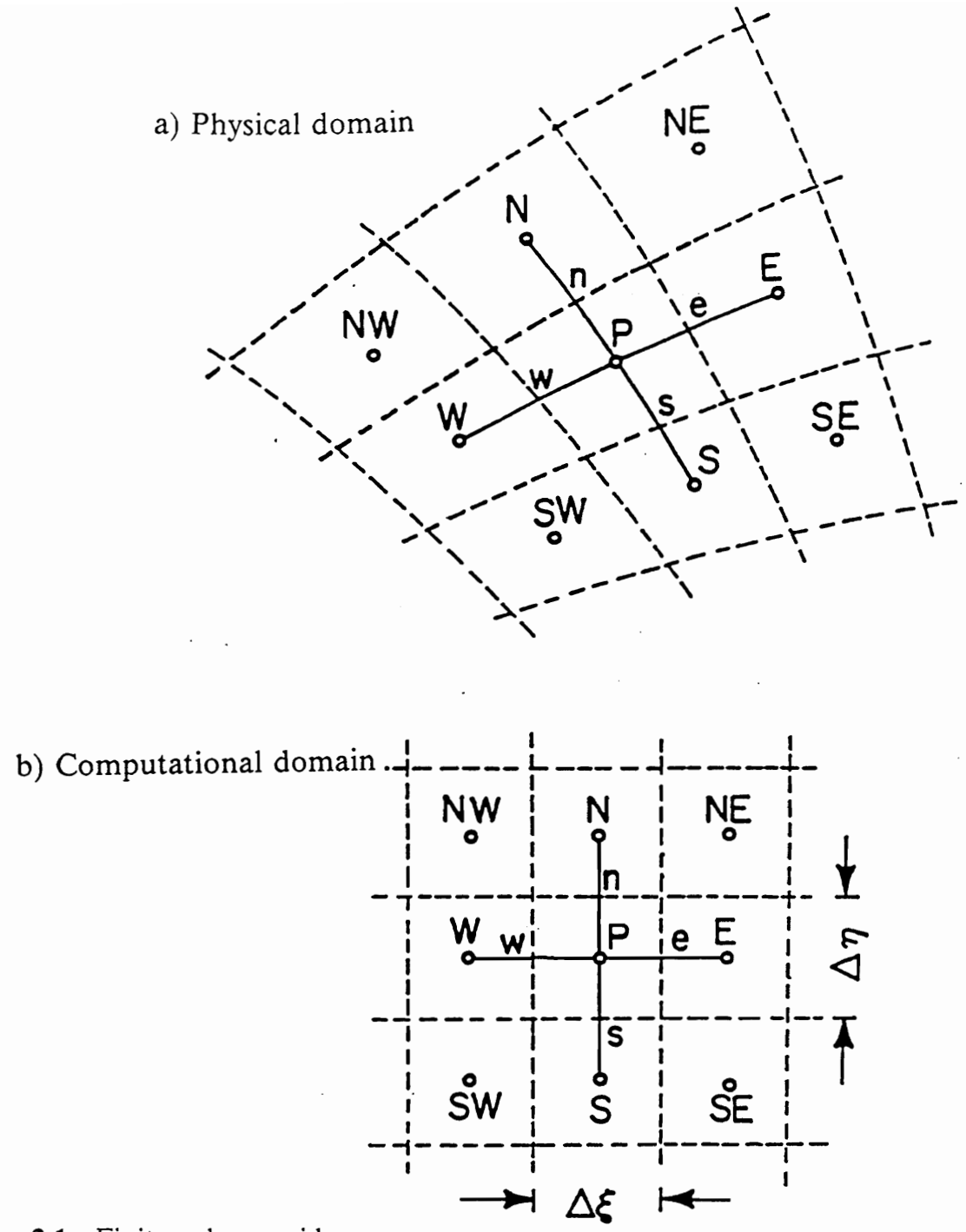

Figure 2.1. Finite volume grid

application. The application of a multigrid system for staggered grid requires a complex calculation and high cost [70].

The transport equations may be transformed into generalized coordinates ξ and η such that

$$\xi = \xi(x,r) \qquad \eta = \eta(x,r) \tag{2.7a,b}$$

The jacobian of the transformation is given as

$$J = \begin{vmatrix} x_\xi & x_\eta \\ r_\xi & r_\eta \end{vmatrix} \tag{2.8}$$

Using the chain rule of calculus, the following transformation of derivatives may be used

$$\frac{\partial}{\partial x} = \frac{1}{J}\left(r_\eta \frac{\partial}{\partial \xi} - r_\xi \frac{\partial}{\partial \eta}\right) \tag{2.9a}$$

$$\frac{\partial}{\partial r} = \frac{1}{J}\left(x_\xi \frac{\partial}{\partial \eta} - x_\eta \frac{\partial}{\partial \xi}\right) \tag{2.9b}$$

Using the above definitions in the transport eq. (2.6), yields

$$\begin{aligned} \frac{\partial(r\rho U\phi)}{\partial \xi} + \frac{\partial(r\rho V\phi)}{\partial \eta} &= \frac{\partial}{\partial \xi}\left[\frac{r\Gamma^\phi}{J}\left(q_1 \frac{\partial \phi}{\partial \xi} - q_2 \frac{\partial \phi}{\partial \eta}\right)\right] \\ &+ \frac{\partial}{\partial \eta}\left[\frac{r\Gamma^\phi}{J}\left(q_3 \frac{\partial \phi}{\partial \eta} - q_2 \frac{\partial \phi}{\partial \xi}\right)\right] + r\,J\,S_\phi\,(\xi,\eta) \end{aligned} \tag{2.10}$$

where U and V are the contravraiant velocity components given as

$$U = ur_\eta - vx_\eta \qquad V = vx_\xi - ur_\xi \tag{2.11a,b}$$

and q_1, q_2 and q_3 are given by

$$q_1 = x_\eta^2 + r_\eta^2 \qquad q_2 = x_\xi x_\eta + r_\xi r_\eta \qquad q_3 = x_\xi^2 + r_\xi^2 \tag{2.12a,b,c}$$

2.5.2 Integration of the Governing Equations

The transport equations for u, v and h may now be integrated over the control volume in the computational domain Fig. 2.1(b). The values at the cell faces are considered to be constant over the face and can be obtained assuming a given profile of the variables between the grid points. This profile will be discussed in detail later. The diffusion term will always be evaluated using central difference, which implies a linear profile been the cell's centers. Moreover, it is assumed $\Delta\xi = \Delta\eta = 1$. Thus, the integration for an axisymmteric grid may be written as follows

$$\int_0^{2\pi}\int_s^n\int_w^e \Bigg[\frac{\partial(r\rho U\phi)}{\partial\xi} + \frac{\partial(r\rho V\phi)}{\partial\eta} = \frac{\partial}{\partial\xi}\left[\frac{r\Gamma^\phi}{J}\left(q_1\frac{\partial\phi}{\partial\xi} - q_2\frac{\partial\phi}{\partial\eta}\right)\right] + \frac{\partial}{\partial\eta}\left[\frac{r\Gamma^\phi}{J}\left(q_3\frac{\partial\phi}{\partial\eta} - q_2\frac{\partial\phi}{\partial\xi}\right)\right] + r\,J\,S_\phi(\xi,\eta)\Bigg] d\xi\, d\eta\, d\zeta \tag{2.13}$$

The integration of the eq. (2.13) gives

$$F_e^\phi - F_w^\phi + F_n^\phi - F_s^\phi = \hat{S}_\phi \tag{2.14}$$

where F_e is the total flux of ϕ passing through the control volume face e, and $\hat{S}_\phi$ is the linearized average of the source term integrated over the control volume as given in Appendix F.

The total flux consists of two elements: convection and diffusion fluxes, which are denoted as F^c and F^d , respectively. The evaluation of these terms is given in the next section.

2.5.3 Flux Calculations

2.5.3.1 Convective Flux

Convective flux will be discussed here in detail for the east face in Fig. 2.1(b). The discussion can be applied to all the other faces and will not be repeated later. The expression for the convective flux at the east face, F_e^c, may be written as follows

$$F_e^c = (r\rho U)_e \phi_e \tag{2.15}$$

Special attention should be taken in the calculation of the variable ϕ at the cell faces. It is known that linear profiles, central differences, will produce oscillations in the solution [62]. In this study, a power-law profile given by Patankar et al [61] was used. The power law scheme is a curve fit to the exact solution for the one dimensional, steady state, diffusion-convection equation. It is accurate to the second order for a Peclet number less than 10 and to the first order upwind at a higher Peclet number. Peclet number is defined as the ratio of R_e and P_r and gives the ratio of convection to diffusion. The Peclet number at the east face is expressed as

$$P_e = \left| \frac{r\rho U}{r\Gamma^{\phi} q_1 / J} \right|_e \tag{2.16}$$

Based on Patankar [63, 12] , the convective flux and the orthogonal part of the diffusive flux at the east face may be written as follows

$$F_e^c = A(P_e) D_e (\phi_p - \phi_E) + (r\rho U)_e \tag{2.17}$$

where

$$A(P) = \max [0, (1 - 0.1 |P|)^5] \tag{2.18a}$$

and D_e is the diffusion coefficient given by

$$D_e = \left(\frac{r\Gamma^{\phi} q_1}{J} \right)_e \tag{2.18b}$$

The calculation of the mass flux term ($r\rho U$) at the cell face (east in the above equations) must be carried out carefully for a non-staggered grid system. Linear interpolation will produce wiggles in the pressure field as a result of decoupling between the pressure and density in incompressible flow problems [62, 69]. This issue will be discussed in some depth later.

2.5.3.2 Diffusion Fluxes

The diffusion fluxes are divided into two parts, the cross stream diffusion and the orthogonal diffusion. These fluxes are calculated using a central difference

scheme. The diffusion fluxes for the east face of the control volume, shown in Fig. 2.1 (b), are given by

$$F^d_e = D_e(\phi_E - \phi_P) + D^c{}_e(\phi_n - \phi_s)_e \tag{2.19}$$

where $D^c{}_e$ is the cross stream diffusion coefficient which for the east face is given by

$$D^c{}_e = \frac{(r\Gamma^\phi q_2)}{J}\Big|_e \tag{2.20}$$

The last term in eq. (2.19) involves the estimation of ϕ_n at the point e. This may be calculated by the linear interpolation between the adjacent nodal values, as shown in Fig. 2.1(b), and is given by

$$(\phi_n - \phi_s)_e = fx(\phi_n - \phi_s)_E + (1 - fx)(\phi_n - \phi_s)_P \tag{2.21a}$$

where fx is the linear interpolation factor. For equally spaced grid system eq. (2.21a) becomes

$$(\phi_n - \phi_s)_e = \frac{1}{4}(\phi_{NE} - \phi_{SE} + \phi_N - \phi_S) \tag{2.21b}$$

The scheme used in this study is implicit for the diffusion fluxes. However, a tridiagonal solver has been used to solve the discretized equation. Thus, the cross stream fluxes are treated explicitly and added to the source term of the equation to avoid producing a nine point implicit scheme. This treatment will

guarantee a five point scheme which can be solved using a tridiagonal solver by sweeping in both directions.

2.5.4 Final Formulation

Substituting with flux values given by eq. (2.17) and (2.21) into the transport equations and making use of the above mentioned linearization, the relation between the unknown values at point P and the neighboring nodes may be expressed as follows

$$\alpha_P \phi_P{}^{n+1} = \alpha_E \phi_E{}^{n+1} + \alpha_W \phi_W{}^{n+1} + \alpha_N \phi_N{}^{n+1} + \alpha_S \phi_S{}^{n+1} - D^c{}_e \left(\frac{\partial \phi}{\partial \eta}\right)_e + D^c{}_w \left(\frac{\partial \phi}{\partial \eta}\right)_w - D^c{}_n \left(\frac{\partial \phi}{\partial \xi}\right)_n + D^c{}_s \left(\frac{\partial \phi}{\partial \xi}\right)_s + S_P \phi_P{}^n + rJ\hat{S}^{\phi}(\eta, \xi) \tag{2.22}$$

where

$$\alpha_E = D_e A(P_e) + \max(0.0, -F_e) \tag{2.23a}$$

$$\alpha_W = D_w A(P_w) + \max(0.0, F_w) \tag{2.23b}$$

$$\alpha_S = D_s A(P_s) + \max(0.0, F_s) \tag{2.23c}$$

$$\alpha_N = D_n A(P_n) + \max(0.0, -F_n) \tag{2.23d}$$

$$\alpha_P = \alpha_E + \alpha_W + \alpha_S + \alpha_N + \max[0.0, (F_e - F_w + F_n - F_s)] \tag{2.23e}$$

$$S_P = \max[0.0, -(F_e - F_w + F_n - F_s)]\ \phi_p{}^n \tag{2.23f}$$

The last term in eq. (2.23e) represents the contribution of the integration of the continuity equation. Many authors have neglected this term assuming that the initial guess and the following iterations will force it to be zero. However, during the iterations, the continuity equation will not be satisfied immediately. Thus, this term should be included to insure the stability of the scheme, especially at higher Reynolds number flows. The cross stream diffusion is calculated explicitly and is lumped into the source term, represented by the $\hat{S}_P$.

2.5.5 Relaxation

The above scheme will guarantee the convergence of linear equations. However, in this study the system of the equation is highly nonlinear. To prevent divergence and to slow down the change between iterations, an under-relaxation factor is applied.

Introducing the under-relaxation factor ω into the discretized equation, the following expression may be developed

$$\frac{\alpha_P}{\omega}\phi_P{}^{n+1} = \alpha_E\phi_E{}^{n+1} + \alpha_W\phi_W{}^{n+1} + \alpha_N\phi_N{}^{n+1} + \alpha_S\phi_S{}^{n+1} + rJ\hat{S}^{\phi}(\eta, \xi) + \frac{1-\omega}{\omega}\alpha_P\phi_P{}^{n} \tag{2.24}$$

A typical values of ω is selected to be less than one to guarantee a smooth convergence of the suggested scheme.

2.6 Cell Face Velocity

To estimate the convective flux, the cell face velocities must be calculated. If a staggered grid is used, the velocities at the cell faces are directly given as the velocity values at the grid system used for the momentum equations. Thus, no

interpolation is needed between the nodal points to find the velocities at the cell faces. For a non-staggered grid, interpolation is needed to estimate the velocities at the cell faces, since they are known at the nodal points only. Special attention must be given to the velocity profiles assumed between nodes. Linear interpolation between nodes will decouple the pressure field from the momentum field, yielding a checkerboard pressure field [61, 1, 2, 48, 52, 58, 69, 64] . To overcome this shortcoming of a non-staggered grid treatment, a method was developed to avoid the occurrence of oscillatory pressure field in the solution [69, 64] . The method consists of determining the cell face velocities from the discretized form of the momentum equations, therefore ensuring the coupling of the velocity and the pressure field.

The primary test code for this method, (reported also by Majumdar and Miller et al [48, 58]) indicates that the solution is dependent on the choice of the under-relaxation factor. This dependency, which is caused by the linearization technique used in the discretization of the momentum equation, can be removed if the under-relaxation factor term is treated separately in the discretized momentum equations [43, 48, 58]. Recently, Kobayashi [44] succeeded in implementing Majumder 's method [48] for calculating the cell face velocities without the dependency on the under-relaxation factor and proving the validity of the method for compressible flow at all Mach numbers. The method is essentially the same as the one suggested by Rhie [70], however the linearization of the under-relaxation term has been performed differently, as will be discussed below.

Consider the discretized equations for points P and E of the grid system shown in Fig. 2.1(b). The equations for the x-momentum are written as follows

$$u_P^{n+1} = Bu_P - hu_P \left.\frac{\partial P}{\partial \xi}\right|_P + huc_P \left.\frac{\partial P}{\partial \eta}\right|_P + \hat{Su}_P + (1-\omega)\, u_P^n \qquad (2.25a)$$

$$u_E^{n+1} = Bu_E - hu_E \left.\frac{\partial P}{\partial \xi}\right|_E + huc_E \left.\frac{\partial P}{\partial \eta}\right|_E + \hat{Su}_E + (1-\omega)\, u_E^n \qquad (2.25b)$$

where

$$Bu_P = \frac{\sum_{i=\mathrm{E,S,W,N}} \alpha_i\, u_i}{\alpha_P} \qquad hu_P = \frac{rr_\eta}{\alpha_P} \qquad huc_P = \frac{rr_\xi}{\alpha_P} \qquad (2.26a,b,c)$$

The source term given in the eq. (2.25) is the same as in the eq. (2.24) except for pressure being included separately in eq. (2.25). The cell face velocity at point e may be obtained , similarly, to be

$$u_e^{n+1} = Bu_e - hu_e \left.\frac{\partial P}{\partial \xi}\right|_e + huc_e \left.\frac{\partial P}{\partial \eta}\right|_e + \hat{Su}_e + (1-\omega)\, u_e^n \qquad (2.27b)$$

where Bu_e and $\hat{Su}_e$ are calculated using a linear interpolation of the values at the the grid points in the physical plane and may be expressed as follows

$$Bu_e = \frac{[\overline{eE}\, Bu_P + \overline{Pe}\, Bu_E]}{(\overline{Pe} + \overline{eE})}$$

These formulations can be applied for both u-velocity and v-velocity at all cell faces . The method will guarantee a strong coupling between the velocity field and the pressure field, provided that the pressure gradient term is calculated by a central difference scheme at all cell faces.

2.7 Pressure Correction

Generally, the tentative velocity field, obtained by solving the momentum equations, will not satisfy the continuity equation. The reason is that the pressure field is given by the previous step, and it, therefore, is inaccurate for the new velocity field. Thus, the pressure field must be updated [61] . Since there is no explicit equation for estimation of the pressure, the continuity equation can be used to correct the pressure, and then, the velocity field in form of a predictor-corrector scheme. The method has been successfully used for incompressible flow cases [62, 1, 5, 8, 12, 23, 31, 43, 58, 66, 68, 74, 76]. Karki et al [37] extended that method to accommodate the case of compressible flow at various Mach numbers for a staggered grid system. Rhie et al and other had extended the method to a non-staggered grid [70, 44, 52, 64, 29]. The code developed for this study is based on the modifications that were introduced by the above mention researchers.

In the formulation used below, the superscript 'asterisk' indicates the modified pressure and velocity fields.

The u-velocity component may be determined implicitly as given by eq. (2.22)

$$u_P^* = Bu^*_P - hu_P \left.\frac{\partial P^n}{\partial \xi}\right|_P + huc_P \left.\frac{\partial P^n}{\partial \eta}\right|_P + \hat{Su}_P + (1-\omega)\, u_P^n \qquad (2.28a)$$

The corrected u-velocity may be written for the corrected pressure field as

$$u_P^{**} = Bu^{**}{}_P - hu_P \left.\frac{\partial P^*}{\partial \xi}\right|_P + huc_P \left.\frac{\partial P^*}{\partial \eta}\right|_P + \hat{Su}_P + (1-\omega)\, u_P^n \qquad (2.28b)$$

The relationship between the corrected pressure and velocity fields may be obtained by subtracting eq. (2.28b) from eq. (2.28a)

$$u_P` = - hu_P \left.\frac{\partial P`}{\partial \xi}\right|_P + huc_P \left.\frac{\partial P`}{\partial \eta}\right|_P \qquad (2.29)$$

where

$$P` = P^* - P^n \qquad u` = u^{**} - u^* \qquad (2.30a,b)$$

Similar expression may be obtained for the v-velocity correction

$$v_P` = - hv_P \left.\frac{\partial P`}{\partial \eta}\right|_P + hvc_P \left.\frac{\partial P`}{\partial \xi}\right|_P \qquad (2.31)$$

Comparing eq. (2.23) & (2.28), the corrections for the velocities at the cell faces e, n -as shown in Fig. 2.1(b)- may be written as

$$u_e` = - hu_e \left.\frac{\partial P`}{\partial \xi}\right|_e + huc_e \left.\frac{\partial P`}{\partial \eta}\right|_e \qquad (2.32a)$$

$$v_e` = - hv_e \left.\frac{\partial P`}{\partial \eta}\right|_e + hvc_e \left.\frac{\partial P`}{\partial \xi}\right|_e \qquad (2.32b)$$

$$v_n` = - hv_n \left.\frac{\partial P`}{\partial \eta}\right|_n + hvc_n \left.\frac{\partial P`}{\partial \xi}\right|_n \qquad (2.32c)$$

$$u_n` = - hu_n \frac{\partial P`}{\partial \xi} \Big|_n + huc_n \frac{\partial P`}{\partial \eta} \Big|_n \tag{2.32d}$$

The density field will respond to the correction in the pressure field as follows

$$\rho` = \left(\frac{\partial \rho}{\partial P}\right)_s P` \qquad K = \left(\frac{\partial \rho}{\partial P}\right)_s = \frac{1}{a^2} \tag{2.33a,b}$$

The flow is assumed to undergo an insentropic process, so that the $\frac{\partial \rho}{\partial P}$ is equal to the inverse of the speed of sound, while other references had assumed an isothermal process [24, 37]. However, at convergence, the pressure correction and the density correction will vanish. Both of the above assumptions have been applied in this study, and the results show that the isentropic process produces faster convergence than the isothermal one. Thus, in all the cases of this study, the isentropic assumption was used.

The continuity equation may be used to produce an equation for the pressure correction. The continuity equation for a general cell may be written as

$$F_e - F_w + F_n - F_s = 0 \tag{2.34}$$

where

$$F_e = r_e \rho_e [r_\eta u - x_\eta v]_e \qquad F_n = r_n \rho_n [r_\xi v - x_\xi v]_n \tag{2.35a,b}$$

The mass flux linearization for the east face may be written

$$F_e = r_e [\rho^n + \rho`]_e \; [r_\eta (u^* + u`) - r_\xi (v^* + v`)]_e \tag{2.36}$$

Thus

$$F_e = r_e\rho^n{}_e[r_\eta u^*{}_e - x_\eta v^*]_e + r_e\rho^n{}_e[r_\eta u' - x_\eta v']_e + r_e\rho'_e[r_\eta u^* - x_\eta v^*]_e + r_e\rho'_e[r_\eta u' - x_\eta v']_e \tag{2.37}$$

Each term of the above equation must be examined carefully to insure the proper correction and hence convergent solution. The first term represents the mass unbalance at the east face which results from use of the predicted velocity field. As stated previously, the cell face velocity must be estimated using the discretized momentum equation to insure a strong coupling of the pressure and velocity fields. Cell face density may be estimated using any scheme. In this study, linear interpolation has been used.

The second term represents the diffusion-like term. A second order scheme was used to estimate the pressure gradient needed to evaluate the cell face velocities. This will ensure the coupling of the pressure and velocity fields. Substituting of the eq. (2.32) into the second term, the pressure correction contribution of this term is written as

$$r_e\rho_e{}^n\Big[r_\eta|_e[\overline{huc}_e(\frac{\partial P'}{\partial\eta})_e - \overline{hu}_e(P'_E - P'_P)] - x_\eta|_e[-\overline{hv}_e(\frac{\partial P'}{\partial\eta})_e + \overline{hvc}_e(P'_E - P'_P)]\Big] \tag{2.38}$$

The bar in the above equation symbolizes the interpolation between grid points. The cross derivative term of eq. (2.38) was explicitly estimated. This allows for the use of a tridiagonal solver.

The third term represents the convective-like term. Special attention should be given to its discretization. Preliminary runs have shown the impact of the convective term on the scheme's stability. The term includes the density correction at the cell face. This correction must vanish for the incompressible flow limits. Thus, Mach number should be used as the governing parameter for the continuity equation, instead of the Peclet number used for the discretization of the transport equations. Thus, the convective-like term should exhibit the correct dependency of the discretized equation on the Mach number. The resulting equation should be elliptic for a subsonic regime, and hyperbolic in the supersonic regime, with a smooth transition form subsonic to supersonic. A first-order upwind scheme, based on the contravariant face velocity, has been used in the present study. This scheme has been recommended by Karki et al and Issa [37, 29] . Therefore, the density correction at the cell face is written

$$\rho`_e = \rho`_P \frac{\max[0,U_e]}{|U_e|} + \rho`_E \frac{\max[0,-U_e]}{|U_e|} \tag{2.39}$$

Introducing the pressure-density relations given by eq. (2.33) into eq. (2.39), the third term may be written as

$$r_e\left[K_P P`_P \max[0,U_e] - K_E p`_E \max[0,-U_e]\right] \tag{2.40}$$

where the contravariant velocity is

$$U_e = \left[r_\eta u^* - x_\eta v^*\right]_e \tag{2.41}$$

The fourth term, neglected by most researchers, represents the nonlinear correction. As the solution converges, this term will be negligibly small. However, during iterations, this may not be the case. Shyy et al [76] recommended to include this term to insure the scheme's stability. In this study, it was found that this term increases the convergence rate of the scheme. Thus, in the developed code, this term is treated explicitly and is included in the source term of the pressure correction equation.

The above derivation was given for the east face. Similar expressions for the other faces may be deduced following the same discussions as for the east face. Introducing all these terms for all the faces into the continuity equation, the final form of the pressure correction may be obtained as

$$a_P P'_P = a_E P'_E + a_W P'_W + a_N P'_N + a_S P'_S + Sc \tag{2.42}$$

where

$$a_E = r_e \rho^n{}_e [r_\eta \overline{hu} + x_\eta \overline{hvc}]_e + r_e K_E \max[0, -U_e] \tag{2.43a}$$

$$a_W = r_w \rho^n{}_w [r_\eta \overline{hu} + x_\eta \overline{hvc}]_w + r_w K_W \max[0, U_w] \tag{2.43b}$$

$$a_N = r_n \rho^n{}_n [x_\xi \overline{hv} + r_\xi \overline{huc}]_n + r_n K_N \max[0, -V_n] \tag{2.43c}$$

$$a_S = r_s \rho^n{}_s [x_\xi \overline{hv} + r_\xi \overline{huc}]_s + r_s K_S \max[0, V_s] \tag{2.43d}$$

$$a_P = r_e\rho^n{}_e[r_\eta\overline{hu} + x_\eta\overline{hvc}]_e + r_w\rho^n{}_w[r_\eta\overline{hu} + x_\eta\overline{hvc}]_w$$
$$+ r_n\rho^n{}_n[x_\xi\overline{hv} + r_\xi\overline{huc}]_n + r_s\rho^n{}_s[x_\xi\overline{hv} + r_\xi\overline{huc}]_s \qquad (2.43e)$$
$$+ r_eK_P\max[0, U_e] + r_wK_P\max[0, -U_w] + r_nK_P\max[0, V_n] + r_sK_P\max[0, -V_s]$$

$$Sc = -\Big[\, r_e\rho^n{}_e[r_\eta u^* - x_\eta v^*]_e - r_w\rho^n{}_w[r_\eta u^* - x_\eta v^*]_w$$
$$+ r_n\rho^n{}_n[x_\xi v^* - r_\xi u^*]_n - r_s\rho^n{}_s[x_\xi v^* - r_\xi u^*]_s\Big]$$
$$-\Big[r_e\rho`{}_e[r_\eta u` - x_\eta v`]_e - r_w\rho`{}_w[r_\eta u` - x_\eta v`]_w$$
$$+ r_n\rho`{}_n[x_\xi v` - r_\xi u`]_n - r_s\rho`{}_s[x_\xi v` - r_\xi u`]_s\Big] \qquad (2.43f)$$
$$-\left[r_e\rho^n{}_e\left[(r_\eta\overline{huc} + x_\eta\overline{hv})\frac{\partial p}{\partial\eta}\right]_e - r_w\rho^n{}_w\left[(r_\eta\overline{huc} + x_\eta\overline{hv})\frac{\partial p}{\partial\eta}\right]_w\right.$$
$$\left.+ r_n\rho^n{}_n\left[(x_\xi\overline{hvc} + r_\xi\overline{hu})\frac{\partial p}{\partial\xi}\right]_n - r_s\rho^n{}_s\left[(x_\xi\overline{hvc} + r_\xi\overline{hu})\frac{\partial p}{\partial\xi}\right]_s\right]$$

The first bracket term in the eq. (2.43f) , for source term, represents the mass flow rate unbalance caused by the inaccurate velocity and density fields. The purpose of the pressure correction equation is to eliminate this mass unbalance through a series of predictor-corrector procedures. The resulting fields are accurate enough if the Euclidean (L_2) norm of this term has been reduced by six orders of magnitude. The second bracket term is due to the continuity equation's linearization. This term can be estimated using the previous correction values, and it was found to be very useful for acccelerating the convergence of the scheme. The last bracketed term is due to the nonorthogonality of the grid. This term is treated explicitly, based on previous values, to allow for the use of a tridiagonal solver.

It is difficult to satisfy the continuity equation by solving the pressure correction equation just once. Instead, the pressure correction equation should be solved three or more times before updating the velocity and density fields. Appendix G, describes a modification for accelerating the convergence of a tridiagonal solver given by Patankar [62] and Van Doormal et al [79].

2.8 Artificial Dissipation

At high Reynolds numbers, artificial dissipation may be needed to suppress central difference spatial oscillations. A method was developed by Shamroth et al [74] using explicit addition of artificial dissipation. The explicit treatment of the artificial dissipation allows the programmer to control the amount of dissipation that is added. Hence, the dissipation can be enough to suppress the oscillation without deteriorating the solution accuracy.

Referring to the general transport eq. (2.10), the local cell Reynolds numbers in both ξ and η directions, respectively, may be defined as

$$Re_\xi = \frac{\rho ABS(U)}{\Gamma^\phi (x_\eta{}^2 + r_\eta{}^2)/J} \qquad Re_\eta = \frac{\rho ABS(V)}{\Gamma^\phi (x_\xi{}^2 + r_\xi{}^2)/J} \tag{2.44a,b}$$

The artificial dissipation term may be written as

$$\Gamma_{art} = \max\left[0.0,\left[\frac{\max(Re_\eta, Re_\xi)}{Re_{ec}} - 1.0\right]\right] \tag{2.45}$$

where Re_{ec} is the critical cell Reynolds number below which no artificial dissipation is necessary. A typical value of $Re_{ec} = 10$ is suggested by Shamroth

et al [74]. The artificial dissipation calculated by the eq. (2.45) is added to the effective dissipation and is used in the discretized equations.

In this study no artificial dissipation was found to be necessary. All the results are obtained without additional dissipation.

2.9 Boundary Conditions

A proper treatment of the computational domain boundaries is extremely important to convergence. The detailed derivation of the necessary physical and mathematical boundaries may be found in References [3, 8, 15, 25, 26]. The boundary conditions are problem dependent and they are discussed in Chapter III.

2.10 Optical Laser Beam Simulation

To close the system of equations, the laser conservation eq. (2.4) must be solved for the laser beam power. The incoming laser beam is focused by a lens with a focal length "f". Jeng et al [35] suggested that the focal point be placed a short distance downstream of the nozzle throat. The focal plane may be considered to be a point or a circle with a certain radius. The mathematical model assumes that the incoming beam consists of a number of rays. Neglecting beam refraction, the trace of each ray will be a straight line as shown in Fig. 2.2. Assuming a Gaussian distribution of the laser beam, the laser intensity I may be related to the total laser power P_T as follows

$$I = \frac{P_T}{2\sigma^2\pi(1 - e^{-(R_b/\sigma)^2})} \, e^{-(r/\sigma)^2} \tag{2.46}$$

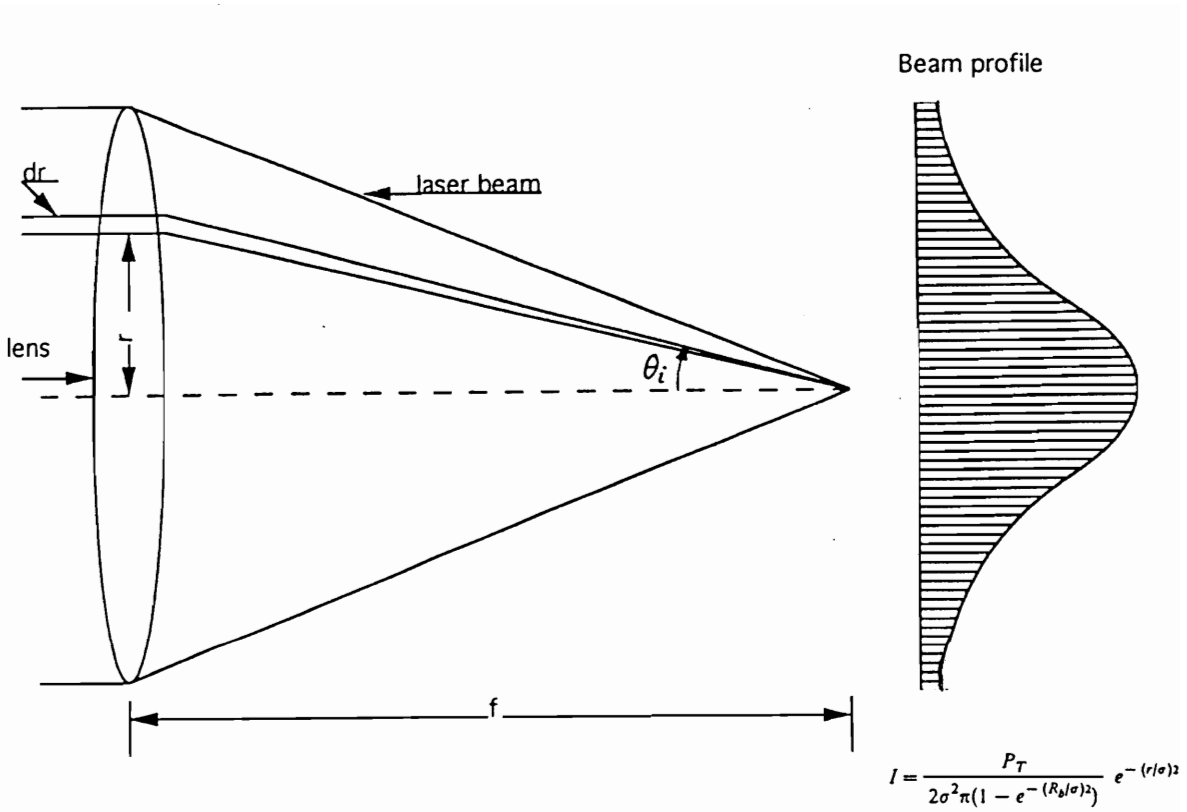

Figure 2.2. Geometry of laser beam

where σ = variance of the distribution is given by $= \frac{R_b}{2.0}$.

The power of any ray may be written as

$$P_i = 2\pi \int_{R_i}^{R_{i+1}} I\, r\, dr \qquad i = \text{ray number} \tag{2.47}$$

The equation governing the local beam energy at any point in the nozzle is obtained from geometrical optics. The incoming beam is split into a number of separate rays, each propagating in a straight line as shown in Fig. 2.2. The equation for the laser beam absorption is written as

$$\frac{\partial P_i}{\partial s} = -\alpha' P_i \tag{2.48}$$

The absorption coefficient, α', is a function of the gas pressure and temperature. The calculation of the absorption coefficient, developed in Appendix B, is based on the work of Kemp [42] . The laser energy equation applied to two stations that represent east and west faces of a cell, with the grid point in the cell center, can be written as

$$P_i^{j+1} = P_i^j \exp\left[-\frac{x_\xi \alpha'}{\cos \theta_i} \right] \tag{2.49}$$

where θ_i is the ray angle, as shown in Fig. 2.2.

The power absorbed into the cell may be found by subtracting P^j from both sides of eq. (2.49) and is given by

$$P_{add} = P_i^j \left[1.0 - \exp(- \frac{x_\xi \alpha'}{\cos \theta_i}) \right] \tag{2.50}$$

This power is considered as energy added for all the cells that lay on the path of a laser ray.

2.11 Solution of the Linearized Equation

As stated previously, a tridiagonal solver is used to solve the momentum, pressure correction, and energy equations. The linearized system of equation is, however, based on five point algorithm. Thus, an alternative direction sweep in both ξ and η is used. A typical equation may be written as

$$a_P \phi_P = a_E \phi_E + a_W \phi_W + a_N \phi_N + a_S \phi_S + Sc \tag{2.51}$$

The sweep in the ξ direction indicates solving the equation line by line in that direction while substituting available values of ϕ along the neighboring lines. The resulting equation becomes

$$a_P \phi_P - a_N \phi_N - a_S \phi_S = (a_E \phi^*_E + a_W \phi^*_W) + Sc \tag{2.52}$$

The * denotes the available values of ϕ . Equation (2.52) can be solved by a tridiagonal solver. The details of the algorithm may be found in Anderson et al [3]. After completing the sweep in the ξ direction, the sweep in η direction can be applied by substituting the values of the neighboring north and south lines with the most recent values.

Vectorization of the tridiagonal solver reduces the CPU time and the cost of the program. The LU decomposition phase is performed in a vectorized sense over the vector of lines to be solved. The back substitution is performed in scalar mode, since the most recent values for ϕ are used to compute the source term in the equation (2.52).

To increase the convergence rate of the tridiagonal solver, two methods can be used. Van Doormal et al [79] suggested the use of over-relaxation factor for the values obtained from the previous iteration. Patankar et al suggested the use of a block correction procedure [61]. The details are given in Appendix G .

2.12 Convergence Criteria

The governing equations are highly nonlinear. The linearization is intended to reduce the computational effort and allow for the use of a tridiagonal scheme. Several criteria were tested to insure stability and convergence of the scheme. During the solution of a given discretized equation (momentum, pressure correction or energy) the iterations are continued until the convergence of this equation is reached. The convergence is checked by calculating the Euclidean norm of the residual. A typical value of the Euclidean norm of the residual is selected to be less than or equal to 10^{-8}. This will guarantee a convergence within a given step.

The scheme reaches adequate convergence when the total mass unbalance is reduced to a very small value. The mass unbalance is checked locally for a given cell and globally for the summation over the computational domain. The total mass unbalance for the domain is

$$\varepsilon = \sum_{i=1}^{i=mx} \sum_{j=1}^{j=my} \left[(r\rho U)^*_{i+1j} - (r\rho U)^*_{i-1j} + (r\rho V)^*_{ij+1} - (r\rho V)^*_{ij-1} \right] \qquad (2.53)$$

A typical value of $\varepsilon = 10^{-8}$. This will guarantee the convergence of the scheme. The same value of ε is used to check the maximum value of the mass unbalance over a cell.

The steady state solution is reached by checking the Euclidean norm of the variation for all variables over all grid points, normalized with the initial Euclidean norm. At least a third order reduction in magnitude is required before the calculations are stopped. The Euclidean norm of the variation for a general variable is defined as follows

$$\|\varepsilon^{\phi}\| = \left[\sum_{i=1}^{i=mx} \sum_{j=1}^{j=my} (\phi^{n+1} - \phi^n)^2 \right]^{1/2} \qquad (2.54)$$

2.13 Calculation Procedure

All the elements of the scheme have been examined and are ready to be integrated into the main code. The solution procedure is summarized in Fig. 2.3. The main steps of the code PBNS are

1. Guess the velocity, pressure and temperature fields. The initial conditions or the previous step solution may be used.

2. Update the density, enthalpy, specific heat, viscosity and all flow properties from the assumed pressure and temperature fields.

3. Evaluate the coefficients for the momentum equation and solve for the new velocity fields u^* and v^*.

4. Calculate the velocity at the interface using eq. (2.25) and the mass unbalance resulting from the new velocity fields.

5. Calculate the coefficients for the pressure correction equation given by eq. (2.42). The nonlinear terms in this equation are estimated using the current available values.

6. Solve the pressure correction equation for P'. Correct the pressure field by eq. (2.30a), velocity fields by eq. (2.31), and density field by eq. (2.33). Since a tridiagonal solver is used, several cycles are implemented to ensure sufficient conversion of the residual of the pressure correction equation.

7. Solve the energy equation for the laser beam, eq. (2.48), and compute the heat energy added to each grid cell .

8. Evaluate the coefficients for the energy equation and solve for the static enthalpy.

9. Calculate the new temperature field using the pressure and the enthalpy fields.

10. Update all the thermodynamic and transport properties of the flow using the new temperature and pressure fields.

11. Check the convergence by calculating the total mass unbalance of the continuity eq. (2.53). Also calculate the Euclidean norm of the variation.

12. Repeat steps 2 through 11 until a steady solution is reached.

2.14 Summary

In this chapter, the conservation of mass, momentum, and energy in a steady axisymmetric form is transformed into a generalized curvilinear transport equation. This equation is discretized using a finite volume technique in conjunction with the power-law for convection-diffusion over non-staggerd curvilinear grid. The implementation of the pressure-weighted interpolation method is introduced to avoid a decoupling of pressure and velocity fields. The pressure correction equation is derived and discretized. The treatment of the density and pressure gradient terms is discussed and it is found that the density correction scheme should be calculated by an upwind biased scheme. The treatment of the nonlinear term, together with the solution of the resulting linear systems, is presented. The conservation equation for the laser energy is discretized along the beam ray. The convergence criteria are applied to insure a fast and

stable solution. Finally, the overall features of the suggested method are summarized, and the formulation for the entire scheme is provided.

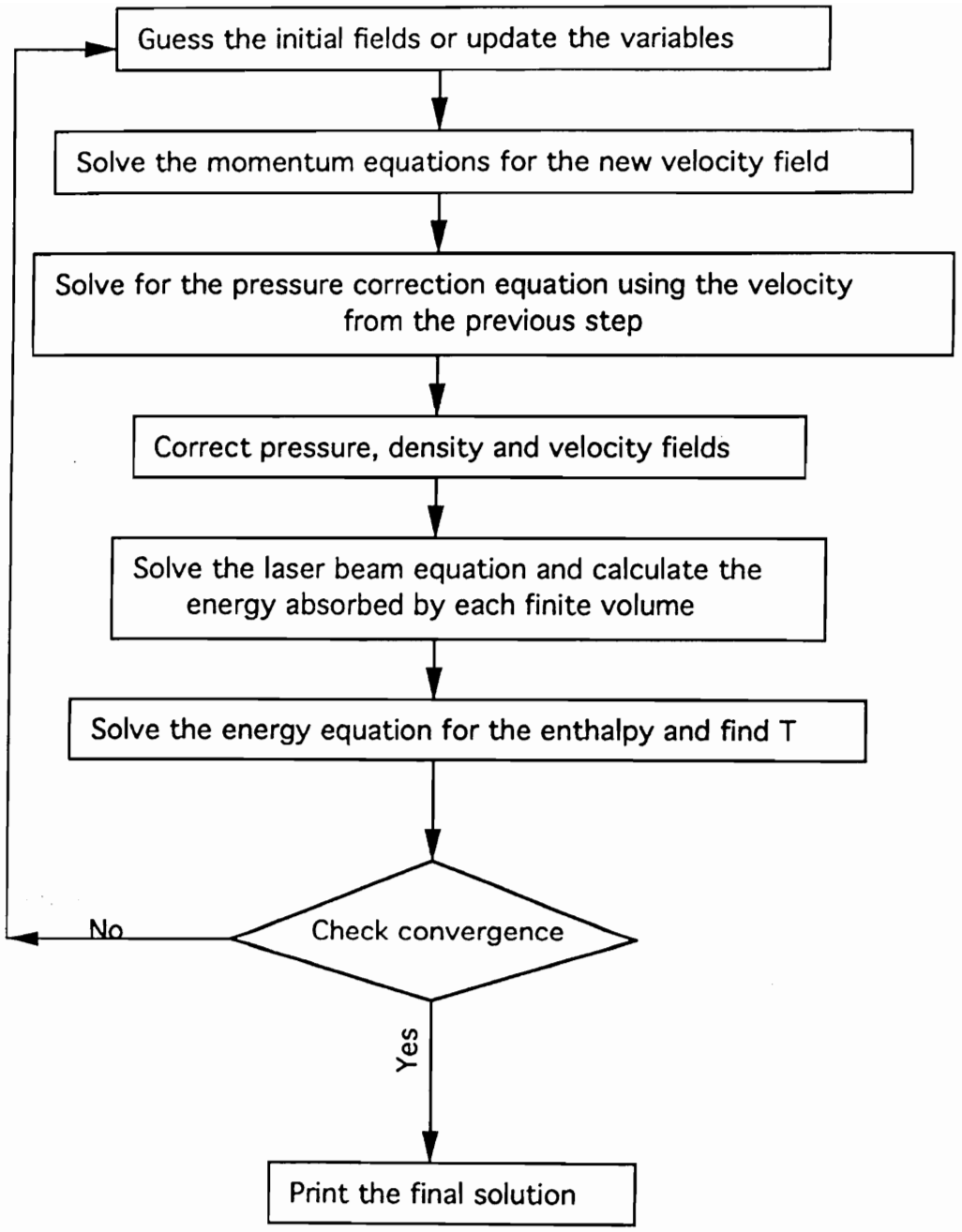

Figure 2.3. Flow chart of the Navier-Stokes solver (PBNS)

Chapter III

TWO APPLICATIONS OF PBNS CODE TO FLOW PROBLEMS

3.1 Introduction

In this Chapter, solutions to two test flow problems are obtained using the pressure-based Navier Stokes solver (PBNS). The first problem is flow over an insulated wall with a zero angle of attack. The solution to this problem is tested by comparing it with an exact solution to the compressible boundary layer equations. The second problem is an internal flow in an axisymmetric nozzle where both subsonic and supersonic regions exist. The goal of this chapter is to test the ability of the PBNS to handle various flow problems before an application to the laser engine may be considered.

3.2 Validation of PBNS code by Calculating Boundary Layer over a Flat Wall

A flow over a flat wall is selected to be the first test case of the developed Pressure-Based Navier-Stokes Solver code (PBNS). This flow is governed by the boundary layer equations, for which exact solution exists. In this study, the exact solution is obtained using Levy-Lees transformation and is compared with the results produced by the PBNS code. A schematic of the flow is shown in Fig. 3.1.

The following assumptions are used: subsonic flow with a free stream Mach number of 0.5, insulated flat plate, perfect gas relations, Reynolds number of 10^4 based on the plate length, and Prandtl number of 0.72.

3.2.1 Computational Mesh

The computational mesh used for the flat wall is shown in Fig. 3.1. The grid is constructed of 91 equally spaced grid points in the streamwise direction and 31 points in the transverse direction. An algebraic stretching along the top solid wall is implemented to resolve the large gradient in the viscous boundary layer. Figure 3.1 represents the cell center points. Since equal control volume cells are preferable, a shifting for the cell centers along the boundary is used, as shown in Fig. 3.1.

3.2.2 Boundary Conditions

3.2.2.1 Inlet Condition

Since the flow is subsonic at the leading edge of the plate, three characteristics enter the computational domain, and only one characteristic comes from the internal solution. This means that three properties have to be imposed on the

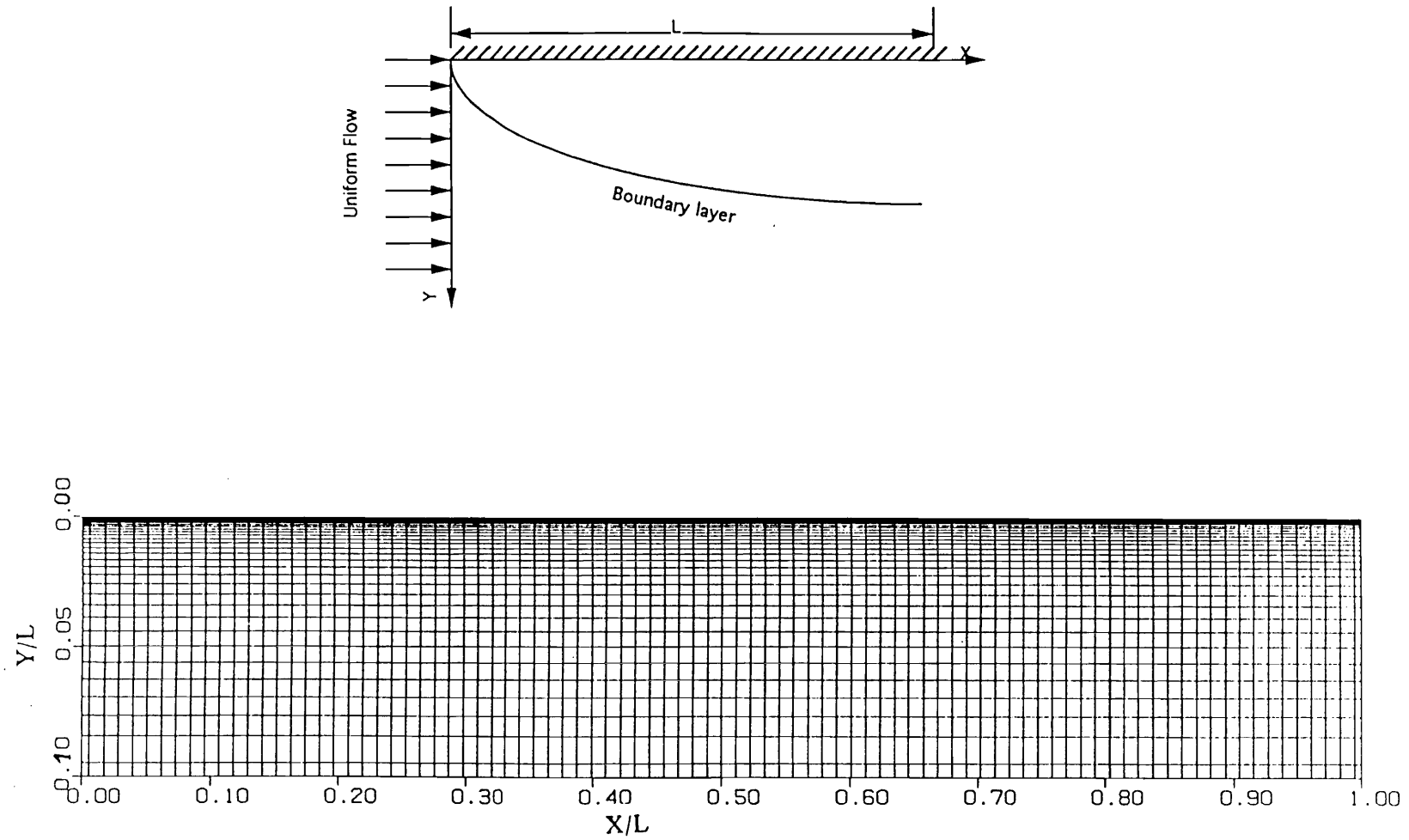

Figure 3.1. 91x 31 grid cell centers used for the calculation of the boundary layer.

boundaries, while one property should be extrapolated from the interior domain. In the calculations, three different ways to implement these subsonic inlet conditions are used. These are distinguished by case I , II , and III.

Case I : The flow is assumed to be isentropic which can correctly be modeled by setting the total pressure and the total temperature to be constant and equal to the free stream condition. The flow direction has been assumed to produce horizontal free stream lines at the leading edge. The u velocity is extrapolated from the interior domain using zero order extrapolation. These conditions may be casted in the following mathematical form

$$P_o = constant \qquad T_o = constant \qquad \tan^{-1}[v/u] = 0.00 \tag{3.1a,b,c}$$

$$u_{i,j} = u_{i+1,j} \quad , i = 1 \tag{3.1d}$$

Case II In this case, the flow is the same as in the case I , expect that the u velocity is determined from the upstream-running Riemann invariant. The downstream- running Riemann invariant R^{-1} , based on the total velocity, is extrapolated from the interior using zero order extrapolation by

$$R_{in}^{-1} = [\,\overline{V} - \frac{2a}{\gamma - 1}\,]_{i+1,j} \tag{3.2}$$

where a is the speed of sound. Knowing the total temperature and using the isentropic relations, the velocity at the leading edge is given by

$$\overline{V}_{in} = [(\gamma - 1)R^{-1} + \frac{\sqrt{4(\gamma + 1)h_o - 2(\gamma - 1)(R^{-1})^2}}{(\gamma + 1)}]_{in} \tag{3.3}$$

where h_o is the total enthalpy at the inlet. The individual velocity components may be determined from the flow angle relation given by the eq. (3.1c) The pressure and temperature may then be found from the isentropic relations. The details of this method are found in Ref. [11].

Case III : This case is called a non-reflecting boundary condition. It uses the characteristic variables at the inlet. The details of this method are given in Appendix H.

3.2.2.2 Exit Condition

At the subsonic exit, three characteristics will be upstream running. Three flow variables are extrapolated from the interior using zero order extrapolations. These are u, v, and h. Only one variable is imposed on the exit flow. The pressure is selected to be fixed on the outlet flow, and its value is set to be equal to the static pressure of the free stream. The exit flow includes both the right (i = Imax) , and the lower (j = Jmax) boundaries.

3.2.2.3 Wall Condition

At the wall (y = 0.0), the no-slip and no penetration conditions have been assumed for the velocity vector. The wall is assumed to be insulated, i.e., the gradient of the temperature is set to be zero. The fourth boundary condition imposes a zero normal gradient of the pressure at the wall. This condition is justified for high Reynolds number viscous flow.

3.2.3 Results and Analysis

A full Navier Stokes equation for 2-D laminar flow has been solved using the pressure-based solver (PBNS). A Reynolds's number of 10000 is defined as

$$R_e = \frac{\rho_{ref} U_{ref} L}{\mu_o} \tag{3.4}$$

where ρ_{ref} is the reference density of 1 kg/m^3 and U_{ref} is the free stream velocity of 1 m/sec, L is the wall length of 1 m, the reference temperature of 1 K, the isentropic exponent γ is 1.4, and the total pressure and the total temperature at the inlet are calculated using the inlet Mach number and the isentropic relations. The reference viscosity is calculated from the given Reynolds number. All the variables are nondimensionalized using the reference values as discussed in Chapter II.

The power law scheme is used to discretize the transport equations as given in Chapter II. The discretized equations for momentum, pressure-correction and energy are solved implicitly using a five point algorithm by ADI method (Alternative Direction Implicit). An under-relaxation factor of 0.60 has been selected after several trials as an optimum value for obtaining the solution of the flat wall problem. No limeters or artificial viscosity is used to obtain the solution.

The results for the different inlet boundary conditions, cases I , II and III, are provided in Fig. 3.2 - 3.4. The exact solution is obtained for a compressible flow over insulated flat plate by using Levy-Lees transformation to obtain the similar solution for the boundary layer equation. The numerical results have been normalized using free stream velocity, free stream temperature and the local

Reynolds number. The figures show the normalized profiles starting from station 5 (x = 0.0389) to station 91 at the end of the plate (x = 1.00).

The results for the case I are shown in Fig. 3.2(a,b,c), compared to the exact similar solution. Figure 3.2(a) shows a comparison between the normalized numerical velocity in the X-direction and the self similar u-velocity which is obtained using 100 points in the Y-direction. The results of comparison show a very good agreement between the PBNS calculations and the exact solutions especially near the wall where a dense grid is used. Figure 3.2(b) shows the comparison for the normalized temperature profile. The computational results agree very well, with a maximum temperature ratio of 1.042 at the wall surface. Figure 3.2(c) shows the normalized numerical velocity in the Y-direction for the different stations. These results show a good profile especially near the wall. The slight difference between the profiles near the free-stream boundary may be related to the assumption of vanishing of the v-velocity component at the leading edge plane of the wall. This behavior has been reported by other researchers. Figure 3.2(d) shows the converging history of the Euclidean (L_2) norm for the variations in the u and v components , the pressure and the temperature. These values have been normalized using the norm variation at the first step.

Figures 3.3(a,b,c) show the computational solutions for the flat wall for the case II at the leading edge boundary. The results are in good agreement, however, it is noticed that this case of the inlet boundary conditions yielded a maximum temperature of 1.0418 at the wall which is less than for the case I.

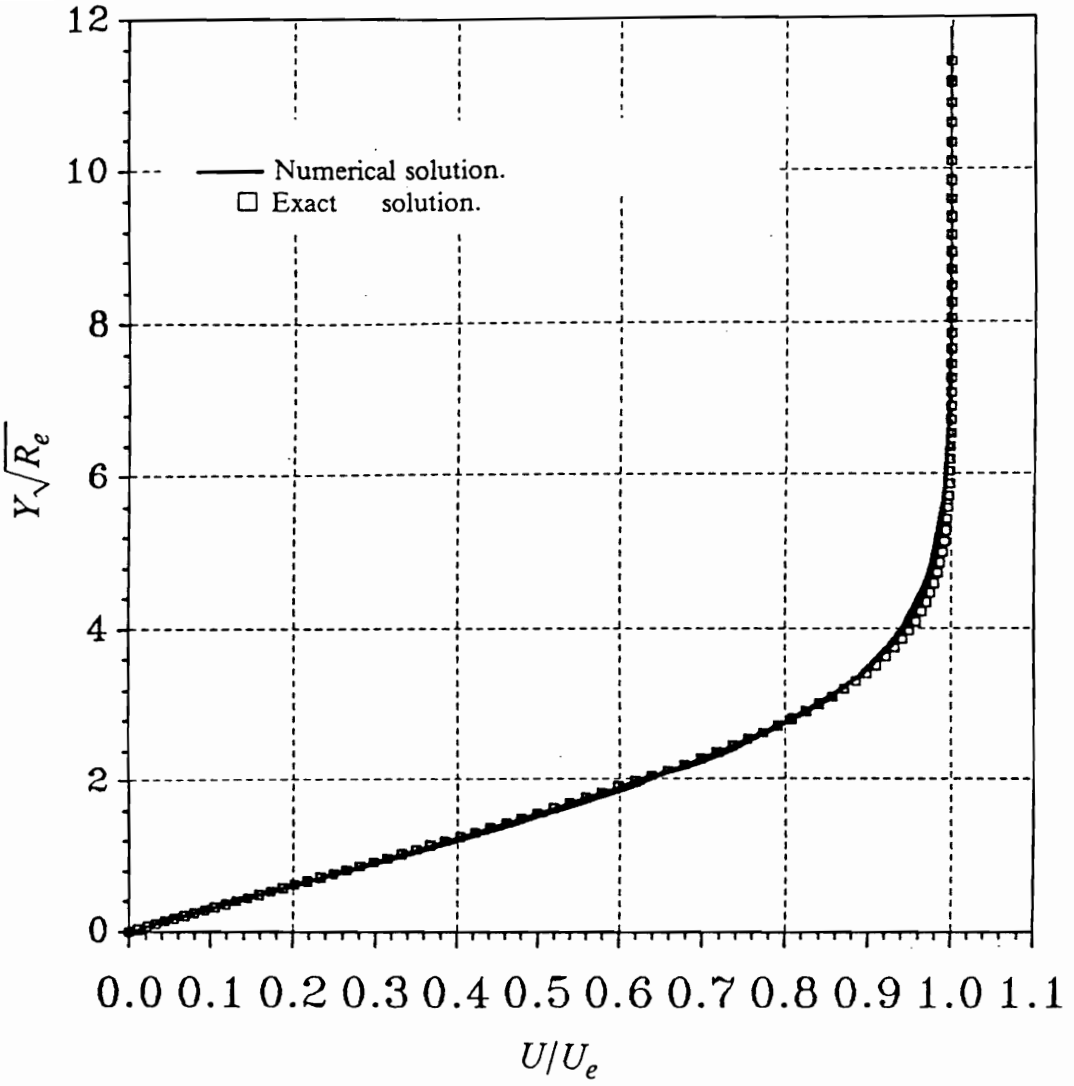

Figure 3.2. (a) Normalized u-velocity profile compared with the exact solution. Case I.

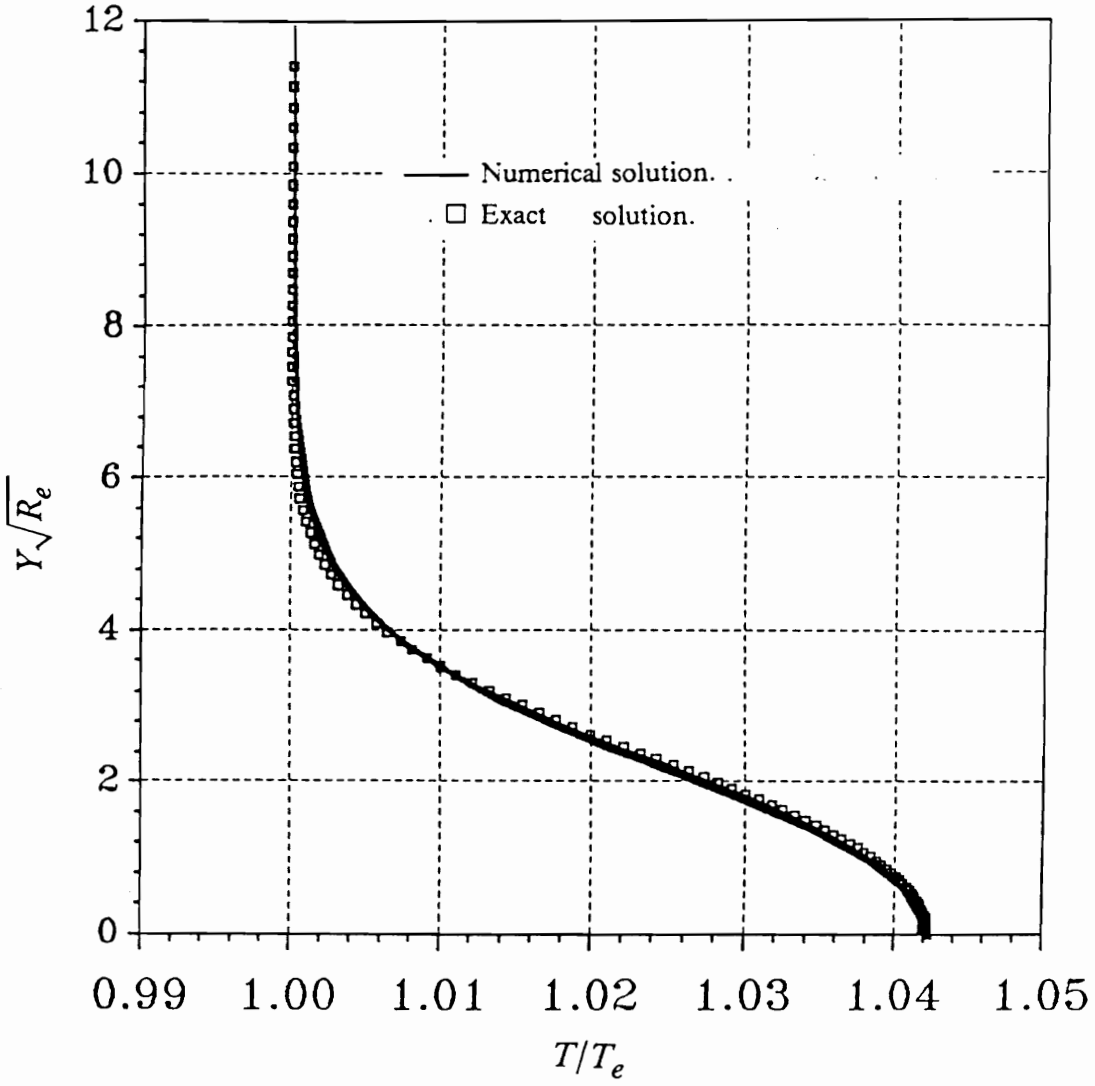

Figure 3.2. (b) Normalized temperature profile compared with the exact solution. Case I.

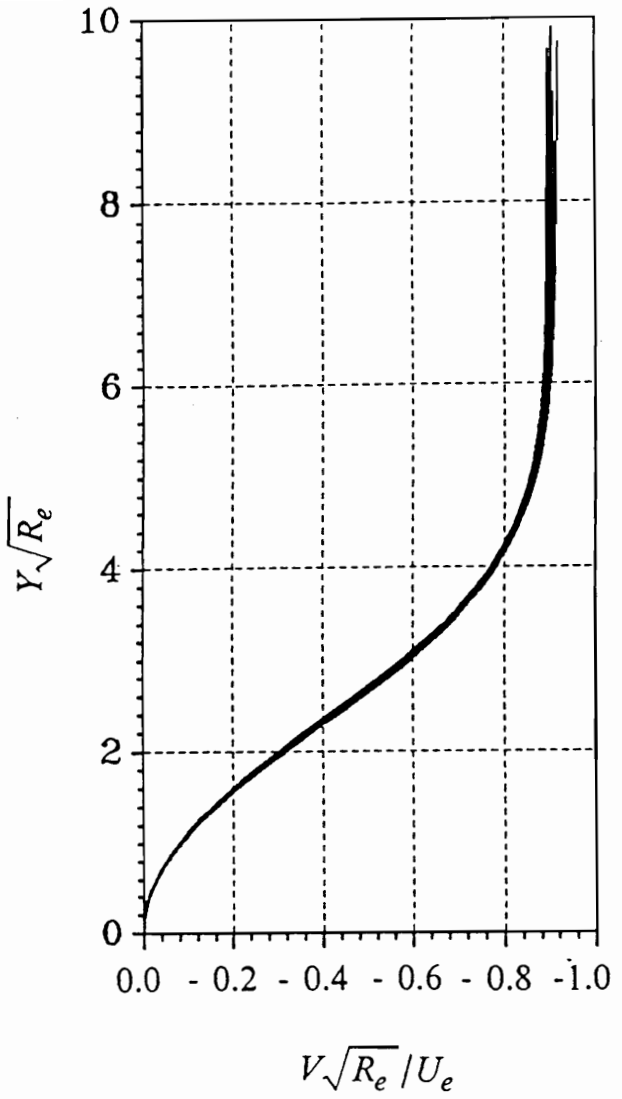

Figure 3.2. (c) Normalized v-velocity profile Case I.

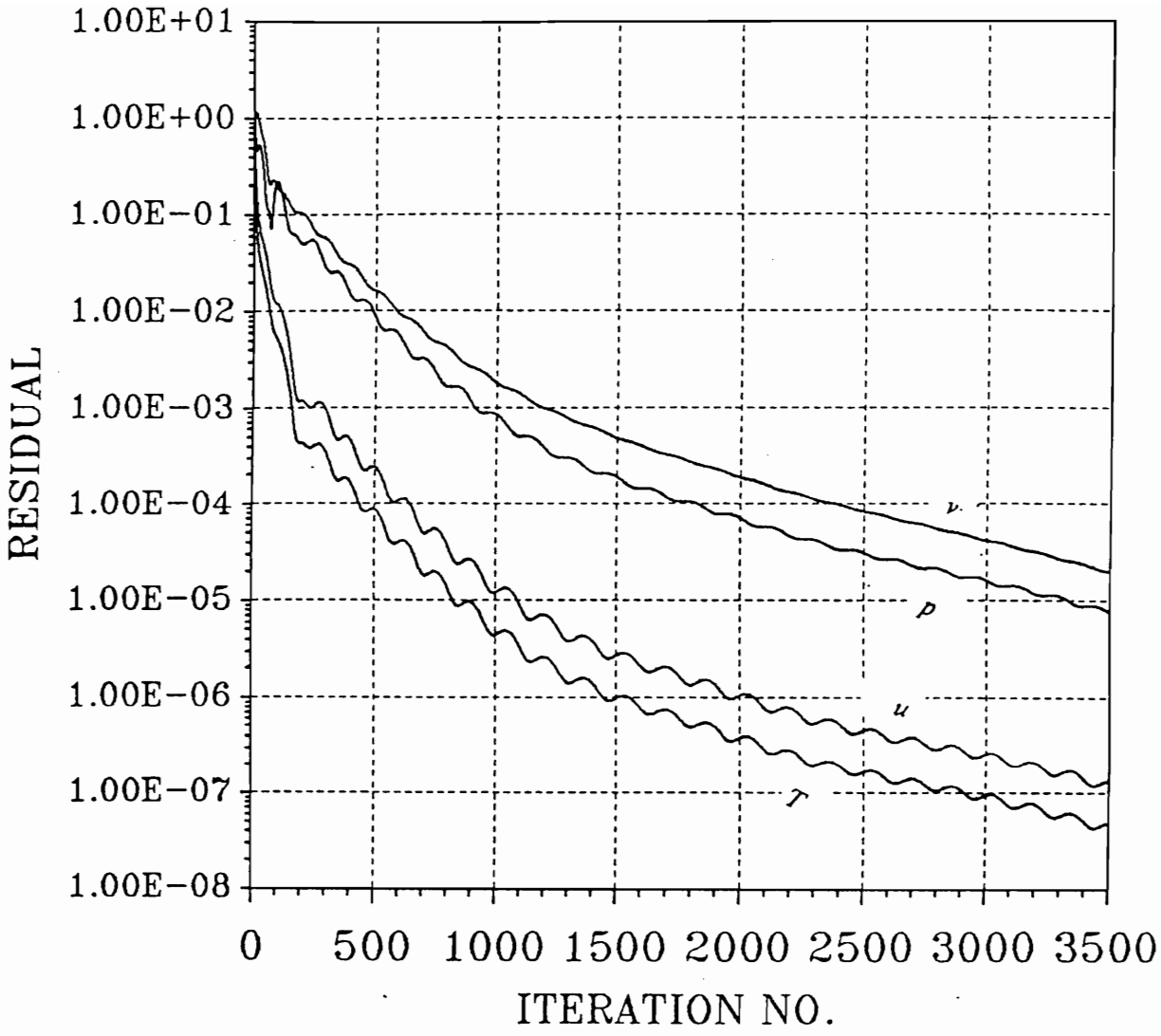

Figure 3.2. (d) Convergence history of norm of variation Case I.

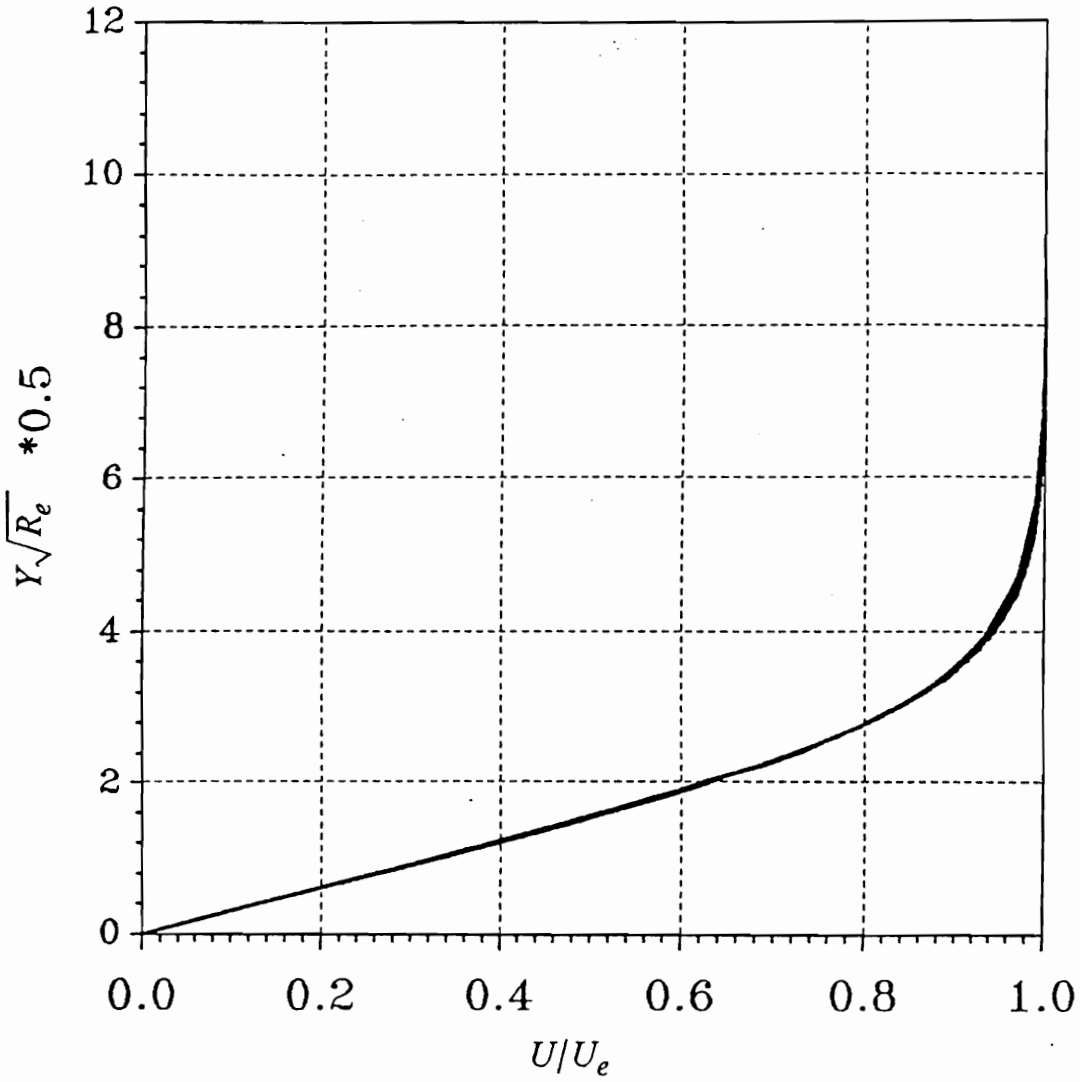

Figure 3.3. (a) Normalized u-velocity profile Case II.

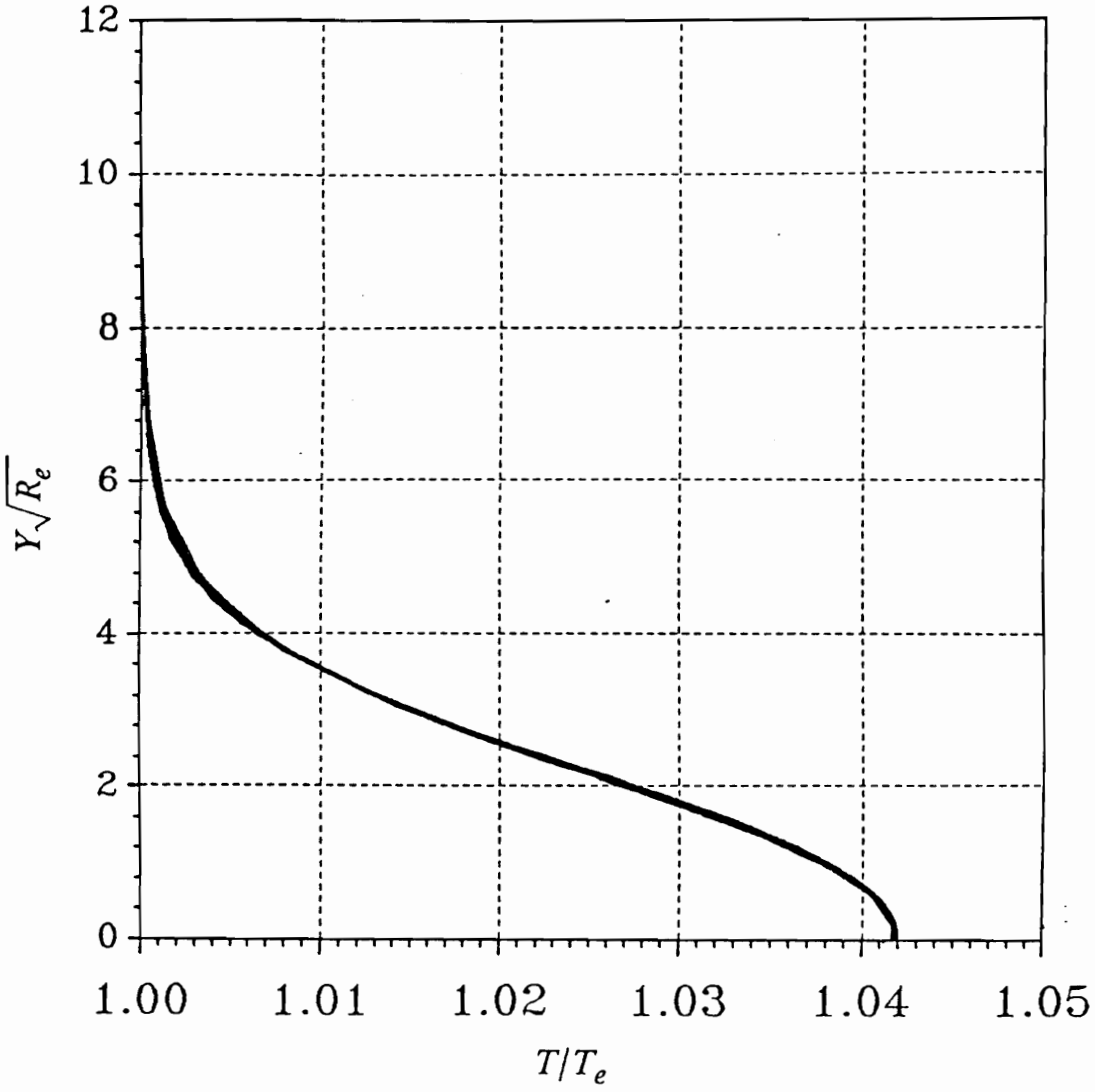

Figure 3.3. (b) Normalized temperature profile Case II.

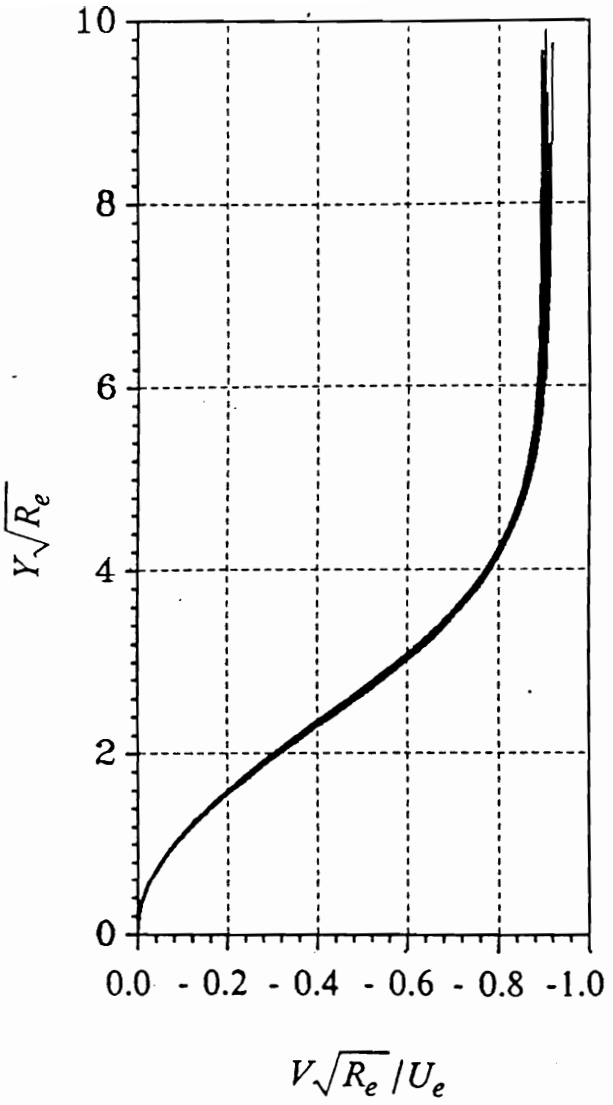

Figure 3.3. (c) Normalized v-velocity profile Case II.

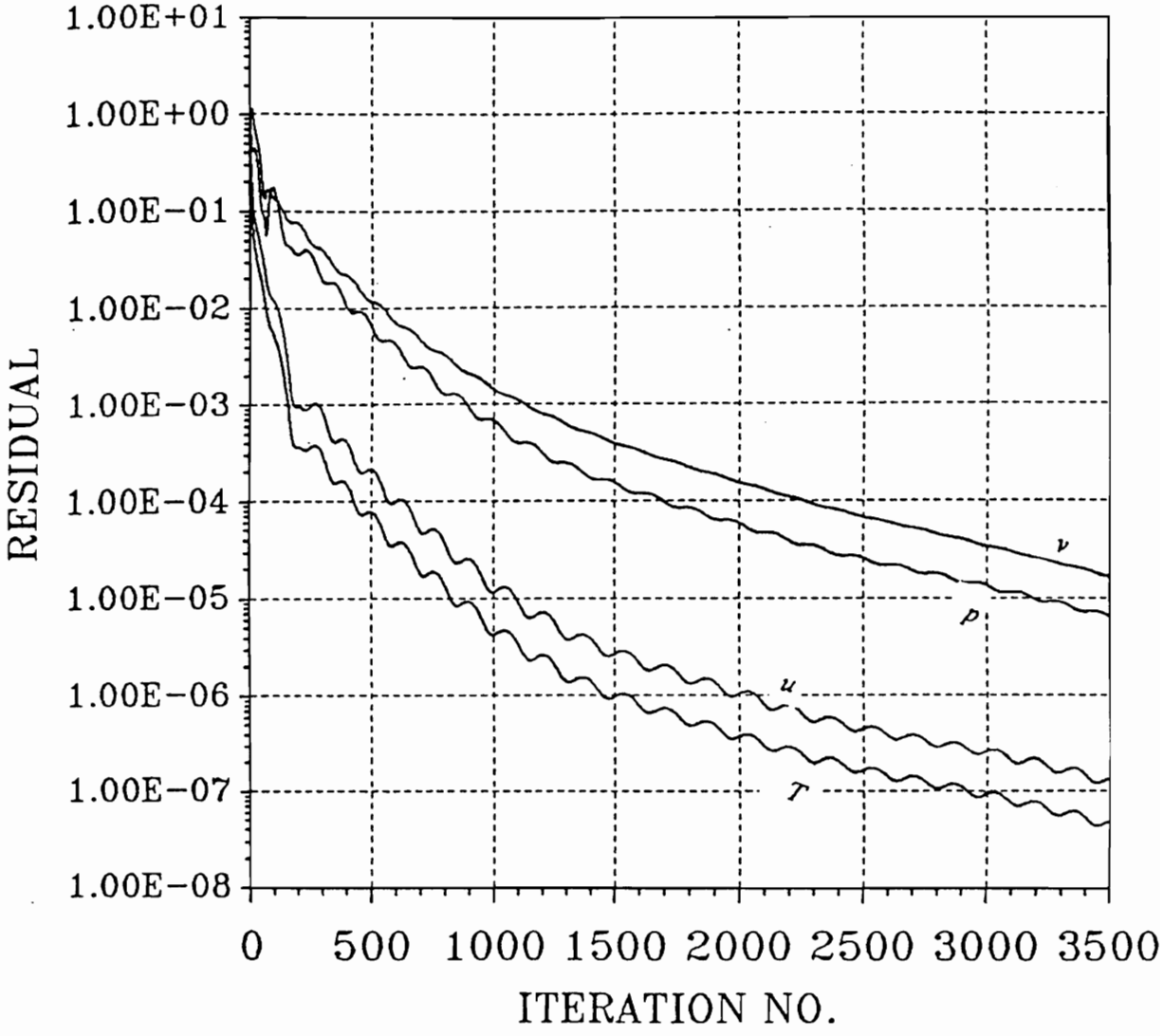

Figure 3.3. (d) Convergence history of norm of variation Case II.

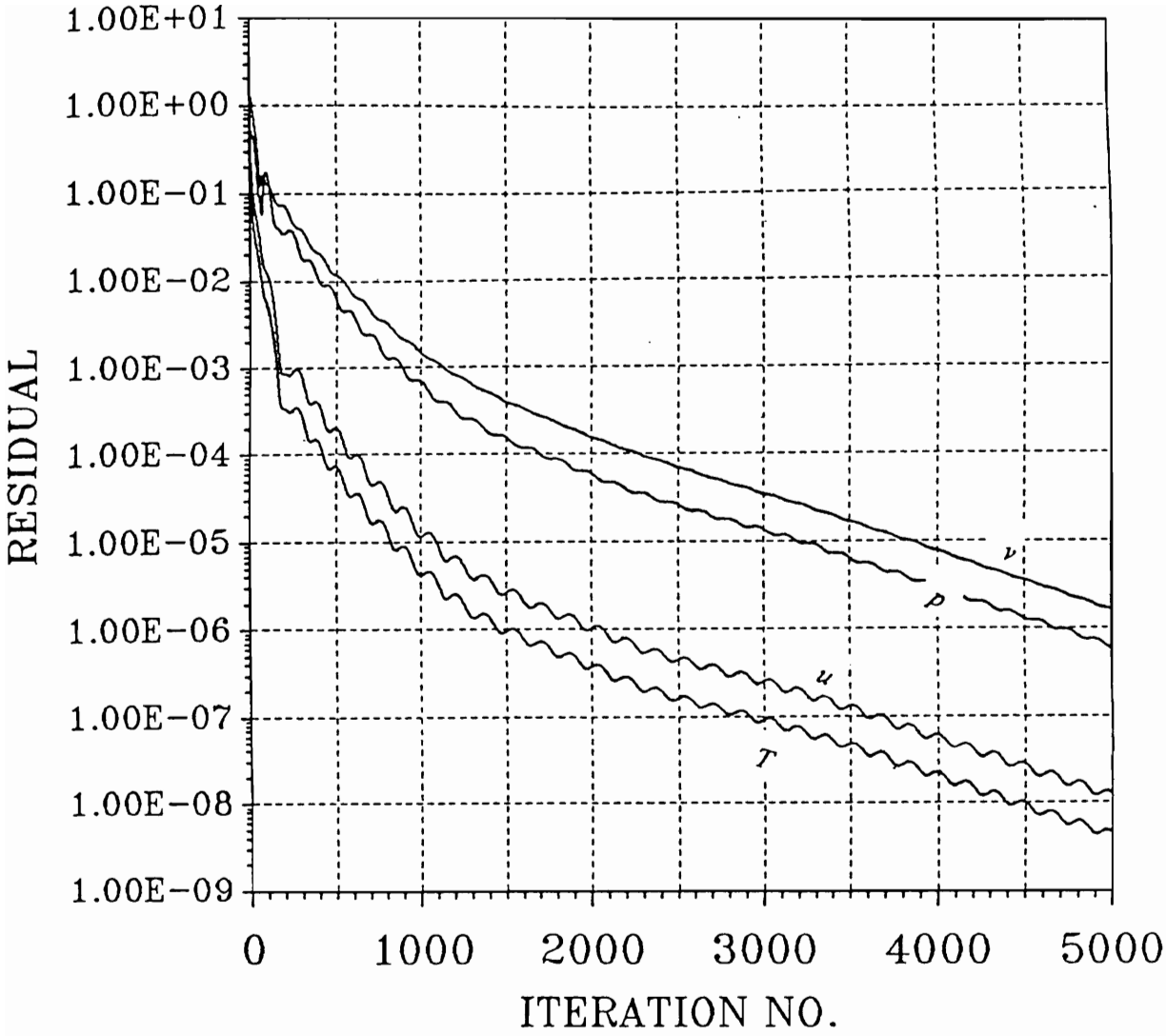

Figure 3.3. (e) Convergence history of norm of variation (5000 iterations). Case II.

Figure 3.3(d) shows the convergence rate of the L_2 norm of the variations. No changes of the solution are found between 3500 and 5000 iterations. However, the norm of the variations is reduced by about two orders of magnitude at 5000 iterations as shown in Fig. 3.3(e).

Figures 3.4(a,b,c) show the numerical results for the case III. These results are found to be close to case II results and agree with the exact solutions. The convergence history for this case is shown in Fig. 3.4(d).

3.2.4 Code Performance and Convergence

The preceding results for the flat wall problem are obtained by the use of an IBM 3090 vector processing computer at Virginia Tech. The developed code (PBNS) is highly vectorized to reduce the computational time. Table 3.1. provides the details of the computing time and code performance for the case I. For the cases II and III, sightly more computational time is required than for the case I.

Table 3.1. Computational time for the flow over a flat wall

No. of iterations	CPU	CPU/iteration
3500	7560 sec	2.15 sec

3.2.5 Conclusion

The purpose of analyzing the flow over an insulated flat wall is to demonstrate that the full Navier Stokes solver code (PBNS) can correctly analyze viscous compressible flow problems. The comparison of the code results with the exact solution increases the confidence level in the code and its validity to handle more complex flow problems.

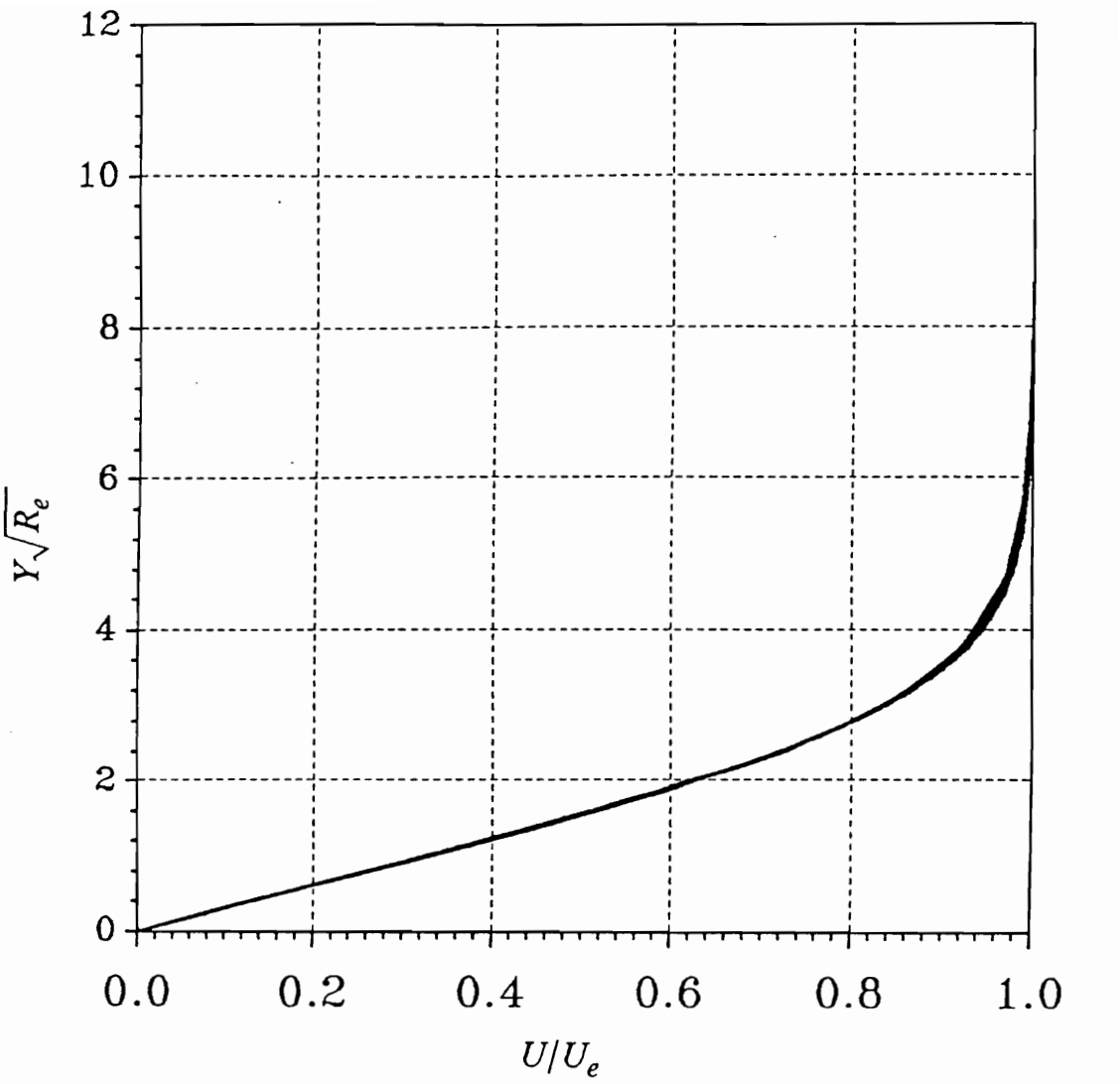

Figure 3.4. (a) Normalized u-velocity profile Case III.

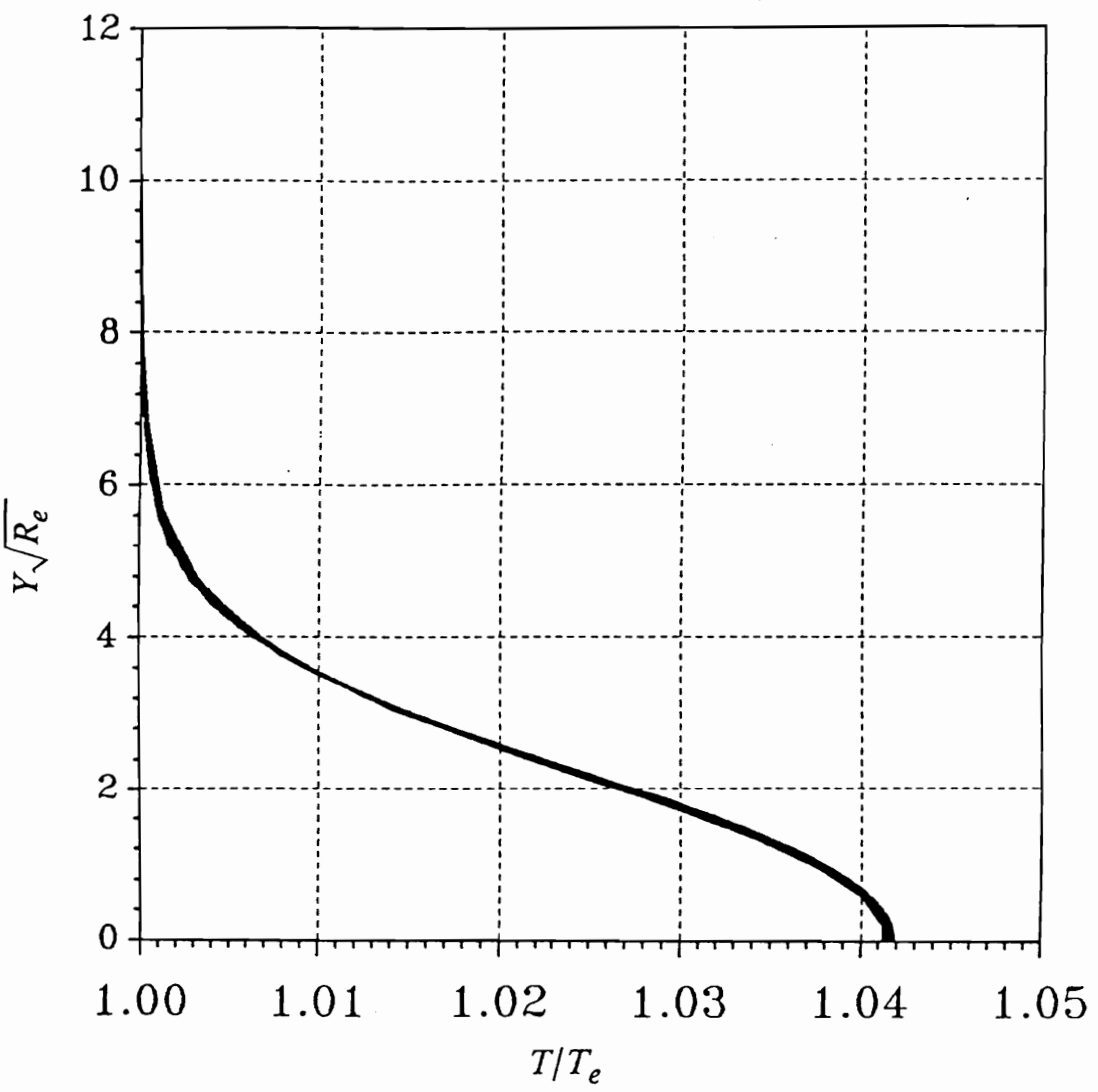

Figure 3.4. (b) Normalized temperature profile Case III.

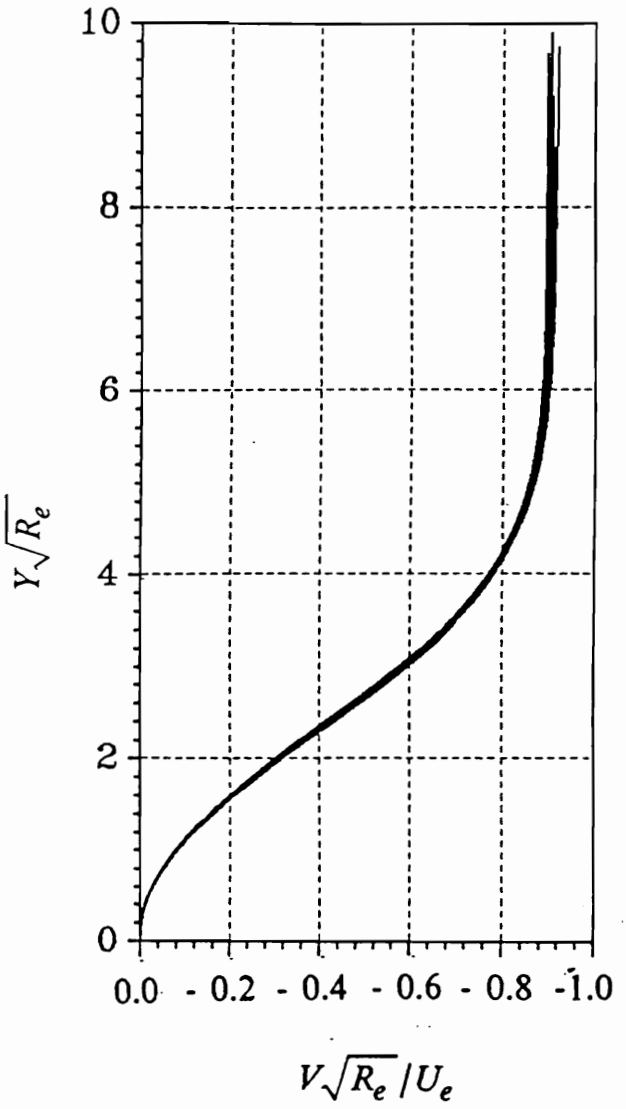

Figure 3.4. (c) Normalized v-velocity profile Case III.

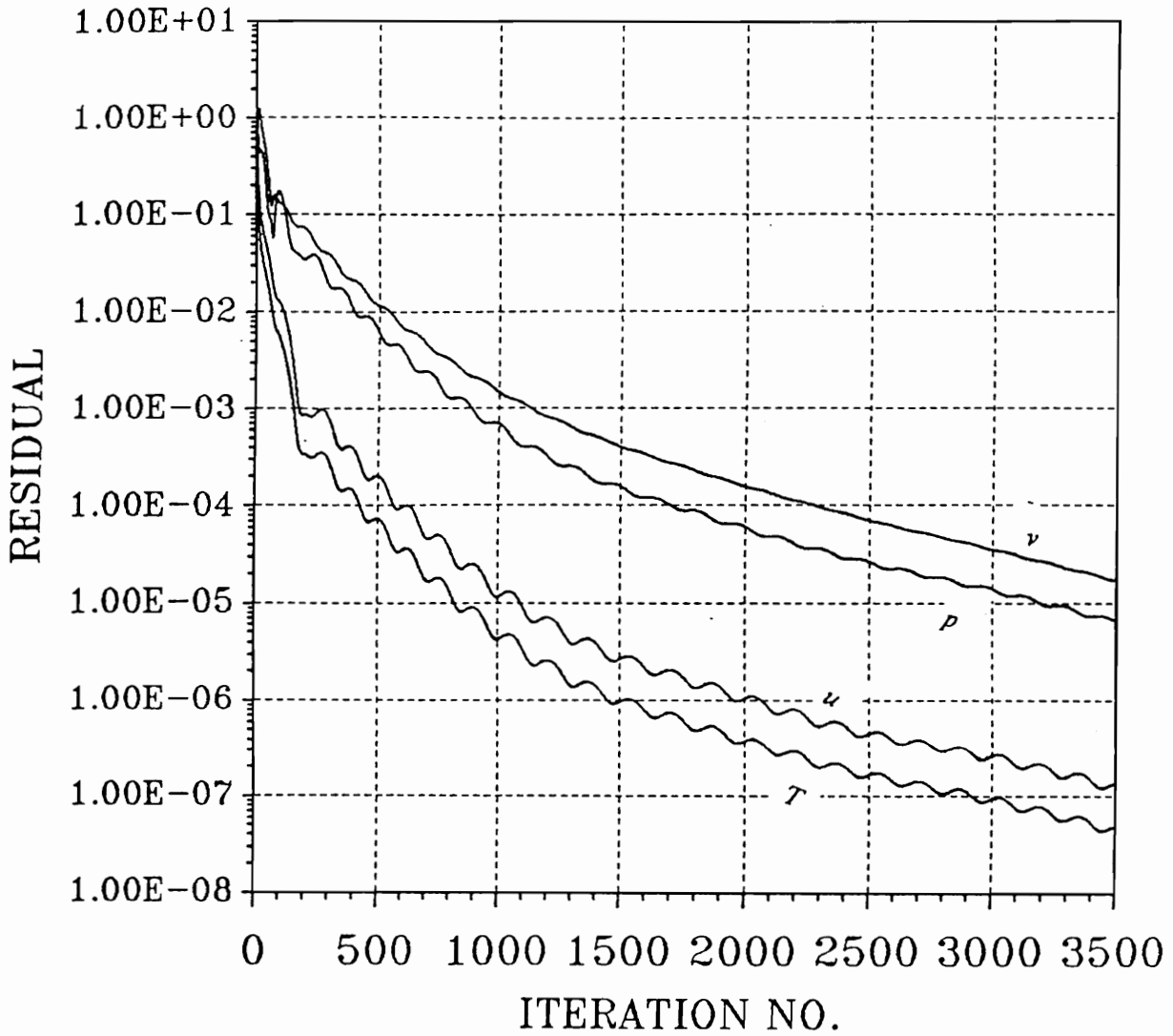

Figure 3.4. (d) Convergence history of norm of variation Case III.

3.3 Application of PBNS Code to an Axisymmetric Nozzle Flow

An internal flow in an axisymmetric nozzle shown in Fig. 3.5 serves as the second test of the performance of the PBNS code. The selected test cases include subsonic/supersonic nozzle. The Mach number varies from very low subsonic flow at the inlet to supersonic flow at the exit passing through a sonic condition at the throat. An axisymmetric condition at the center line of the nozzle requires vanishing of the normal gradients of the pressure, temperature and the axial velocity component. The radial velocity component will also vanish at the symmetric axis. The outlet flow conditions will affect the boundary conditions at the outlet and the solution convergence.

3.3.1 Nozzle configuration and computational mesh

The nozzle shown in Fig. 3.5 is used for the axisymmetric flow application of the PBNS code. The nozzle main parameters are: nozzle length L = 0.75 m, radius at inlet R_o = 0.15 m , and the contraction ratio CR = 0.25. The nozzle consists of a cylindrical tube extended over a distance x_s = 0.35 m, followed by a converging-diverging part. The converging-diverging wall is a cosine curve given by

$$r = R_o - (1 - CR) \times \left[\frac{R_o}{2} \left[1 - \cos(2\pi \frac{x - x_s}{L - x_s}) \right] \right] \tag{3.5}$$

The computational mesh used for the nozzle is shown in Fig. 3.5. The grid is constructed of 91 equally spaced grid points in the streamwise direction and 31 points in the transverse direction. An algebraic stretching along the top solid wall is implemented to resolve the large gradient in the viscous boundary layer.

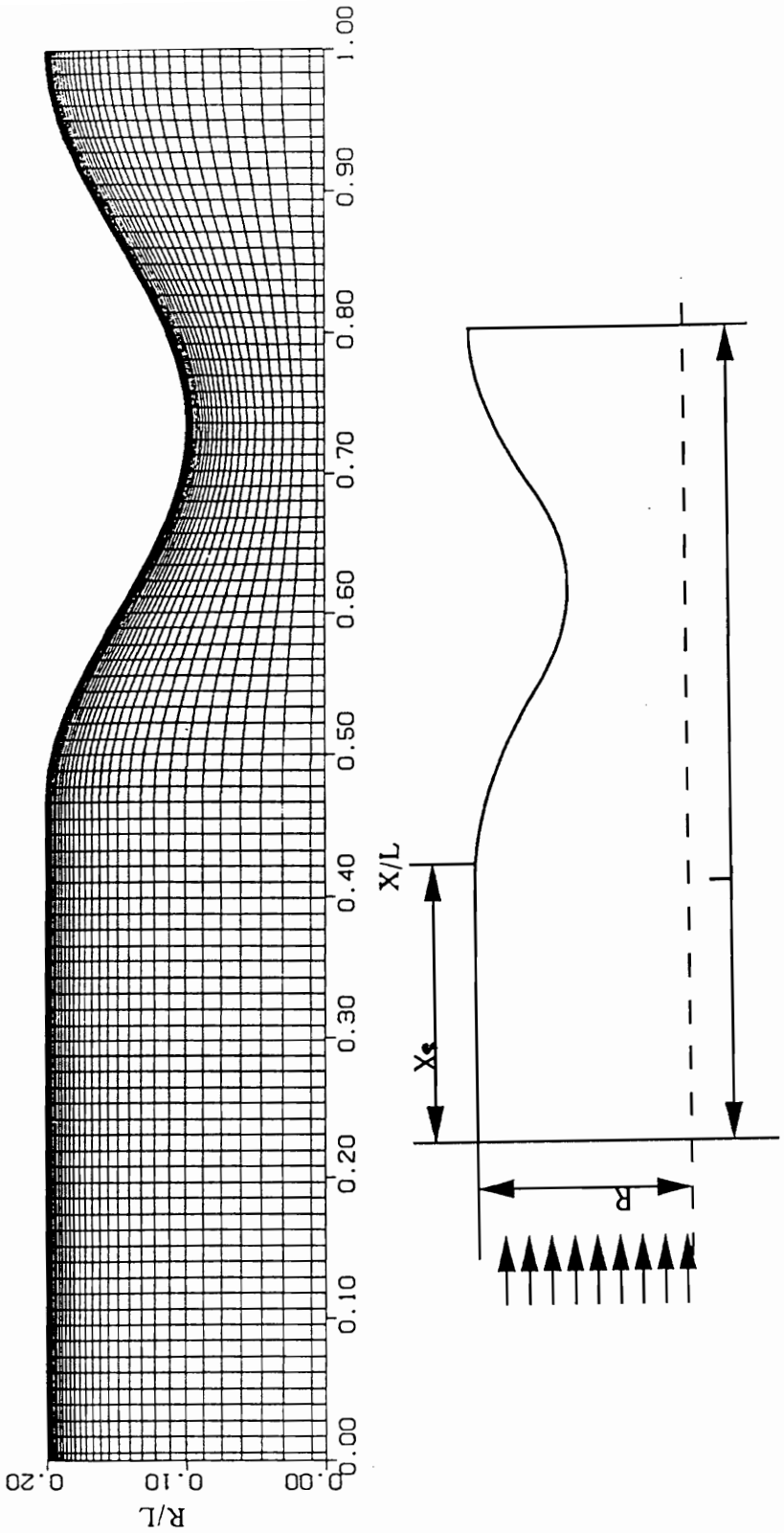

Figure 3.5. 91x 31 grid cell centers used for nozzle calculations

3.3.2 Boundary conditions

3.3.2.1 Entrance conditions

For subsonic inlet, the method of characteristics showed that the specifications of three variables are necessary. A fourth condition may be given mathematically from the interior solution. In this study, total pressure , total temperature and the flow angle are specified at the inlet plane. These conditions can be expressed as follows

$$P_{To} = constant \qquad T_{To} = constant \qquad \tan^{-1}(v/u) = 0.00 \qquad (3.6a,b,c)$$

The selection of these values is analogous to typical physical conditions, where the gas comes from an upstream reservoir. The axial velocity is extrapolated from the interior domain using first order extrapolation. In all of the following cases, the total pressure is set at 15 atm. and the total temperature is 2000 K.

3.3.2.2 Outflow conditions

At the exit plane, two conditions may be considered according to the local Mach number at the exit. For supersonic exit flow, all the characteristics are coming from the inside, implying no boundary condition is required. Thus, at a supersonic exit, the temperature, pressure, and velocity components are extrapolated from upstream conditions using first order extrapolation. An implicit treatment is used at the exit. This condition may be written for a general variable ϕ as follows

$$\Phi^{n+1}_{mx,j} = \Phi^{n+1}_{mx-1,j} + 0.5[\Phi^{n+1}_{mx-1,j} - \Phi^{n+1}_{mx-2,j}] \qquad (3.7)$$

where Φ represents u, v , h and p .

Due to the viscous effects near the wall at the exit plane, a local subsonic flow region may exist. To get an accurate model of the flow in this region, the subsonic characteristics should be considered. The local subsonic region is treated in a similar way as the subsonic exit flow over a flat plate given in Chapter III.

3.3.2.3 Symmetry conditions

Along the line of symmetry, the normal gradients must be set to be zero. This requires the vanishing of the velocity normal to that line. The boundary conditions may be written as

$$\frac{\partial \Phi}{\partial n} = 0 \qquad \text{v} = 0 \tag{3.8a,b}$$

Replacing the normal derivative with a derivative in the computational domain yields

$$\frac{\partial \Phi}{\partial \eta} = \frac{q_2}{q_3} \quad \frac{\partial \Phi}{\partial \xi} \tag{3.9}$$

where q_2 and q_3 are defined in Chapter II. The derivative on the left handside is treated implicitly using second order one-sided discretization. The right handside is discretized explicitly by using the central difference scheme. Thus, eq. (3.9) may be discretized as follows

$$\Phi_{i,1}^{n+1} = \frac{1}{8} \left[9\Phi_{i,2}^{n+1} - \Phi_{i,3}^{n+1} - \frac{3}{2} \left(\frac{q_2}{q_3} \right)_{i,1} [\Phi_{i+1,1}^{n} - \Phi_{i-1,1}^{n}] \right] \tag{3.10}$$

3.3.2.4 Wall conditions

At the nozzle wall, the no-slip no-penetration condition is imposed , i.e., $u = 0$ and $v = 0$. The wall is assumed to be insulated and, therefore, the heat flux $(\partial T/\partial n)$ normal to the wall is set to be zero. The pressure at the wall is determined by assuming the vanishing of its normal derivative at the wall. This may be represented in the computational domain as

$$p_{i,my}^{n+1} = \frac{1}{8}\left[9p_{i,my-1}^{n+1} - p_{i,my-2}^{n+1} + \frac{3}{2}\left(\frac{q_2}{q_3}\right)_{i,my}\left[p_{i+1,my}^{n} - p_{i-1,my}^{n}\right]\right] \tag{3.11}$$

For solving the pressure correction equation it is not necessary to have any assumption for p', since no correction is needed at the boundaries of the computational domain. However, it has been found that better convergence may be obtained if the pressure correction at the boundaries possesses the same behavior as the behavior of the pressure there.

3.3.3 Results

To examine the code performance and ability five different cases have been tested for the nozzle shown in Fig. 3.5. These cases include different boundary conditions and different gas properties. Hydrogen is the flowing gas for all these test cases. Table 3.2 gives the different inputs for these cases. The following parameters are selected to nondimensionalize the Navier-Stokes equations

$\mu = 318.2^{-7}\, N\,\mathrm{sec}/m^2 \quad k = 0.878 W/mK \quad \rho = 0.1815 kg/m^3 \quad T = 2000.0K$
$U_{ref} = 50.0 m/\mathrm{sec} \quad X_{ref} = 0.75m \quad c_{pref} = 18.25 kj/kgK \quad \gamma = 1.408$

Table 3.2 Test cases for the axisymmetric nozzle

Case	Equation of state	Relaxation	Trasnport properties	Inlet condition	Exit condition
1	Perfect gas	0.25	Constant	Non-reflecting	All supersonic
2	Perfect gas	0.25	Constant	u extrapolation	All supersonic
3	Perfect gas	0.45	Constant	u extrapolation	All supersonic
4	Perfect gas	0.45	Constant	u extrapolation	All supersonic local subsonic
5	Equilibrium	0.25	Variable	u extrapolation	All supersonic local subsonic

The results of these cases are presented in Figs. 3.6 to 3.10, showing axial velocity, radial velocity, pressure , temperature contours and the convergence history for each case.

3.3.3.1 Case 1

The results, shown in Figs. 3.6 a-e show an agreement with the one dimensional inviscid solution, near the center line. The one dimensional solution is obtained using the following relation

$$\frac{A}{A^*} = \sqrt{\frac{1}{M^2}\left[\frac{2}{\gamma+1}\left(1+\frac{\gamma-1}{2}M^2\right)\right]^{\gamma+1/\gamma-1}} \tag{3.12}$$

where A^* is the sonic nozzle area. Solving for the Mach number at various locations along the nozzle, the pressure, temperature and u-velocity may be obtained from the isentropic relations. The viscous effects are clear in the flow near the wall, however, it is noticed that more points are needed near the wall to accurately predict the boundary layer flow. The v-velocity shows a negative value in the convergent part and a positive value in the divergent part of the nozzle, with zero value at the wall and the symmetry axis. The temperature increases gradually from its value at the center line to the adiabatic value at the wall for the subsonic part of the nozzle. A wall temperature of 1999.54 K existed at the wall. For the supersonic part, the temperature decreases from the center line due to the accelerating effect of the flow. Then, the temperature increases due to the boundary layer effect at the wall. The Mach number contour is related to the behavior of the temperature contour. No subsonic zone near the wall is reported for the exit plane, since, at that plane, all the grid points were assumed

to have a supersonic characteristics. This implies that the background pressure is low enough to allow for supersonic flow at the exit plane. The convergence is insured by monitoring the norm of the variations of all the variables. Also, the global and local mass imbalance are checked to be less that 10^{-8}. The inner loop is repeated till the norm of the residual dropped to 10^{-10}. The convergence history is shown in Fig. 3.6(f). All the second norms of the dependent variables variations were reduced to six orders of magnitude with the pressure to be the last variable to converge.

3.3.3.2 Case 2

The case 2 is similar to the case 1 as shown in Table 3.2 except that the numerical inlet conditions are determined by $U_{1,j} = U_{2,j}$ for all j along the inlet. The results of this case are found to be identical to the results obtained for the case 1. The contours of the velocity components ,Mach number, temperature and pressure are shown in Figs. 3.7 a-e. The convergence history of the L_2 norm of the variations, Fig. 3.7(f), is found to be similar to the convergence history of the previous test case. This shows that both the non-reflecting boundary and this treatment are identical, with a small improvement in CPU time for the latter one.

3.3.3.3 Case 3

This case is exactly the same as the case 2 with an under-relaxation factor of 0.45 instead 0.25 used for the previous cases. This value of under-relaxation has been found to be optimum for the nozzle. The results of this test case show identical behavior to the previous test cases and are presented in Figs. 3.8 a-e.

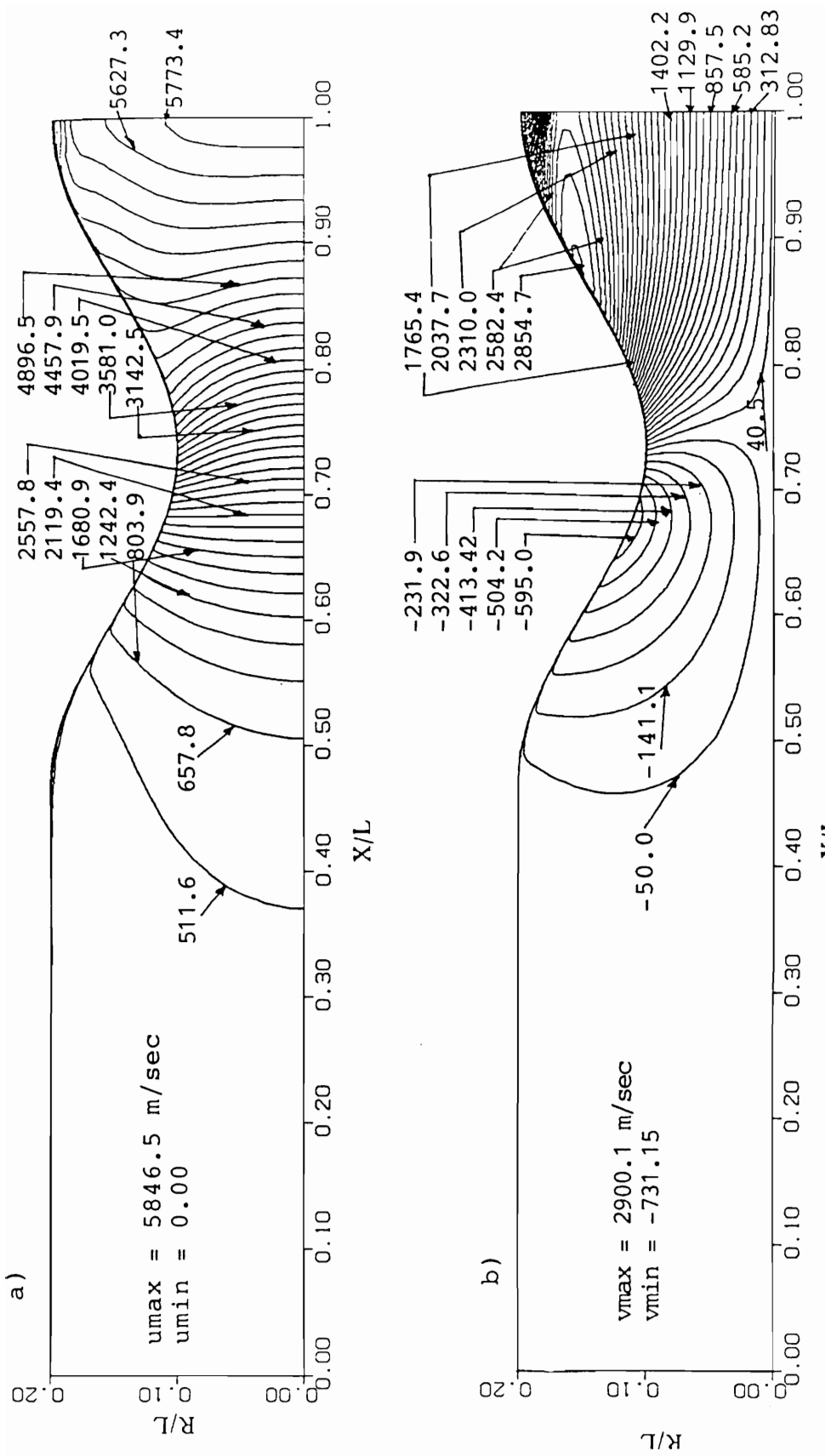

Figure 3.6. (a) u-velocity contour , (b) v-velocity contour, Case 1

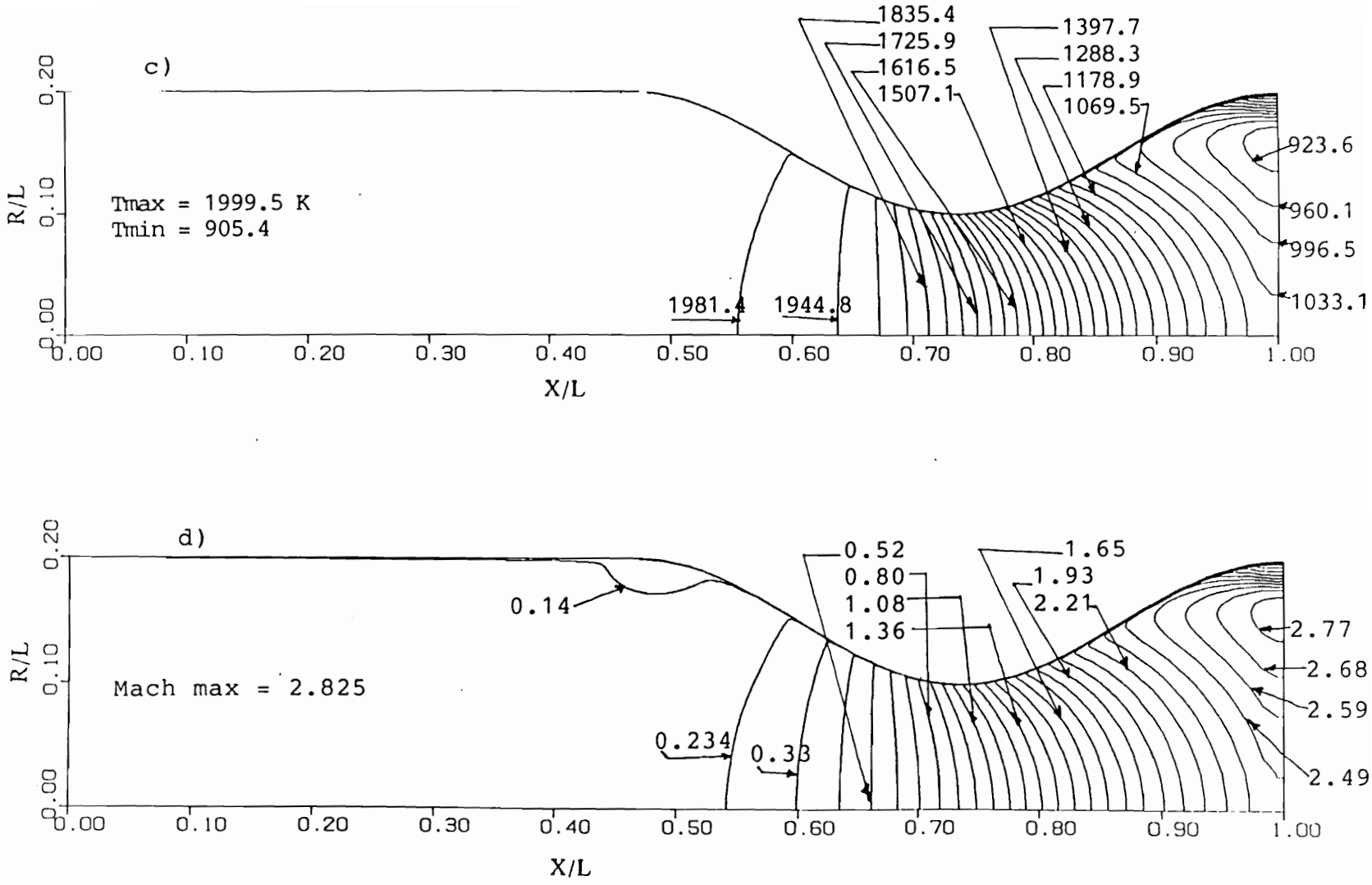

Figure 3.6. (c) Temperature contour , (d) Mach contour, Case 1

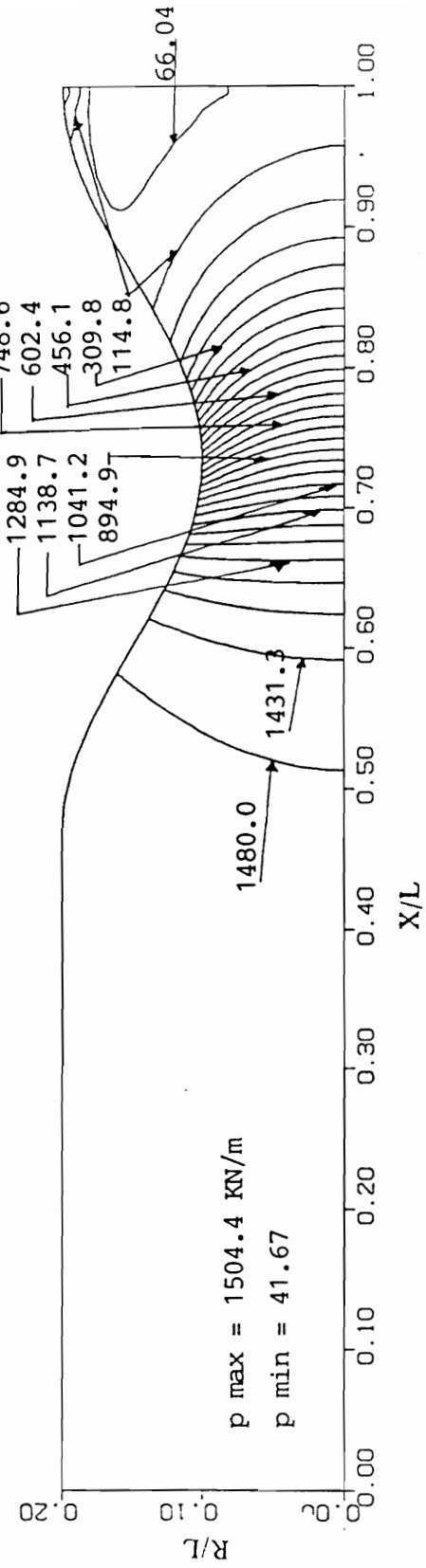

Figure 3.6. (c) Pressure contour, Case 1

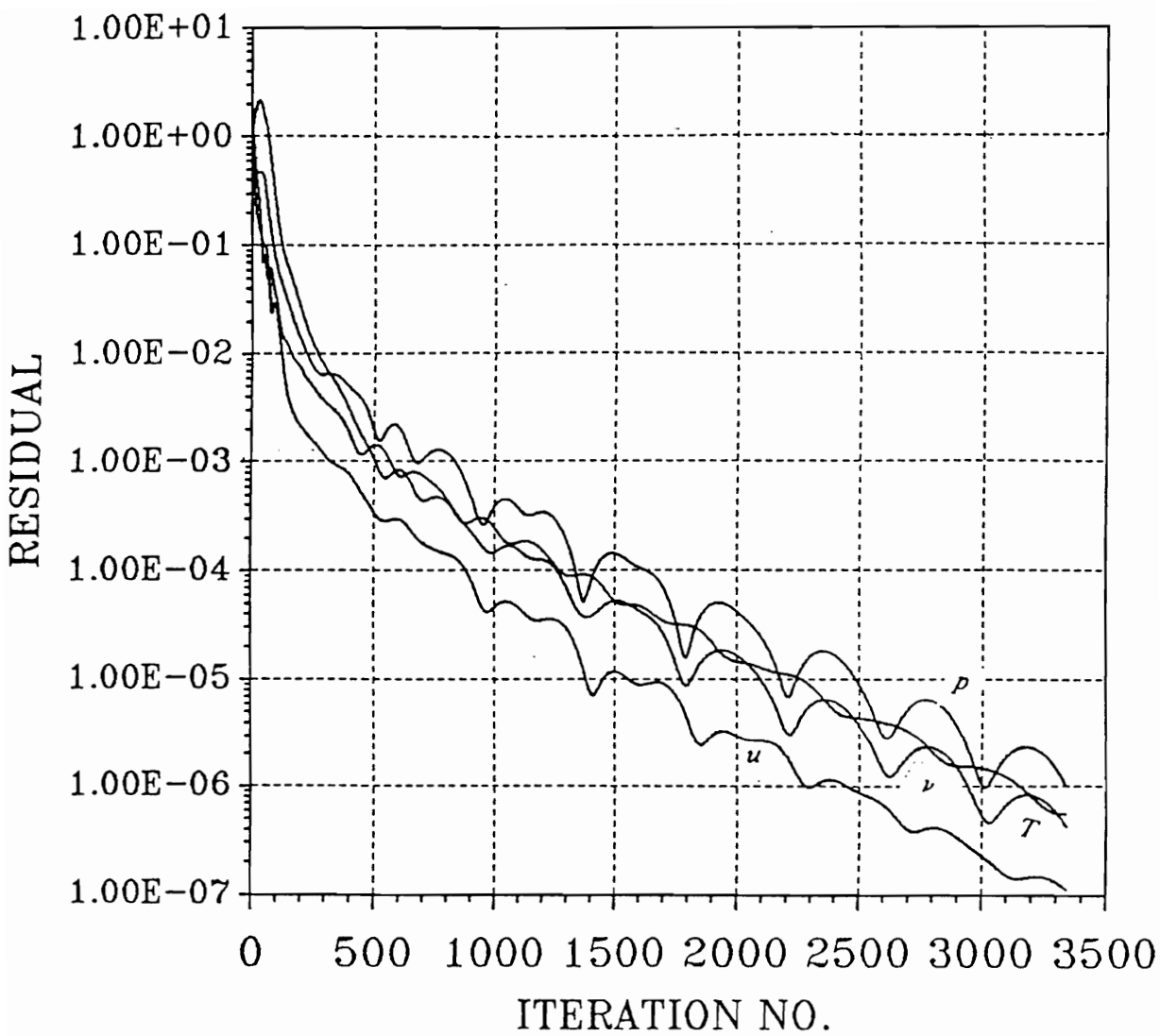

Figure 3.6. (f) Convergence history of the L_2 norm of variations, Case 1

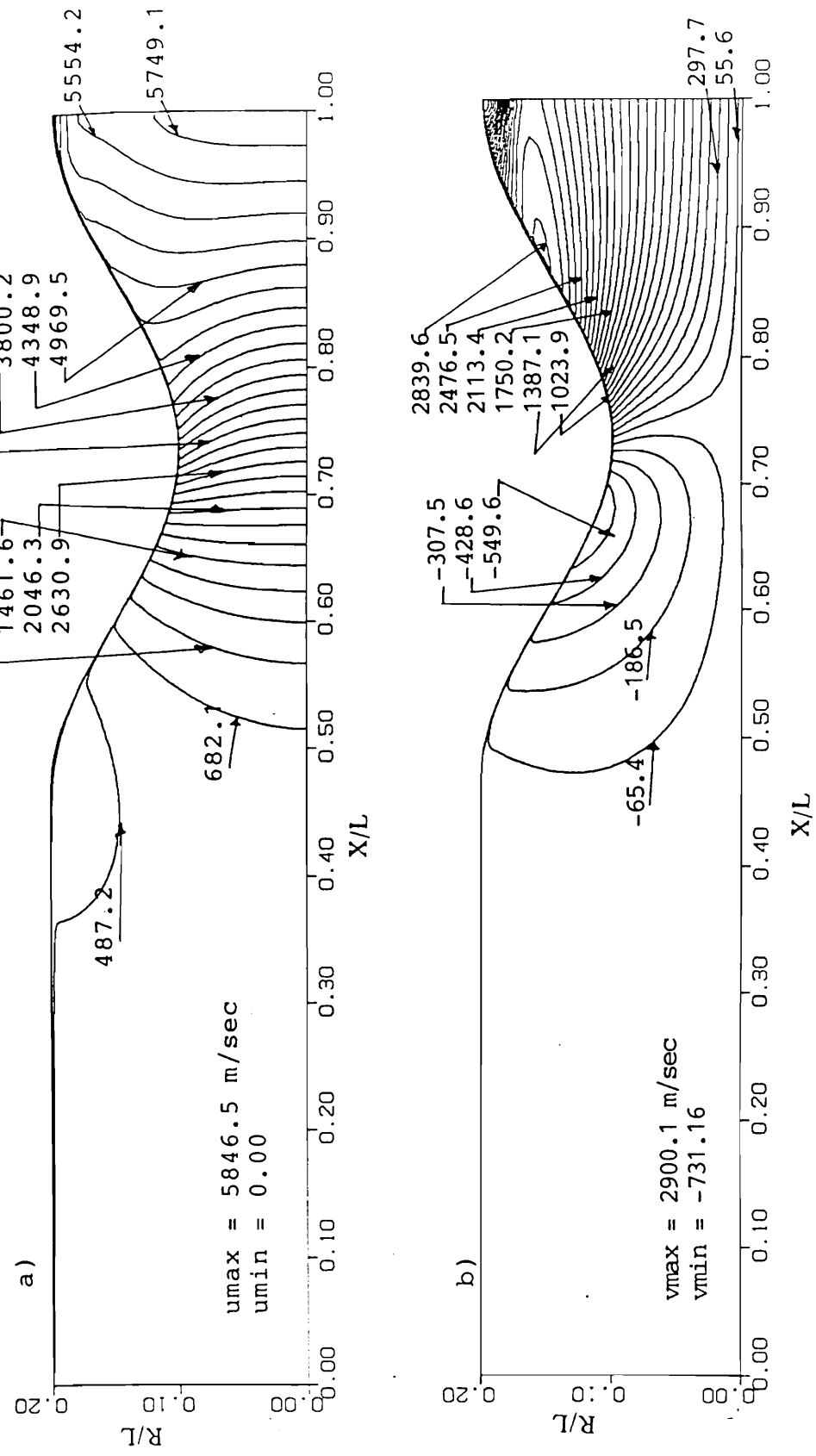

Figure 3.7. (a) u-velocity contour , (b) v-velocity contour, Case 2

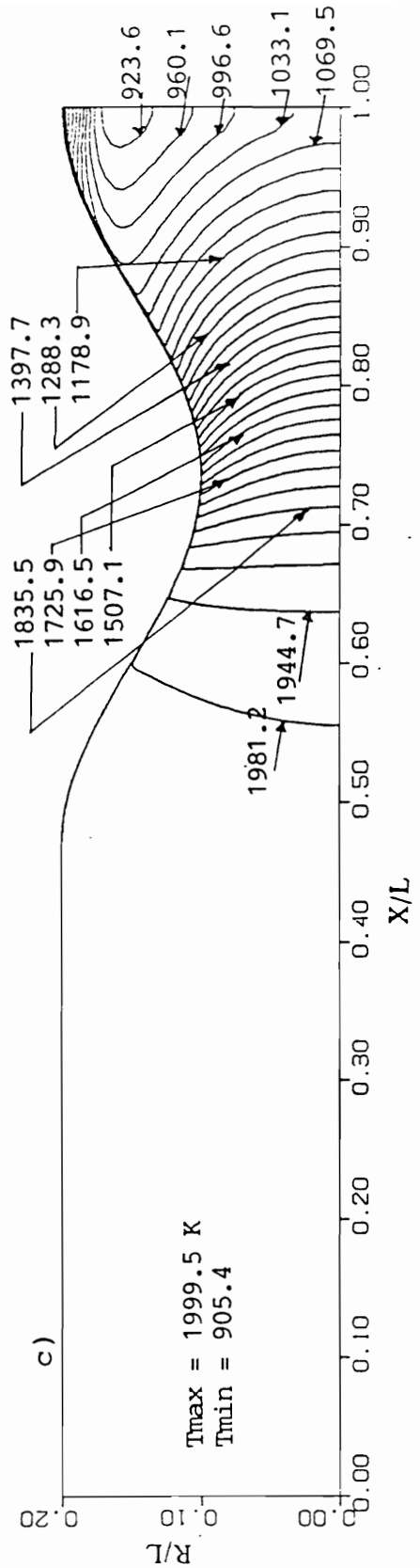

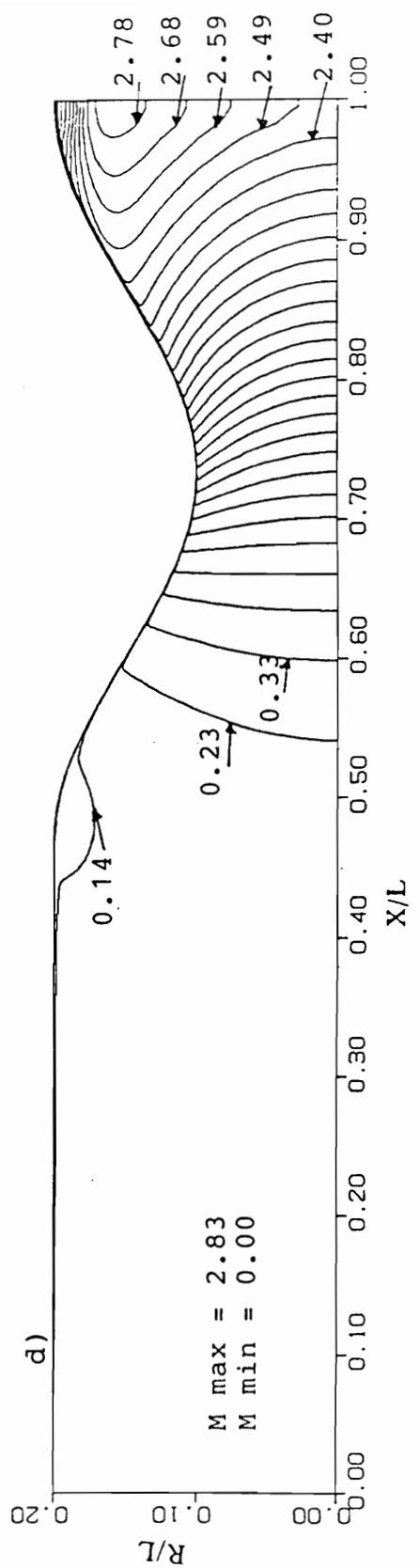

Figure 3.7. (c) Temperature contour , (d) Mach contour, Case 2

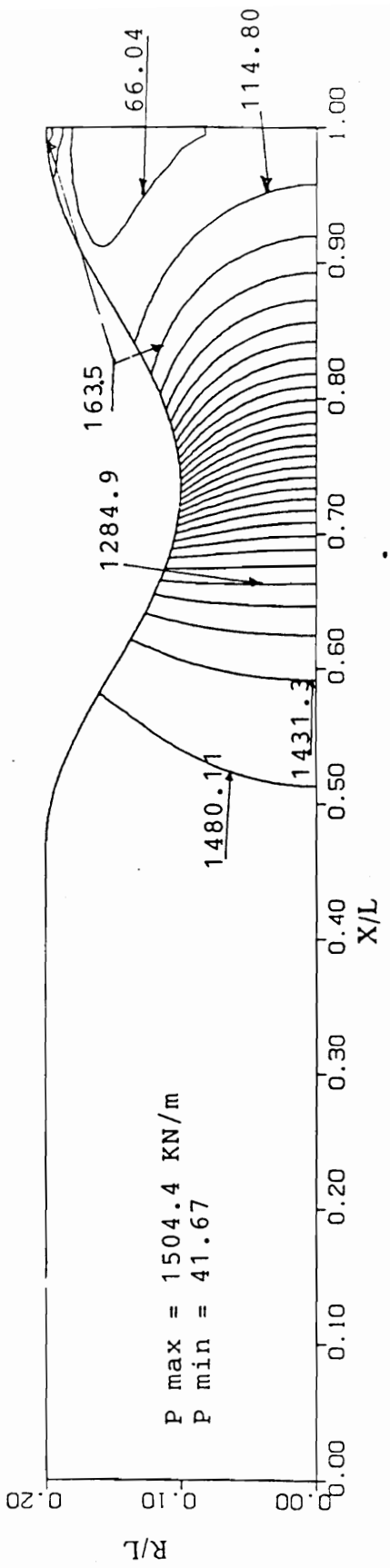

Figure 3.7. (e) Pressure contour, Case 2

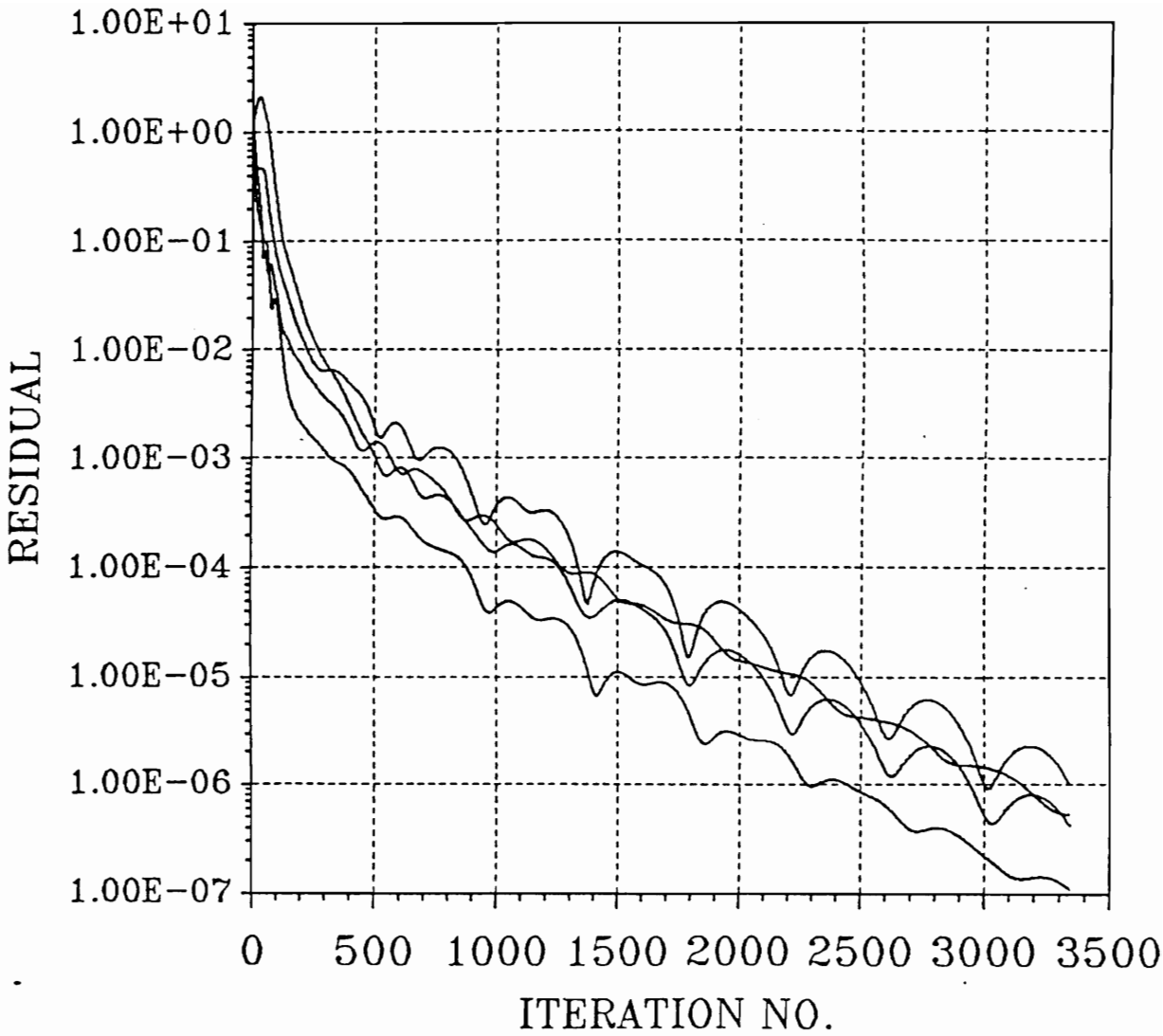

Figure 3.7. (f) Convergence history of the L_2 norm of variations, Case 2

The convergence history shows that only 1720 iterations are needed to achieve a convergence, as shown in Fig. 3.8(f). Thus, about half the number of iterations required for the previous case (3340 iterations) are needed to achieve the same convergence level. It is noticed that increasing the under-relaxation factor to 0.6 causes the code to diverge.

3.3.3.4 Case 4

In all the previous cases, all the points on the exit plane are assumed to have supersonic characteristics and the extrapolations are zero order on all the boundaries. However, a viscous subsonic region may exist near the wall because of the boundary layer effect. This can be modeled, by considering the subsonic outflow conditions for the grid points where the subsonic region exists. Such treatment of the exit boundary is used for this case together with the first order extrapolation at all the boundaries. The results for the case 4 are shown in Figs. 3.9 a-e. These results show smoother contours at all the boundaries as a result of using higher order extrapolation. Also, the results show a subsonic region near the wall at the exit plane. This region is not found in the previous cases. The subsonic region predicted by this case is found in the numerical data but since dense grid is used near the wall is not clear in the contour plots. The contours are found to be very close to what was predicted for the previous cases.

3.3.3.5 Case 5

The final case tested includes accurate calculations of thermodynamic and transport properties of the flowing gas. Hydrogen in equilibrium condition is used for this case. The detailed calculations of hydrogen properties are included

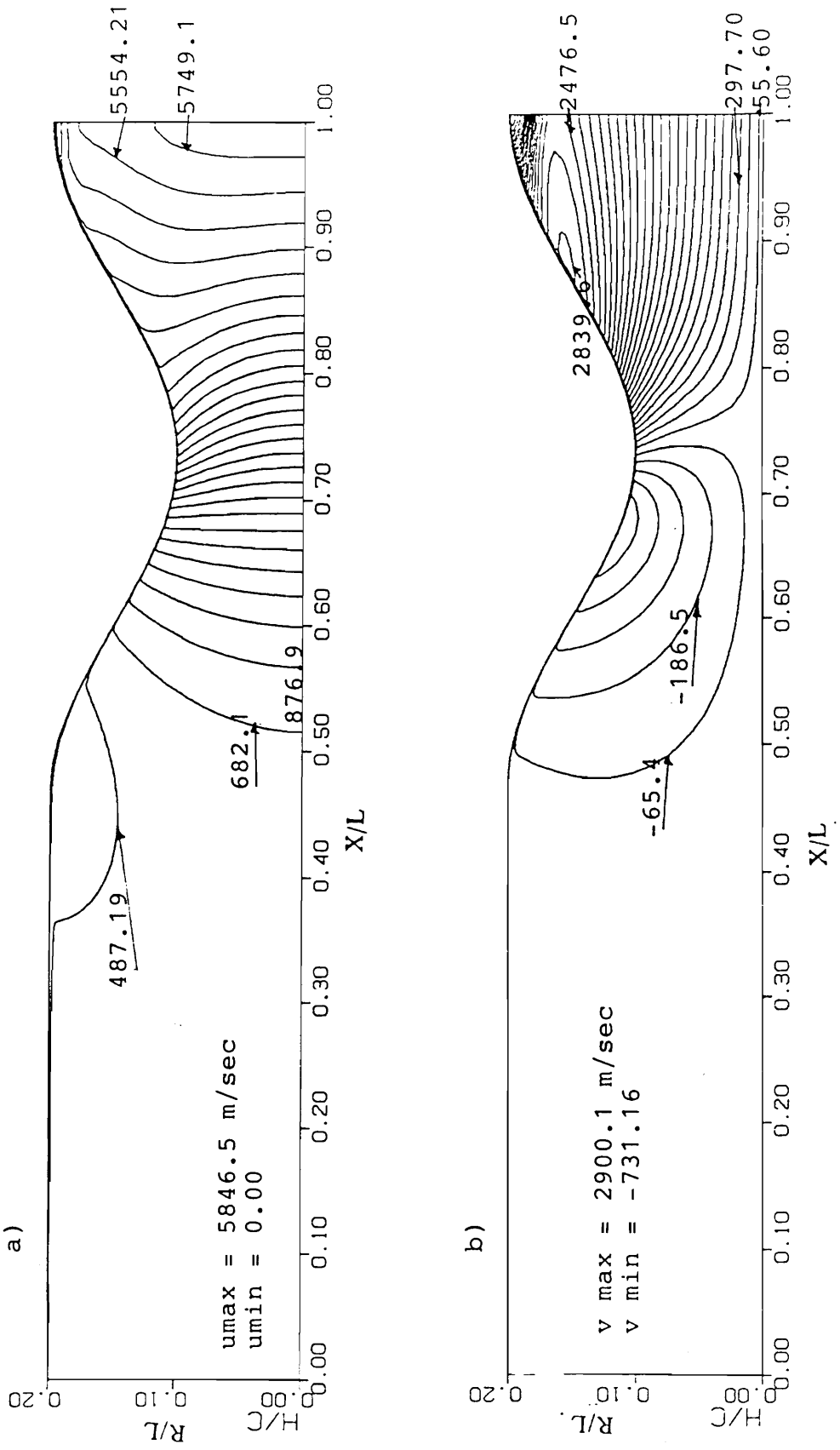

Figure 3.8. (a) u-velocity contour , (b) v-velocity contour, Case 3

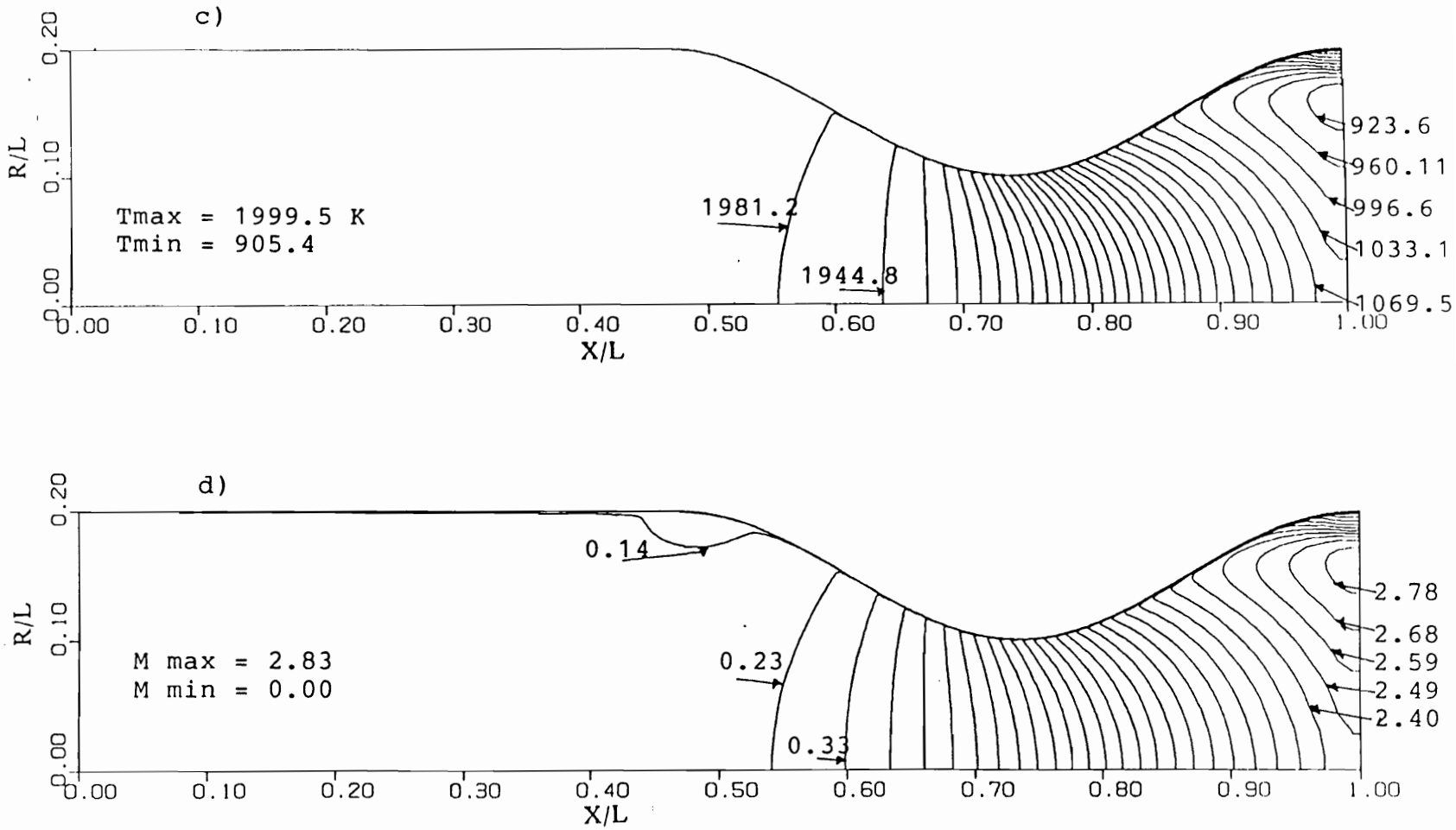

Figure 3.8. (c) Temperature contour , (d) Mach contour, Case 3

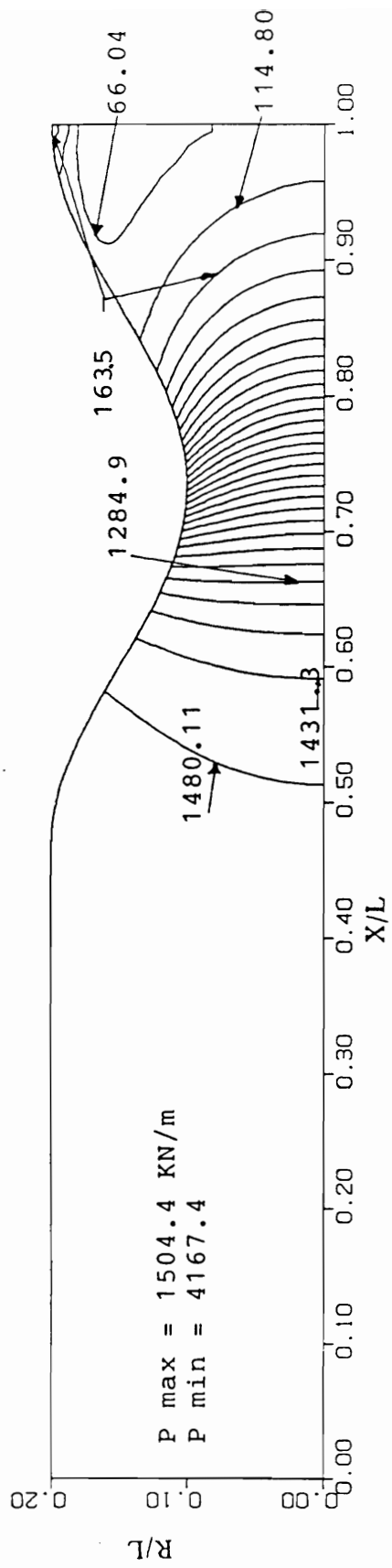

Figure 3.8. (e) Pressure contour, Case 3

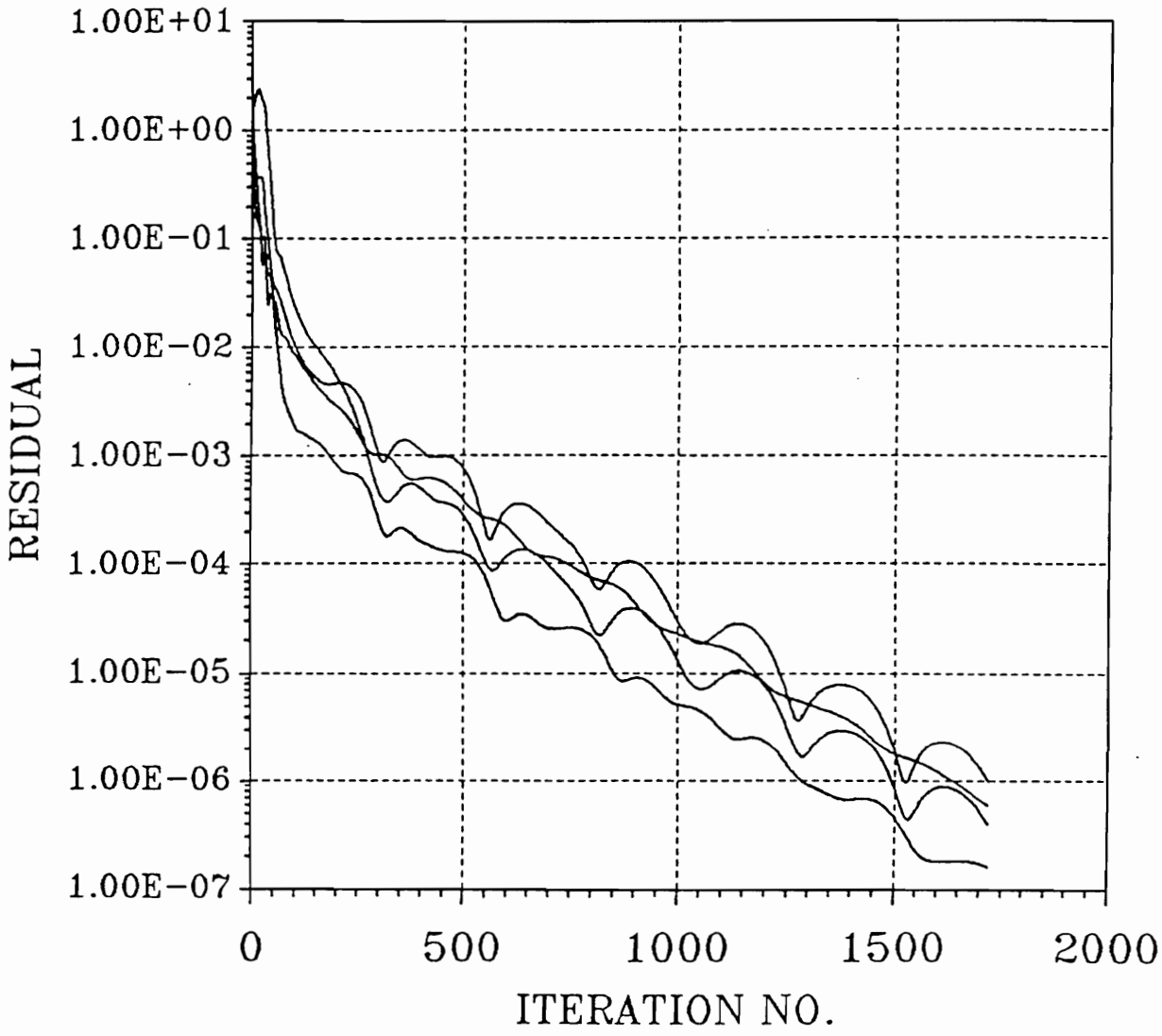

Figure 3.8. (f) Convergence history of the L_2 norm of variations, Case 3

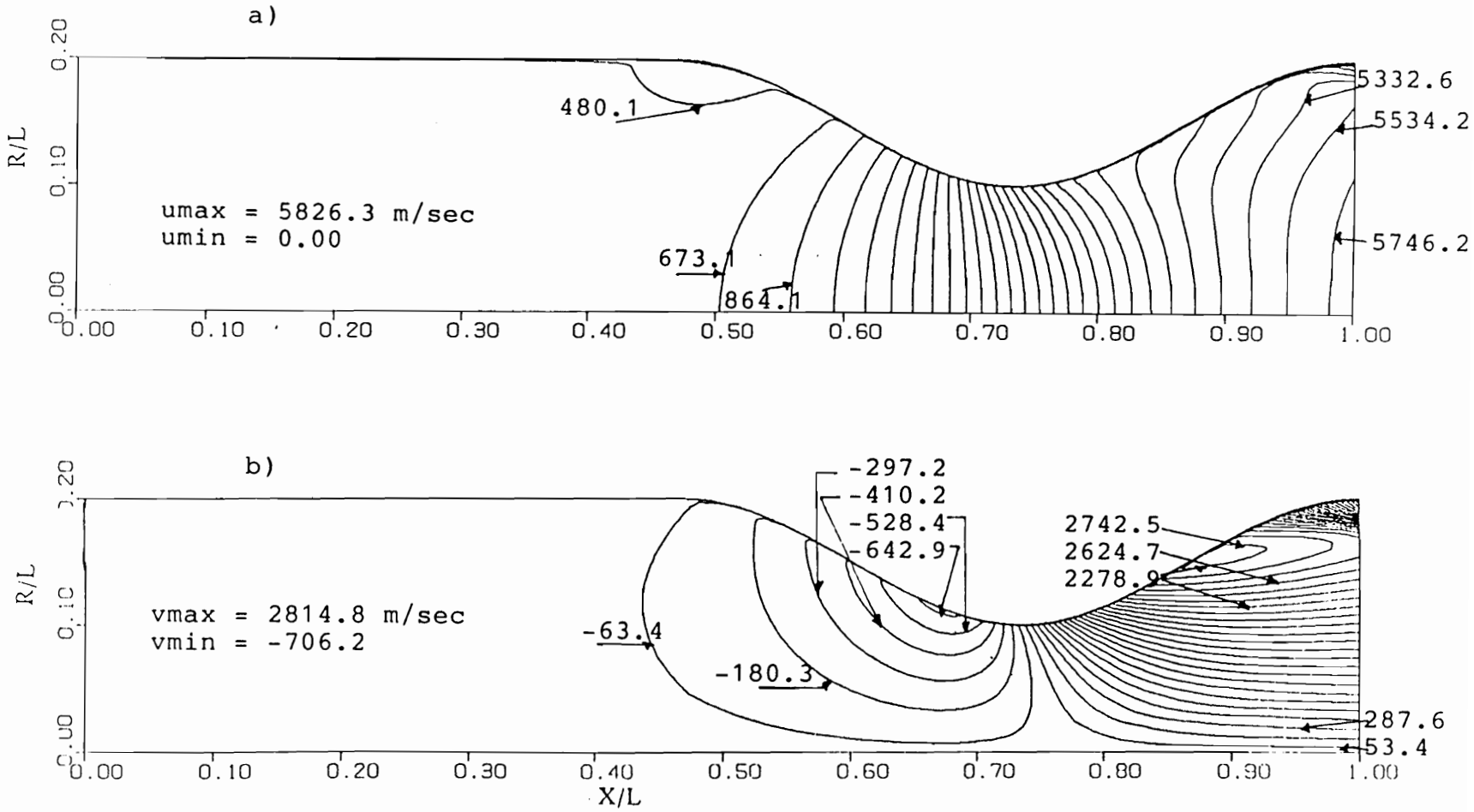

Figure 3.9. (a) u-velocity contour , (b) v-velocity contour, Case 4

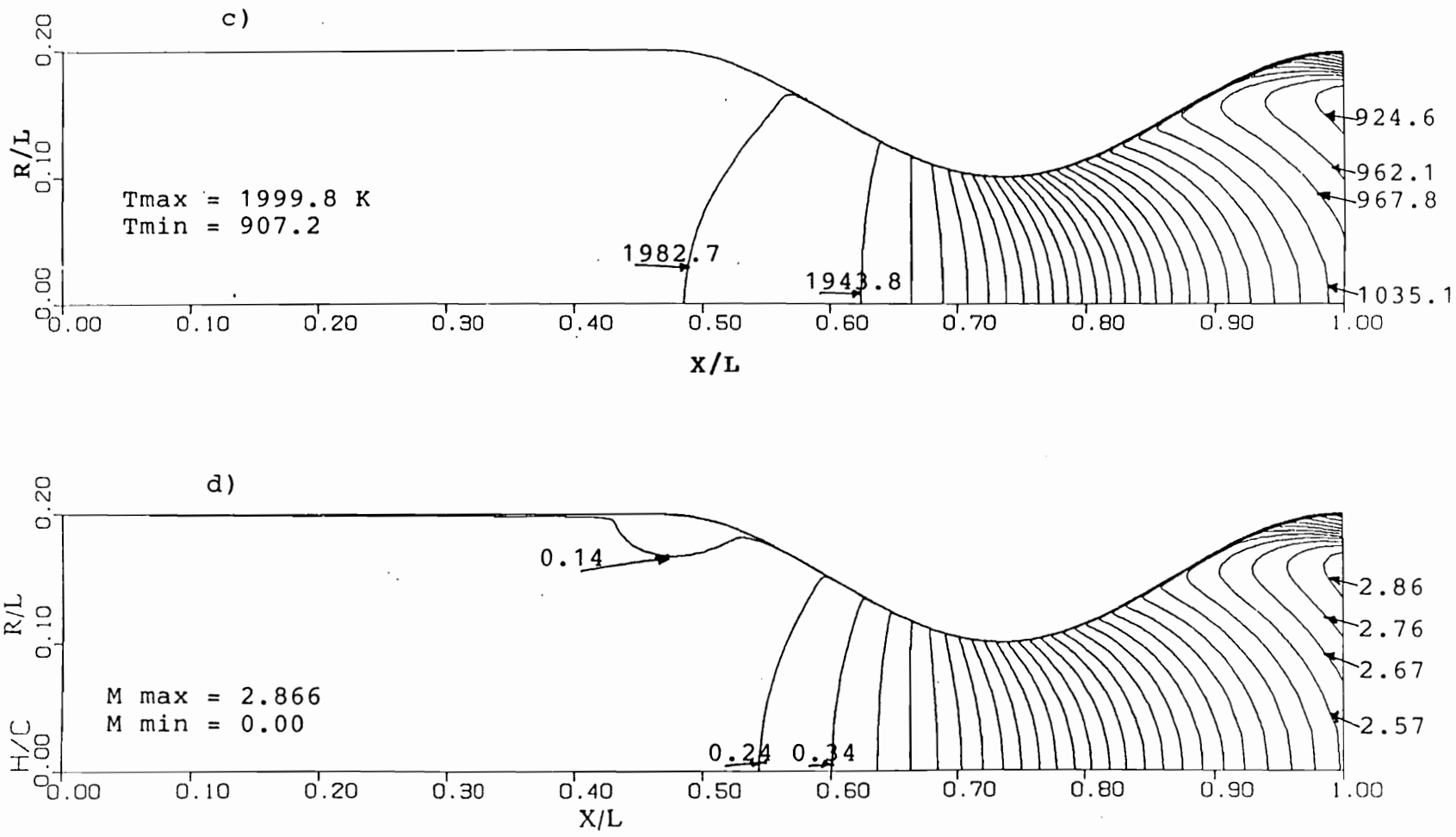

Figure 3.9. (c) Temperature contour , (d) Mach contour, Case 4

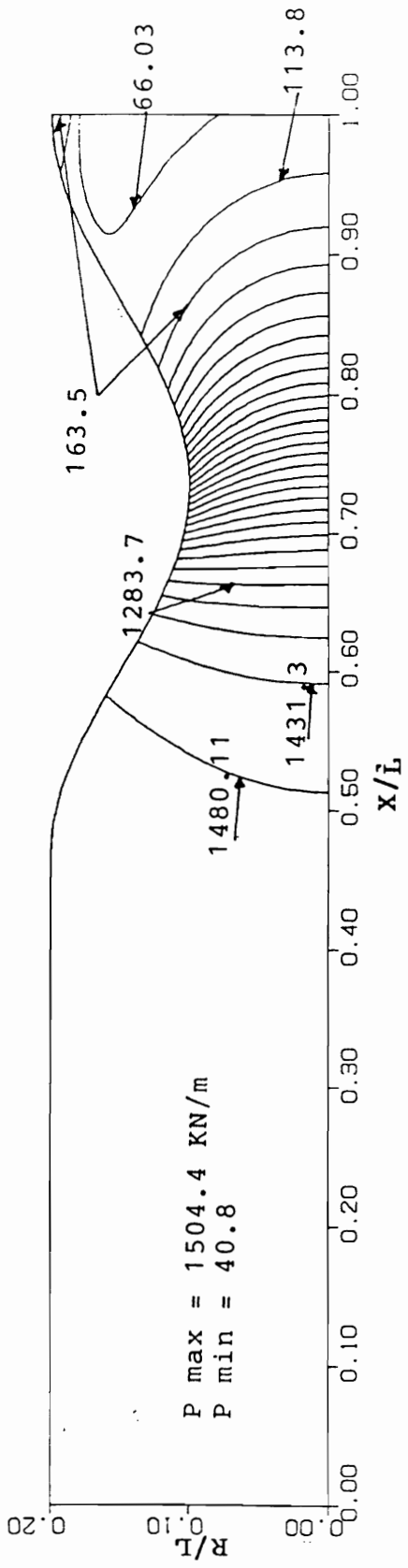

Figure 3.9. (c) Pressure contour, Case 4

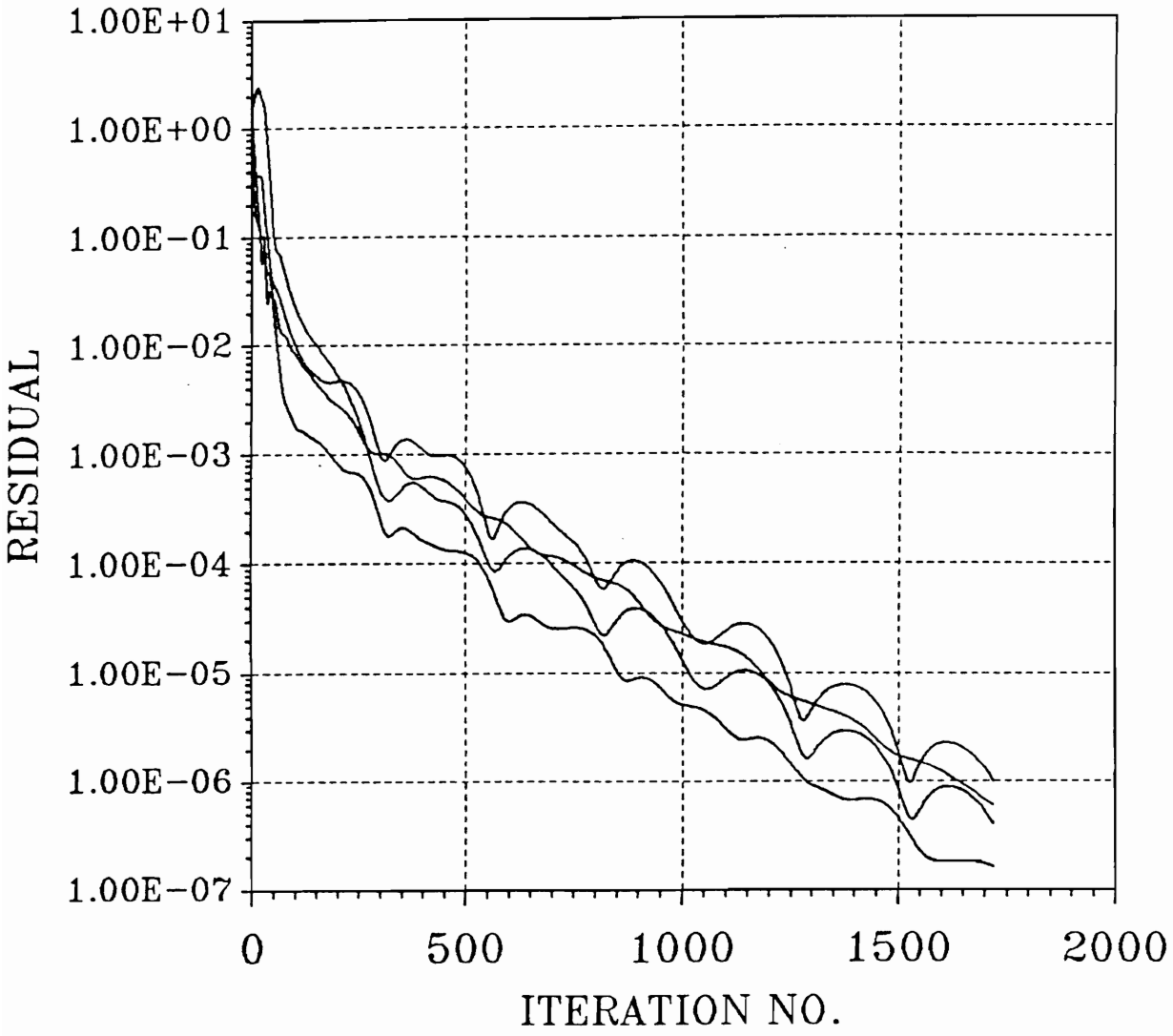

Figure 3.9. (f) Convergence history of the L_2 norm of variations, Case 4

in Appendices A, B and C. Boundary conditions used in this case are the same as those used for the case 4. Under-relaxation factor for case 5 is reduced to 0.25, due to the high nonlinearity that is expected. The results are shown in Figs. 3.10 a-e, and they are found to be in very good agreement with the previous cases. This agreement is, however , expected, since hydrogen behaves as a perfect gas for the tested temperature and pressure ranges. Contours of all the variables show the same trends, with slight differences in the numerical values.

The convergence for this case satisfied the selected criteria for the local and global mass balance together with the second norm of the residual reduced to be of order 10^{-8} for all the variables. However, only 2.5 order of magnitude reduction is reported for the L_2 norm of the variations in temperature. This is believed to be caused by the way that is used in the extraction of the temperature field from the enthaply field. The code (PBNS) uses linear interpolation for such inversion. Since there is no tendency of increasing in these norms, the results can still be accepted. Better behavior may be obtained by the application of a multi-grid system and accurate curve fitting for the enthalpy-temperature relation.

3.3.4 Code Performance and Convergence

Table 3.3 provides the details of the computing time and code performance for all the above mention cases. Case 5 needs more CPU time because of the additional calculations of hydrogen properties, which have been performed using the HPC code.

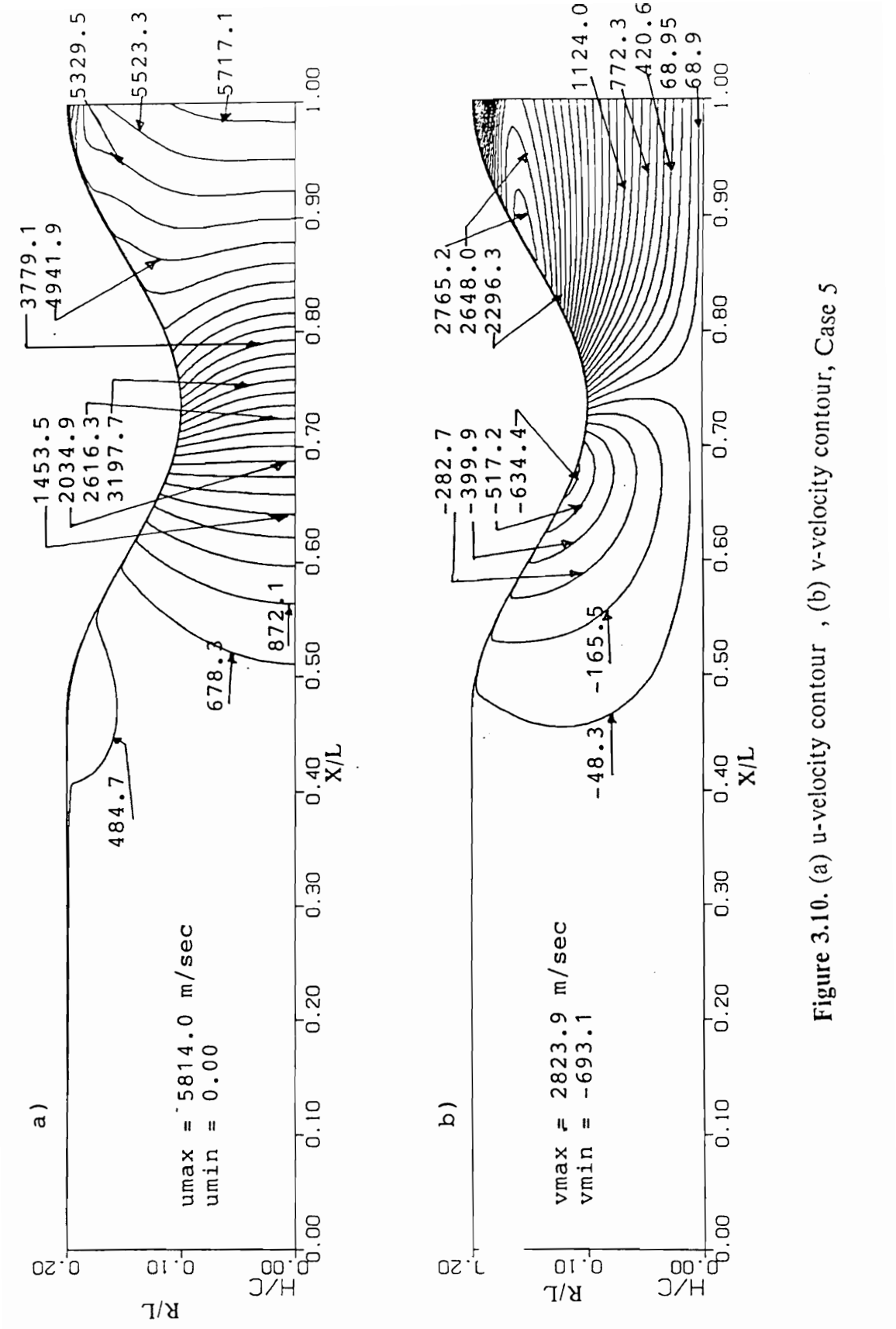

Figure 3.10. (a) u-velocity contour , (b) v-velocity contour, Case 5

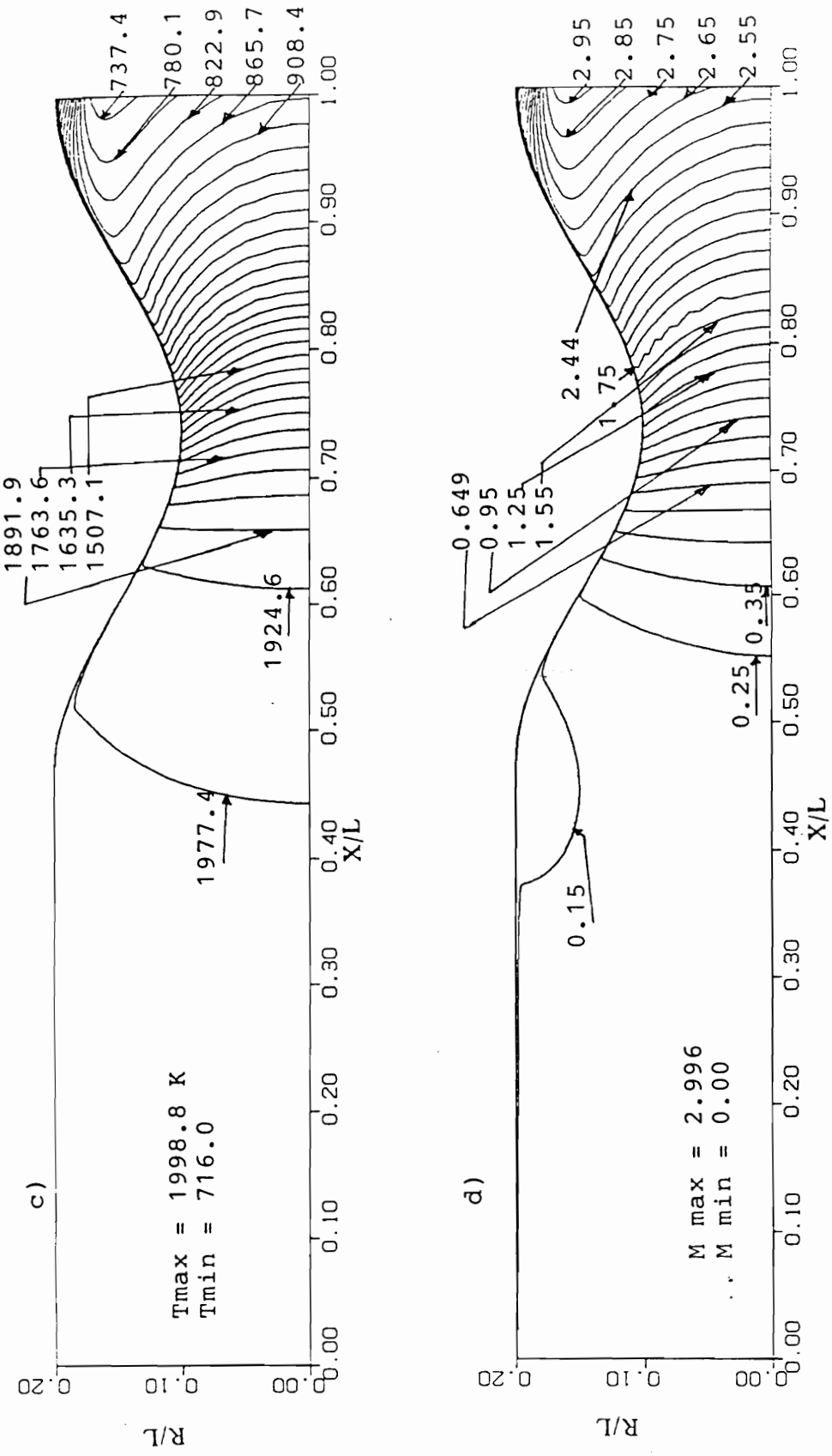

Figure 3.10. (c) Temperature contour , (d) Mach contour, Case 5

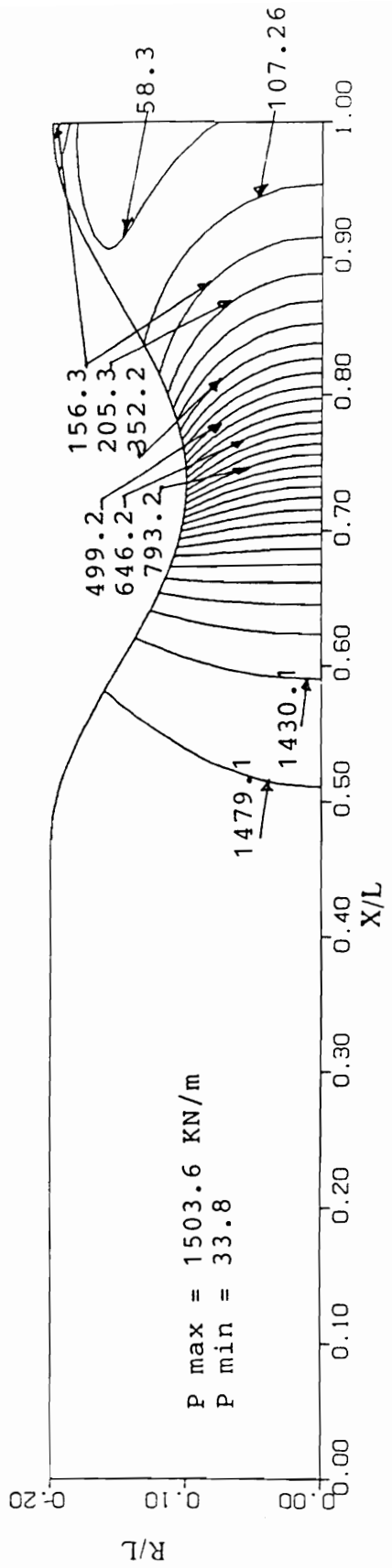

Figure 3.10. (c) Pressure contour, Case 5

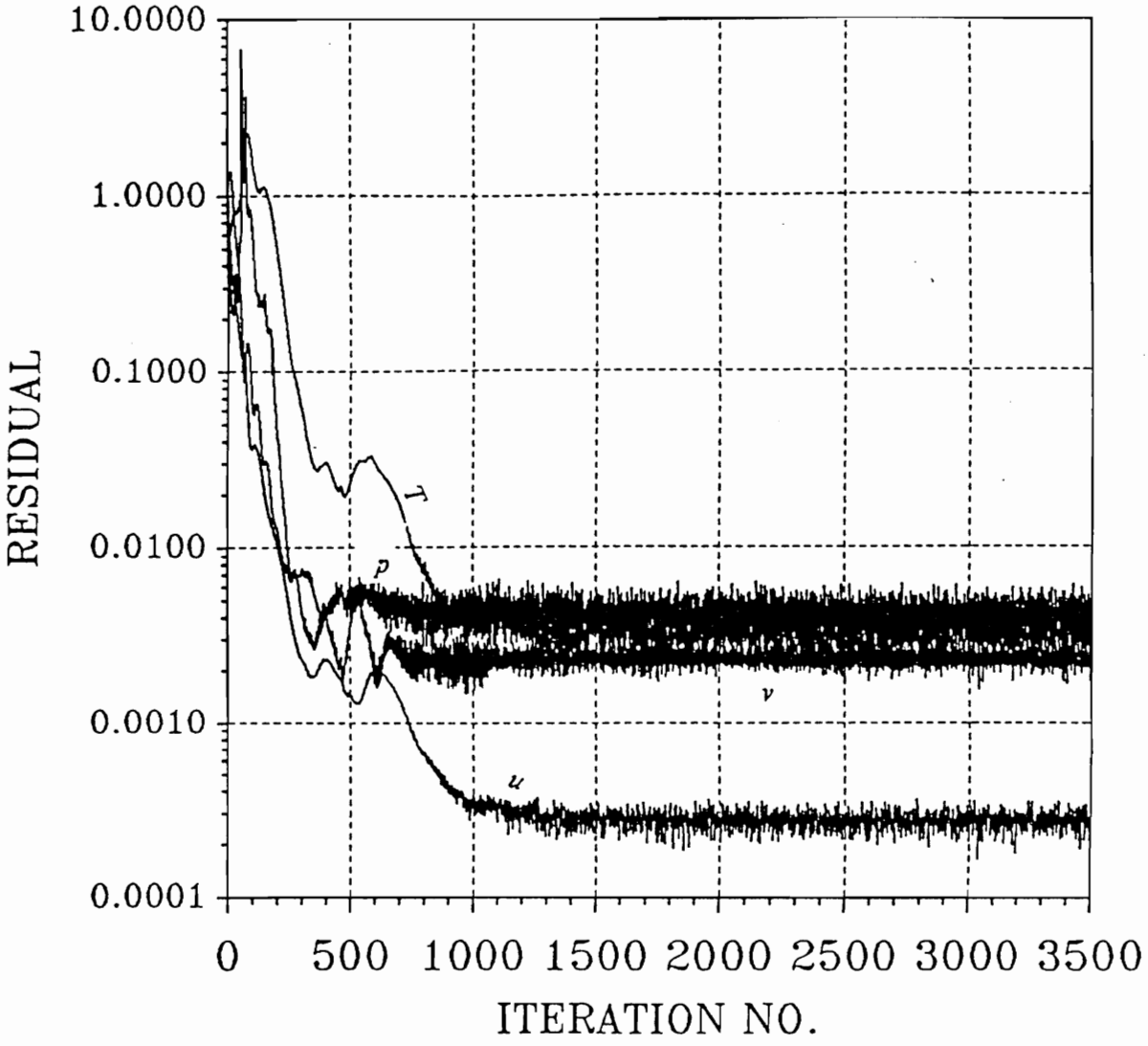

Figure 3.10. (f) Convergence history of the L_2 norm of variations, Case 5

Table 3. 3. Computational time for the axisymmetric nozzle

Case no.	Iterations no.	CPU	CPU/iteration
1	3339	7620 sec	2.28 sec
2	3340	7500 sec	2.24 sec
3	1720	3900 sec	2.27 sec
4	1720	3480 sec	2.02 sec
5	3500	11200 sec	3.2 sec

3.3.5 Conclusions

The purpose of analyzing the flow in an axisymmetric nozzle is to test the performance of the developed full Navier-Stokes solver code (PBNS) with different boundary conditions. An accurate modeling of boundary conditions will affect both the stability and convergence of the solution. The code PBNS has provided a consistent and physically sound solution for all the test cases. The implementation of the HPC code for hydrogen properties calculations raised the confidence level in both PBNS and HPC codes. The code is judged to be ready to handle the flow in a laser engine.

Chapter IV

APPLICATION OF PBNS TO AN AXISYMMETRIC LASER ENGINE

This chapter is divided into two parts. The first part is a study of the main physical and computational aspects associated with a laser engine. This includes laser power absorption, plasma radiation, and nozzle configuration. No attempt is made to improve the engine specific impulse, and the main goal is to gain understanding of the laser engine simulation in general. The second part aims at a more realistic analysis of the laser engine. Several attempts are made to improve the performance of the laser thruster.

The theoretical model given in Chapter II is applied to two different nozzle configurations. The governing equations for the laser engine, eq. (2.3), include the axisymmetric Navier-Stokes equations, and energy conservation equations. Equilibrium hydrogen is used as a propellant, and its thermodynamic and

transport properties are calculated by the code HPC. The PBNS code is used for the solution of the governing equations.

In the first part of this chapter, several parameters that are influencing laser engine performance are analyzed. These parameters include geometrical configurations of both the engine and the laser beam, laser physical characteristics such as the type of laser used, and flow inlet conditions. A combination of these parameters is tested to study their effects on the engine performance. The performance is examined through the estimation of the mass flow rate, thrust, specific impulse, laser power absorbed, and radiation losses by the optically thin assumption. Two different designs of the thrust chamber are considered. The first one is shown in Fig. 4.1(a). It consists of a cylindrical tube followed by a cosine shape converging-diverging nozzle. The propellant is injected in the x-direction along the left plane. The second design is shown in Fig. 4.1(b). The propellant is injected radially from the radial openings to the absorption chamber. This will produce good mixing between the hot plasma core and the rest of the propellant.

Plasma is initialized in the flow by two numerical schemes. In the first one, a region of high temperature (above 12000 K) near the focal point is initially assumed as an initial condition of the flow. The position and size of this region is determined by trial and error. The second scheme assumes a high absorption coefficient flow region near the focal point and is kept fixed in the initial condition and successive iterations until the hydrogen temperature reaches a high value over a small region around the focal point. Then this high numerical

absorbability is bypassed and the true absorption coefficient of the flow is used. No difference between these two schemes in the steady state solution has been noticed.

4.1 Computational Mesh

The computational meshes used for the thrust chambers are shown in Figs. 4.2(a,b). Each grid is constructed of 91 equally spaced grid points in the streamwise direction and 31 points in the transverse direction. An algebraic stretching along the top solid wall and at the centerline is implemented to resolve the large gradients in the viscous boundary layer and in the neighborhood of the laser beam focal point. Such a grid system will guarantee a fair contour resolution without excessive tax of the total CPU time. The computational mesh for solving the laser energy conservations is constructed of 11 beam rays as shown in Figs. 4.2 (a,b).

4.2 Boundary conditions

The boundary conditions for the thrust chamber I are the same as the boundary conditions used for the case 4 and 5 in Chapter III. For the thrust chamber II, the boundary conditions are the same as for the thrust chamber I along the symmetric line, exit and top thruster wall. At the leftmost wall (i = 1) the no-slip, no penetration, and vanishing of the normal derivatives of temperature and pressure are used. The flow through the radial slots is assumed to be subsonic. For the subsonic slots, the following boundary conditions are used

$$P_{To} = constant \qquad T_{To} = constant \qquad \tan^{-1}(u/v) = 0.0 \tag{4.1}$$

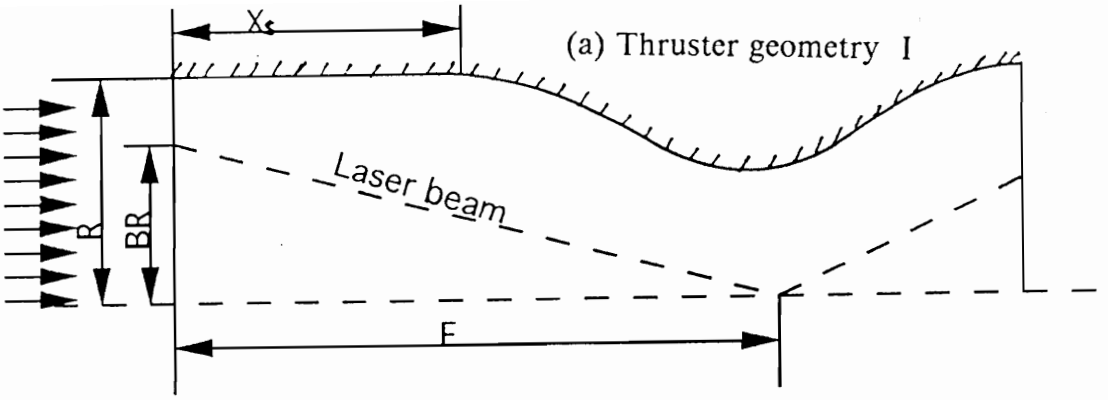

(b) Thruster geometry II

Case	θ_{in} degree	θ_{ex} degree	h cm
1-6	25.0	15.0	0.5
10	30.0	30.0	1.4
11-13	24.8	30.0	1.12
14	24.8	15.0	1.12
15	24.8	30.0	1.12
16-21	23.0	30.0	1.12

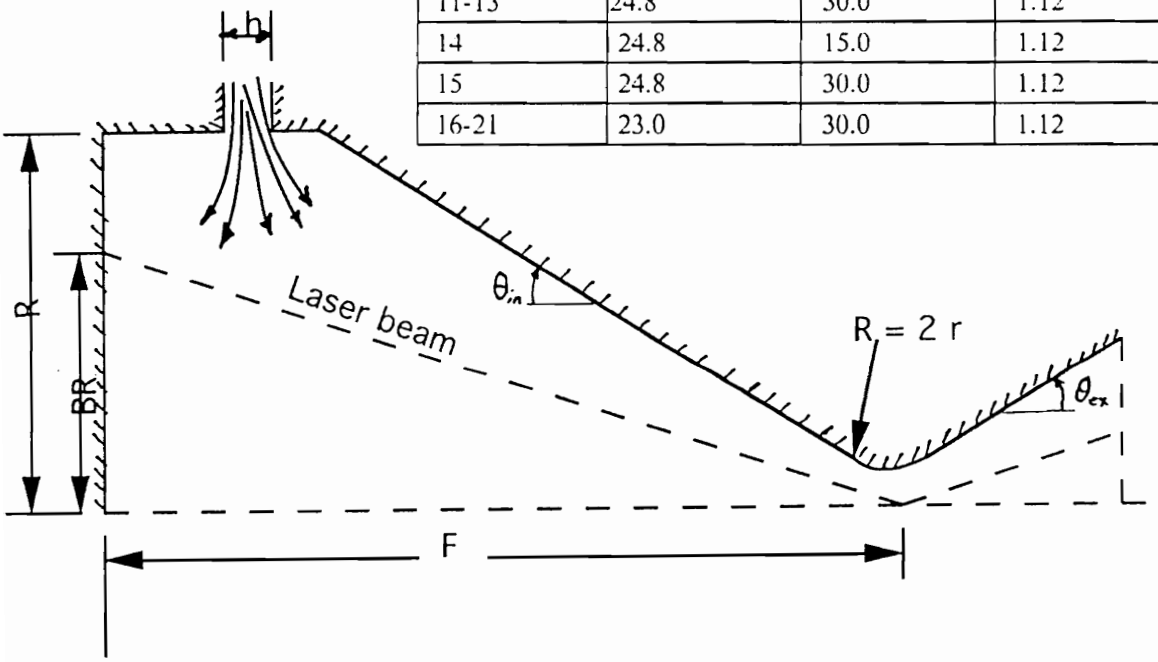

Figure 4.1. Laser engine thrust chambers (a) Thruster geometry I (b) Thruster geometry II

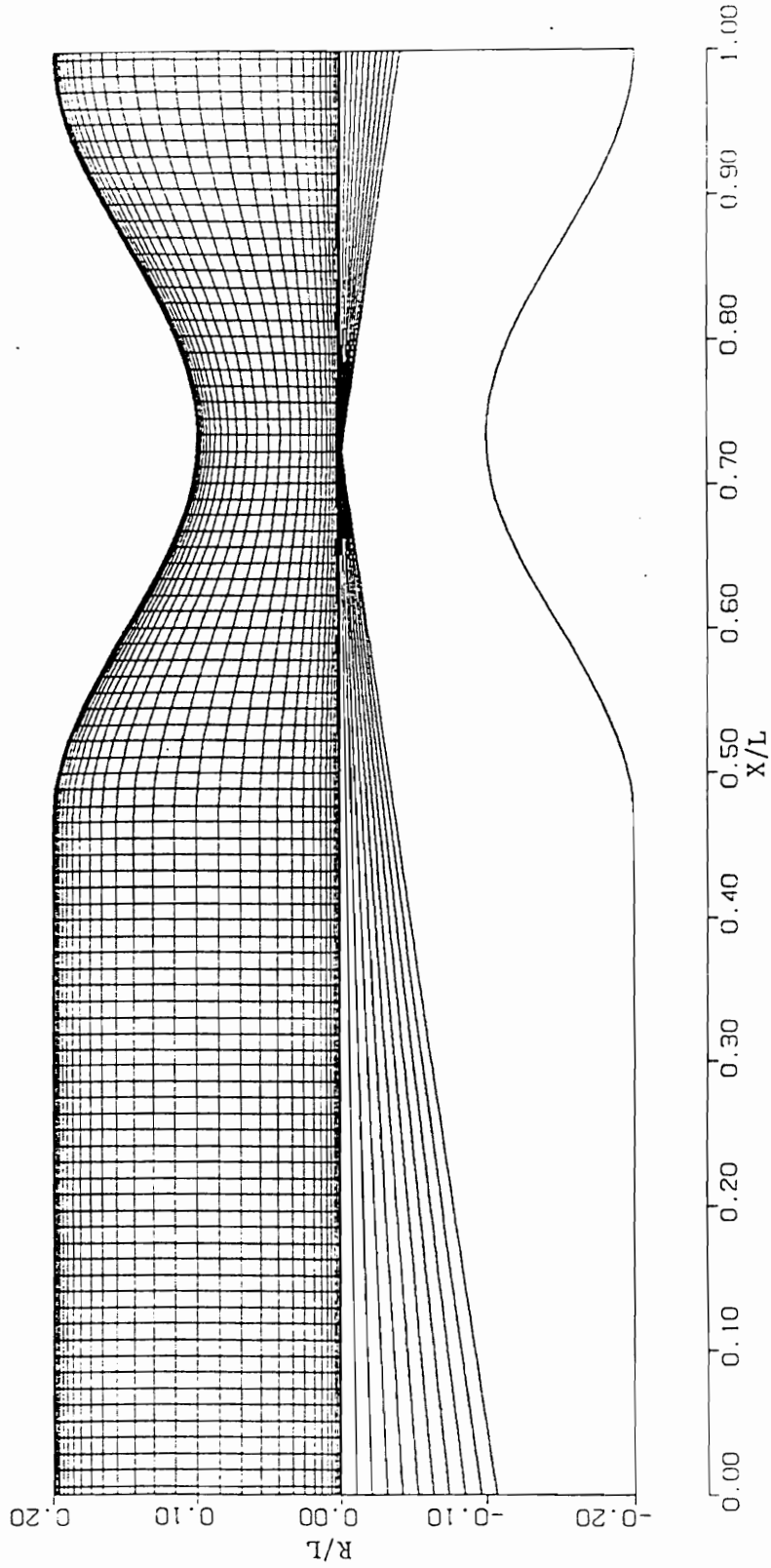

Figure 4.2. (a) 91x 31 grid cell centers used for thruster I

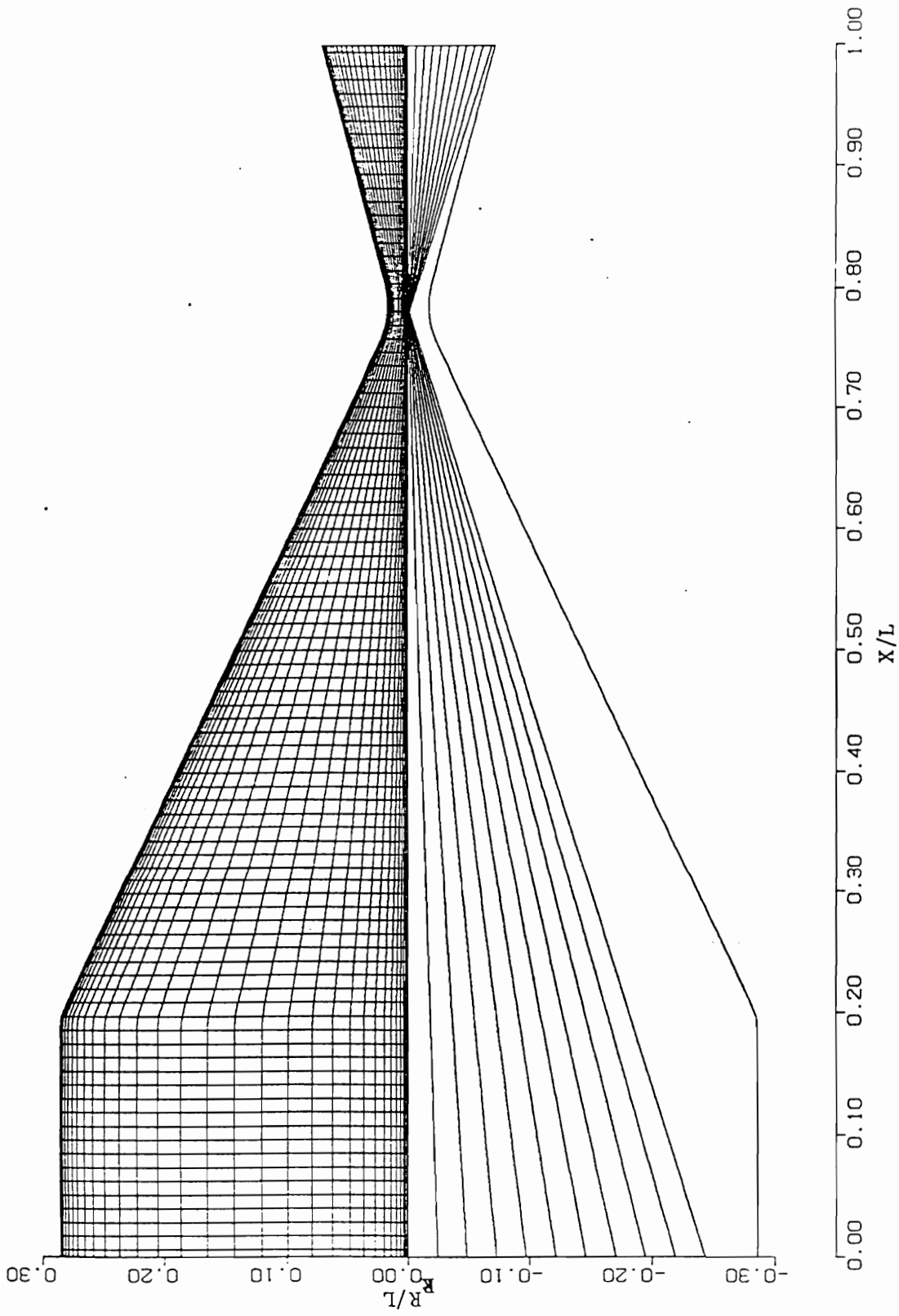

Figure 4.2. (b) 91x 31 grid cell centers used for thruster II

The fourth boundary condition is obtained by extrapolating the radial velocity from the interior domain using first order extrapolation.

4.3 Initial Testing of Laser Engine Parameters

The various parameters of the different test engines used in this part of the study are summarized in Table 4.1.a. the thrust chamber shown in Fig. 4.1 (a), and nozzle II is shown in Fig. 4.1(b). The radial slot for nozzle II ends at two grid lines from the inlet corner of the convergence cone.

4.3.1 Results and Analysis

The contour plots of the solutions for the different test cases are shown in Figs. 4.3 to 4.11. Although, it is difficult to analyze the flow characteristics of a laser thruster from these contour due to the small plasma size, some important features of a laser thruster may be pointed out. All the temperature contour shows a plasma flow that occupied only a small portion of the flow in the thruster, except for the case 3. Temperature contour are characterized by dense lines near the focal point with the maximum temperature at the centerline. Temperature decreases in the radial direction and then increases again near the thruster wall. The plasma fronts are always located upstream of the focal point. Large temperature gradient is recorded at the leading edge of the the plasma because at that place heat transfers by convection and conduction are in opposite directions. These characteristics of the plasma are similar to those reported by Jeng et al [35]. The u-velocity contour show increase of the axial velocity component towards the exit of the thruster which is a characteristics of a nozzle flow. However, a greater increase is found along the center line due to the

expanding of the hot core gases, resulting in converting the thermal energy of the propellant into kinetic energy. The v-velocity contour show that the flow tends to move upward at the leading edge of the plasma due to the great reduction in the density caused by increasing the temperature of hydrogen. At the tail of the plasma, the flow tends to have move downward due to the cooling of the plasma.

Comparison of the performance of these cases (Table 4.1.b) against their test parameters (Table 4.1.a.) several conclusions may be drawn. Since, the thruster II - cases 1 through 6- is smaller than the thruster I - cases 7,8 and 9 - lower mass flow rate is calculated for the thruster II. This allows the use of much smaller laser power. However the absorption of this power is better for the thruster I, except in the case 5 where 54% absorption is obtained with a laser power of 300 kW. Comparison between the cases 1 and 2, which are identical except for the inlet temperature, shows that the both the plasma size and the absorption of the laser power are not affected by the inlet temperature of hydrogen. However, the specific impulse increases by about 20% for the case 2 over the case 1. Doubling the inlet pressure for the case 3 at the same laser power as in the case 2, results in doubling the mass flow rate which appears to be higher than the capacity of the laser beam would allow. The initial plasma near the focal point is unable to sustain itself at this flow rate and no absorption is reported for the case 3. Trying to improve the absorption, the case 4 has been tested for a laser power of 80 kW. A 16% absorption is achieved in this case. To analyze the effect of laser power level, the case 5 is tested for the same conditions as case 1, but with a laser power of 300 kW. A 54% absorption is obtained although not much improvement is

found in the specific impulse. Looking at the temperature contour (Fig. 4.7.a) this can be justified by noticing that the plasma grows to be near the focal lens where most of the absorption occurs. With an insufficient mixing between the hot and the cold gas, the specific impulse is still low. This case proved that the plasma moves upstream of the focal point at an increased laser power. The case 6 is similar to case 1, but it assumes a constant absorption coefficient of 20 m^{-1} everywhere in the flow field. A bigger plasma size is noticed in the temperature contour. This case shows that, if all the design parameters are the same a seeded hydrogen with higher absorption coefficient will increase the specific impulse of a thruster. A scheme using a seeded propellant was analyzed Merkel et al [56].

Cases 7, 8 and 9 have a bigger size thruster which make them suitable for the application of higher laser power level. The greater radius of the lens will allow for that level of power without damaging the lens provided that the latter will be sufficiently cooled. Case 7 uses a high inlet pressure of 15 atm. with a 5 MW CO_2 laser. About 99% of the laser power is absorbed by the propellant, which is the highest absorption ratio that is achieved in the initial test cases. Although the specific impulse of this case increases to 625 sec, it is still below what is expected from a laser engine which may be explained by noticing that most of the propellant is not affected by the laser. Case 8 uses iodide laser at 1 MW power level. For an iodide laser beam having a wave length of 1.315 μm, the absorption coefficient of hydrogen is less than for CO_2 laser. This may explain a longer plasma core for this case, see Fig. 4.10.a. A shorter and smaller nozzle is used for

Table 4.1. a Engine parameters in initial tests

Case	Thruster	R m	CR	Xt/L m/m	Power kW	λ μ m	BR/F m/m	To K	Po kN/m^2	Tw K
1	II	20 x 10^{-3}	.06	55/70 x 10^{-3}	30	10.16	17/55 10^{-3}	1000	150	1000
2	II	20 x 10^{-3}	.06	55/70 x 10^{-3}	30	10.16	17/55 10^{-3}	1500	150	1500
3	II	20 x 10^{-3}	.06	55/70 x 10^{-3}	30	10.16	17/55 10^{-3}	1500	300	1500
4	II	20 x 10^{-3}	.06	55/70 x 10^{-3}	80	10.16	17/55 10^{-3}	1500	300	1500
5	II	20 x 10^{-3}	.06	55/70 x 10^{-3}	300	10.16	17/55 10^{-3}	1000	150	1000
6	II	20 x 10^{-3}	.06	55/70 x 10^{-3}	30	10.16	17/55 10^{-3}	1000	150	1000
7	I	.15	.25	.55/.75	5000	10.16	.08/.55	2000	1519.875	2000
8	I	.15	.25	.55/.75	1000	1.316	.08/.55	2000	1519.875	2000
9	I	.12	.16	.40/.60	1000	1.316	.10/.40	2000	1519.875	2000

R	Thruster radius at x = 0.0
CR	Contraction ratio
Xt	Distance between the lens and the throat
L	Thruster length
Power	Laser beam power
λ	Laser wavelength
BR	Laser beam radius
F	Focal length of the lens

Table 4.1. b Engine performance in initial tests

Case	Mass flow *kg/* sec	Power abs. W	Absorption %	Radiation loss W	Thrust N	I_{sp} sec	I_{spt} sec
1	232.95 x 10^{-6}	716	2.38 %	13 x 10^{-6}	1.11	449.85	484.51
2	191.33 x 10^{-6}	723	2.41 %	14 x 10^{-6}	1.09	533.47	581.25
3	396.93 x 10^{-6}	0.0	0.00 %	0.0	2.24	537.21	576.39
4	389.64 x 10^{-6}	12,977	16.22 %	13 x 10^{-3}	2.24	546.49	587.14
5	190.91 x 10^{-6}	162,771	54.3 %	4170 x 10^{-3}	1.08	532.93	575.76
6	223.98 x 10^{-6}	5,775	19.25 %	46 x 10^{-6}	1.11	470.57	505.93
7	6.504	5,000,000.0	100.0 %	748.538	39,823.56	555.22	624.07
8	6.535	474,864.74	47.48 %	60.583	39,863.16	553.13	621.80
9	2.655	592,961.24	59.30 %	1,231.83	16,940.85	596.83	650.31

Power abs. — total power absorbed by hydrogen
Radiation loss — total radiation loss from the plasma (optically thin part)
I_{sp} — specific impulse
I_{spt} — vacuum specific impulse

the case 9. Here, a lower mass flow rate of hydrogen is used and a bigger plasma is obtained with an absorption of about 60%. However, the specific impulses for all the previous test cases, see Table 4.1. (b), are still below what is expected from a laser thruster. This low performance may be a result of insufficient mixing between the hot plasma core and the cold flow.

The radiation losses to the thruster walls - optically thin radiation- is calculated for all the above cases and are found to be insufficient to raise the propellant thermal energy to its assumed values at the injection slots.

To improve the performance, a higher power of laser may be need. However, this alone without sufficient mixing between the cold and hot gases, will not reveal the full ability of the laser engine. Rocketdyne design group [72] suggested injection of small carbon particles , less than 1 μm radius, to enhance the efficiency of radiation absorption in the visible and infrared wavelength region. However, carbon has high molecular weight, and will reduce the specific impulse of the engine.

4.4 Improved Design for Laser Engine

The design process is a trial and error one. The optimal design may be reached through several test cases. However, based on the results of the initial test cases, the basic physics that may help to define steps toward an improved thruster design. In this part, thruster II is selected to perform the test cases because it achieves good mixing and recirculating flow which is believed to improve the performance of a laser thruster.

The focal point of the lens is chosen to be downstream of the nozzle throat. The contraction ratio should be selected such that will force a large percentage of the flow to pass through a narrow area where it is exposed to a high intensity laser beam. The dimensions of the thruster 10 is calculated from the one dimensional analysis developed by Rocketdyne [72] for a 5 MW laser engine. The test cases following the test case 10 are additional improvements on thruster 10. These improvements include smaller contraction ratio, smaller thruster dimensions, larger laser power, and higher injection pressure. These factors are found to be effective in improving the performance of laser engines.

Parameters for new laser engine test cases are given in Table 4.3.a., while the performance of these cases is given in Table 4.3.b. Figures 4.12 to 4.23 show the contour plots of the results for these test cases. The contour shows behavior of flow fields similar to the previous cases but on a larger scale, since the plasmas produced in these cases are much larger than for the previous cases. Also, the velocity contour plots show two recirculation zones, one near the inlet at the wall corner and the other near the focal lens.

The design used in the case 10 achieves 97% absorption with a larger plasma size, Fig. 4.12.a., than the previous cases. Test case 11 represents an improvement of the design used in the case 10 by reducing the nozzle dimensions to allow for better mixing between the hot and cold gases. About a further 10% increase in the specific impulse is gained for this case. Increasing the input laser power to 6000 kW in the case 12 with the same design as used in the case 11, increases the specific impulse to 725 sec. However, a relatively a small

improvement is gained in the case 13 by increasing the laser power to 10 MW. The radiation- optically thin- increases by a factor of 2, while the absorption increases by a factor of 1.1 only. This explains a relatively small improvement gained in the case 13 over the case 12. The radiation loss to the walls, which is 141.2 kW, is sufficient to raise the propellant injection temperature to 2000 K.

The angle of the diverging cone is reduced from 30 degrees in the case 13 to 15 degrees for the case 14. Other than that, the case 14 is similar to the case 13 and shows the effect of the expansion area ratio (exit area to throat area) on the performance of the engine. The results, as shown in Figs. 4.16 a-e, show a gradual expansion of the flow in the supersonic part of the nozzle, which reduced cooling rate of the exhaust gases. This test shows that a better performance can be achieved by increasing the expansion ratio of the nozzle, just as with a chemical thrusters. The case 15 utilizes the same nozzle used in the case 13, but with a power level of 15 MW. The specific impulse jumps to 814 sec with a plasma occupying more than 50% of the flow field near the throat, see Fig. 4.17(a). A 10% increases in the specific impulse is calculated for the case 16, which uses a smaller thruster. A specific impulse of 890 sec is obtained in this case, with a smaller radiation loss than in the case 15. The case 17 uses the same thruster as the case 16 but with a laser power of 20 MW. Small improvement occurs in the specific impulse with almost doubled the radiation loss over the previous case, which results from having a bigger plasma, as shown in Fig. 4.19 (a), for this case than the case 16. The case 18 demonstrates the effect of the injection pressure on the plasma formation. This case uses the same nozzle and

same power level as the case 17, but an injection pressure of 10 atm instead of 3 atm. The specific impulse jumps to 1537 sec with a 100% absorption achieved inside the chamber. However,the radiation loss from the plasma increases to 7.7 MW. A very effective cooling is needed to protect the thruster for this design. This case shows the ability of the laser engine to produce a high specific impulse of more than 1000 sec.

The cases 19 through 21 utilize an iodide laser beam, which has a $1.316\mu m$ wavelength. Hydrogen has a much lower absorption coefficient at that wavelength. However, a higher absorption can be achieved by increasing the injection pressure. The case 19 uses the same dimensions of the thruster as the case 18 and the same level of power, but with an injection pressure of 15 atm. The temperature contour, see Fig. 4.21(a), show a slender plasma with smooth contour lines. Only 22% of the laser power is absorbed. Still the specific impulse is calculated to be 778 sec. An injection pressure of 20 atm is used for the case 20, which uses the same thruster and laser beam as the case 19. Although the absorption increases to 37% and the thrust level is improved, the specific impulse increases only slightly to 783 sec. This small increase in the specific impulse may be related to a significantly increased radiation losses. The last case (21) utilizes a laser power of 25 MW and an injection pressure of 20 atm. All the other design parameters are kept the same as for the case 20. Although a higher power level is used, the same absorption ratio is obtained. The plasma size is larger and the specific impulse increases to 827 sec.

Table 4.2.a. Engine parameters in final tests.

Case	Thruster	R m	CR	Xt/L m/m	Power kW	λ μ m	BR/F m/m	To K	Po kN/m^2
10	II	0.10	.0156	0.2/0.25	5000	10.16	.09/.20	2000	303.9
11	II	0.09	.01	0.2/0.25	5000	10.16	.09/.21	2000	303.9
12	II	0.09	.01	0.2/0.25	6000	10.16	.09/.21	2000	303.9
13	II	0.09	.01	0.2/0.25	10,000	10.16	.09/.21	2000	303.9
14	II	0.09	.01	0.2/0.25	10,000	10.16	.08/.205	2000	303.9
15	II	0.09	.01	0.2/0.25	15,000	10.16	.08/.205	2000	303.9
16	II	0.085	.00886	0.2/0.25	15,000	10.16	.08/.205	2000	303.9
17	II	0.085	.00886	0.2/0.25	20,000	10.16	.08/.205	2000	303.9
18	II	0.085	.00886	0.2/0.25	20,000	10.16	.08/.205	2000	1013.25
19	II	0.085	.00886	0.2/0.25	20,000	1.316	.08/.205	2000	1519.875
20	II	0.085	.00886	0.2/0.25	20,000	1.316	.08/.205	2000	2026.50
21	II	0.085	.00886	0.2/0.25	25,000	1.316	.08/.205	2000	2026.50

R	Thruster radius at x = 0.0
CR	Contraction ratio
Xt	Distance between the lens and the throat
L	Thruster length
Power	Laser beam power
λ	Laser wavelength
BR	Laser beam radius
F	Focal length of the lens

Table 4.2.b Engine performance in final tests.

Case	Mass flow rate *kg/* sec	Power abs. W	Absorption %	Radiation loss W	Thrust N	I_{sp} sec	I_{spt} sec
10	37.50 x 10^{-3}	4,856,427.36	97.13 %	36,219.93	228.71	577.56	621.73
11	19.79 x 10^{-3}	4,332,576.02	86.65 %	55,978.47	134.07	650.58	690.42
12	18.84 x 10^{-3}	5,116,001.03	85.27 %	74,121.90	134.17	686.61	725.80
13	17.42 x 10^{-3}	9,400,899.6	94.01 %	141,220.34	134.97	749.48	790.02
14	17.44 x 10^{-3}	9,198,331.77	91.98 %	140,448.04	133.37	726.21	779.67
15	16.96 x 10^{-3}	14,171,158.39	94.47 %	336,673.49	135.36	770.72	813.65
16	10.89 x 10^{-3}	13,097,473.73	87.31 %	258,004.0	94.96	848.56	889.20
17	11.22 x 10^{-3}	18,851,982.06	94.26 %	465,282.97	99.98	866.30	907.98
18	20.43 x 10^{-3}	20,000,000.0	100.0 %	7,699,451.2	308.01	1490.8	1537.2
19	63.29 x 10^{-3}	4,389,032.64	21.95 %	300,029.8	482.9	738.18	777.79
20	83.45 x 10^{-3}	7,492,424.47	37.46 %	797,829.68	641.0	743.42	783.04
21	79.32 x 10^{-3}	9,334,169.0	37.33 %	1,219,073.4	644.13	785.79	827.74

Power abs. total power absorbed by hydrogen
Radiation loss total radiation loss from the plasma (optically thin part)
I_{sp} is specific impulse
I_{spt} is vacuum specific impulse

The results for the iodide laser show that the absorption of the laser power can still be achieved for shorter laser wavelength, if a sufficiently high injection pressure is used. However, only low absorption of the laser beam power is achieved for the tested nozzle configuration. A nozzle with a long throat area may improve the performance of a thruster using an iodide laser.

4.5 Code Performance and Convergence

All the results of the simulation of a laser engine were obtained using an IBM 3090 vector processing computer at Virginia Tech. The average CPU per iteration for 91 x 31 grid was 3.5 seconds.

The convergence of the solutions has been checked by insuring that the produced fields satisfied both the global and local mass unbalance to 10^{-6} . Also, the L_2 norm of the residuals for the velocities , pressure, and enthalpy was insured to reach a value of 10^{-10}. Typical L_2 norm of variations of the variables are shown in Figs. 4.24 a-e . It is required that the normalized value of these norms should be reduced by three orders of magnitude before the integration could be stopped. It is noticed that some of the cases produced only 2.5 reduction in the order of magnitude of the norm of variation of the temperature field. Increasing the number of iterations produced no further change in the solution fields. This slow convergence in the temperature field may be explained by noting that a linear interpolation is used to get the temperature field from the enthalpy and pressure fields. A cubic curve spline interpolation may tighten the convergence of the temperature field. Also, the use of multi-grid system may be useful for damping out long wave oscillations in the solution.

4.5.1 Conclusions

The results presented in this chapter indicate that a laser engine can provide high specific impulse at various thrust levels. The main limitations to laser propulsion application will be the availability of the space-based high-power laser station and advances in the optical technology.

A specific impulse of about 1540 is predicted for one of the calculated thrust chambers. A 100% absorption of the laser power can be achieved with a suitable selection of design parameters. The best design configuration is the one that will guarantee good mixing between the hot and the cold gas. The recirculation of the flow is a very important factor for improving the performance of the engine. The results showed that the best performance of the engine may be obtained if the focal point of the lens is set to be at a small distance downstream of the nozzle throat. A long nozzle was found to be preferable with the iodide laser power. Using higher injection pressure, the engine operated with an iodide laser can compete with the one using CO_2 laser. A specific impulse of 840 sec was calculated for one of the engines using an iodide laser. The low radiation loss, extended plasma, and the short wave behavior of the iodide laser makes it favorable for space missions. However, the lower absorbability of the iodide laser must be considered in the design process.

The radiation loss from the hot core plasma is, typically, quite high. By applying a regenerative nozzle wall cooling scheme, this radiation loss can be used for increasing the thermal energy of the propellant entering the thrust chamber. The high inlet temperature of the propellant (2000 K) is an indication of such a

scheme. The position and the size of the plasma depend on many factors such as the optical train of the laser beam, the laser power level, and nozzle configuration.

In summary, the PBNS was used to solve Navier-Stokes equations for equilibrium hydrogen flow inside the laser engine. The code was shown to be able to evaluate performance of the laser engine under various design and input conditions.

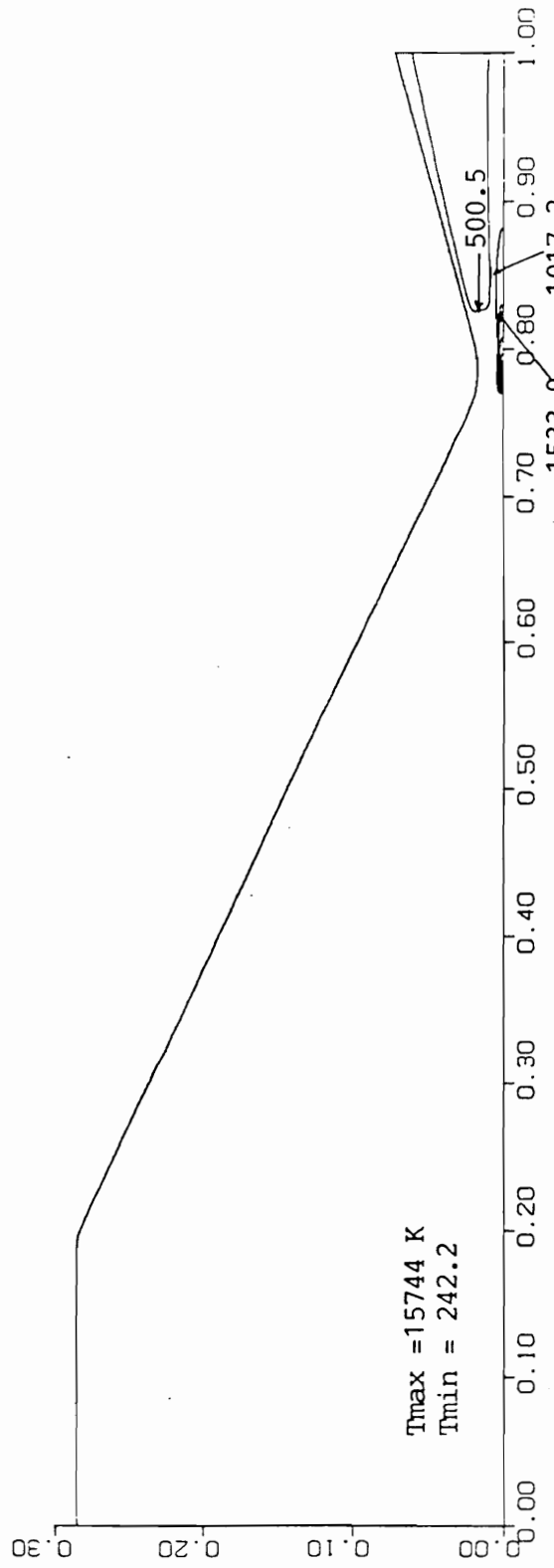

Figure 4.3. (a) Temperature contour, Case 1

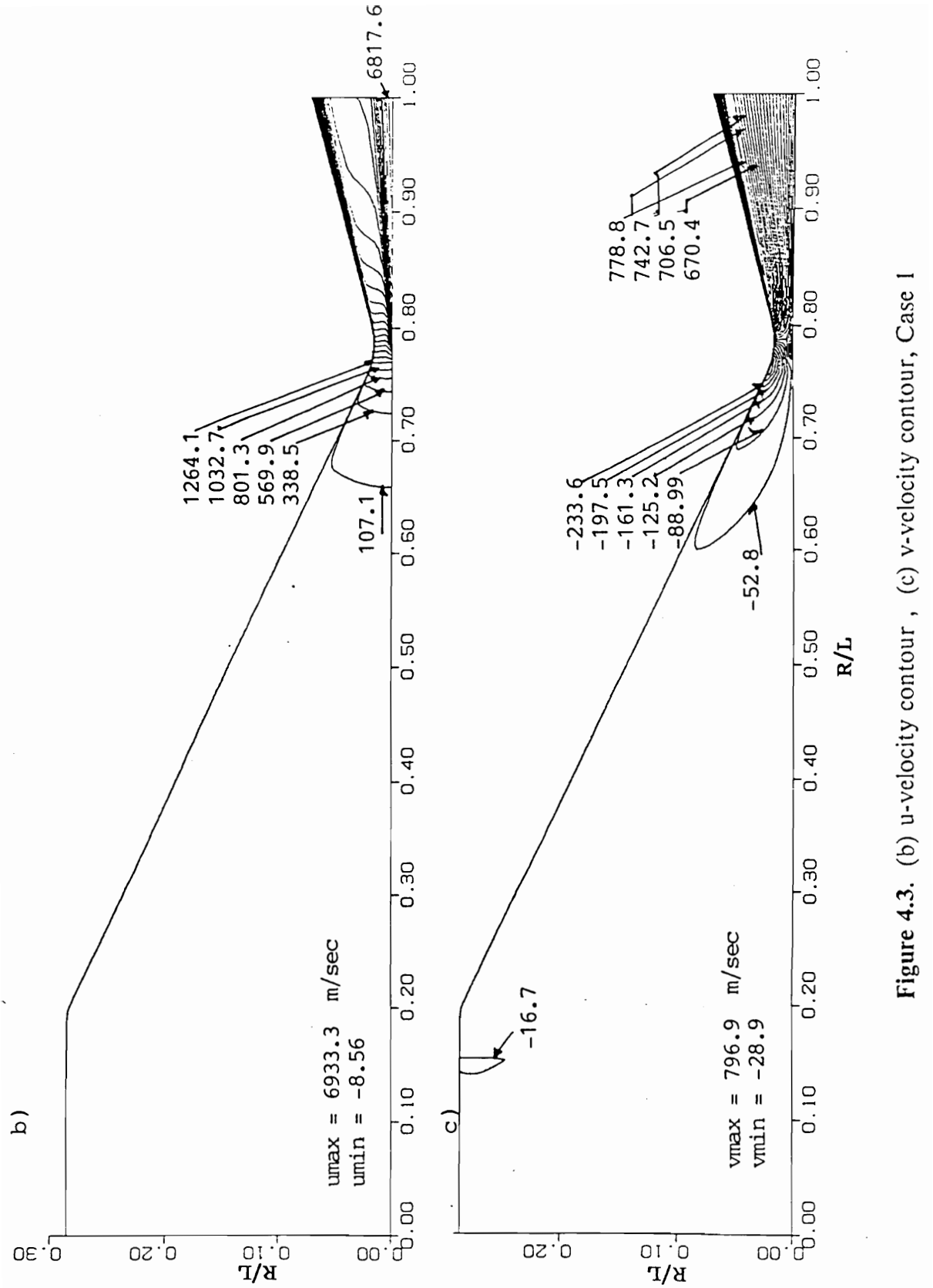

Figure 4.3. (b) u-velocity contour , (c) v-velocity contour, Case 1

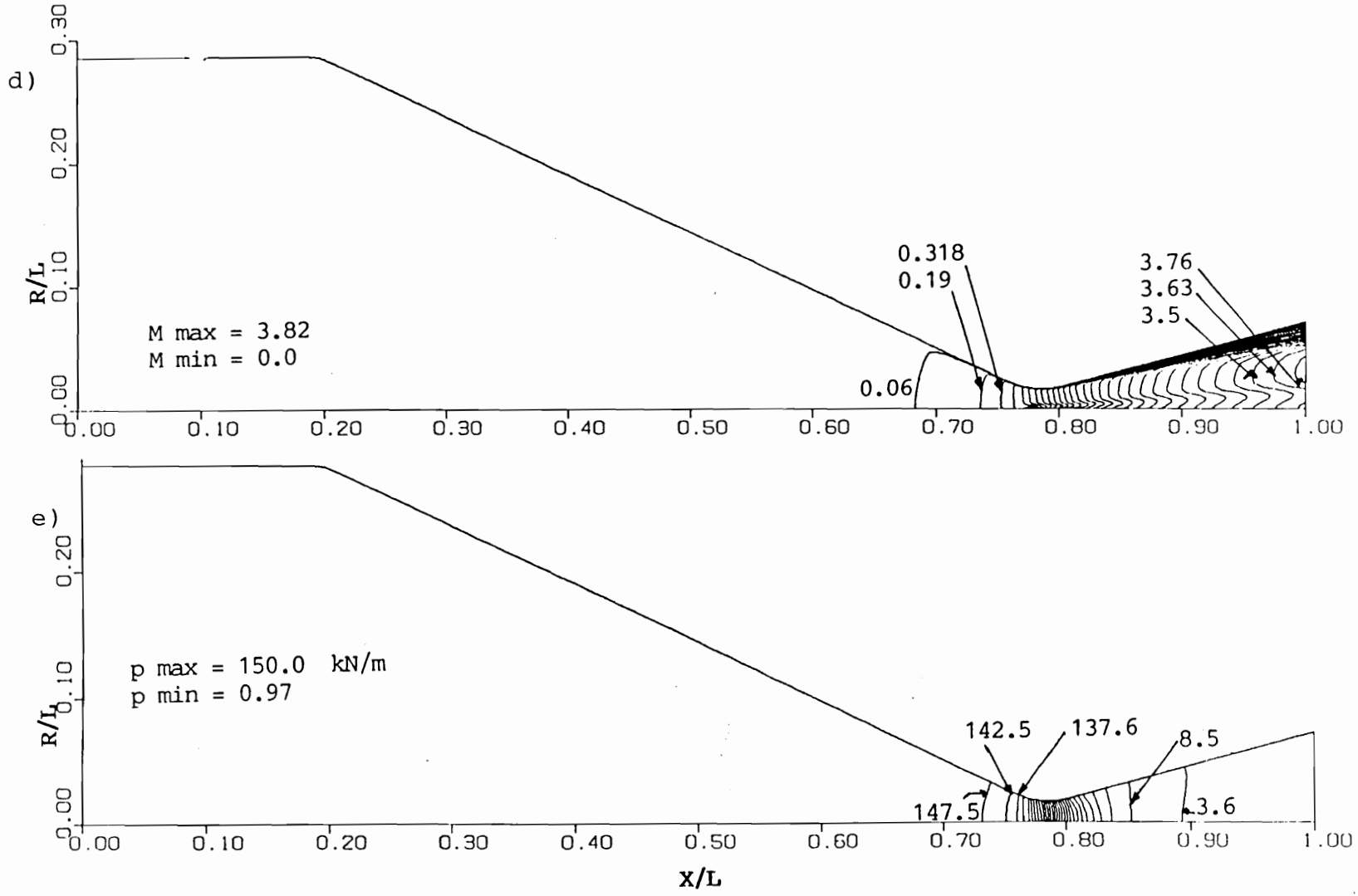

Figure 4.3. (d) Mach contour , (e) Pressure contour, Case 1

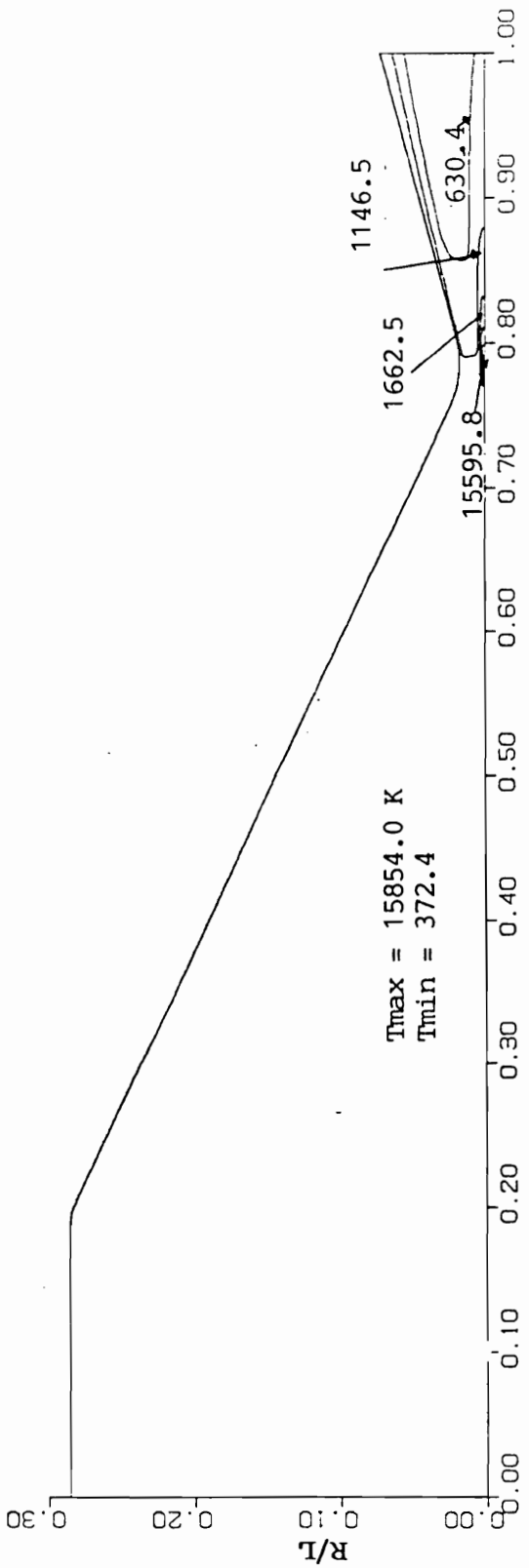

Figure 4.4. (a) Temperature contour, Case 2

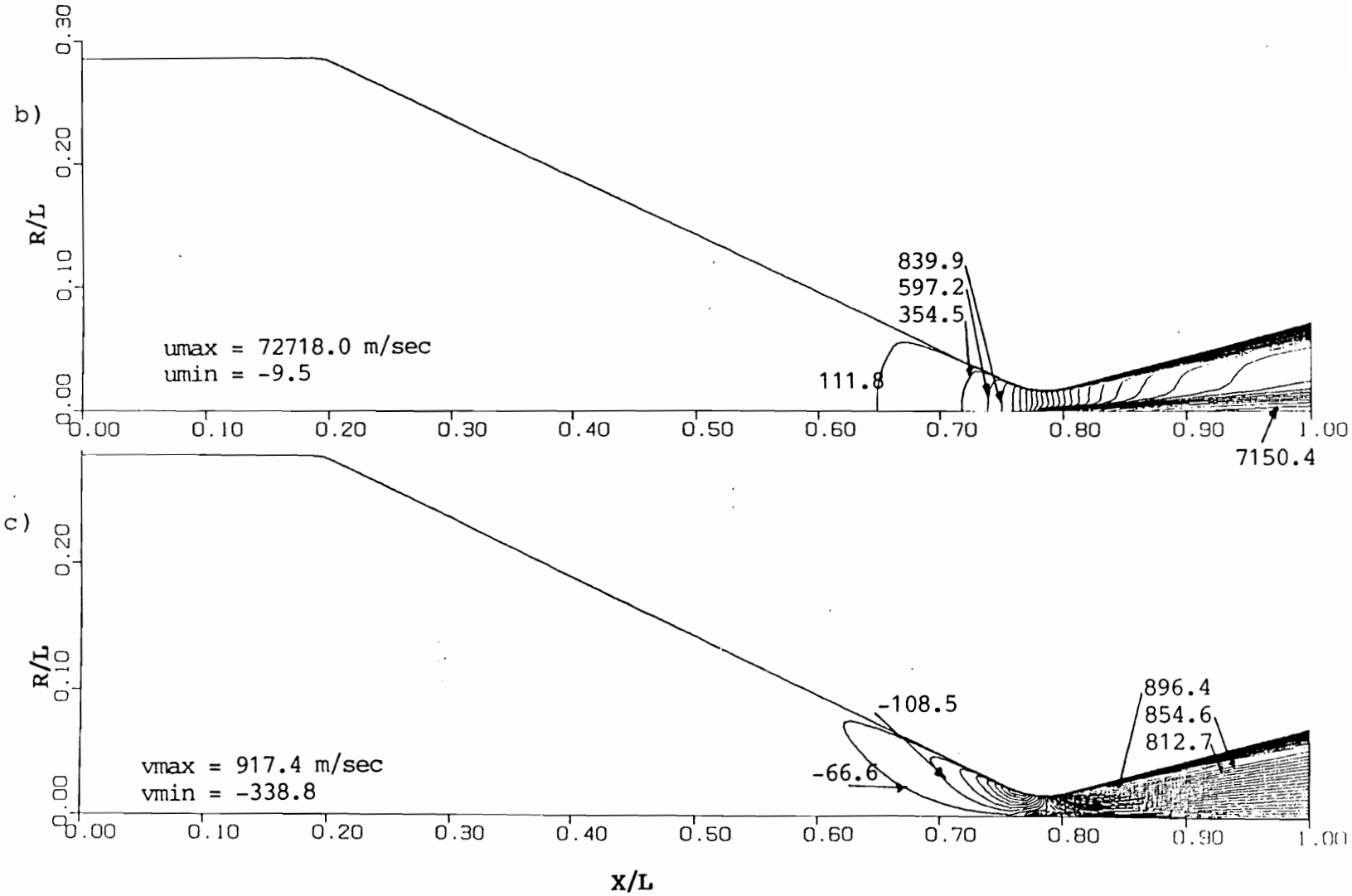

Figure 4.4. (b) u-velocity contour , (c) v-velocity contour, Case 2

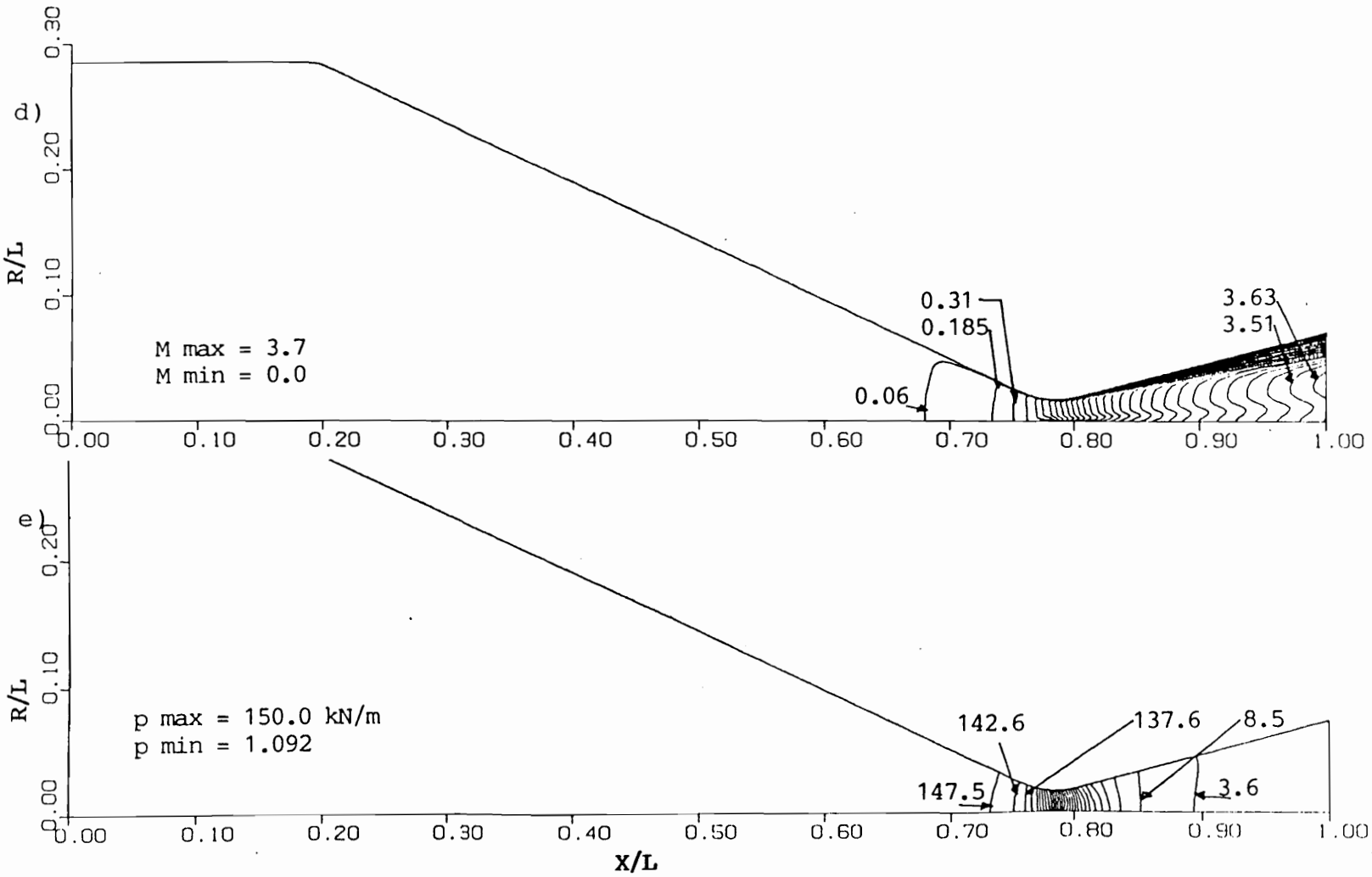

Figure 4.4. (d) Mach contour , (e) Pressure contour, Case 2

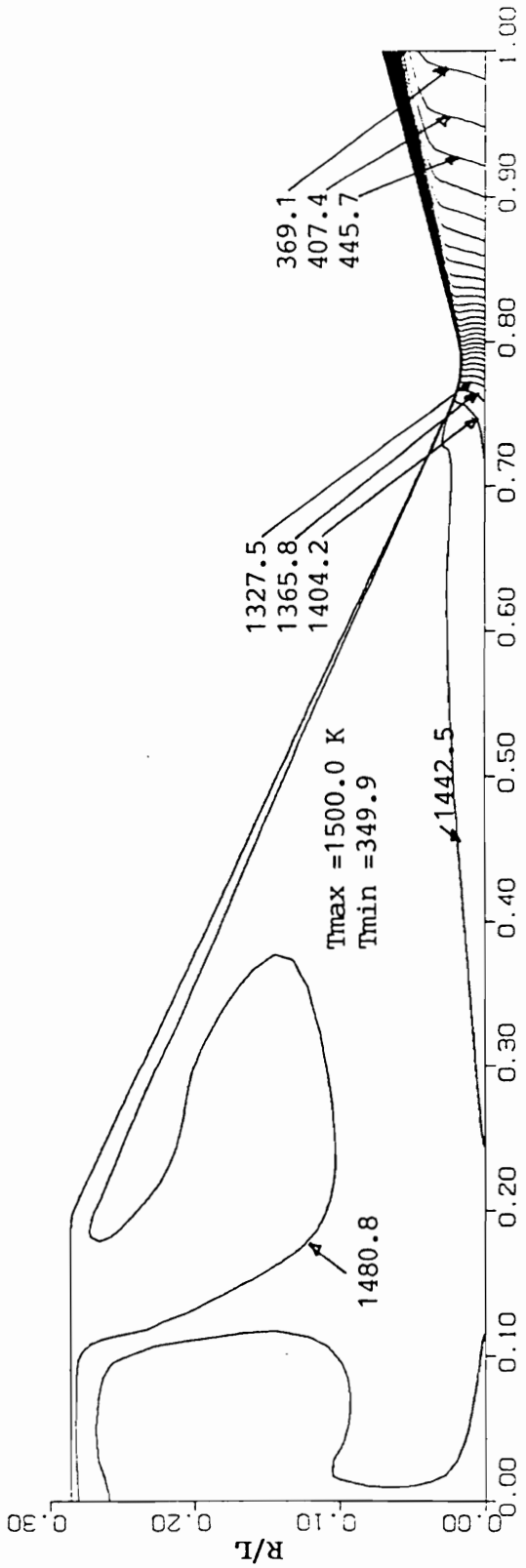

Figure 4.5. (a) Temperature contour, Case 3

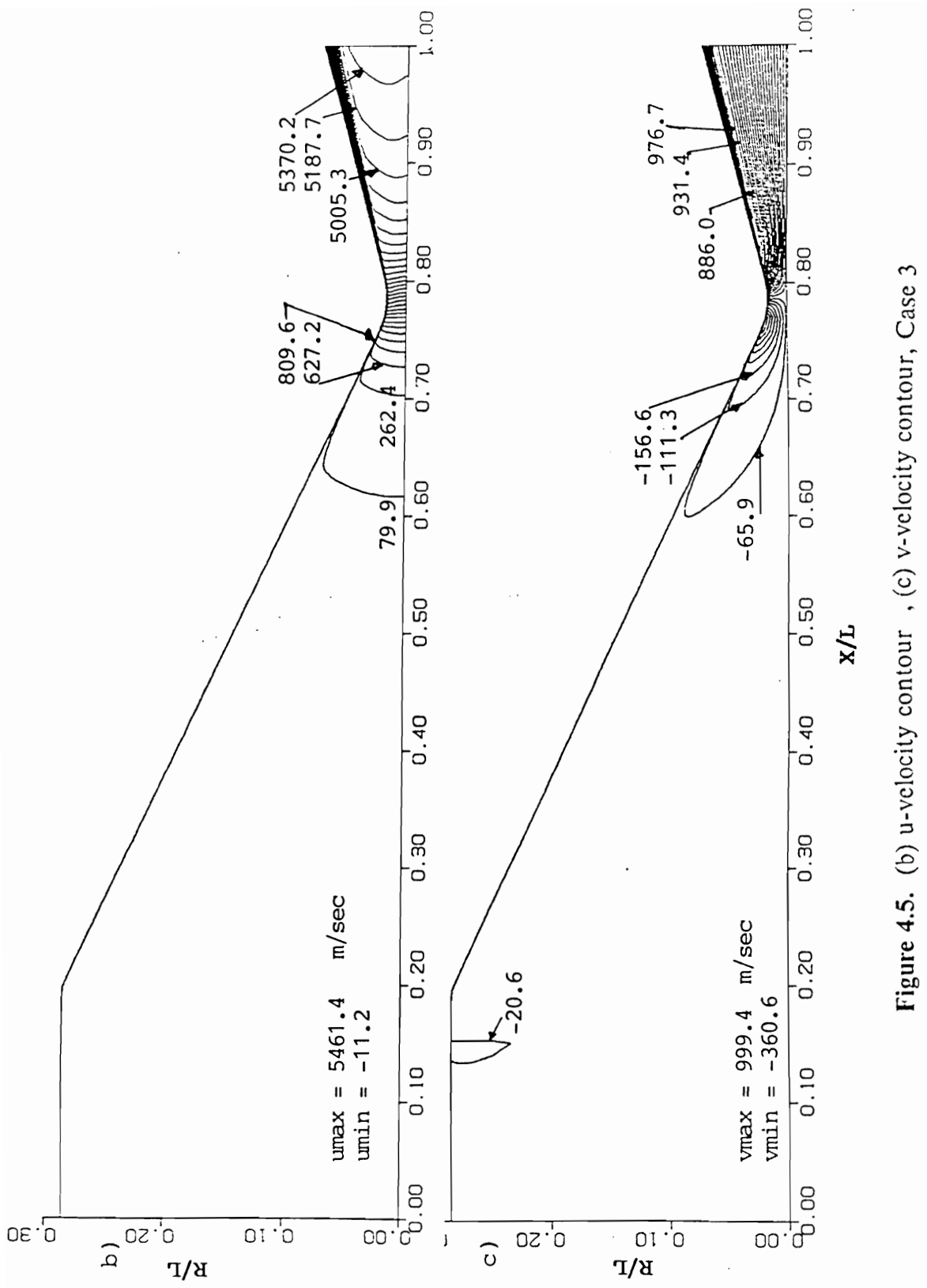

Figure 4.5. (b) u-velocity contour , (c) v-velocity contour, Case 3

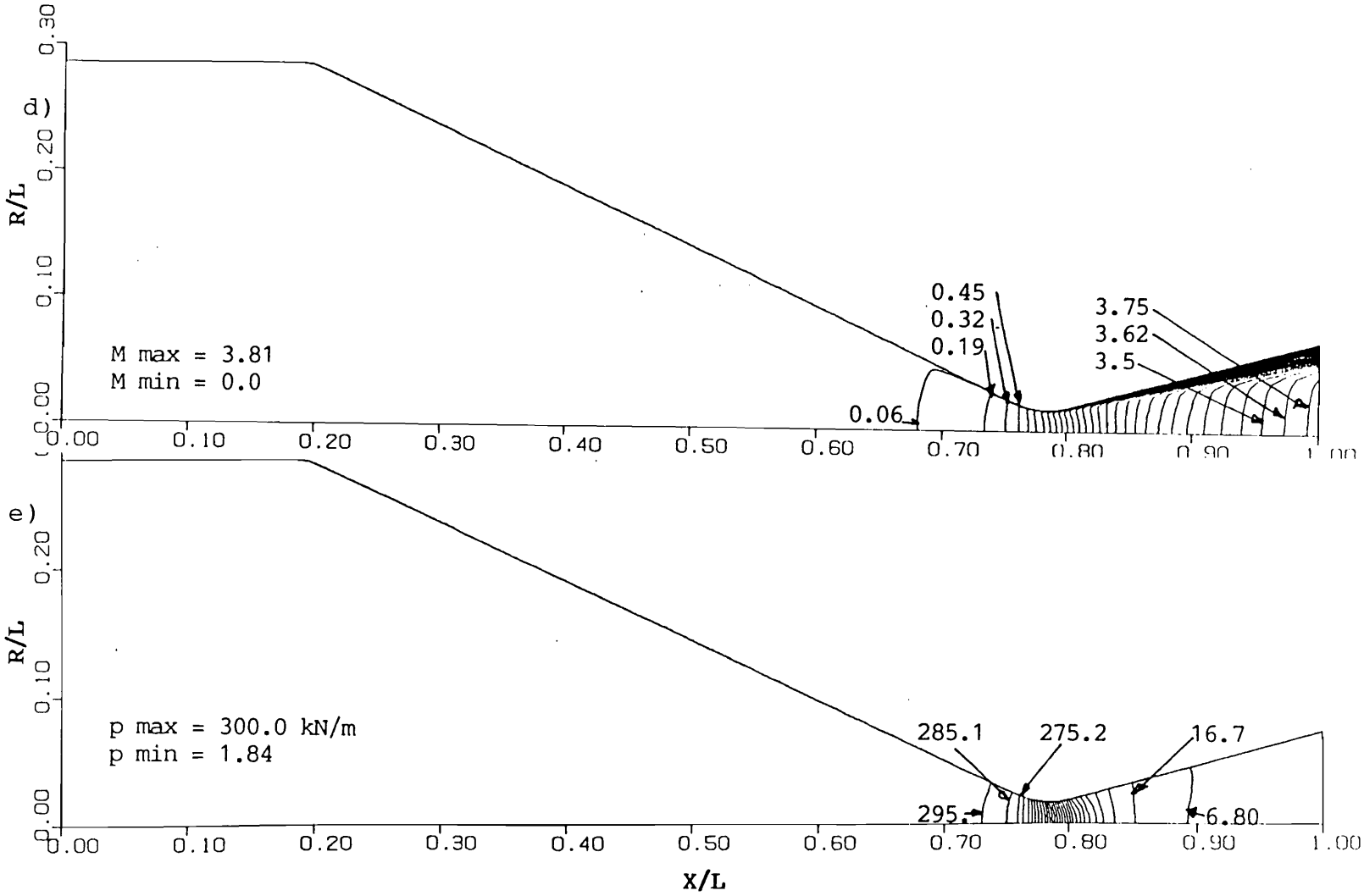

Figure 4.5. (d) Mach contour , (c) Pressure contour, Case 3

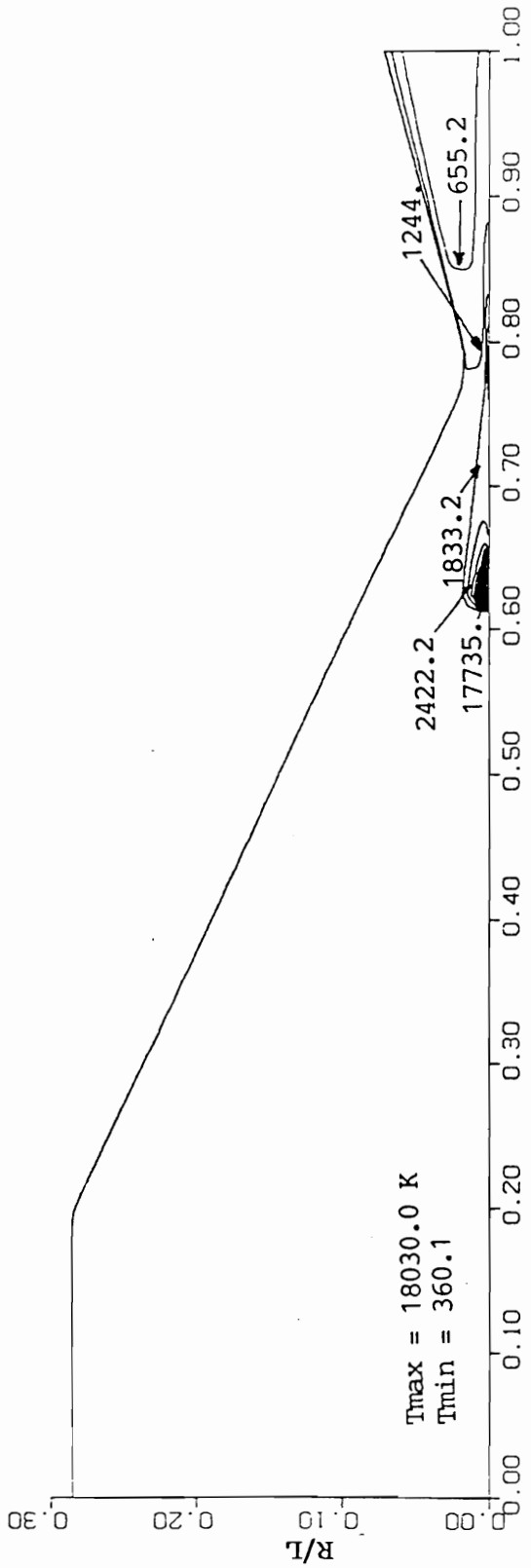

Figure 4.6. (a) Temperature contour, Case 4

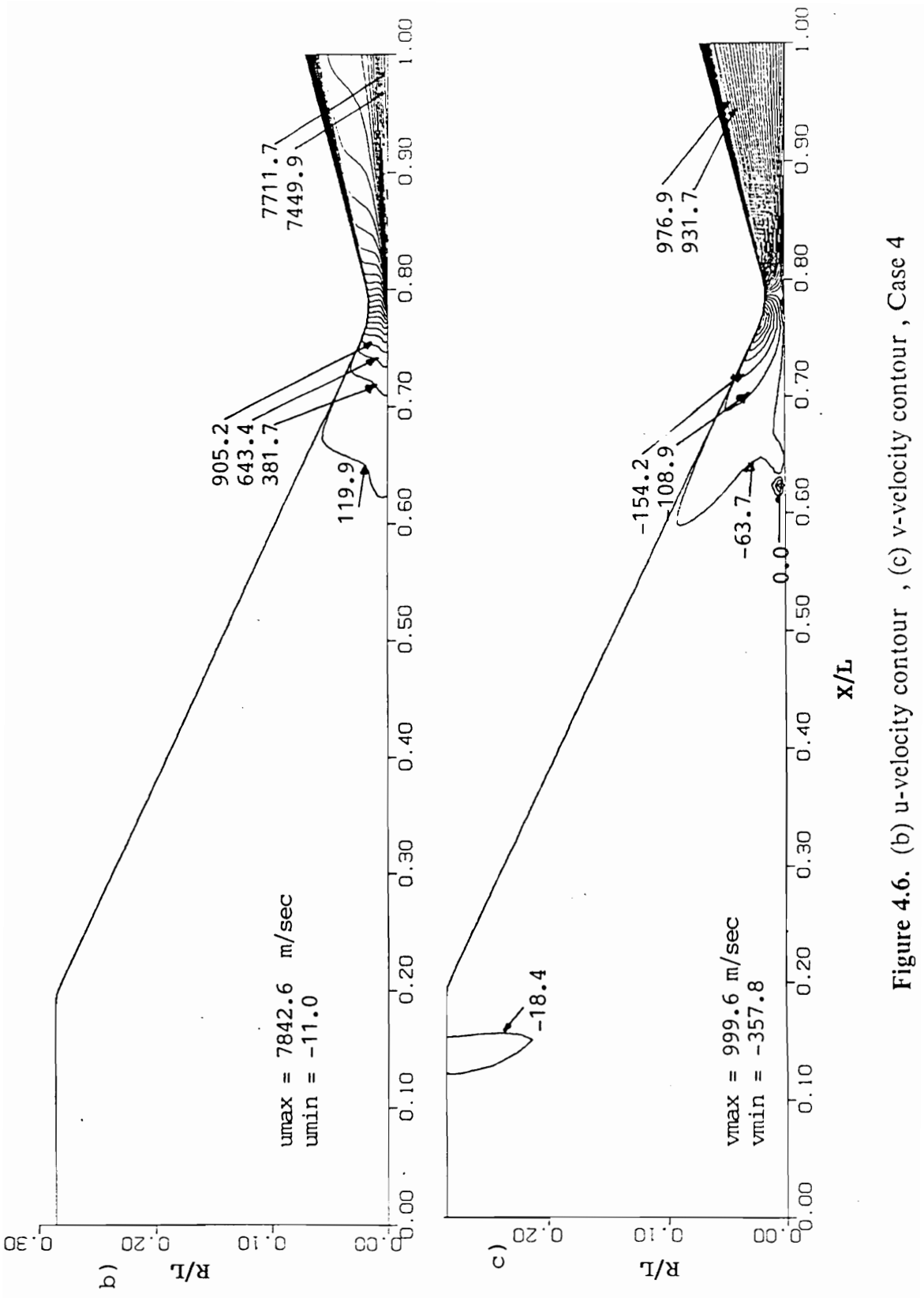

Figure 4.6. (b) u-velocity contour , (c) v-velocity contour , Case 4

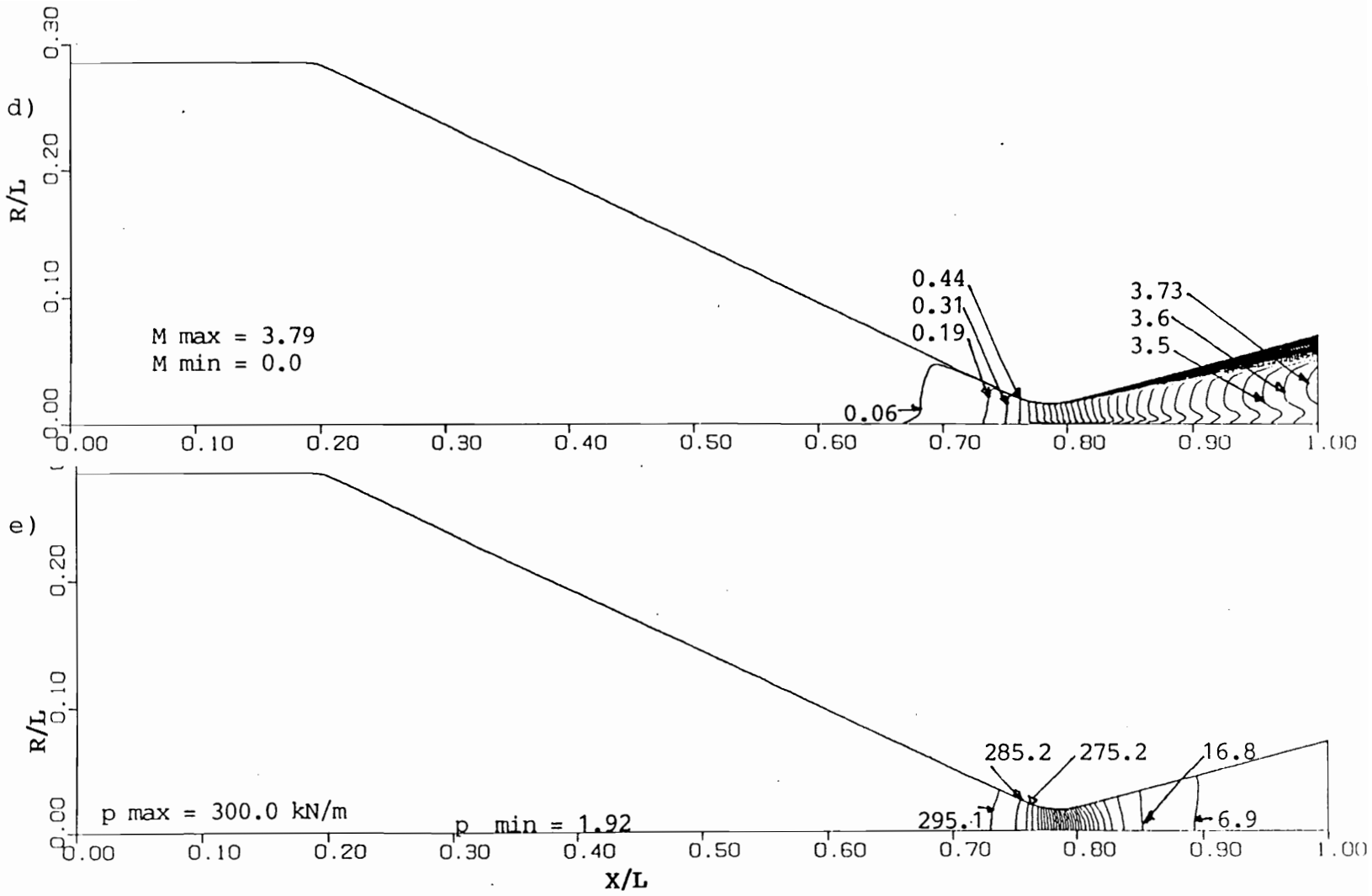

Figure 4.6. (d) Mach contour , (e) Pressure contour, Case 4

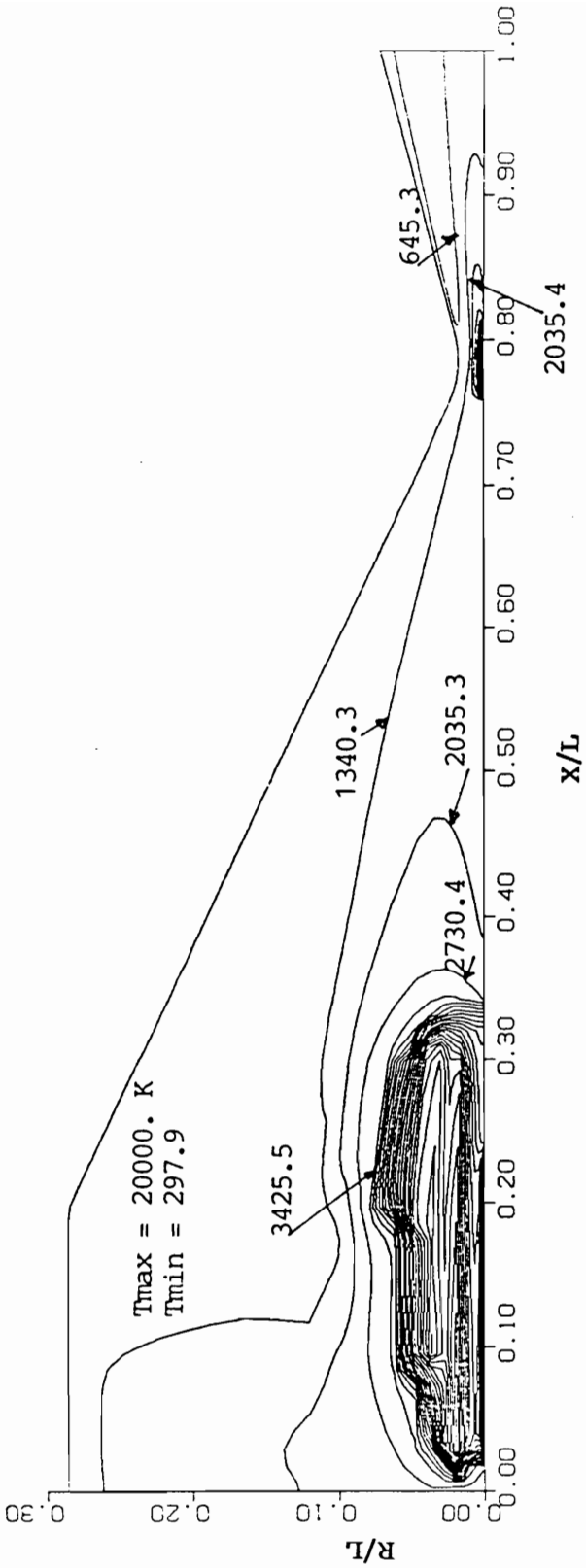

Figure 4.7. (a) temperature contour, Case 5

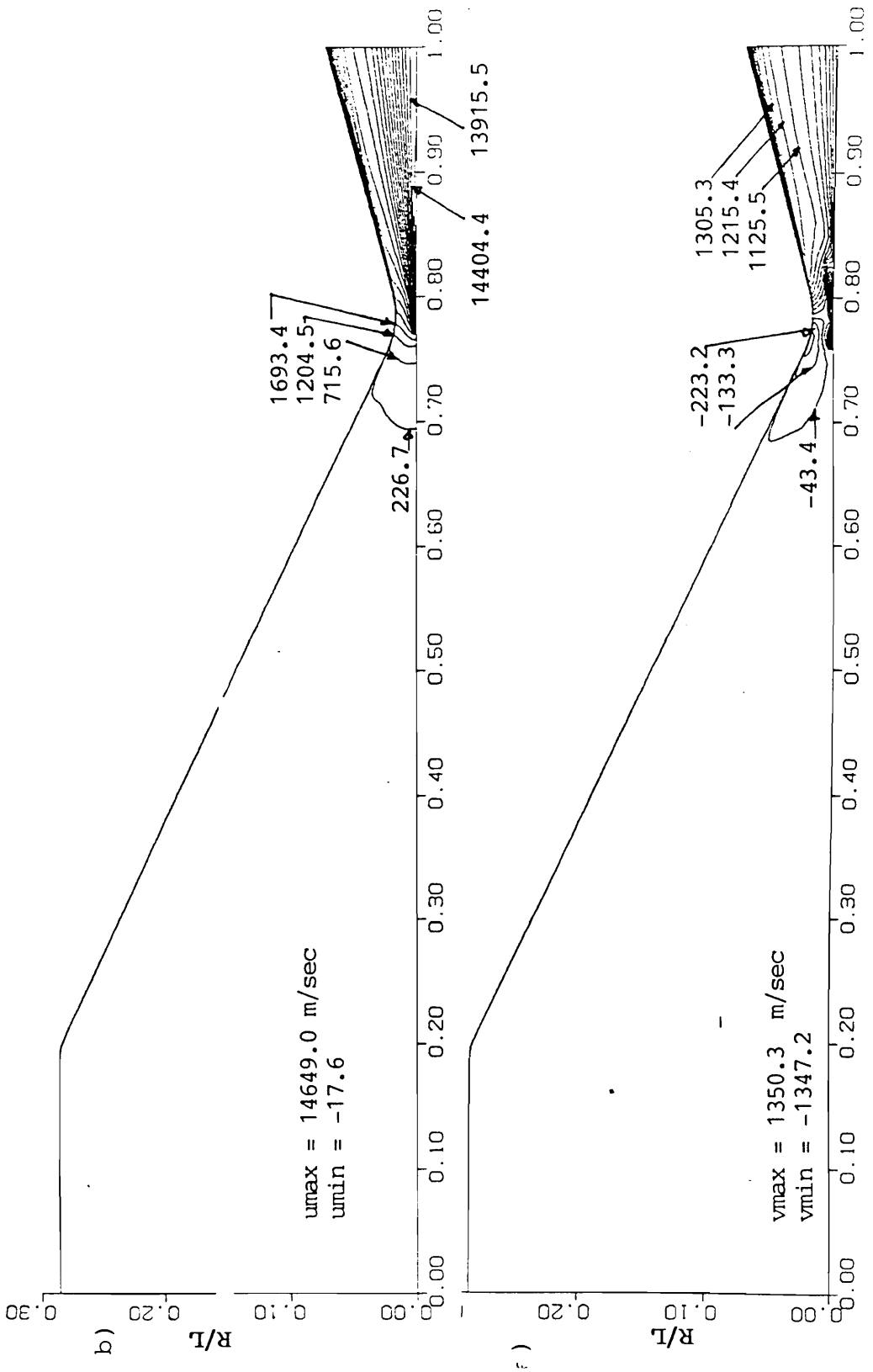

Figure 4.7. (b) u-velocity contour , (c) v-velocity contour, Case 5

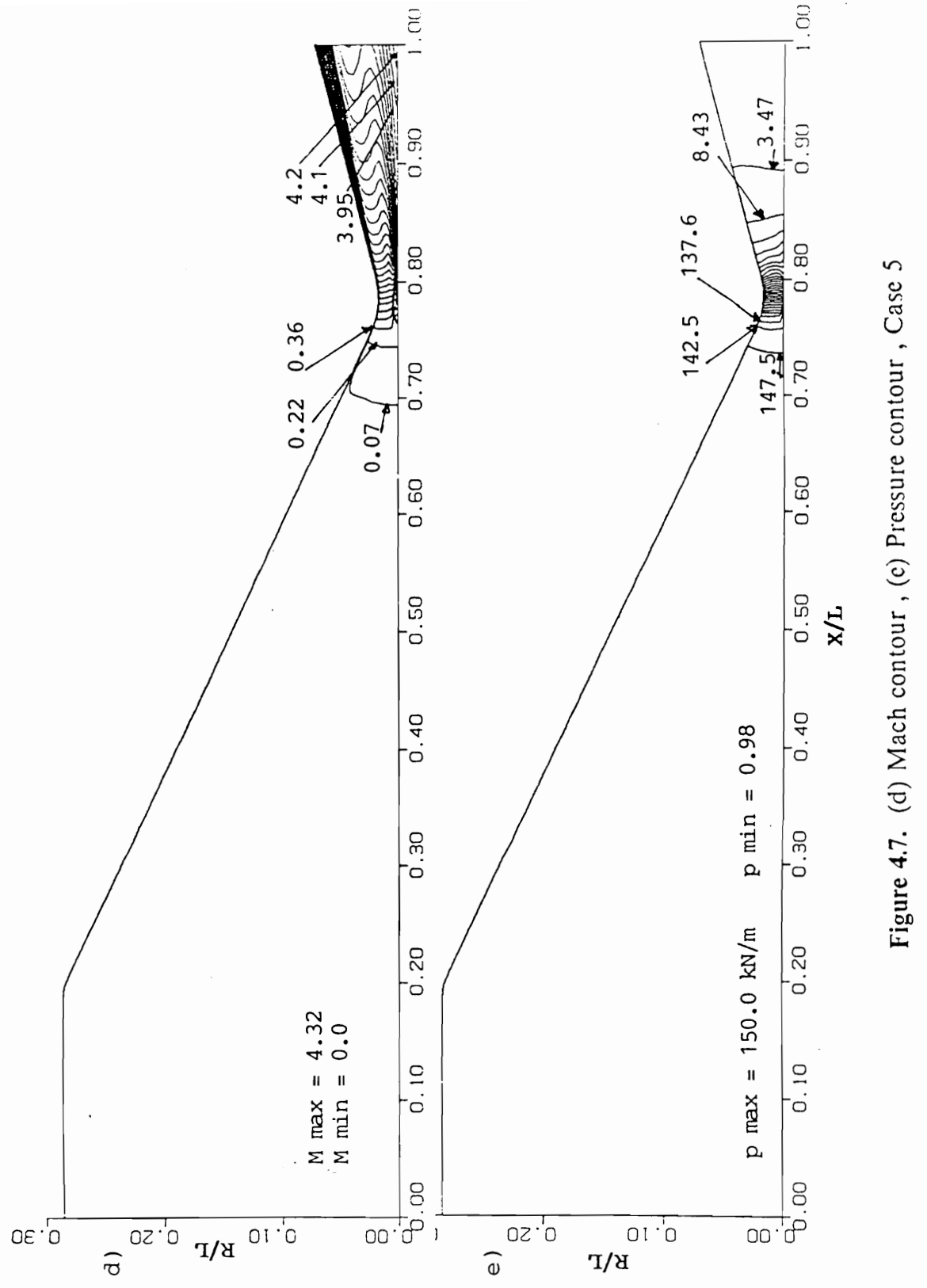

Figure 4.7. (d) Mach contour , (e) Pressure contour , Case 5

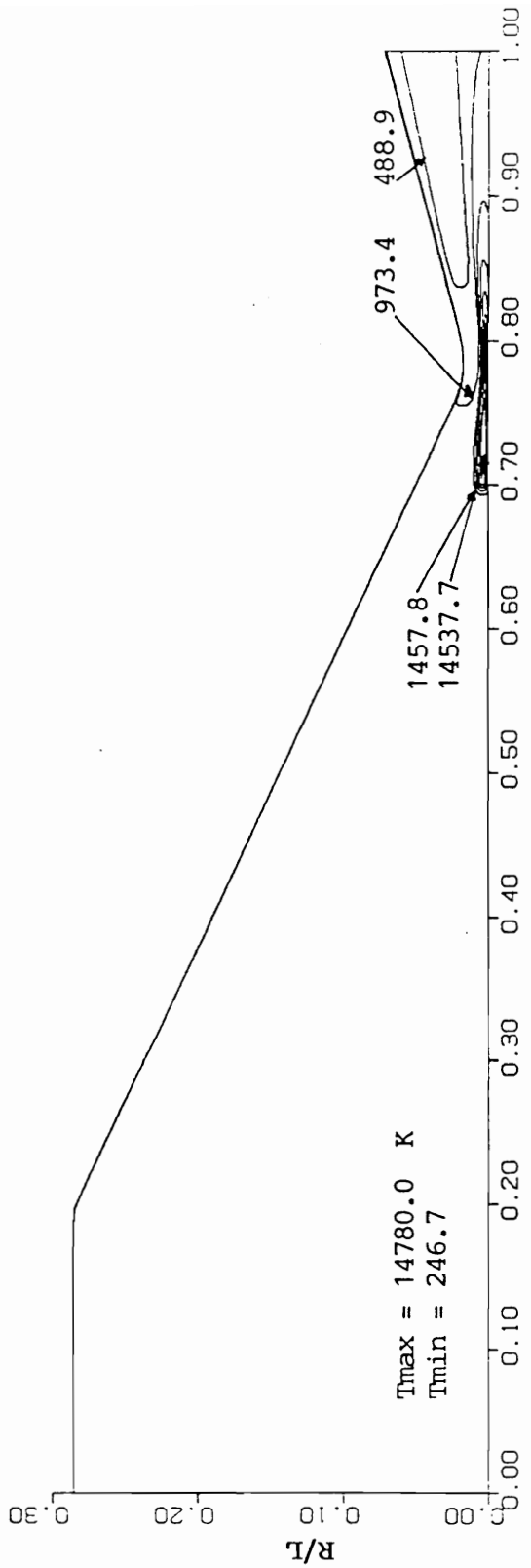

Figure 4.8. (a) Temperature contour, Case 6.

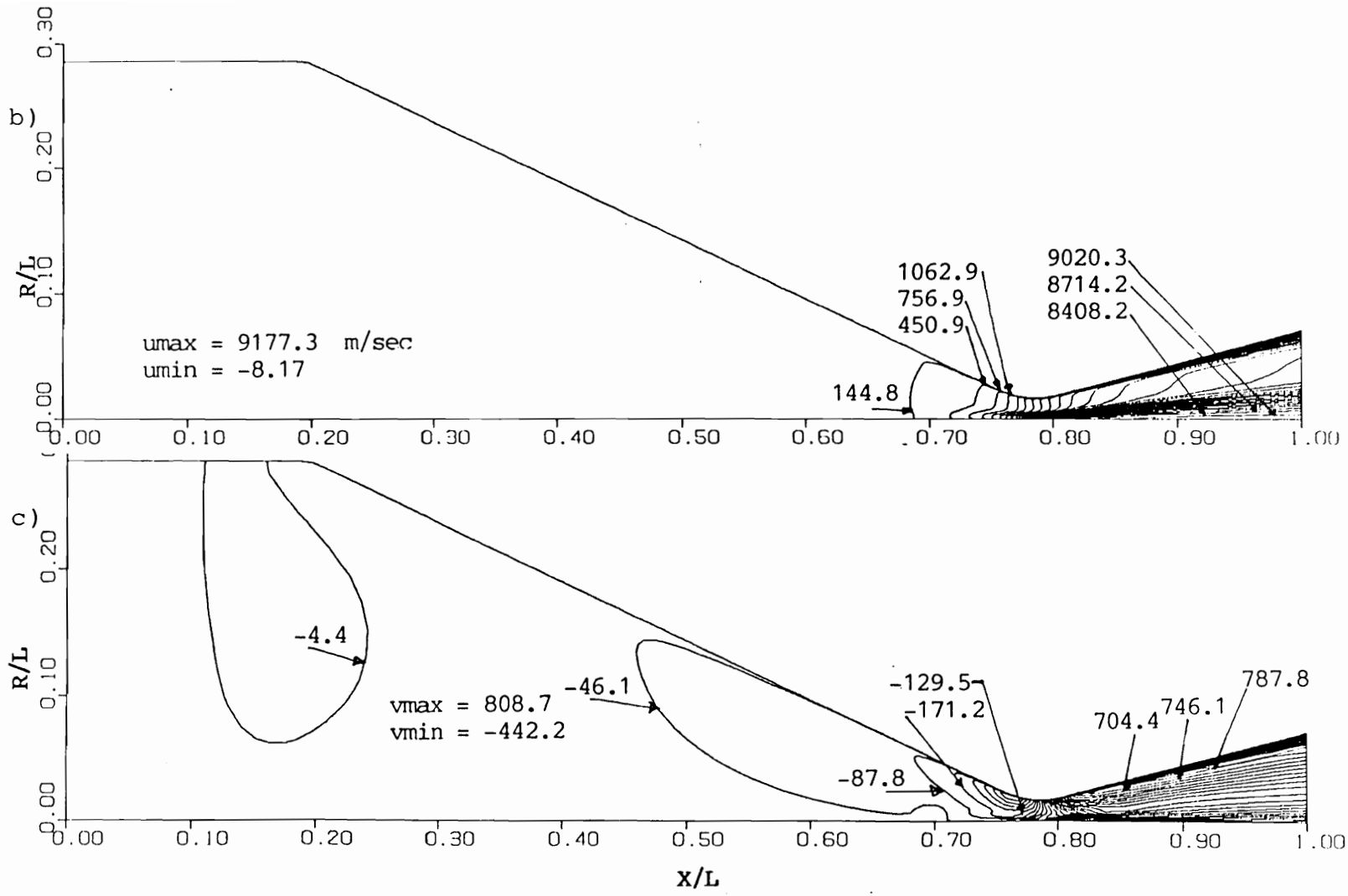

Figure 4.8. (b) u-velocity contour , (c) v-velocity contour, Case 6

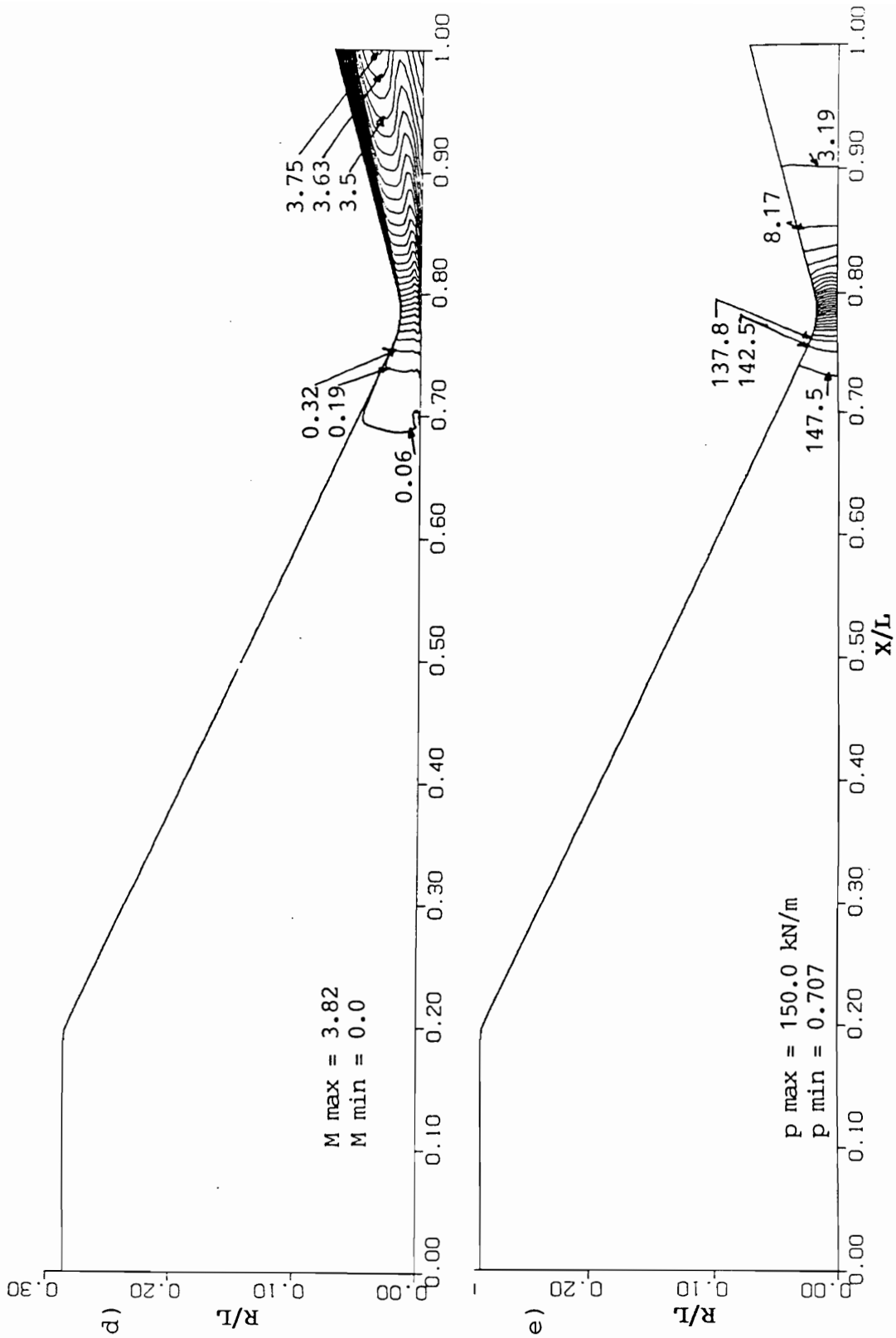

Figure 4.8. (d) Mach contour , (e) Pressure contour, Case 6

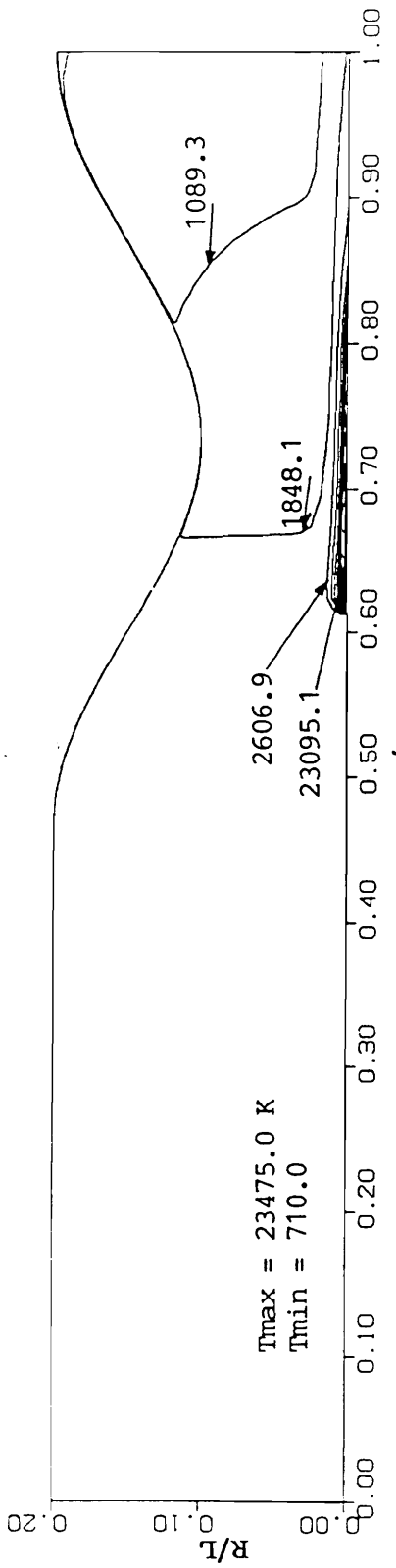

Figure 4.9. (a) Temperature contour, Case 7

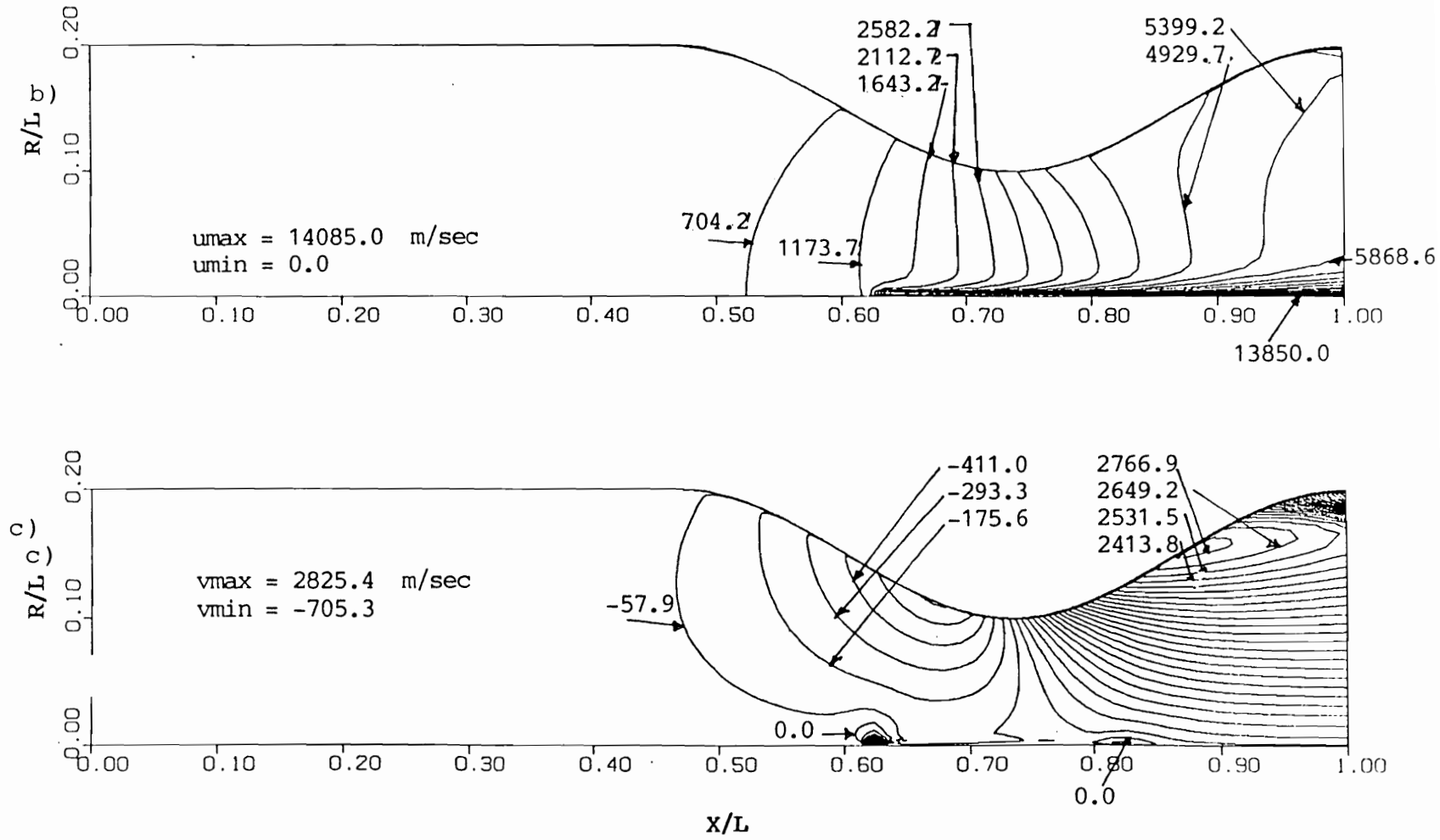

Figure 4.9. (b) u-velocity contour , (c) v-velocity contour, Case 7

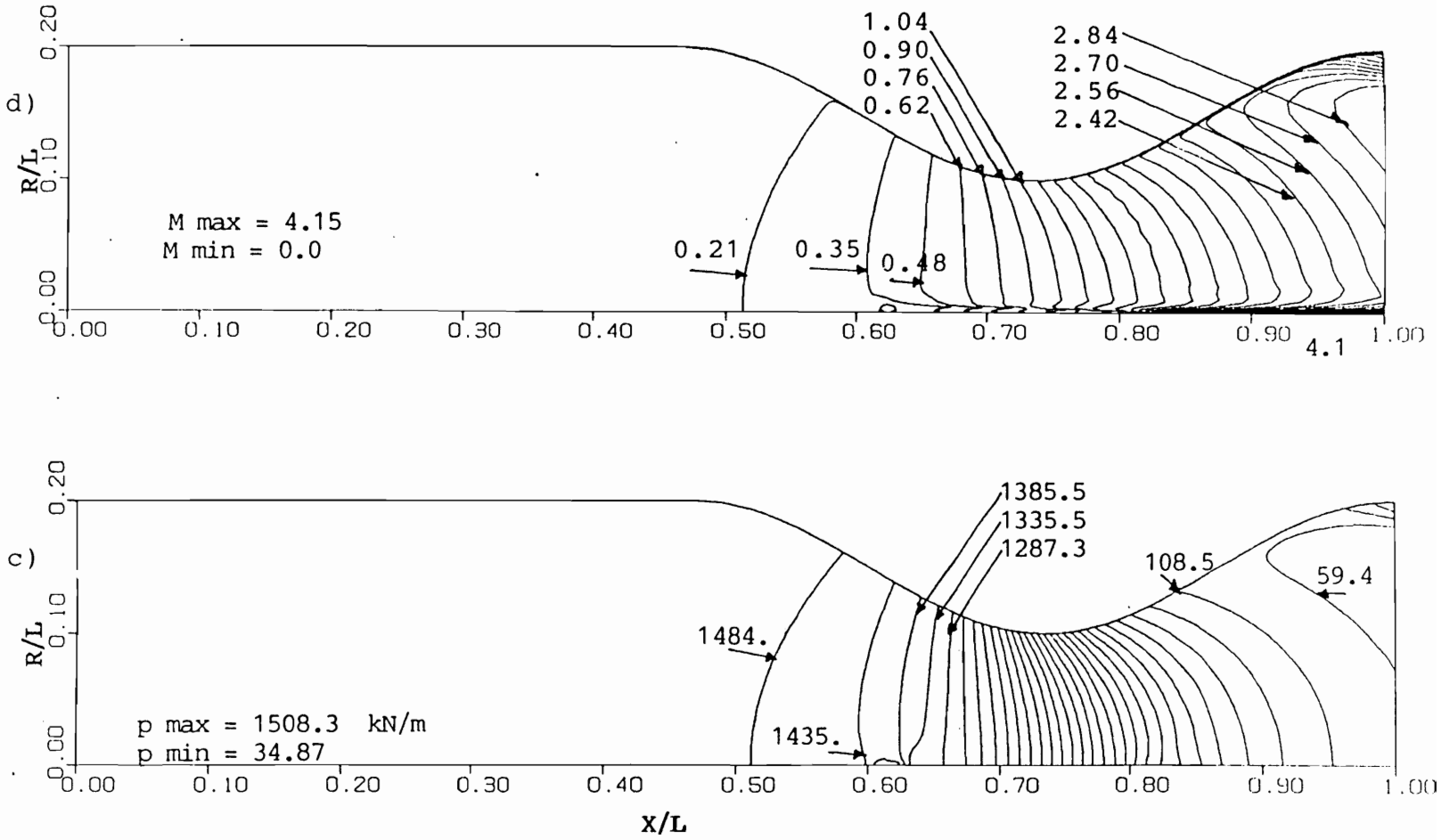

Figure 4.9. (d) Mach contour , (e) Pressure contour, Case 7

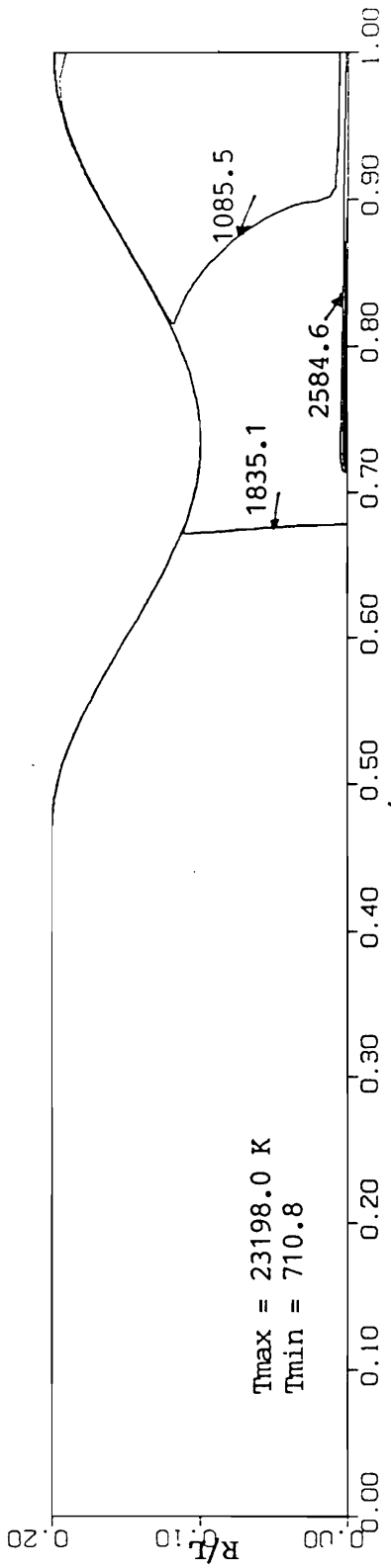

Figure 4.10. (a) Temperature contour, Case 8

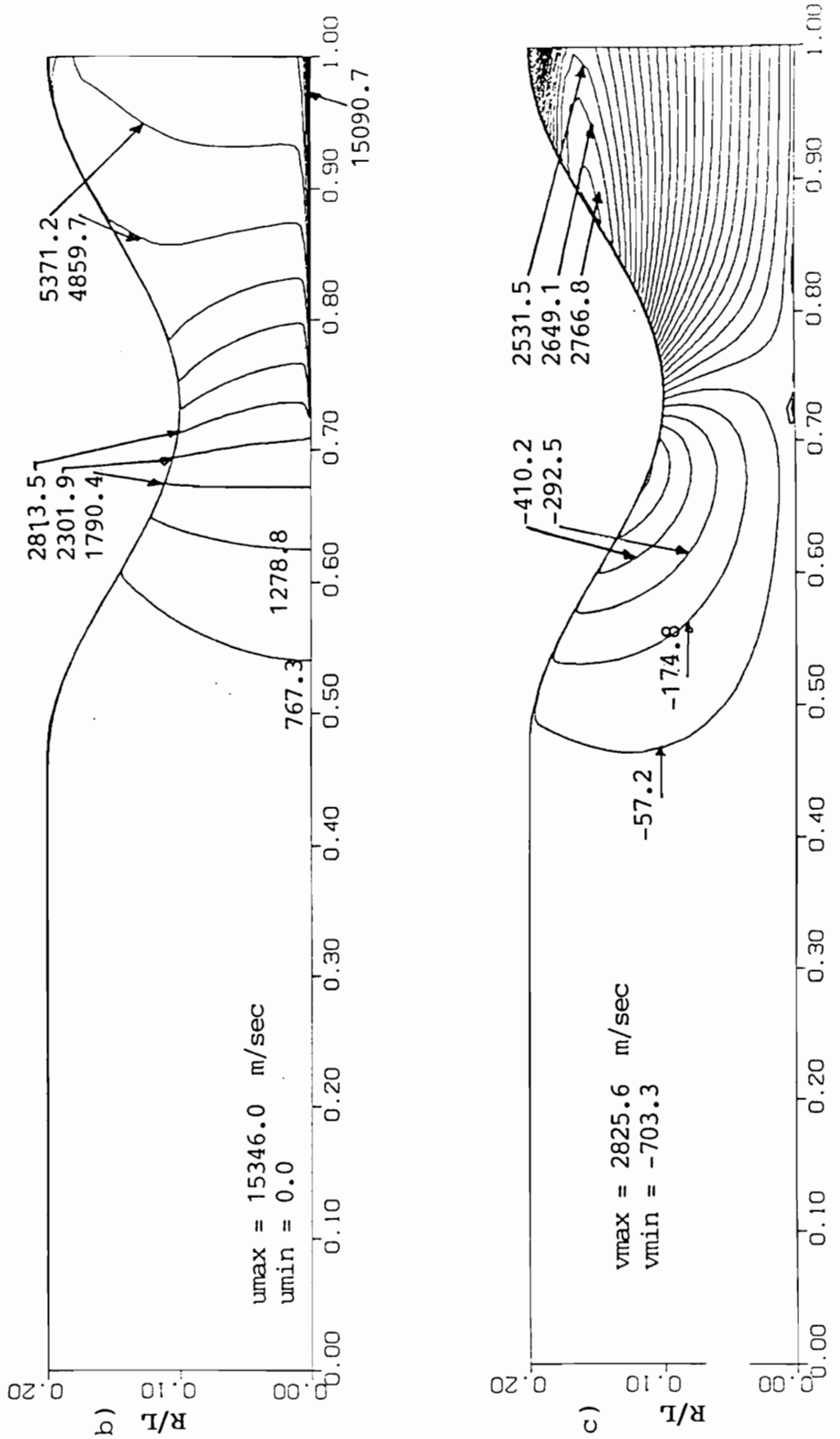

Figure 4.10. (b) u-velocity contour , (c) v-velocity contour, Case 8

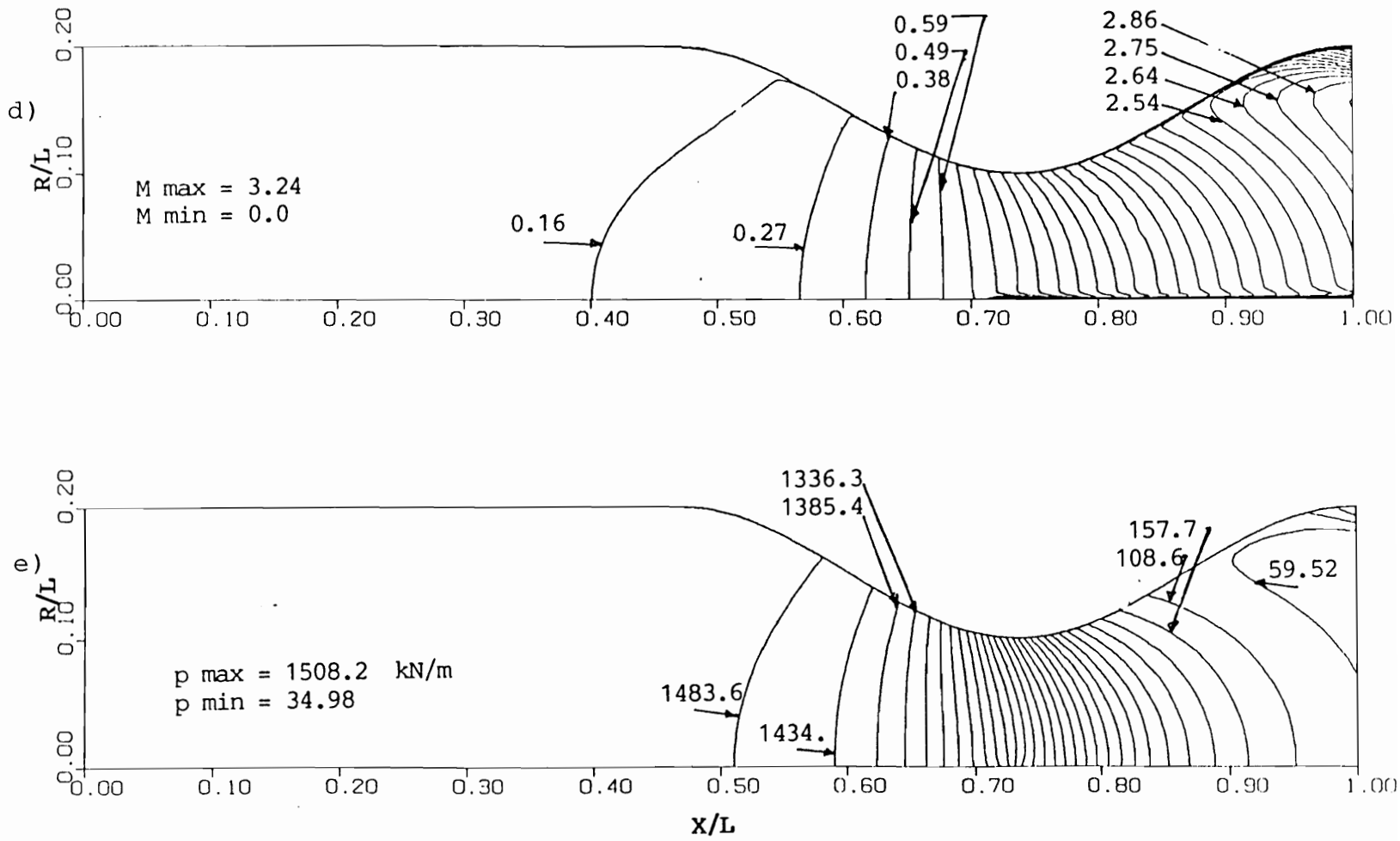

Figure 4.10. (d) Mach contour , (e) Pressure contour, Case 8

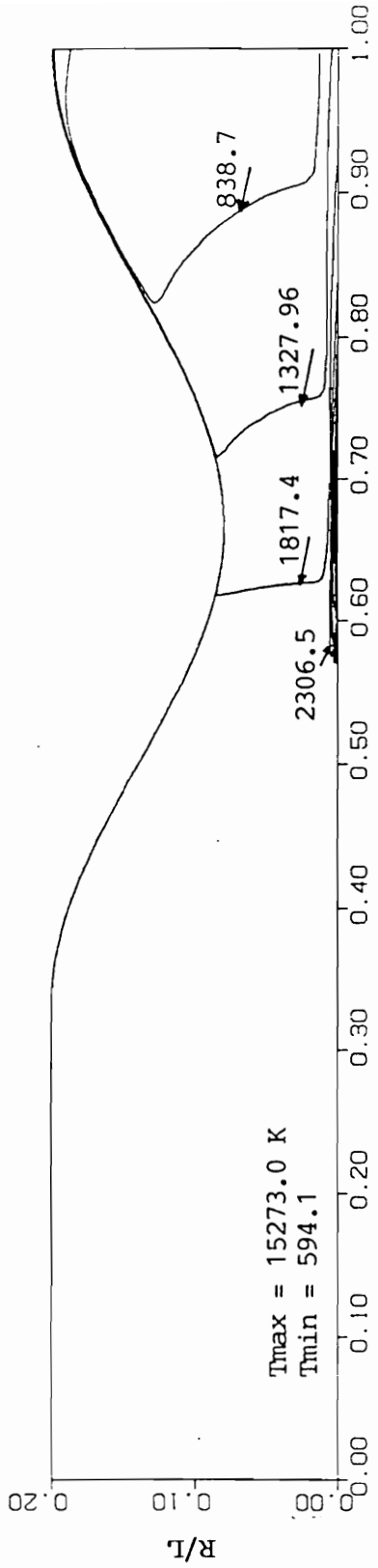

Figure 4.11. (a) Temperature contour, Case 9

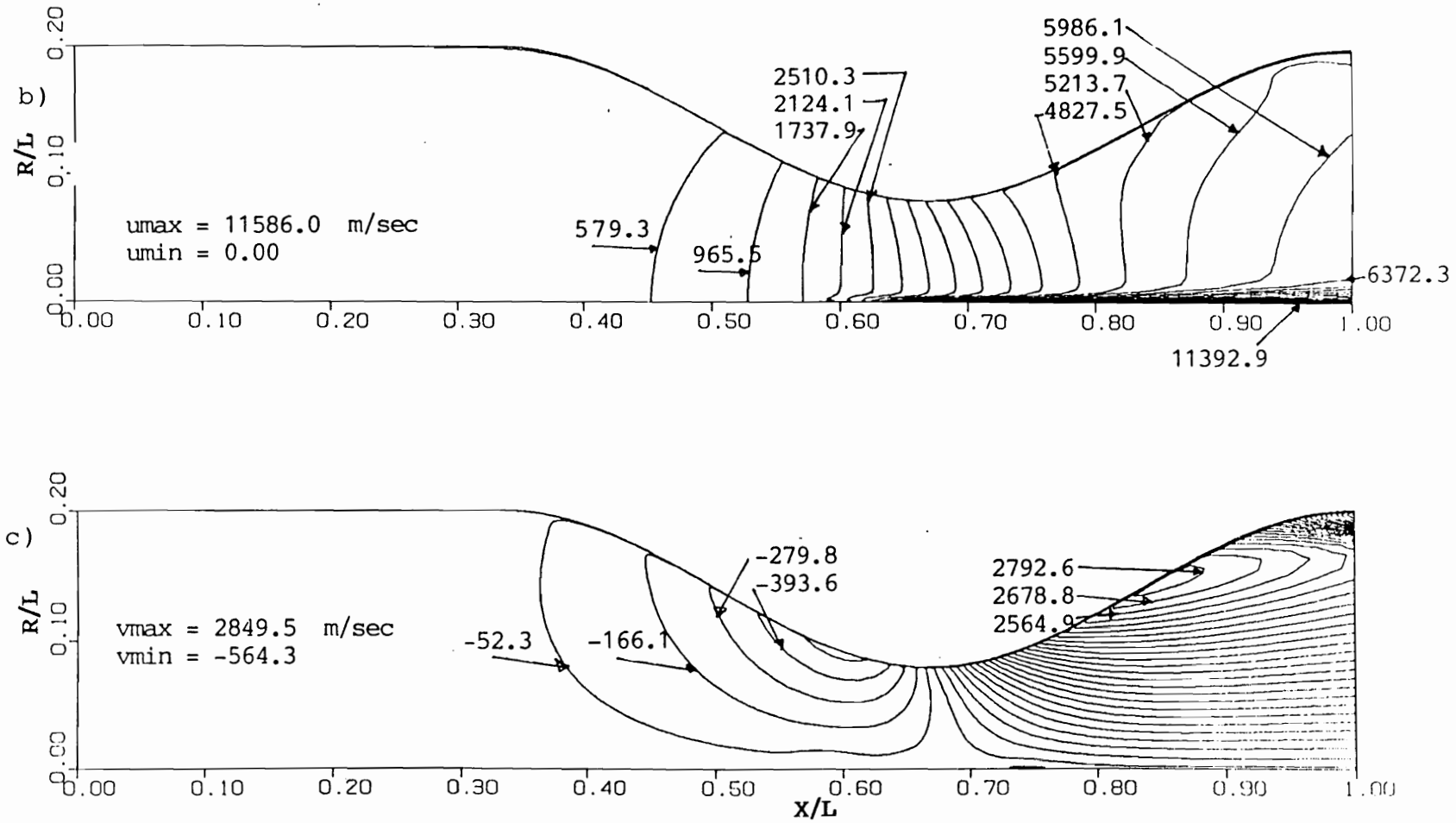

Figure 4.11. (b) u-velocity contour , (c) v-velocity contour, Case 9

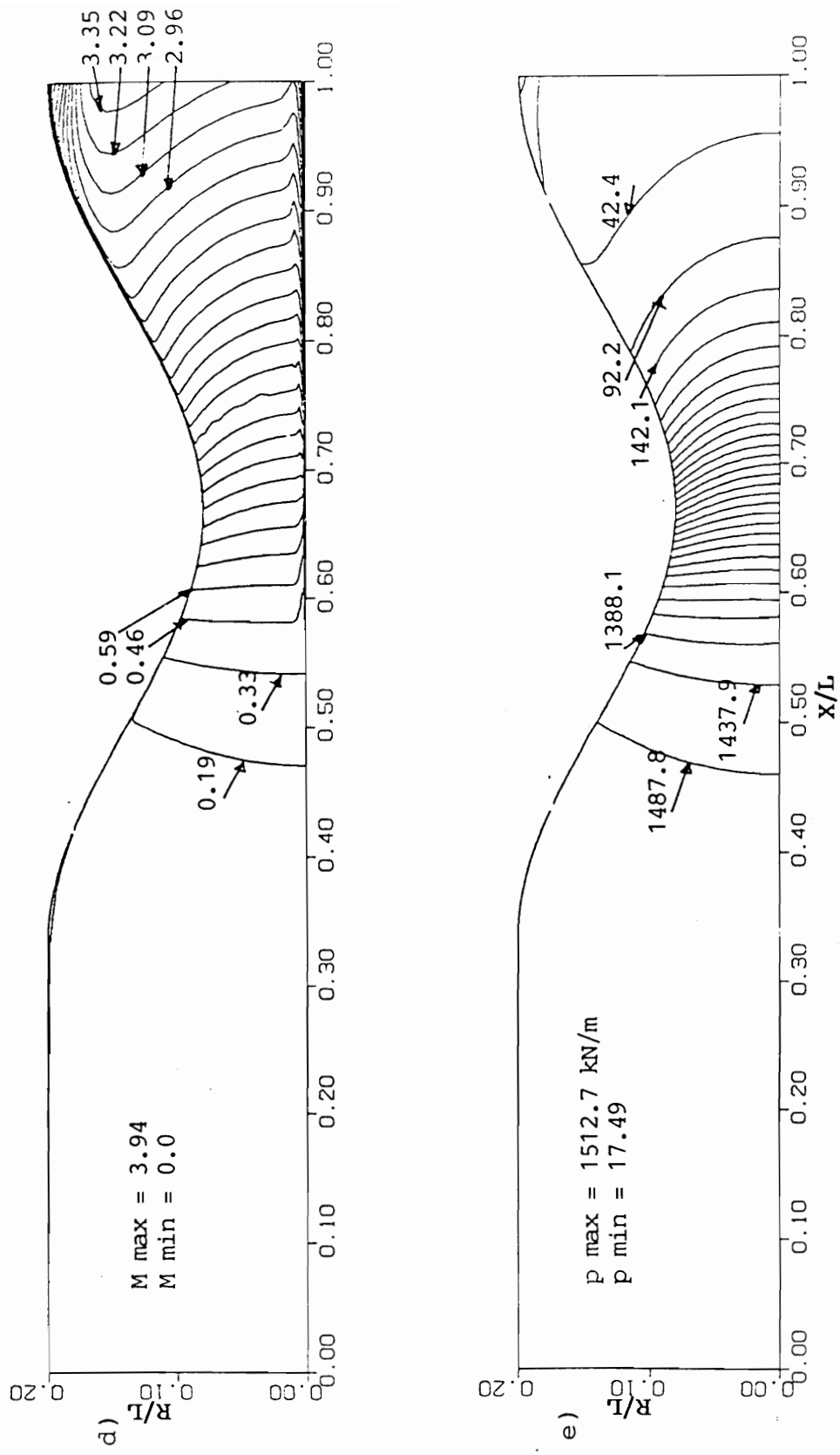

Figure 4.11. (d) Mach contour , (e) Pressure contour, Case 9

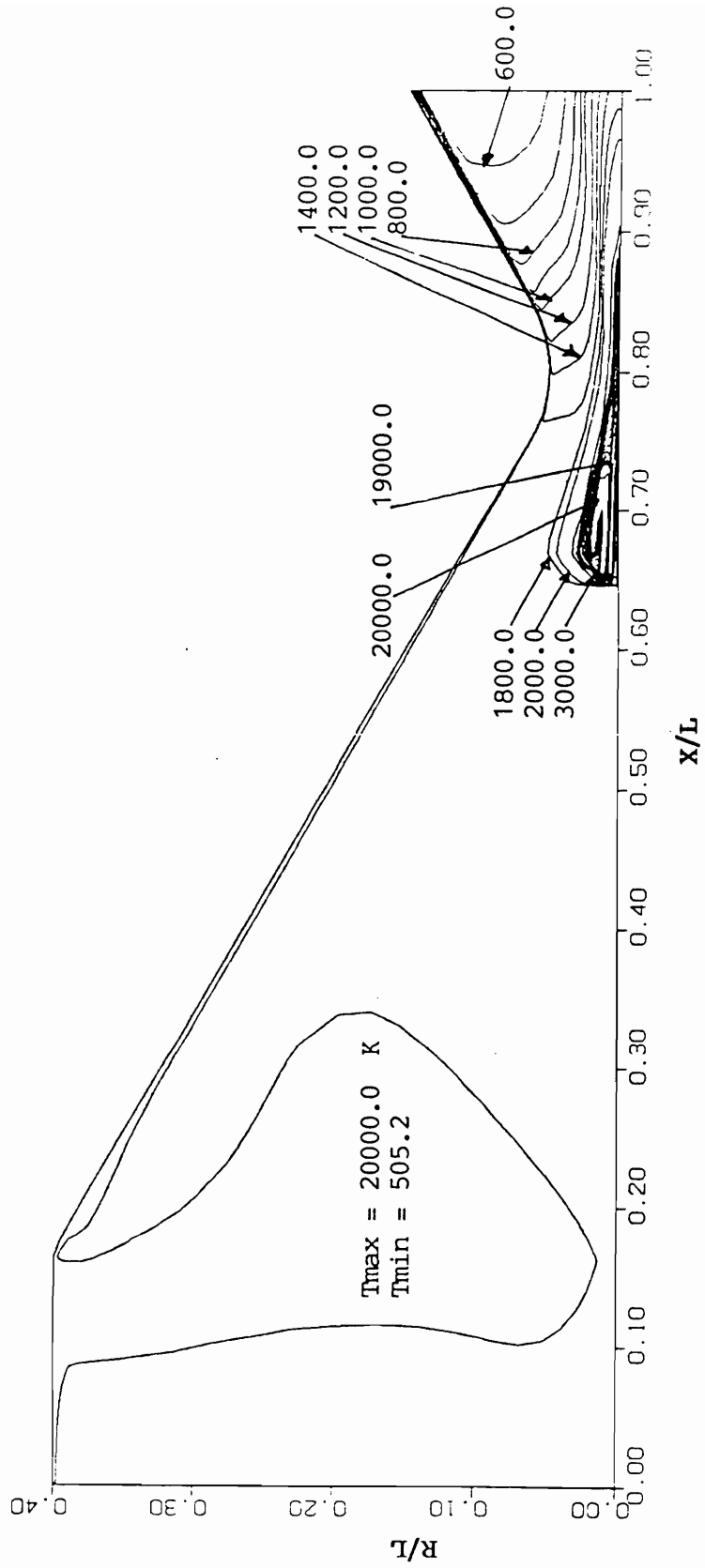

Figure 4.11. (a) temperature contour, Case 10

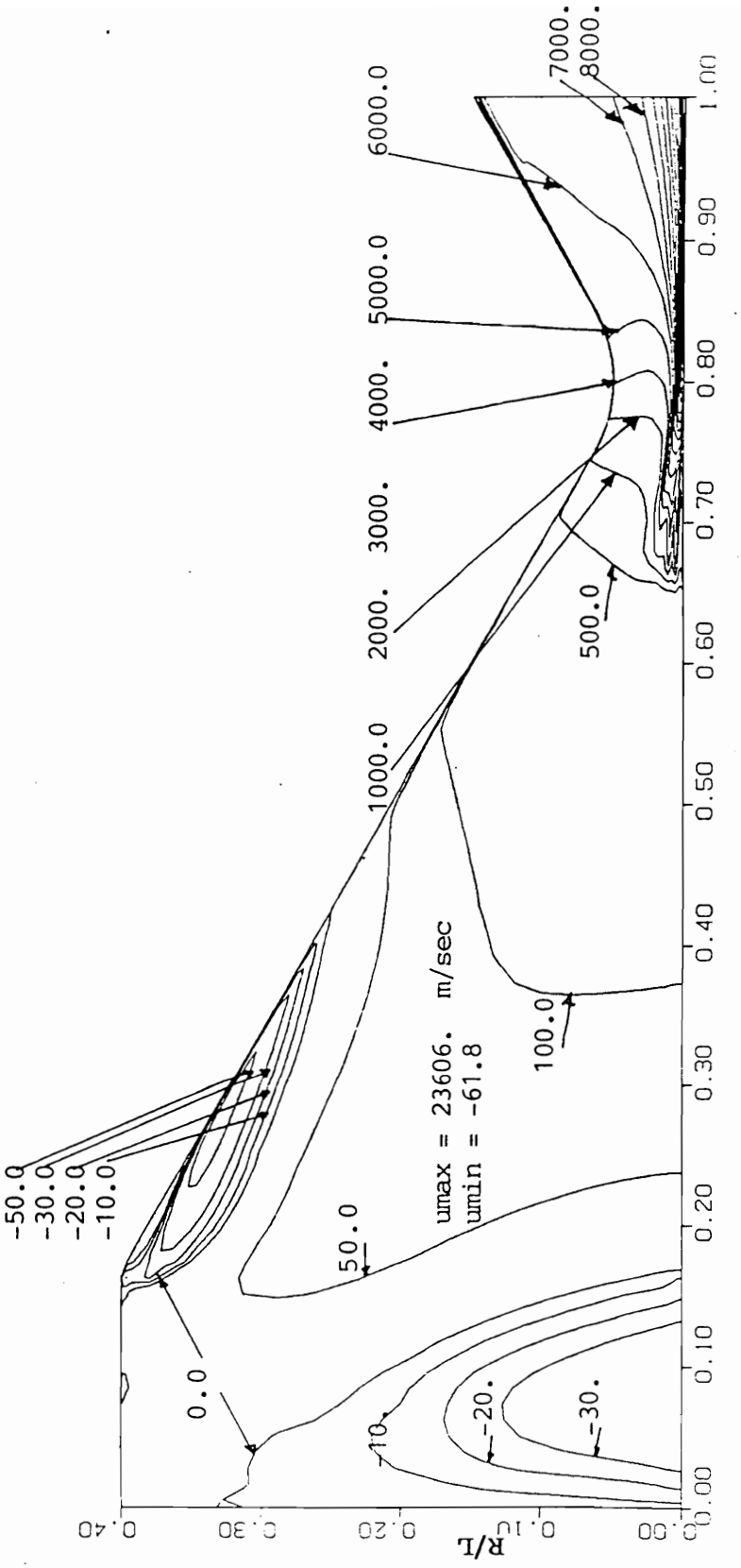

Figure 4.12. (b) u-velocity contour, Case 10

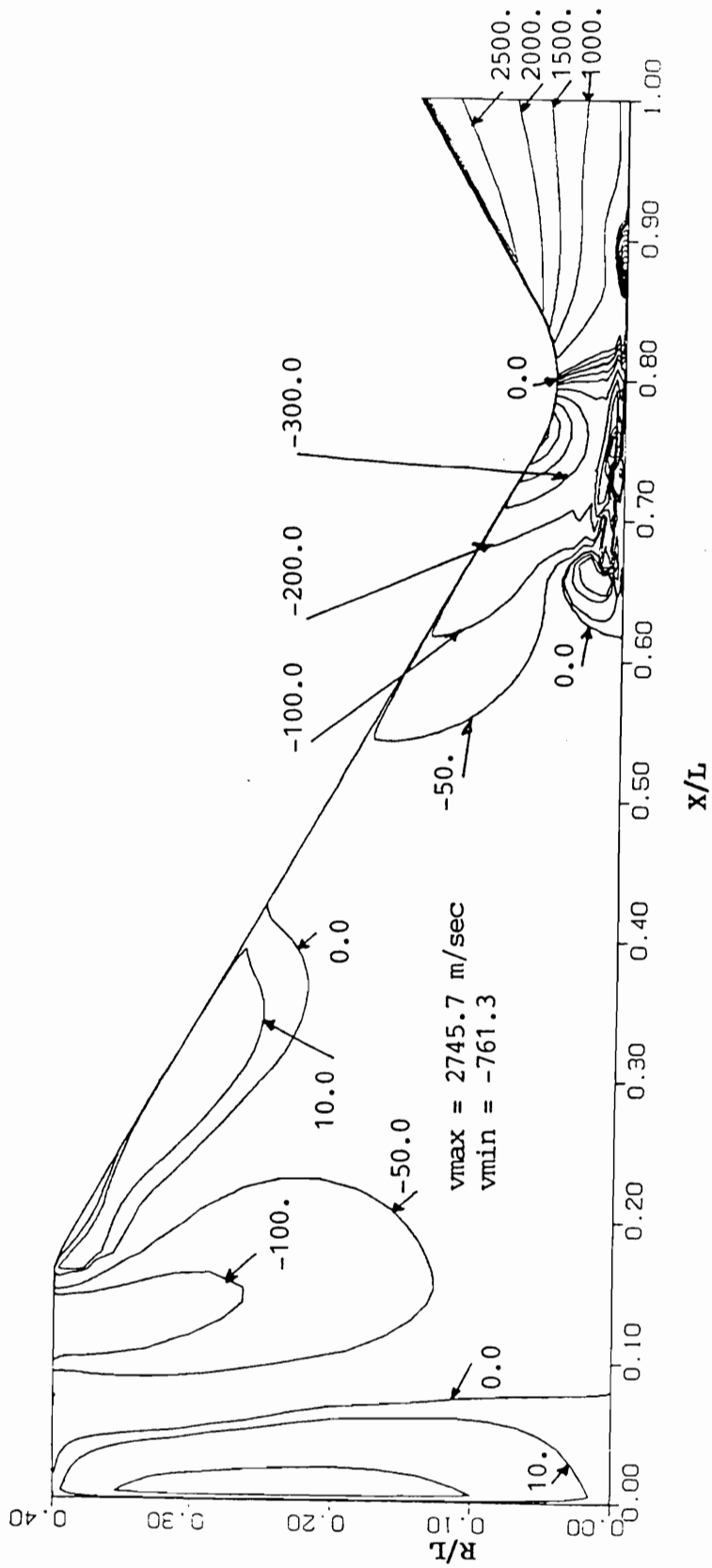

Figure 4.12. (c) v-velocity contour, Case 10

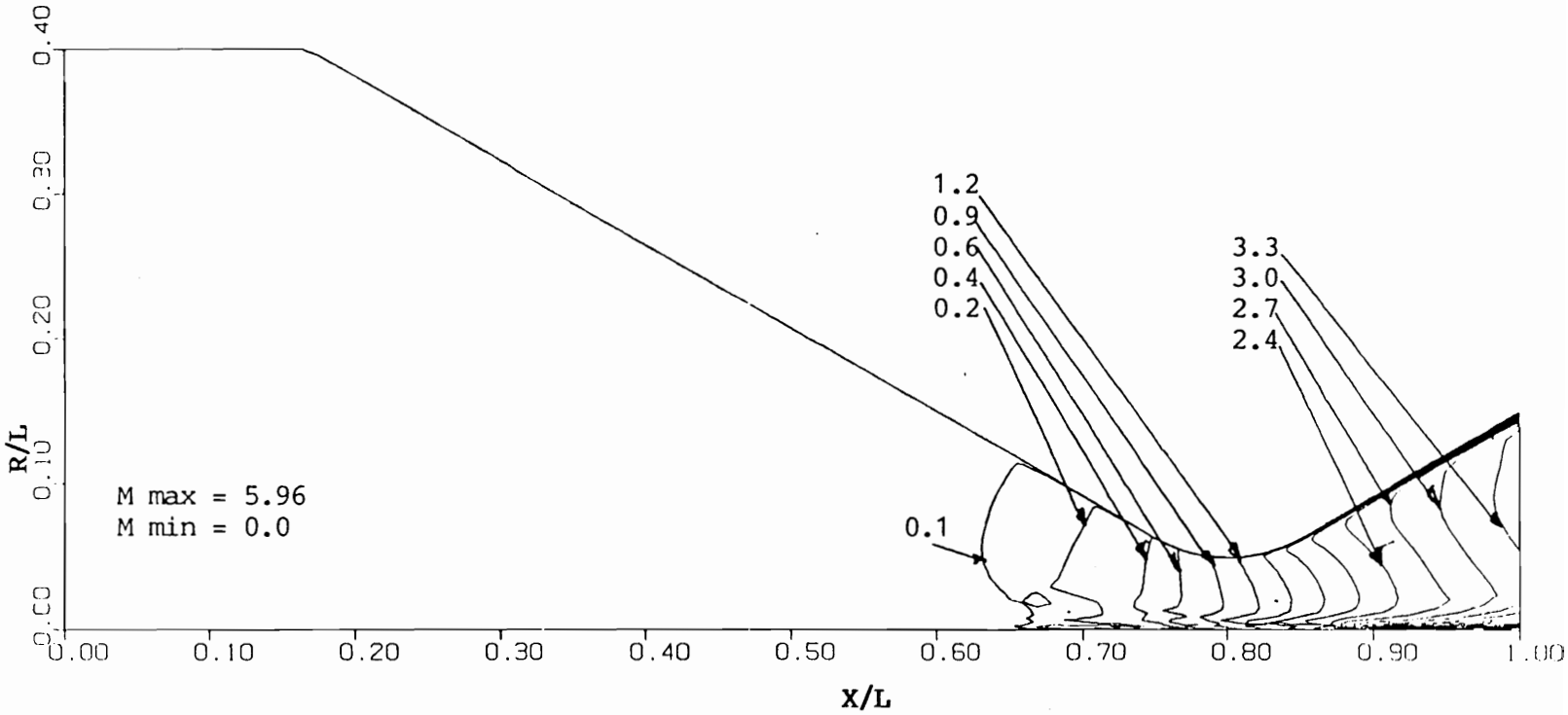

Figure 4.12. (d) Mach contour, Case 10

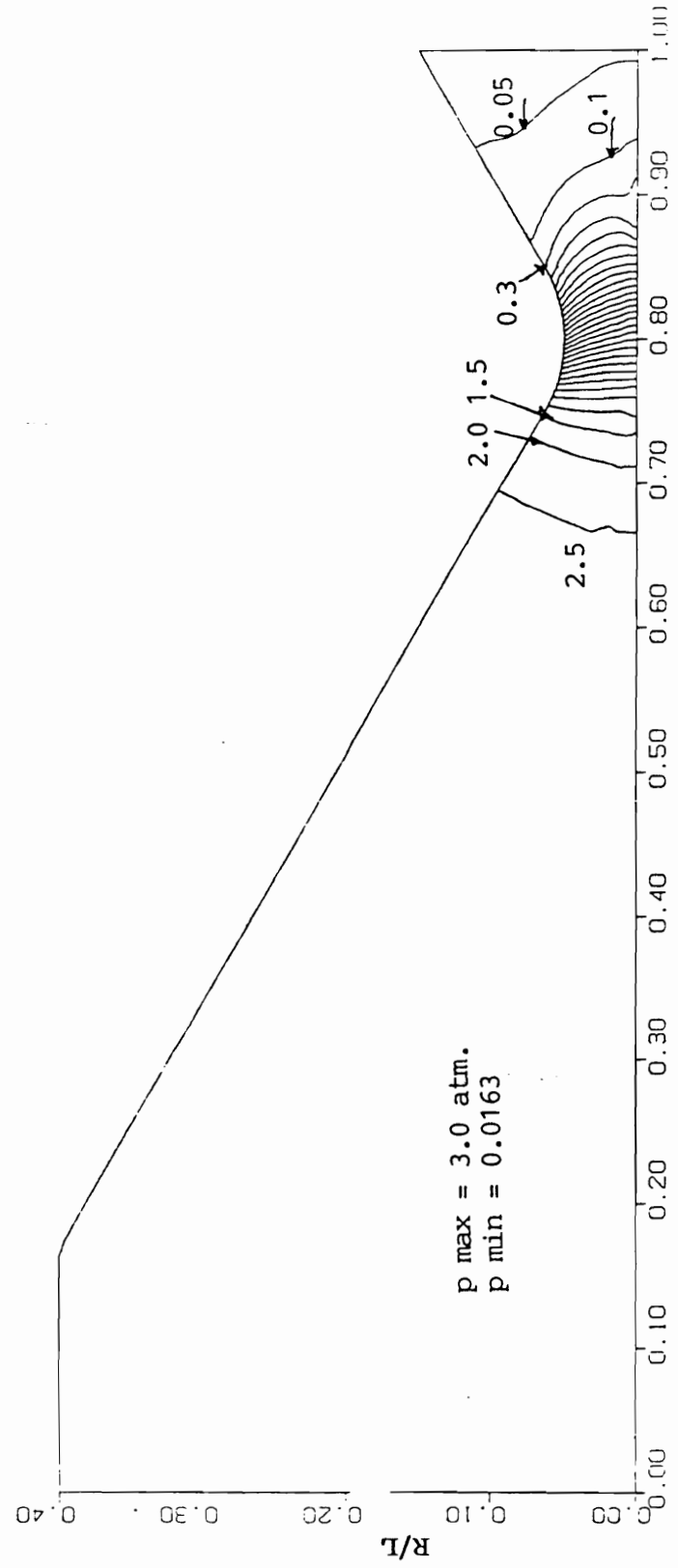

Figure 4.12. (e) Pressure contour, Case 10

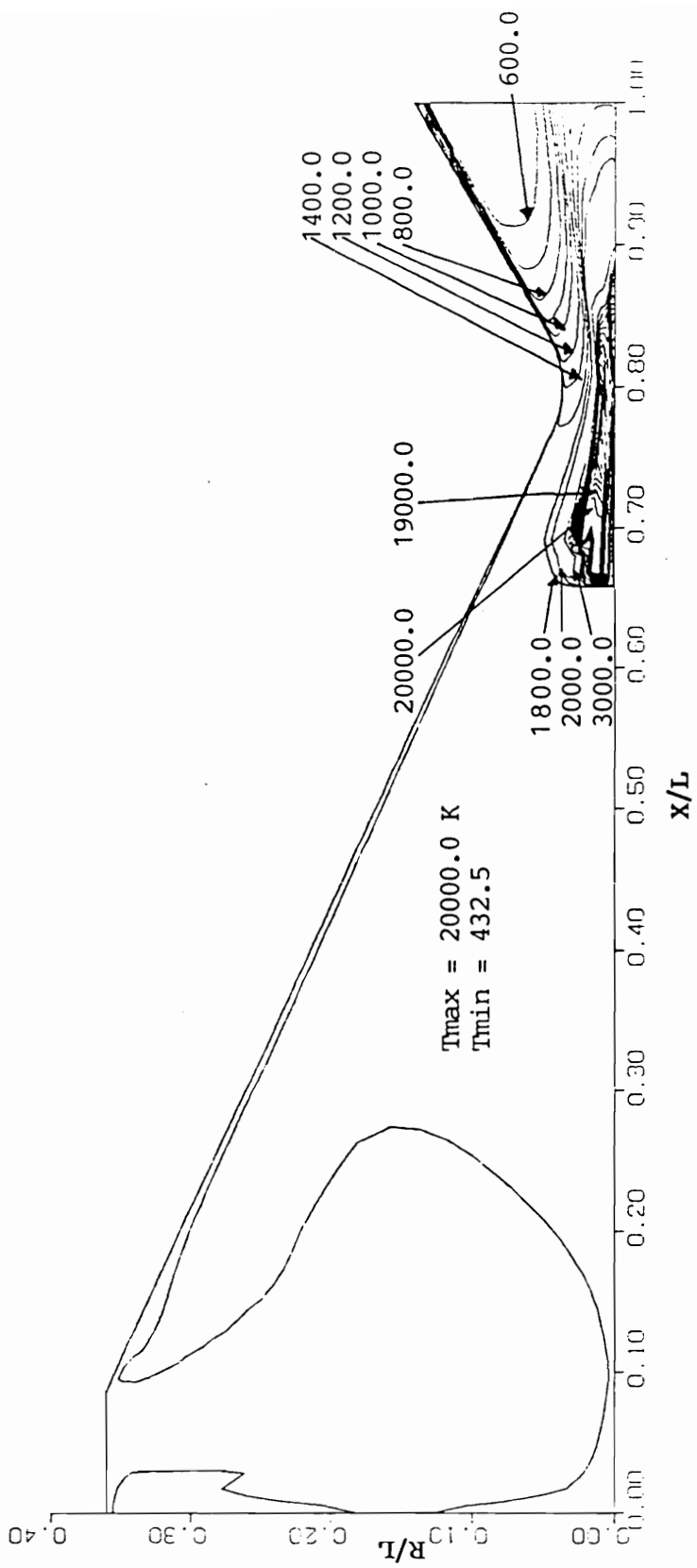

Figure 4.13. (a) Temperature contour, Case 11

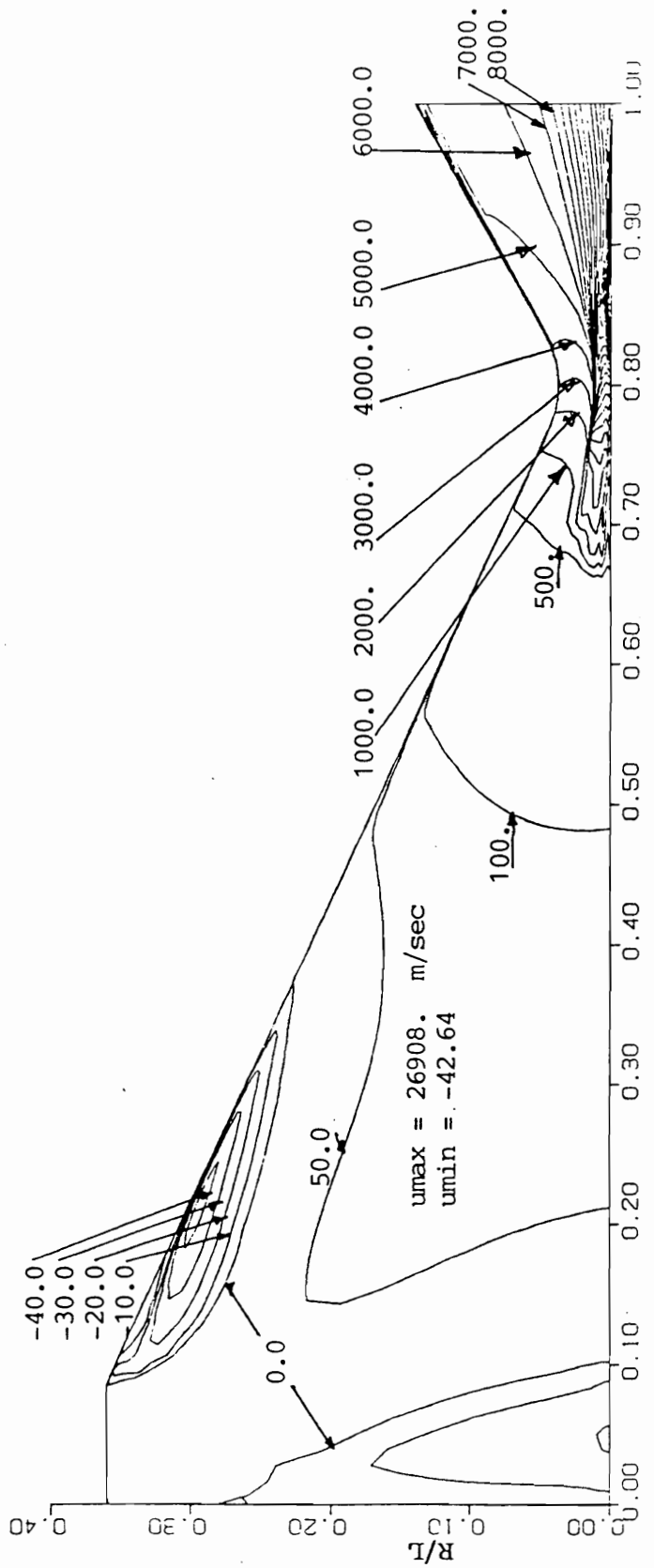

Figure 4.13. (b) u-velocity contour, Case 11

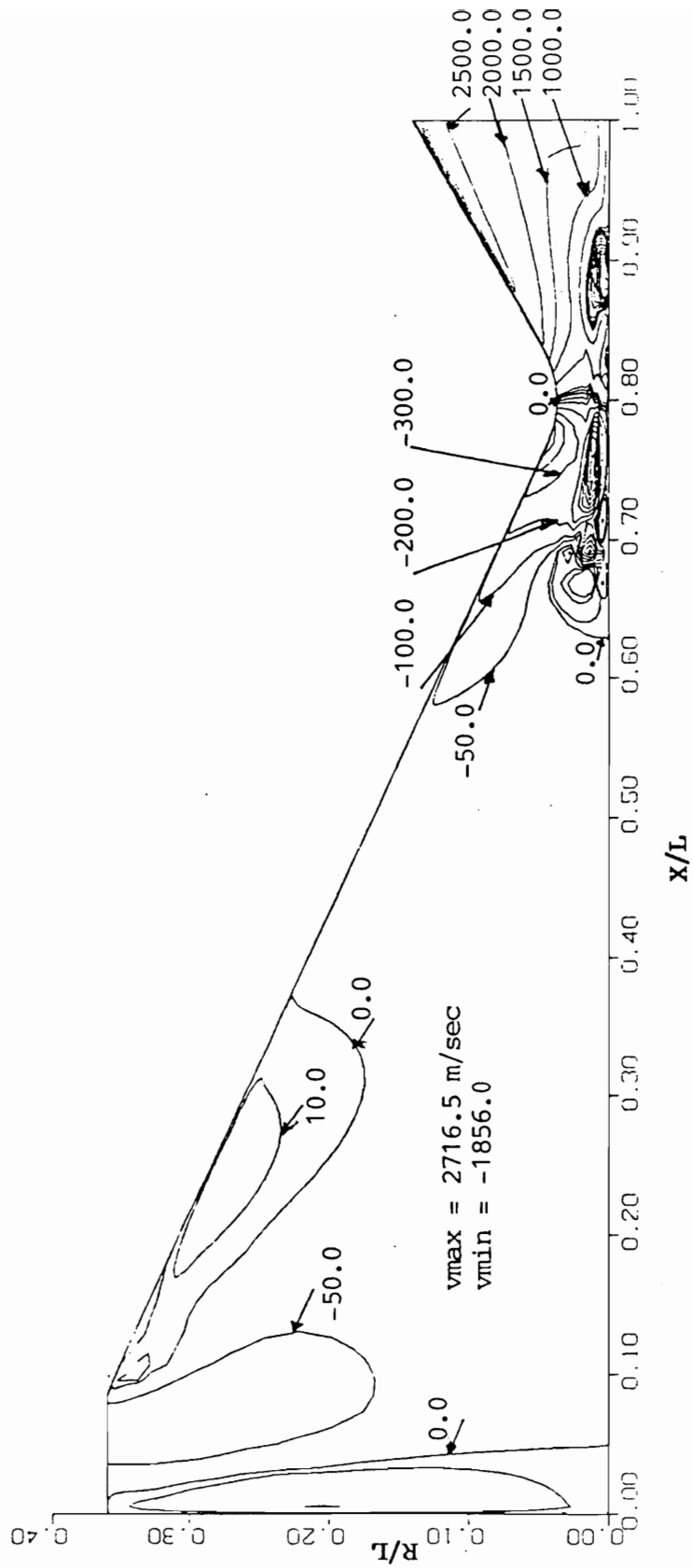

Figure 4.13. (c) v-velocity contour, Case 11

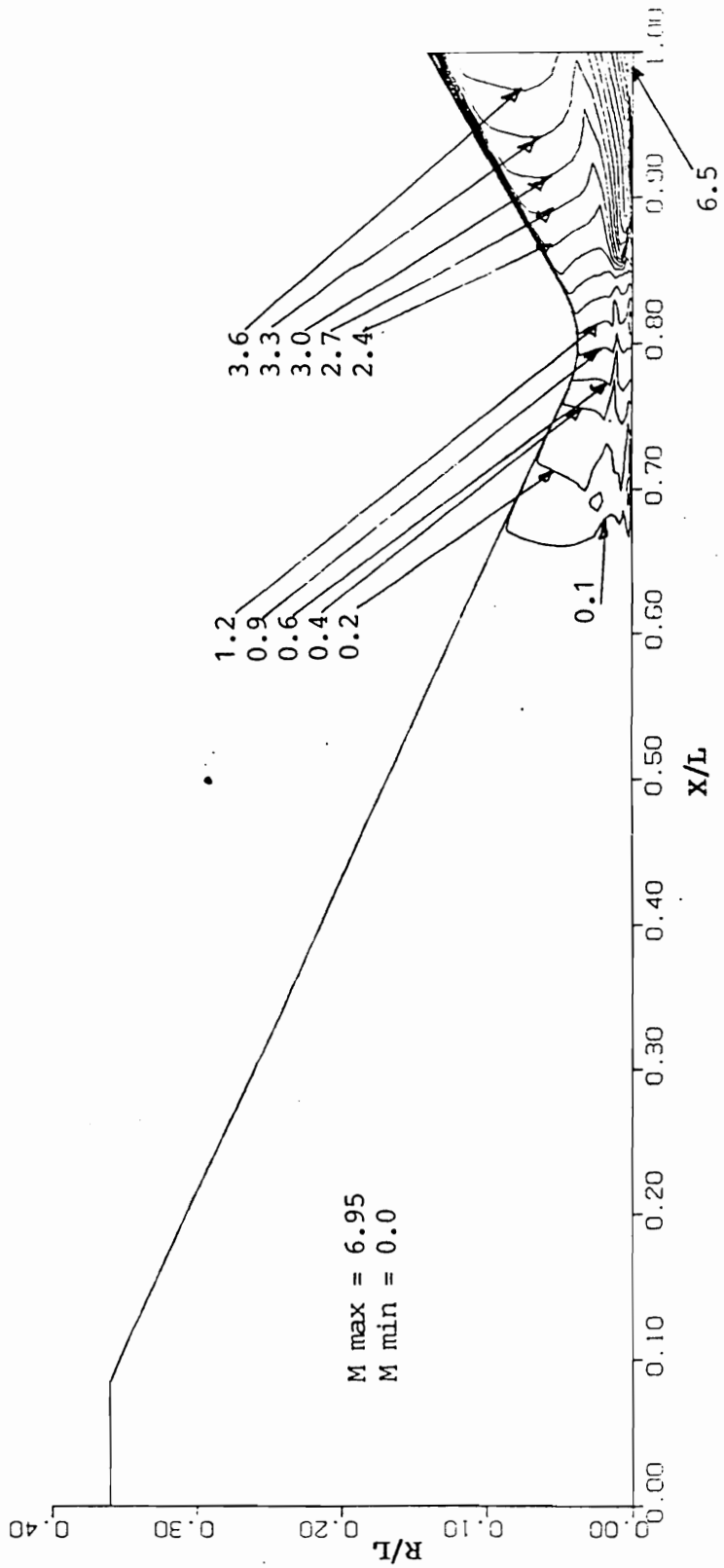

Figure 4.13. (d) Mach contour, Case 11

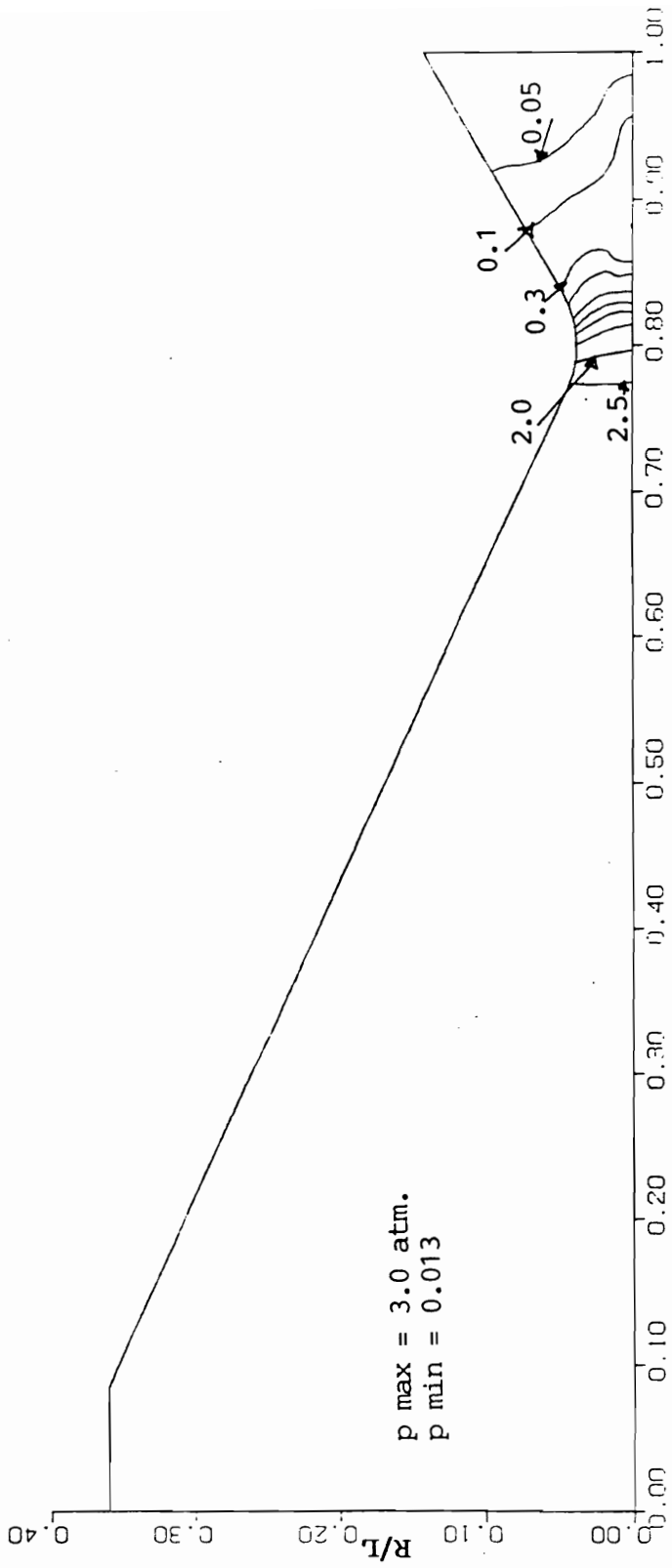

Figure 4.13. (e) Pressure contour, Case 11

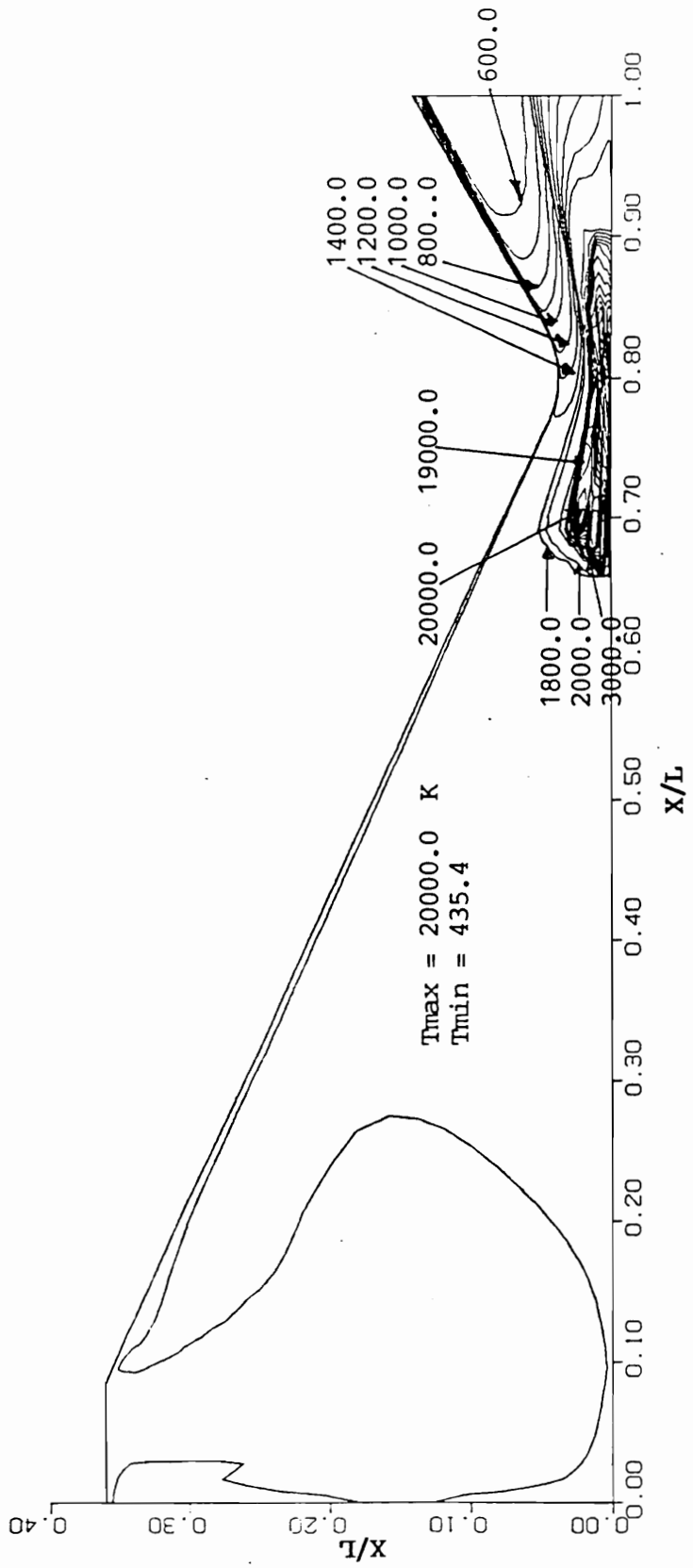

Figure 4.14. (a) Temperature contour , Case 12

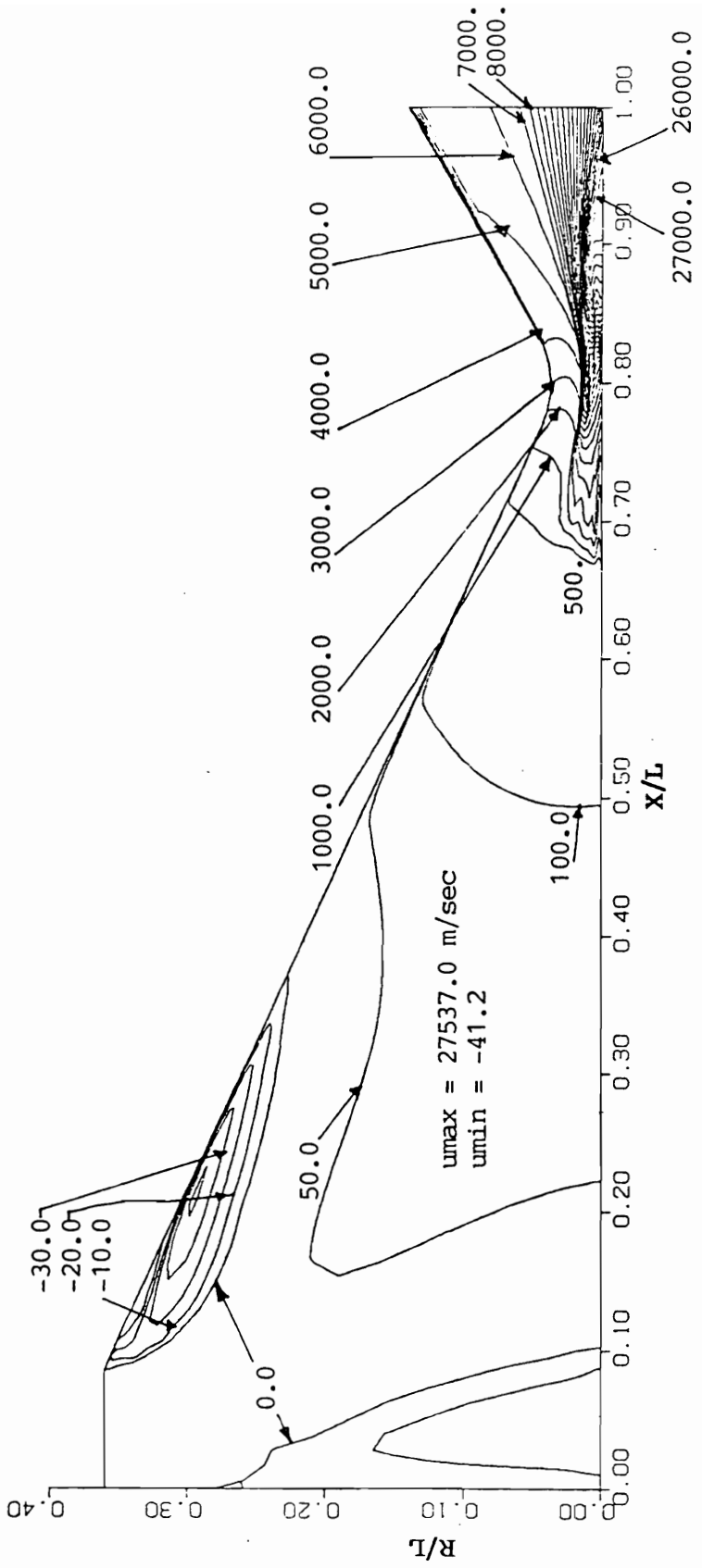

Figure 4.14. (b) u-velocity contour, Case 12

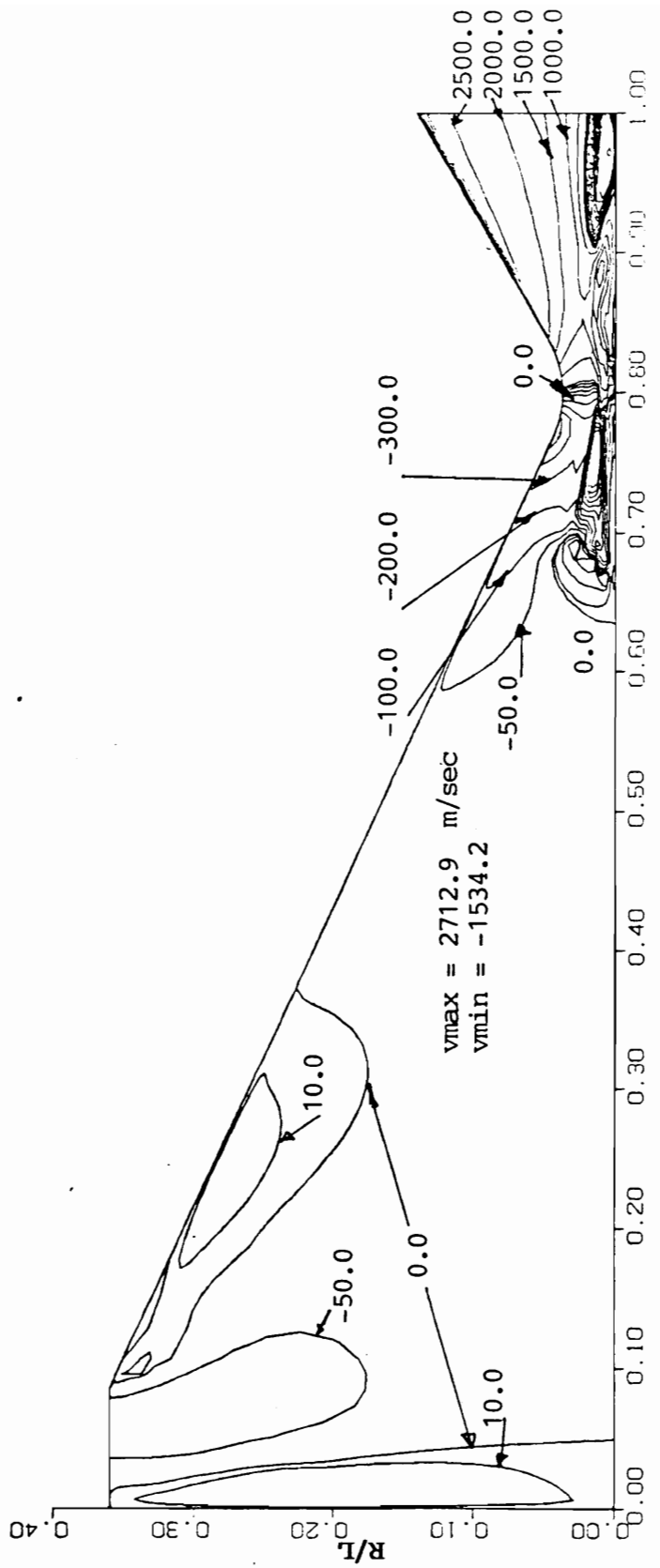

Figure 4.14. (c) v-velocity contour, Case 12

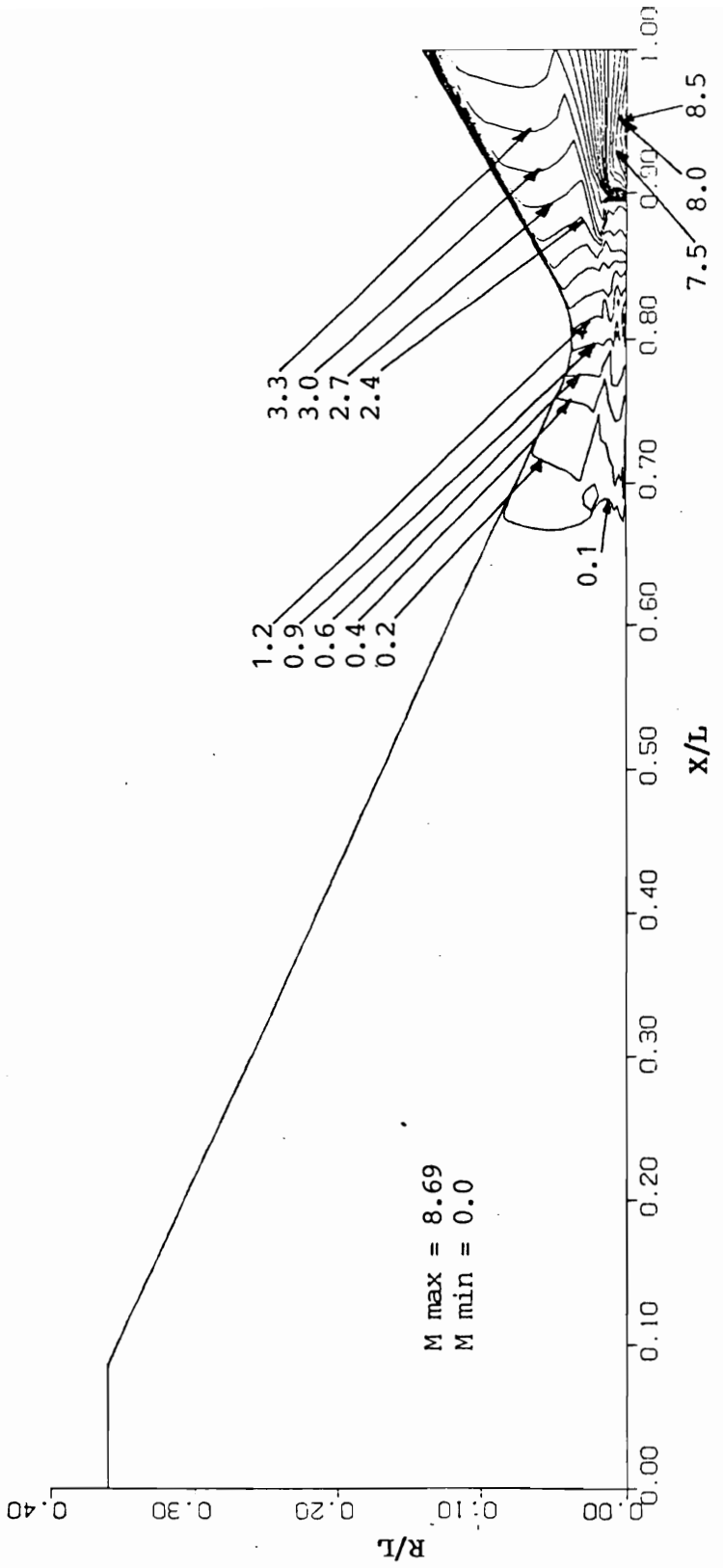

Figure 4.14. (d) Mach contour, Case 12

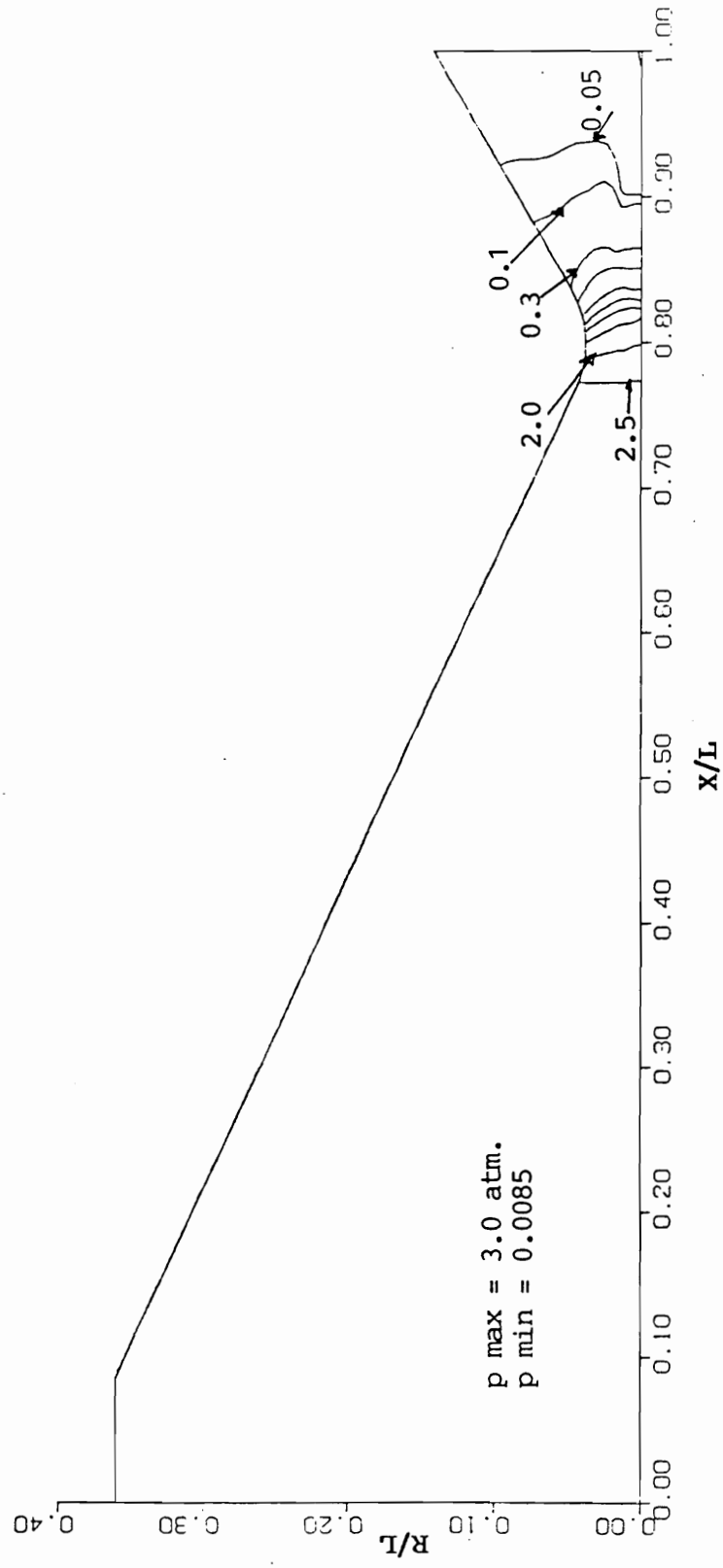

Figure 4.14. (c) Pressure contour, Case 12

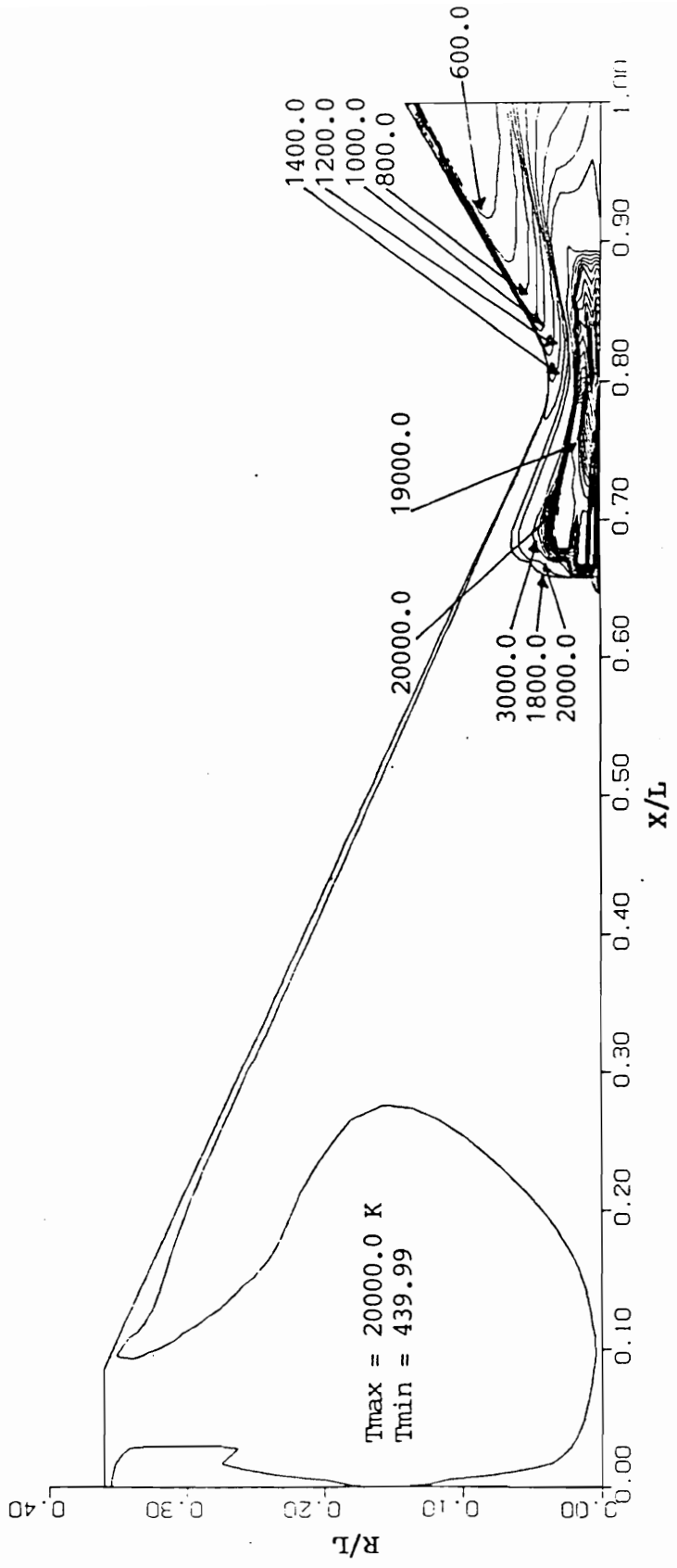

Figure 4.15. (a) Temperature contour, Case 13

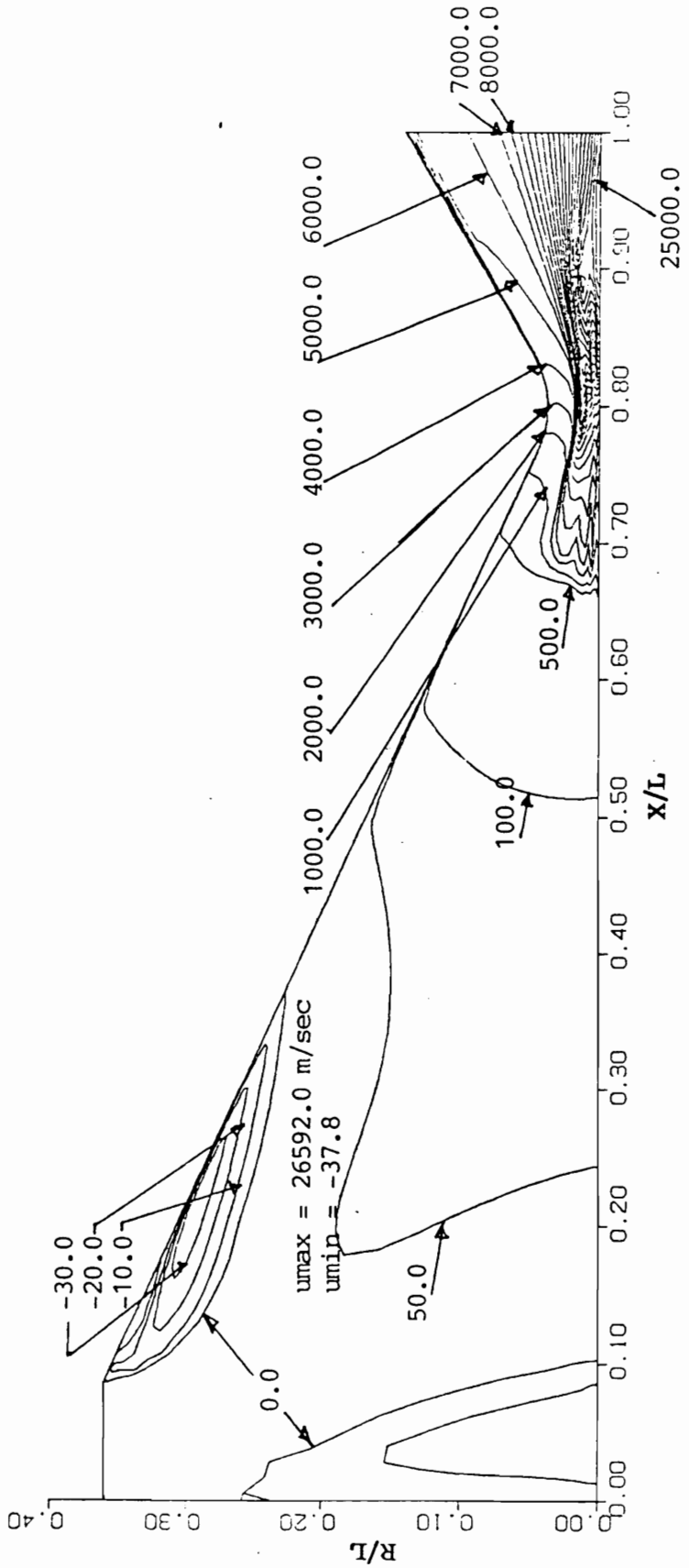

Figure 4.15. (b) u-velocity contour, Case 13

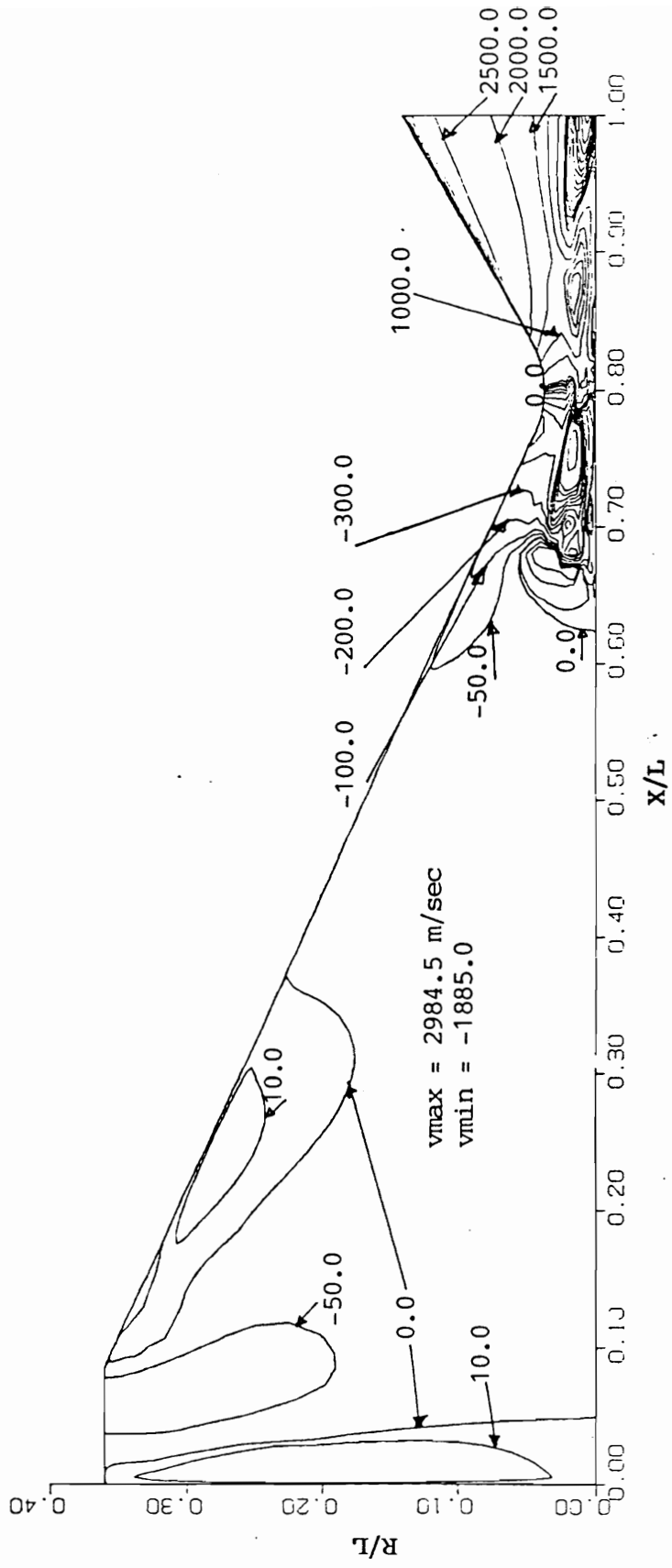

Figure 4.15. (c) v-velocity contour, Case 13

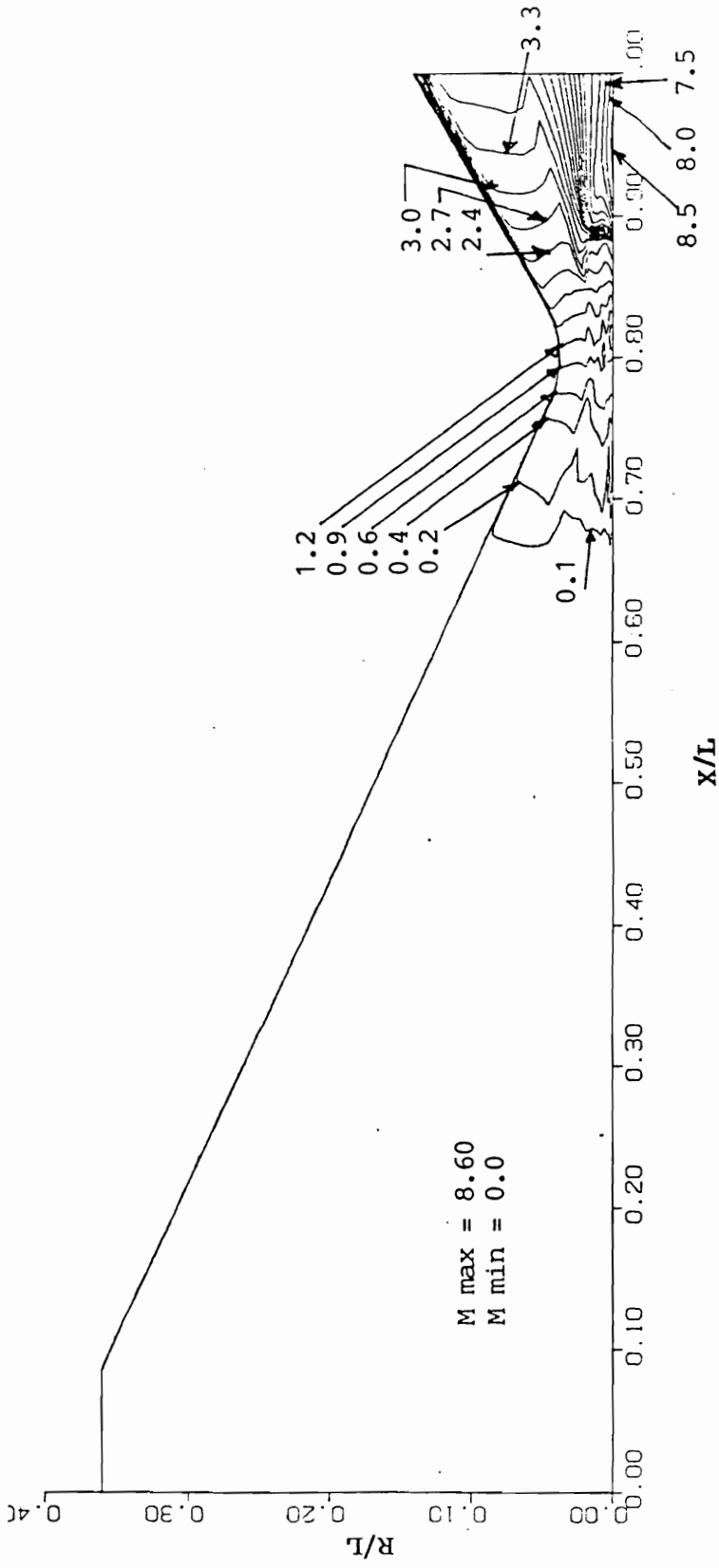

Figure 4.15. (d) Mach contour, Case 13

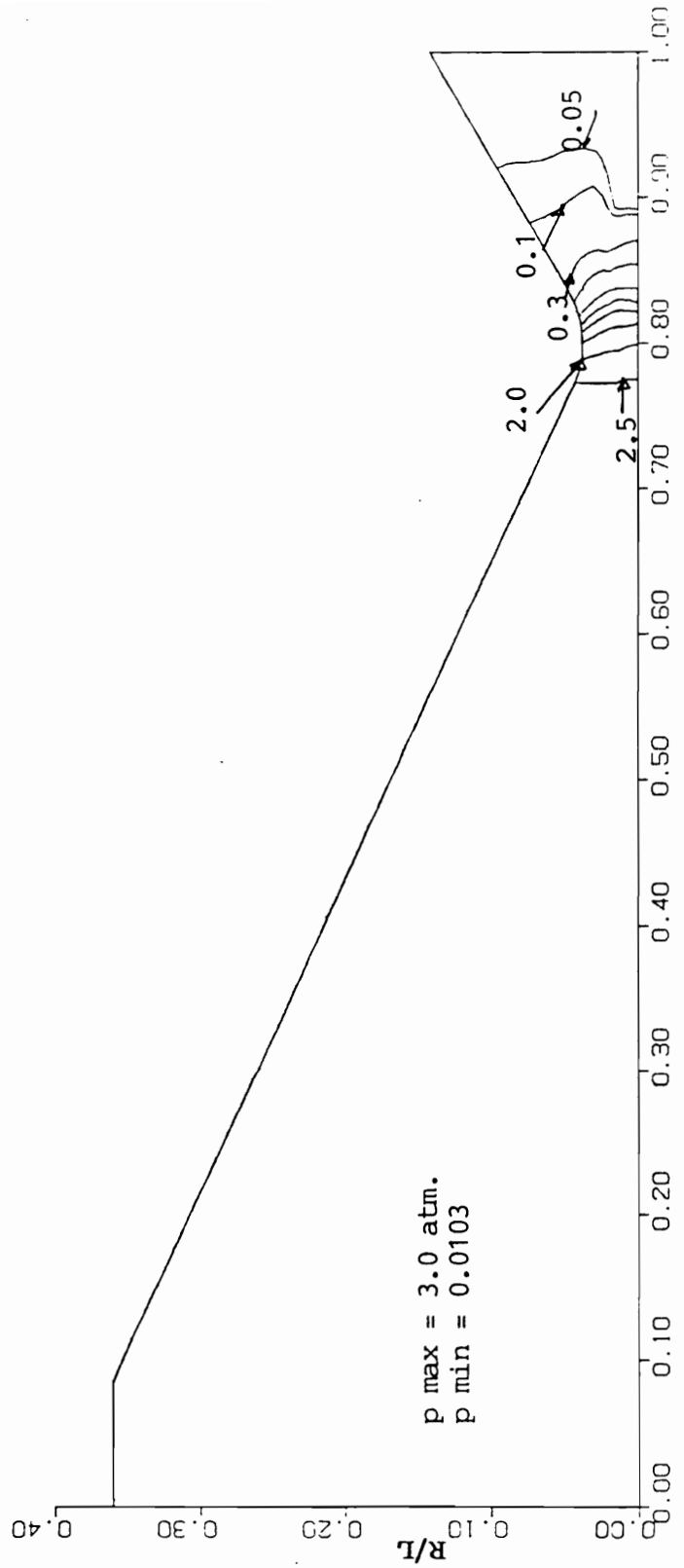

Figure 4.15. (e) Pressure contour, Case 13

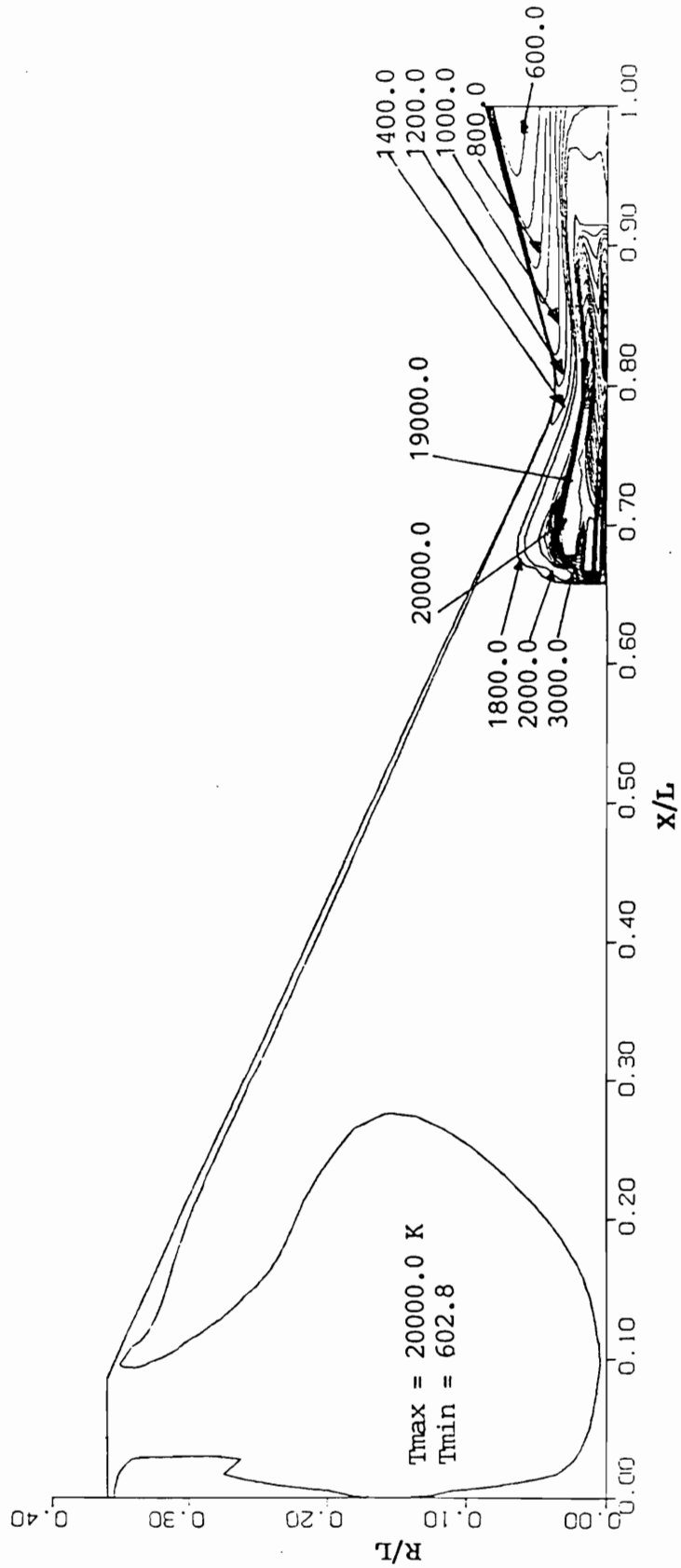

Figure 4.16. (a) Temperature contour, Case 14

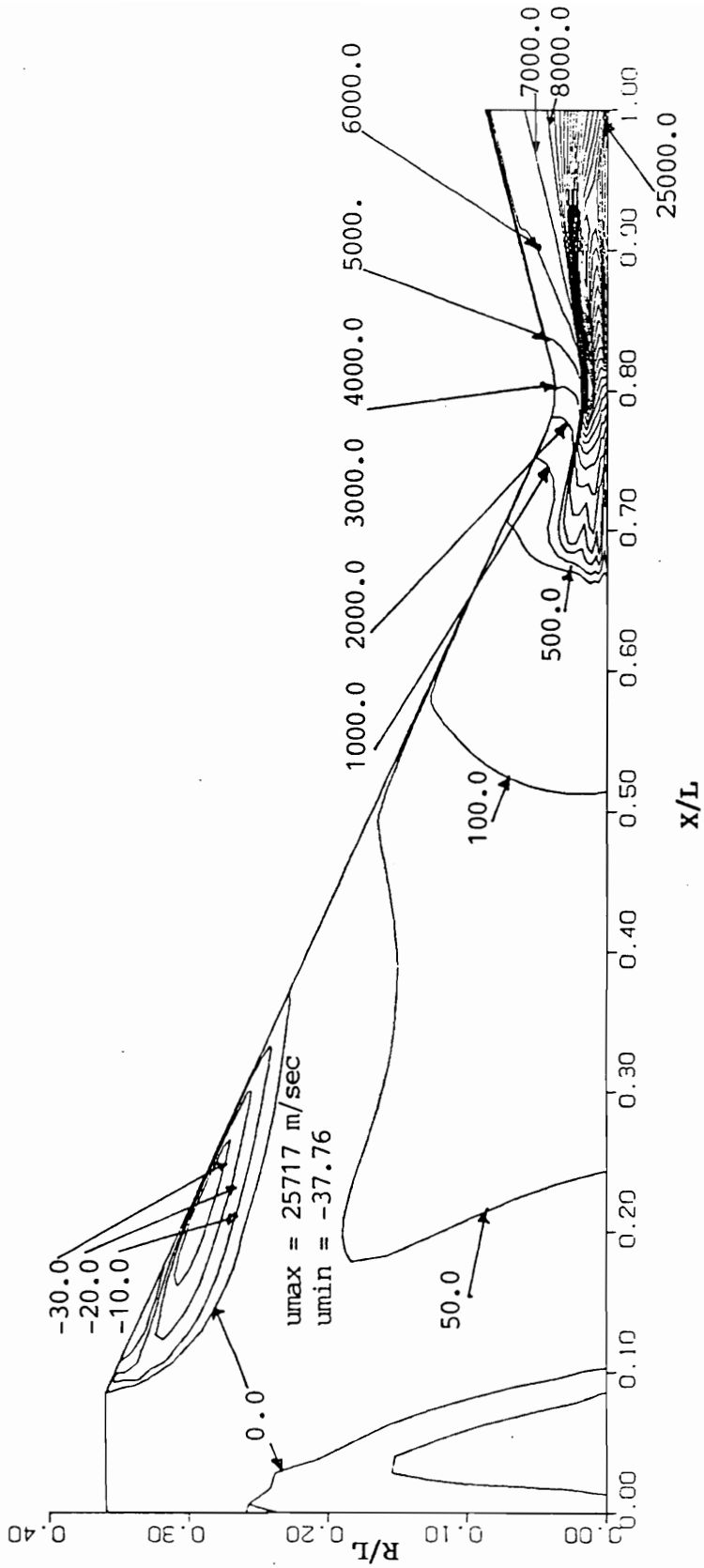

Figure 4.16. (b) u-velocity contour, Case 14.

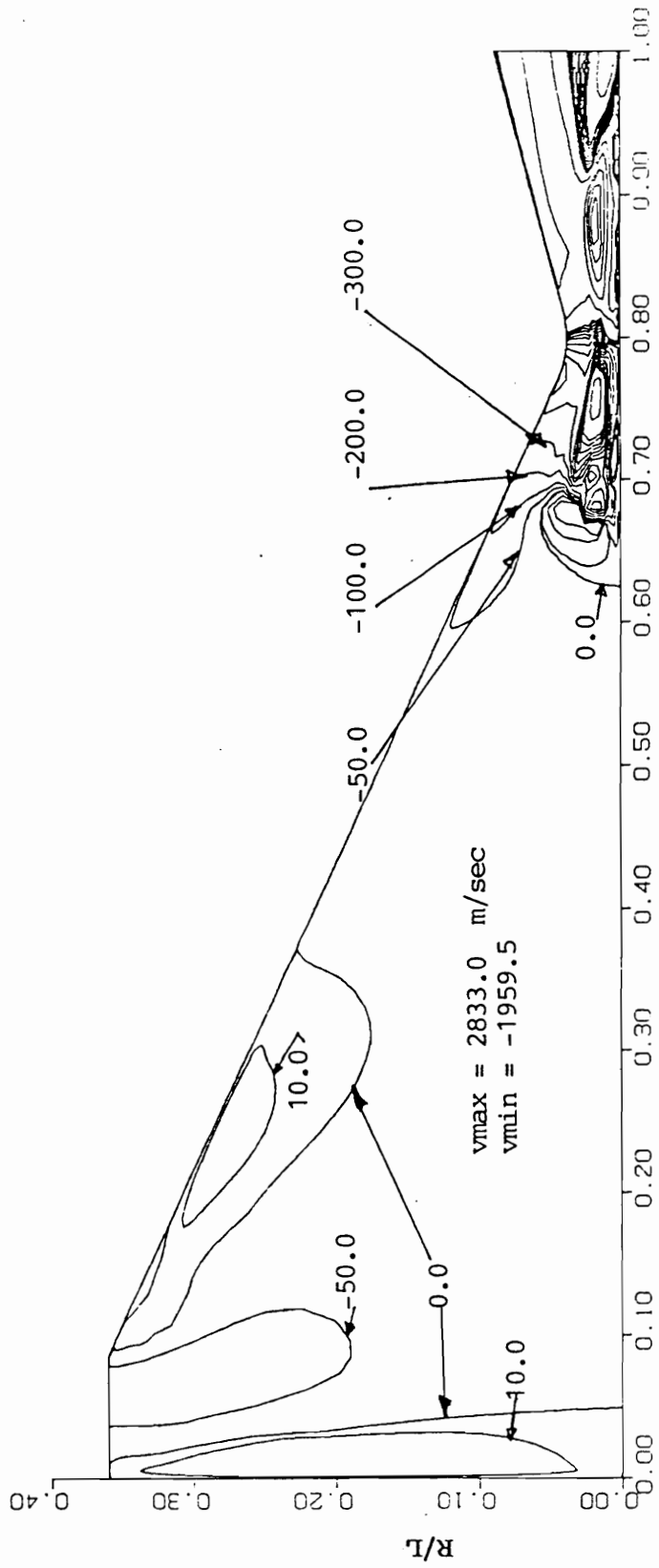

Figure 4.16. (c) v-velocity contour, Case 14

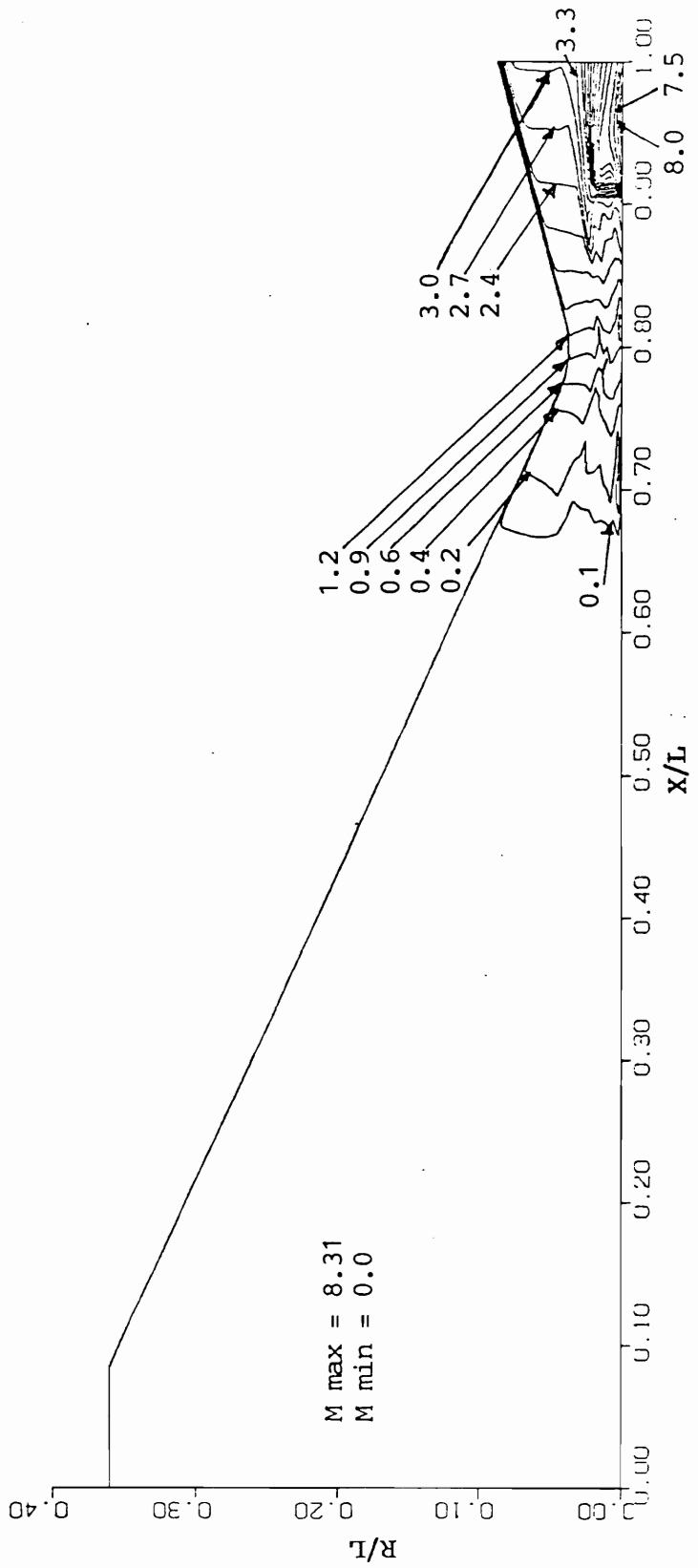

Figure 4.16. (d) Mach contour, Case 14

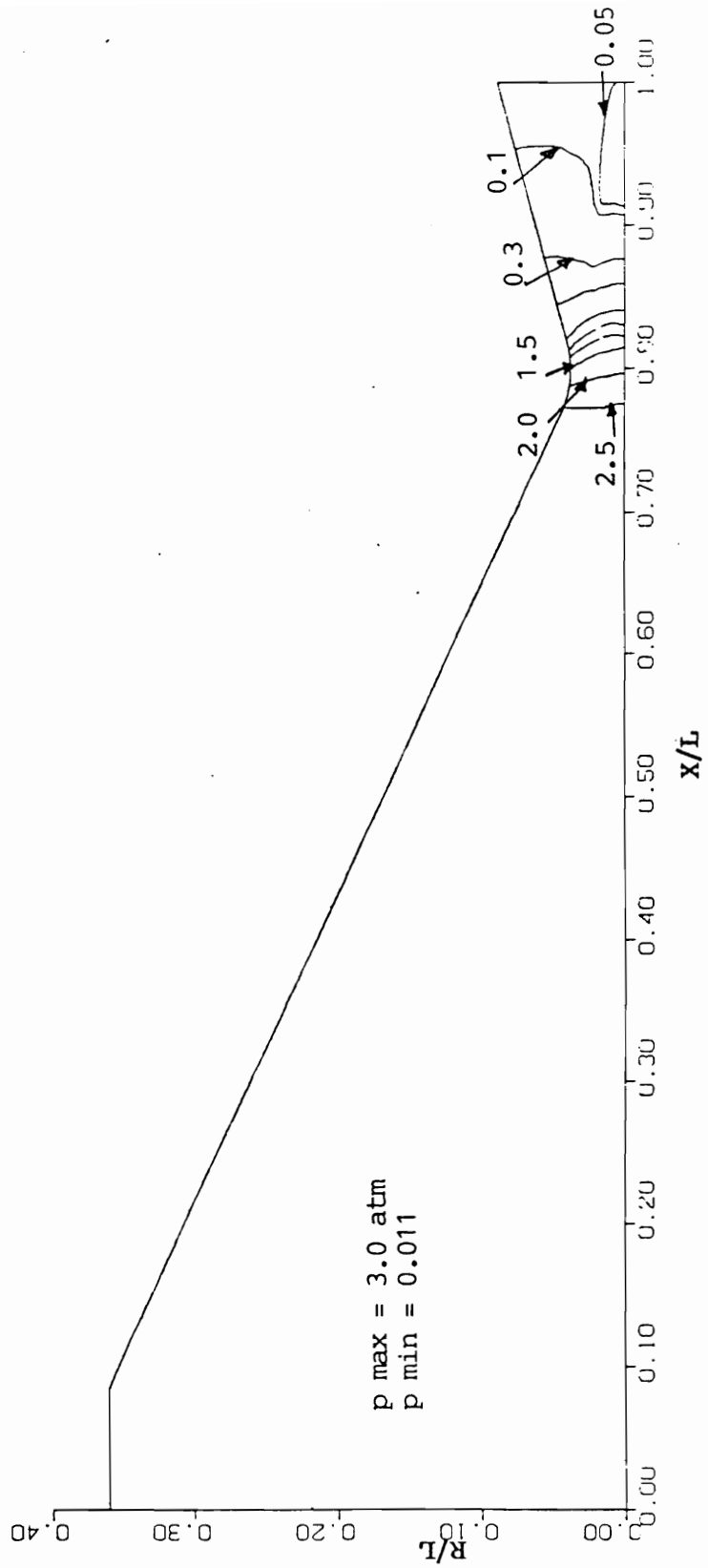

Figure 4.16. (e) Pressure contour, Case 14

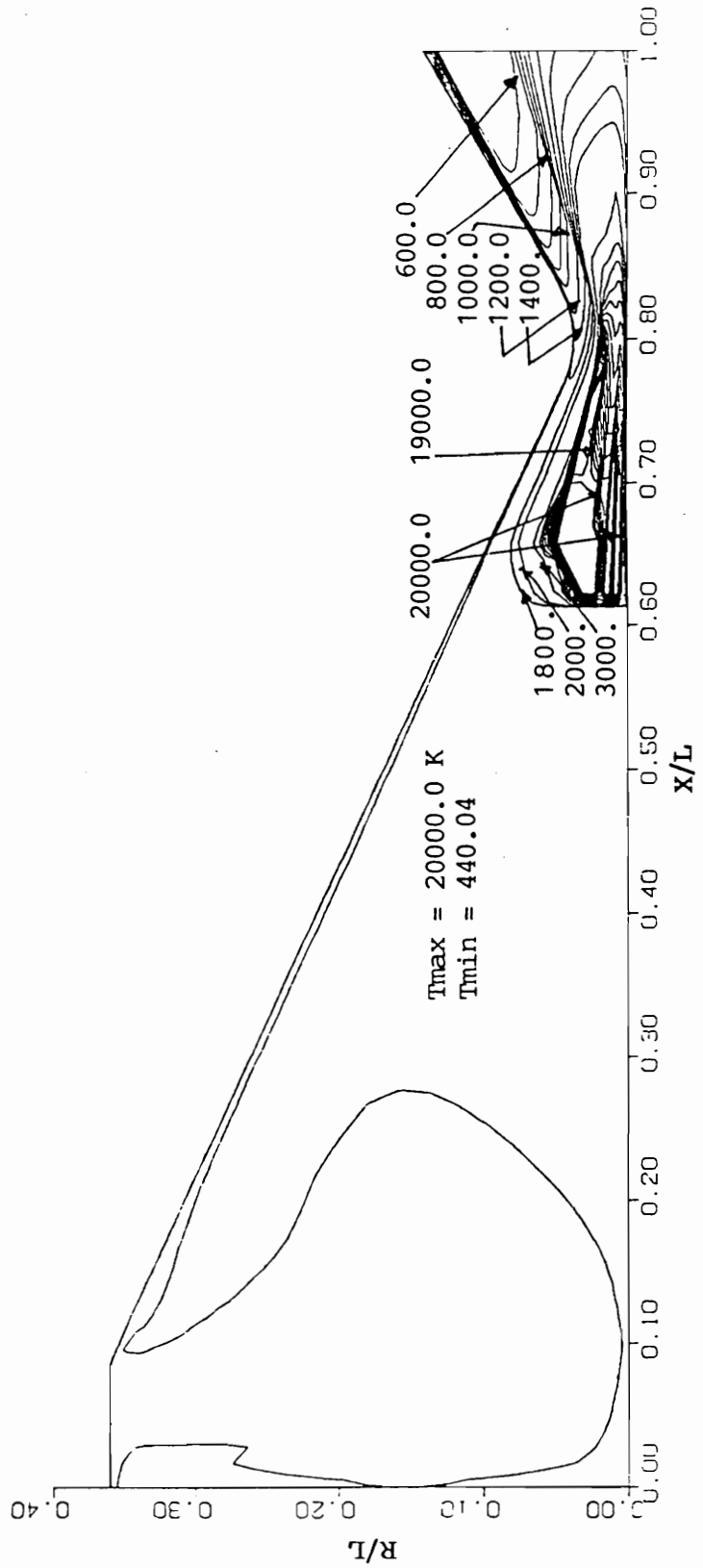

Figure 4.17. (a) Temperature contour, Case 15

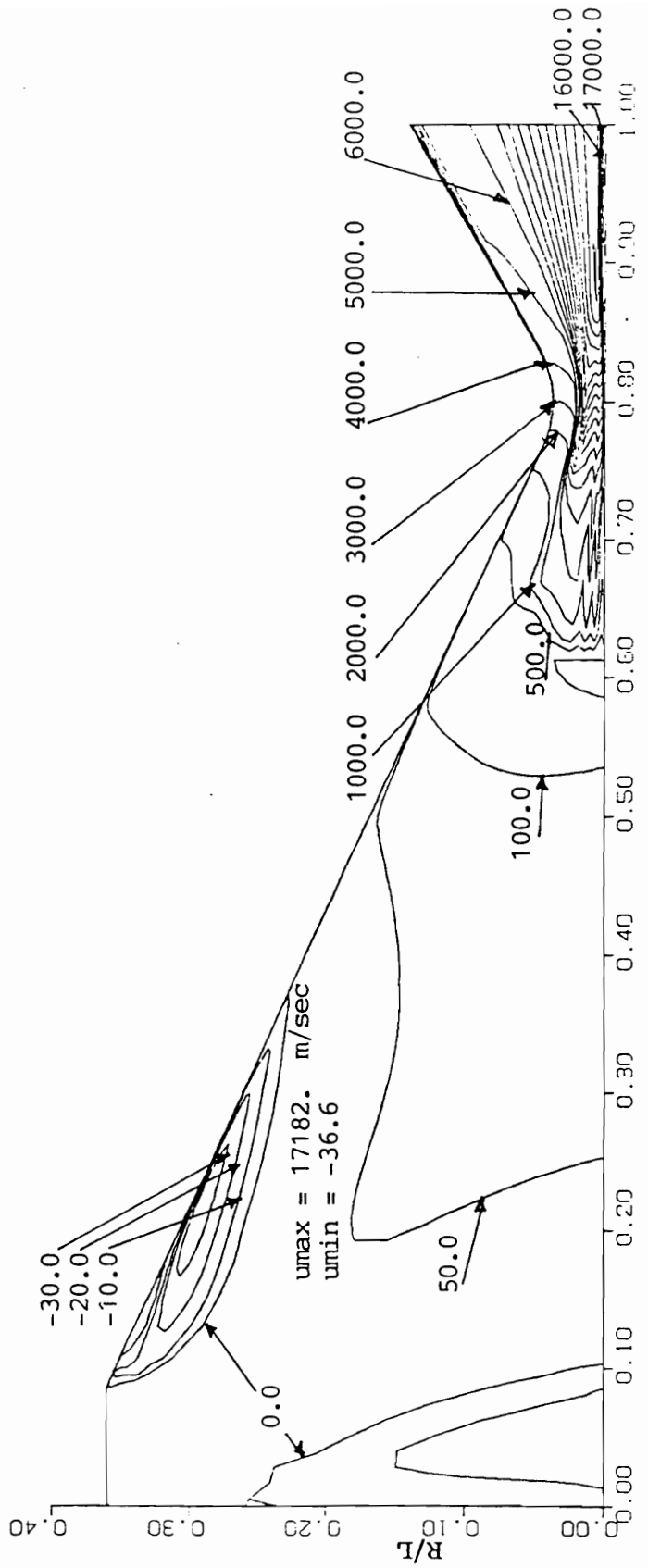

Figure 4.17. (b) u-velocity contour, Case 15

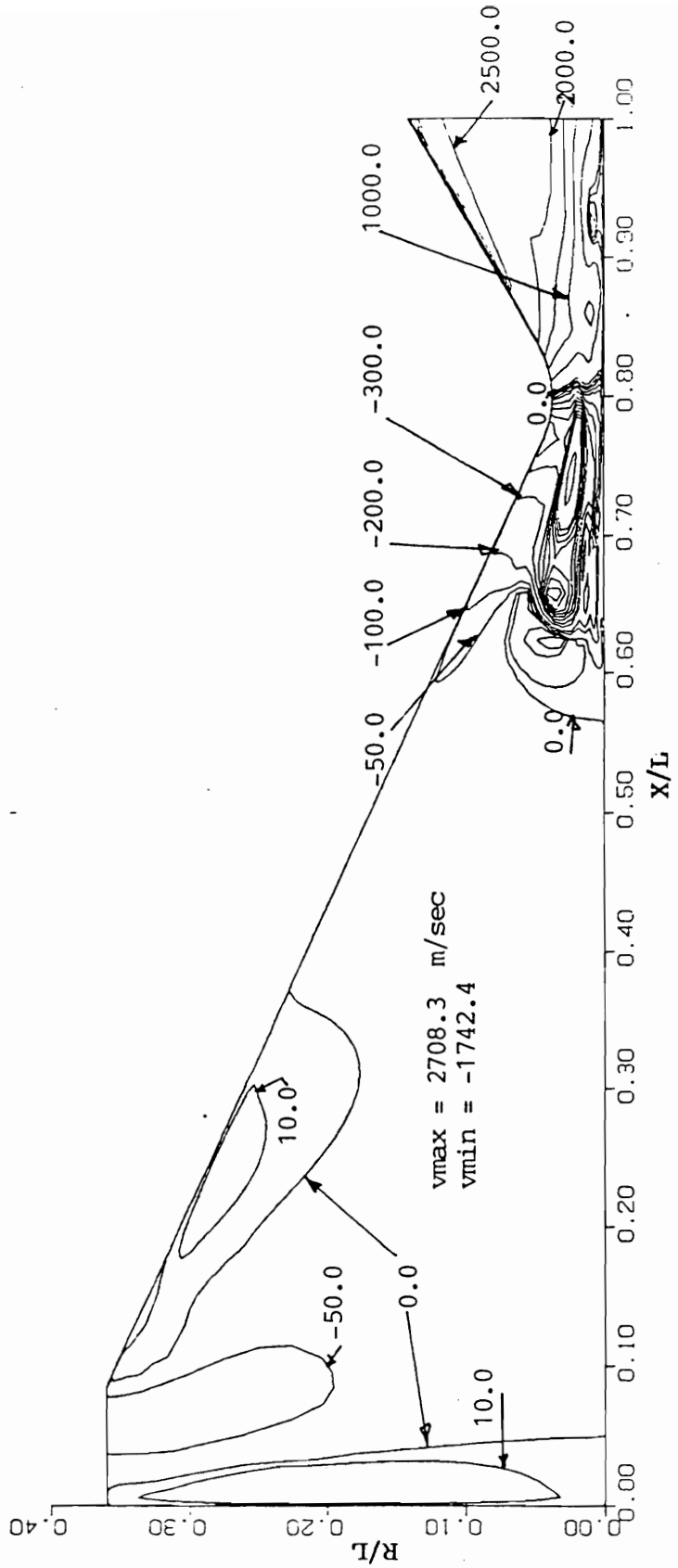

Figure 4.17. (c) v-velocity contour, Case 15

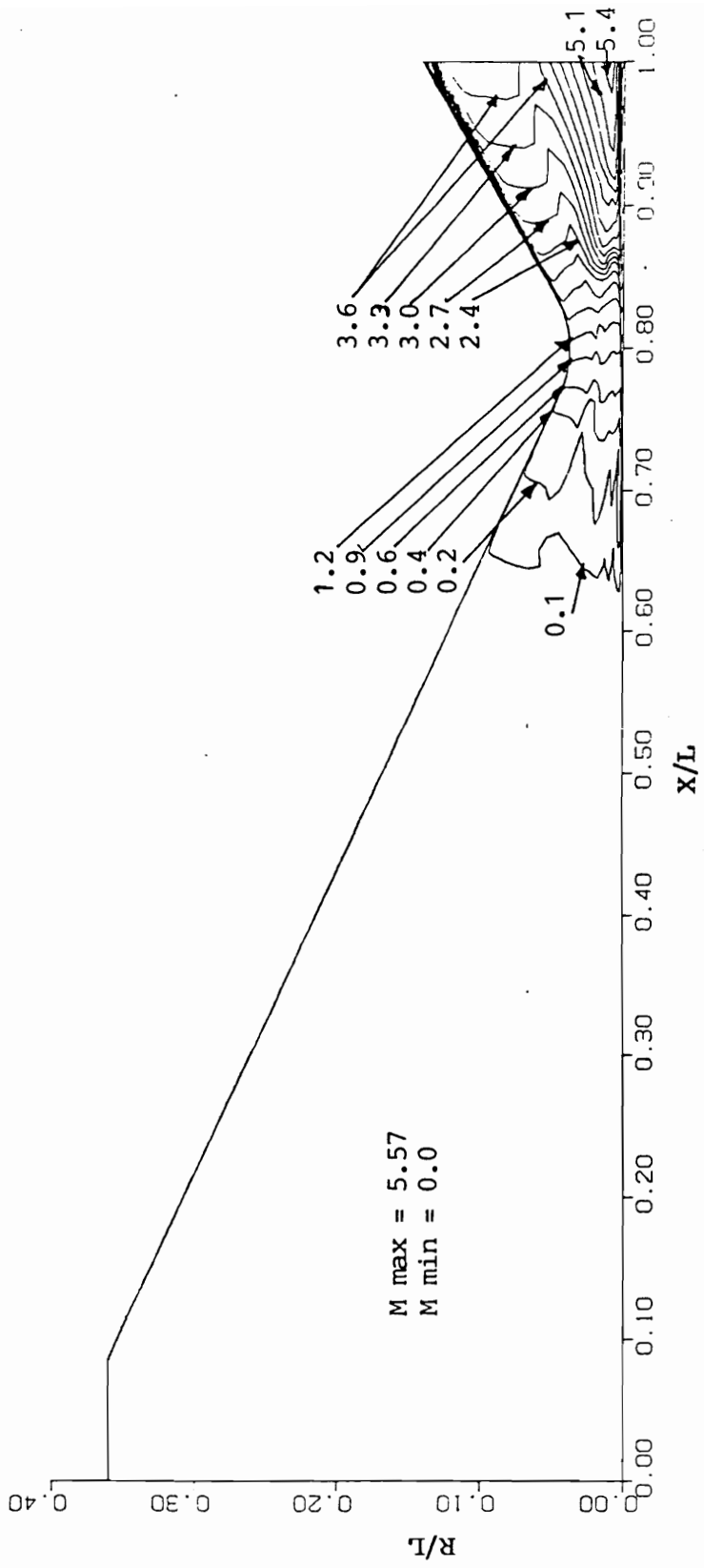

Figure 4.17. (d) Mach contour, Case 15

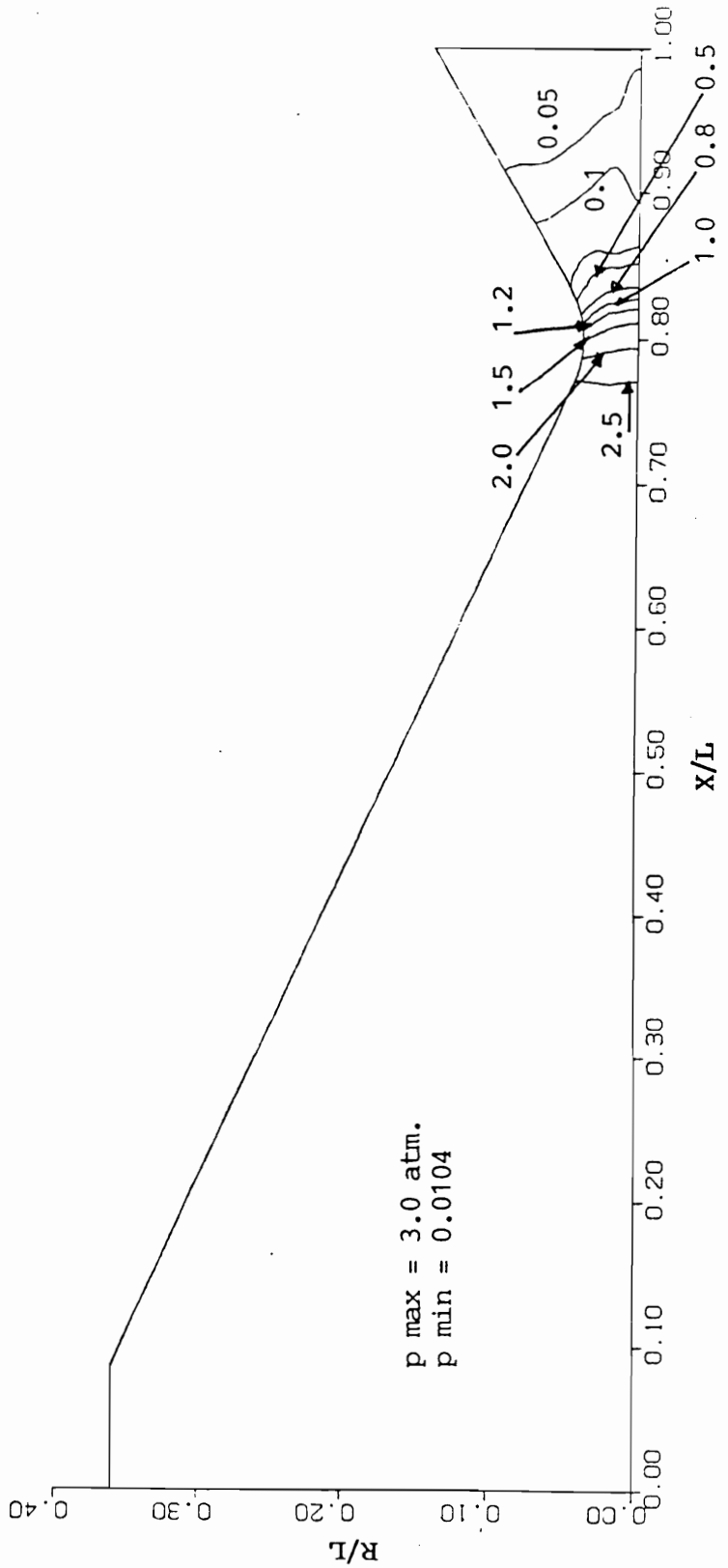

Figure 4.17. (e) Pressure contour, Case 15

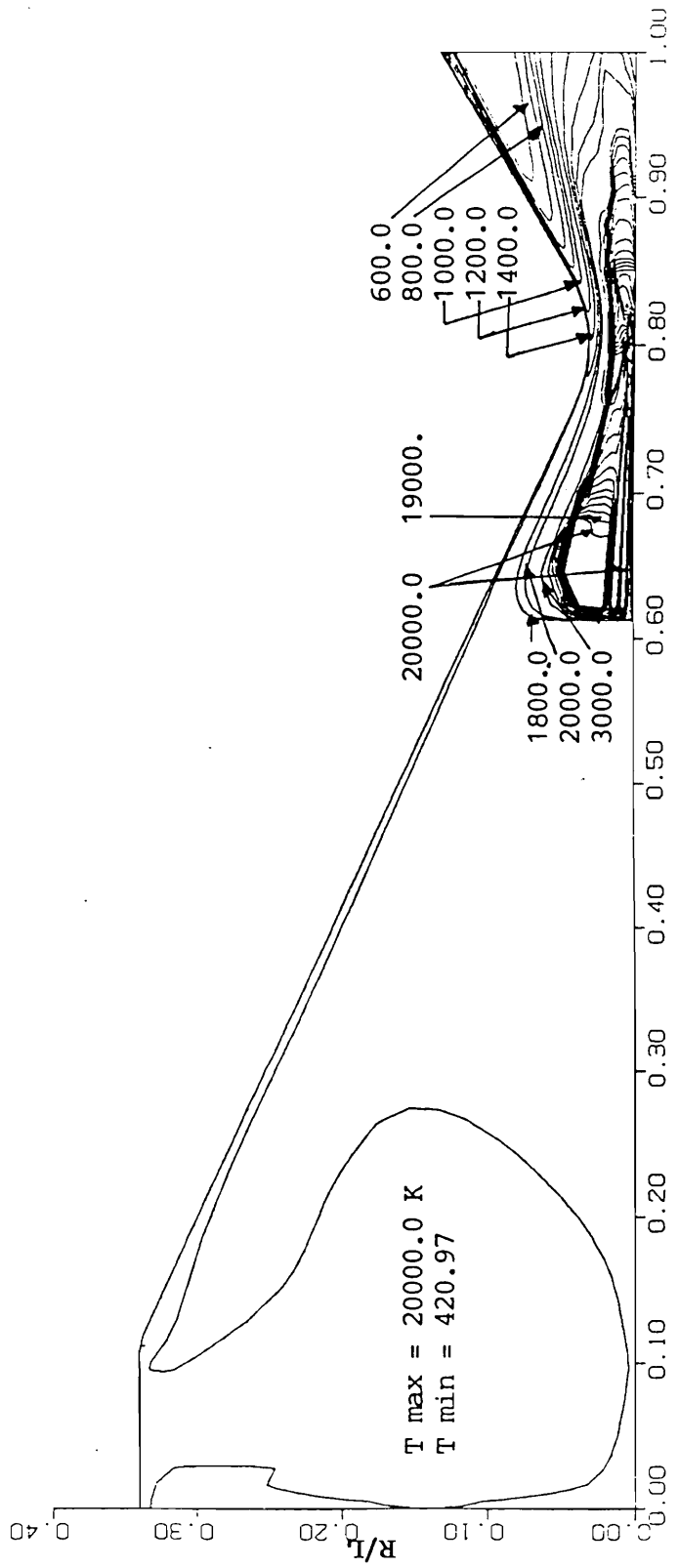

Figure 4.18. (a) Temperature contour, Case 16

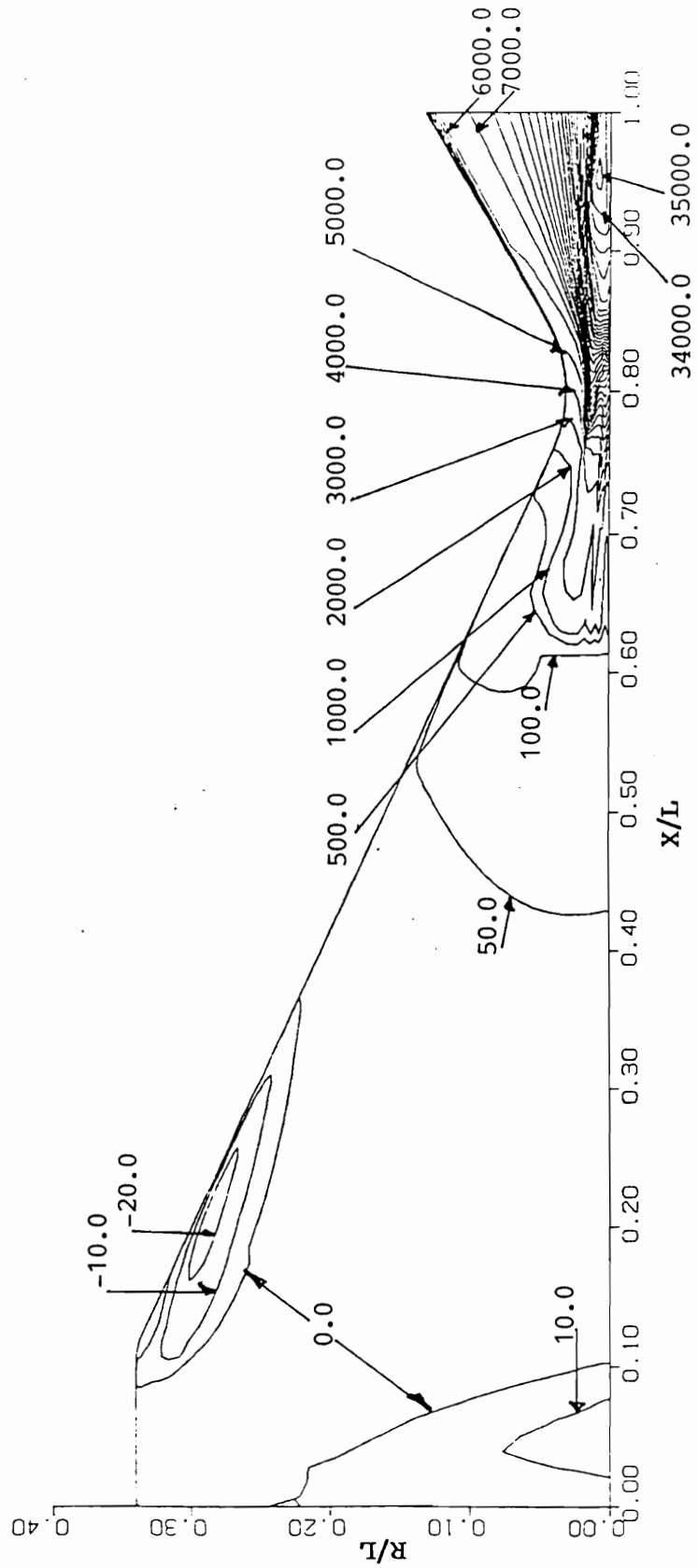

Figure 4.18. (b) u-velocity contour, Case 16

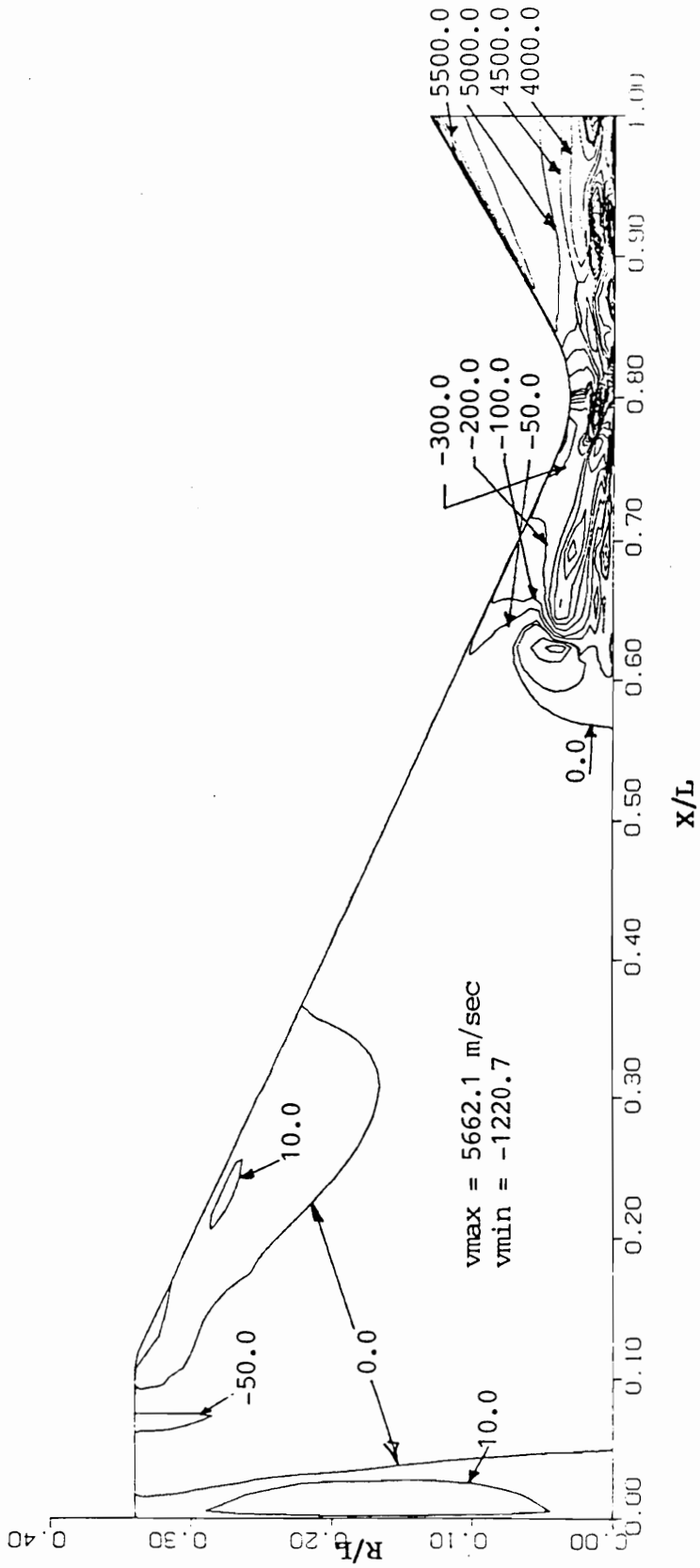

Figure 4.18. (c) v-velocity contour, Case 16

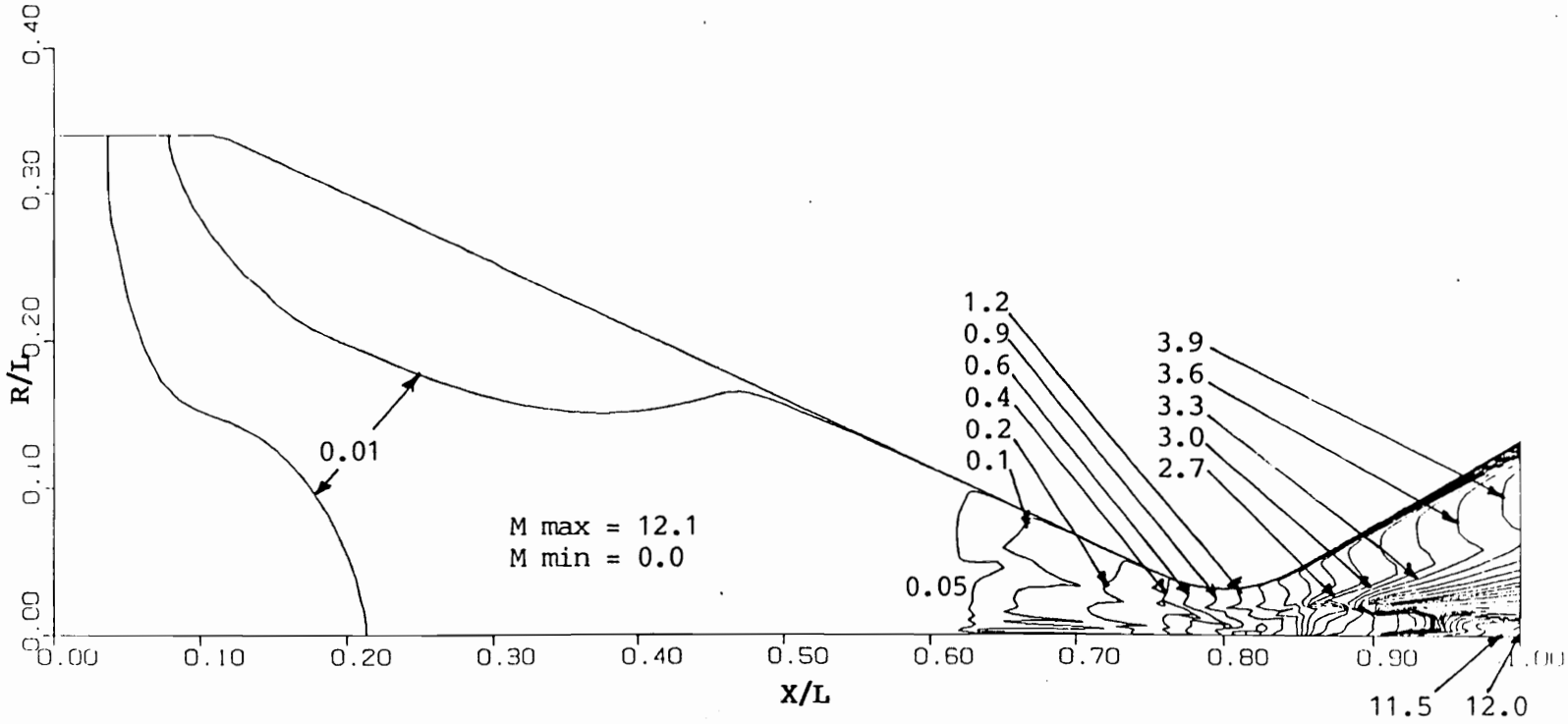

Figure 4.18. (d) Mach contour, Case 16

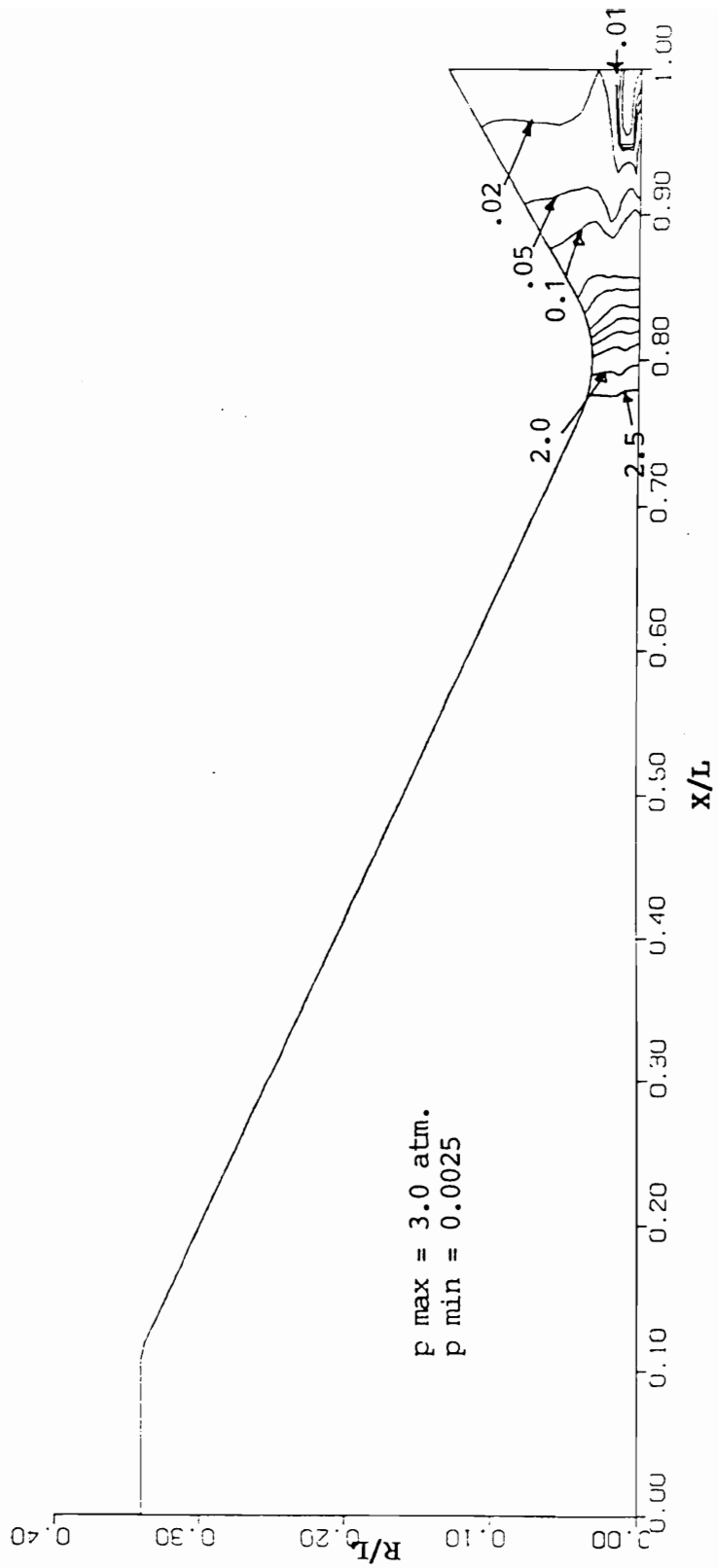

Figure 4.18. (c) Pressure contour, Case 16

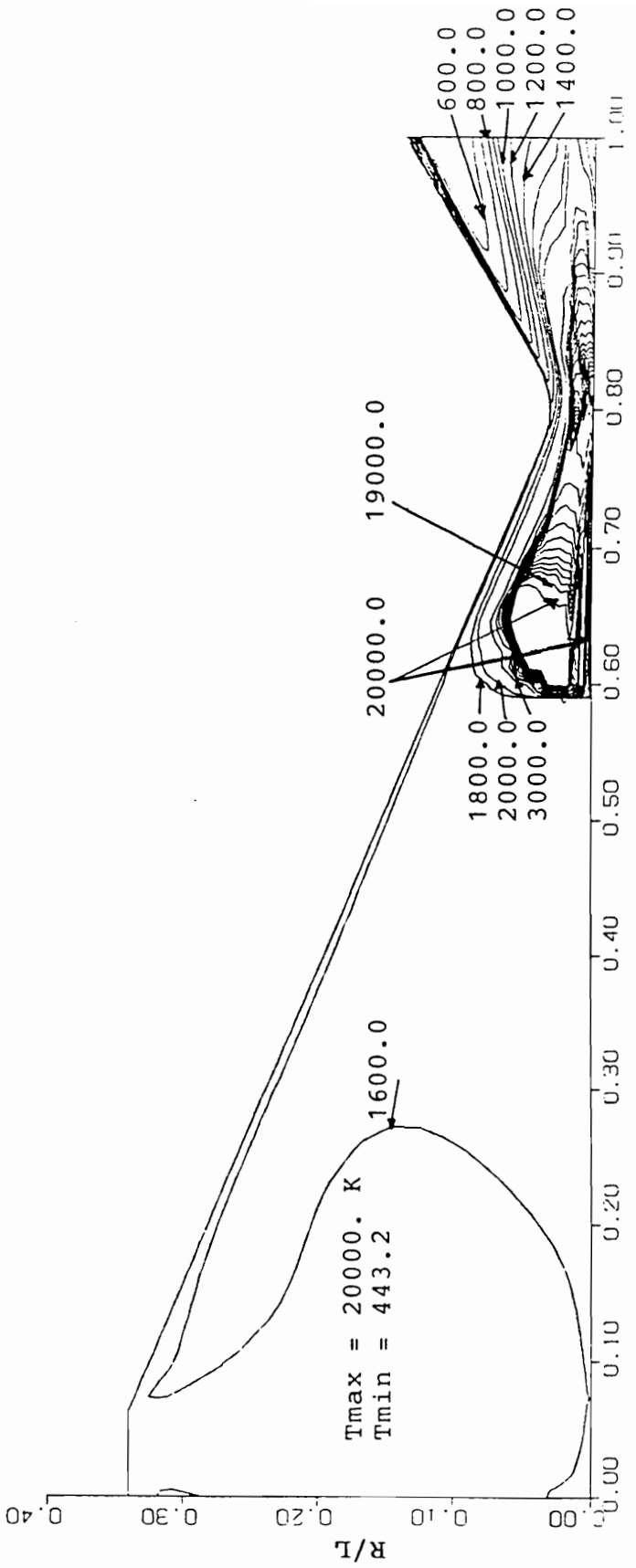

Figure 4.19. (a) Temperature contour, Case 17

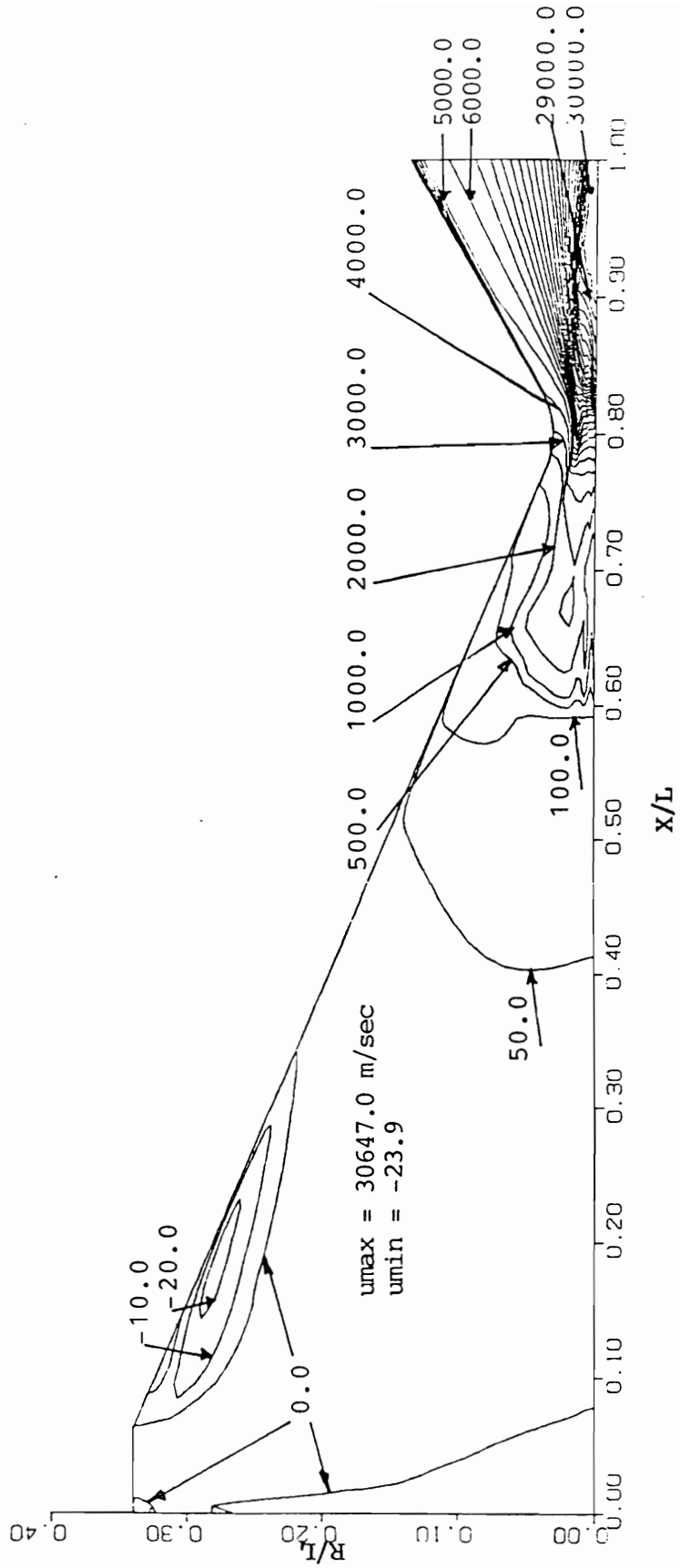

Figure 4.19. (b) u-velocity contour, Case 17

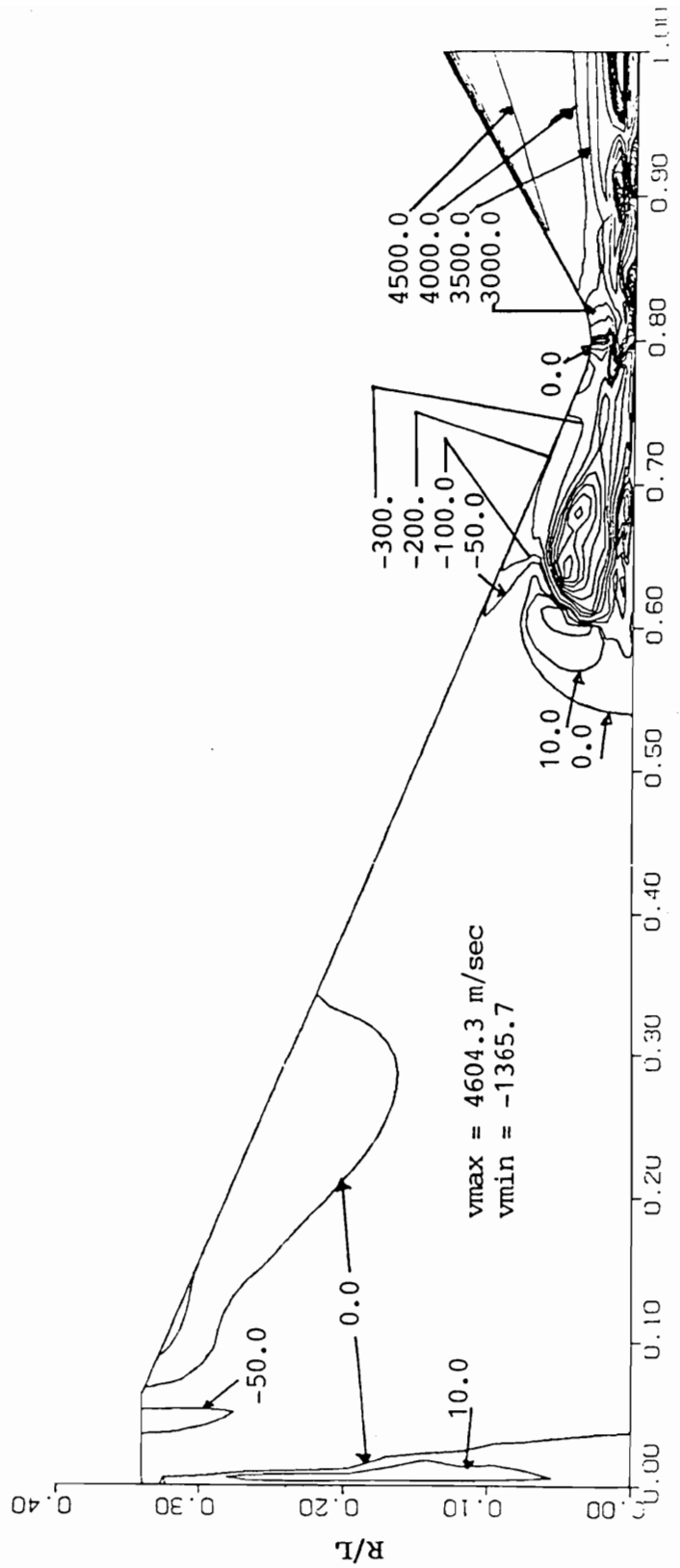

Figure 4.19. (c) v-velocity contour, Case 17

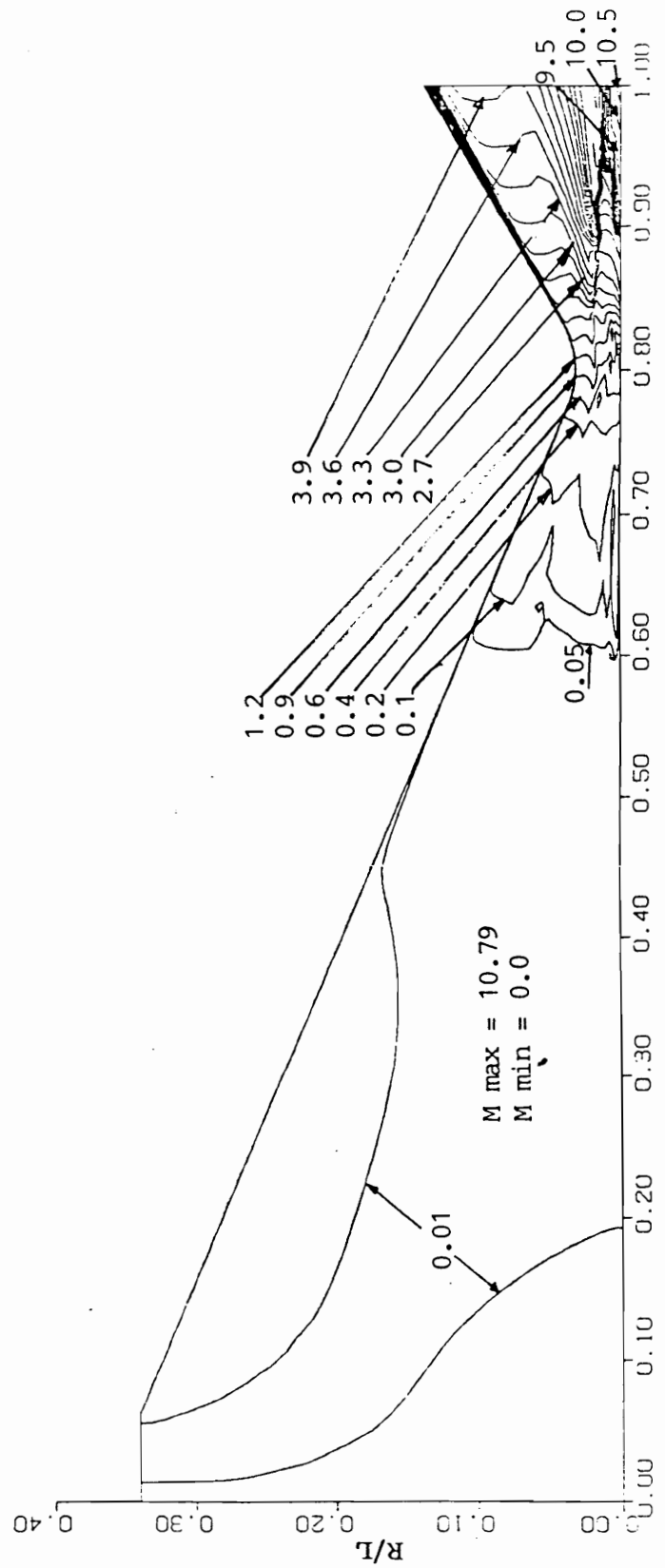

Figure 4.19. (d) Mach contour, Case 17

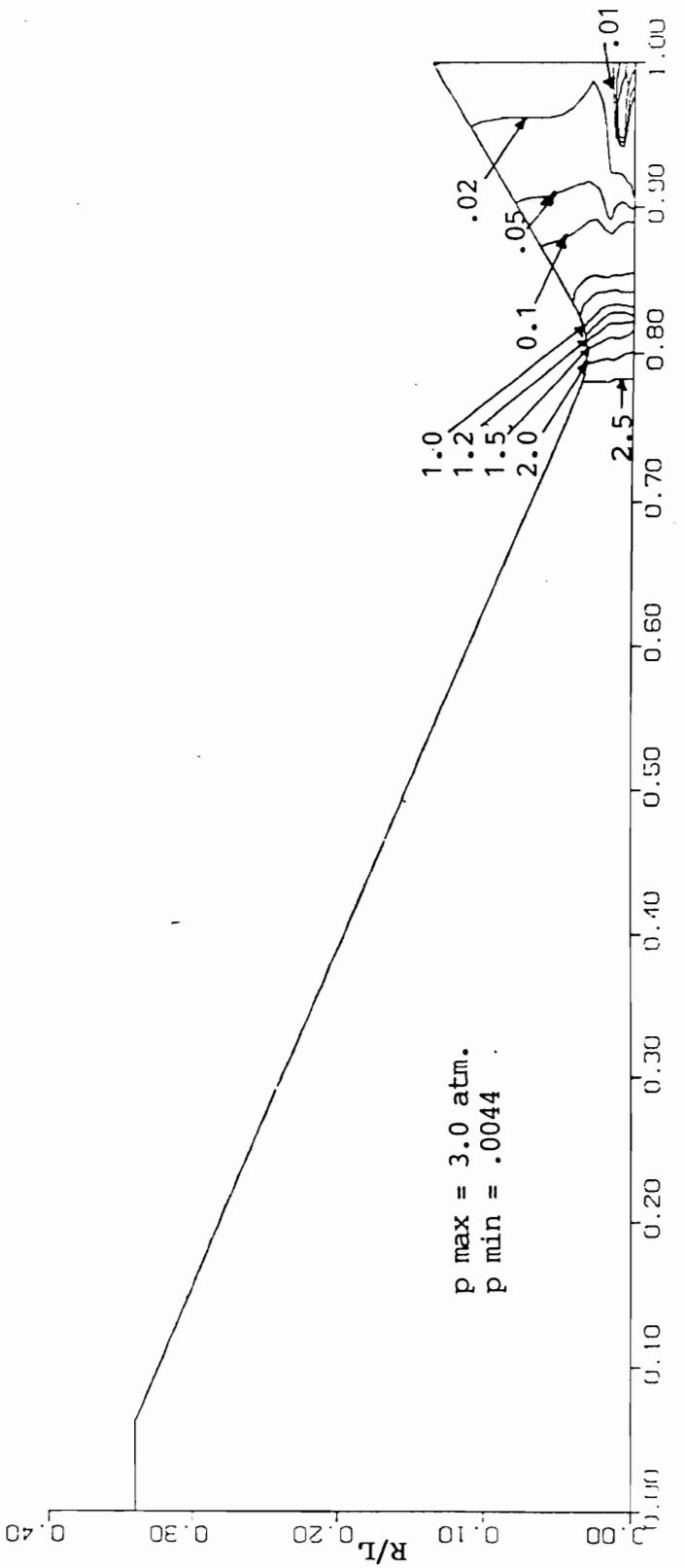

Figure 4.19. (e) Pressure contour, Case 17

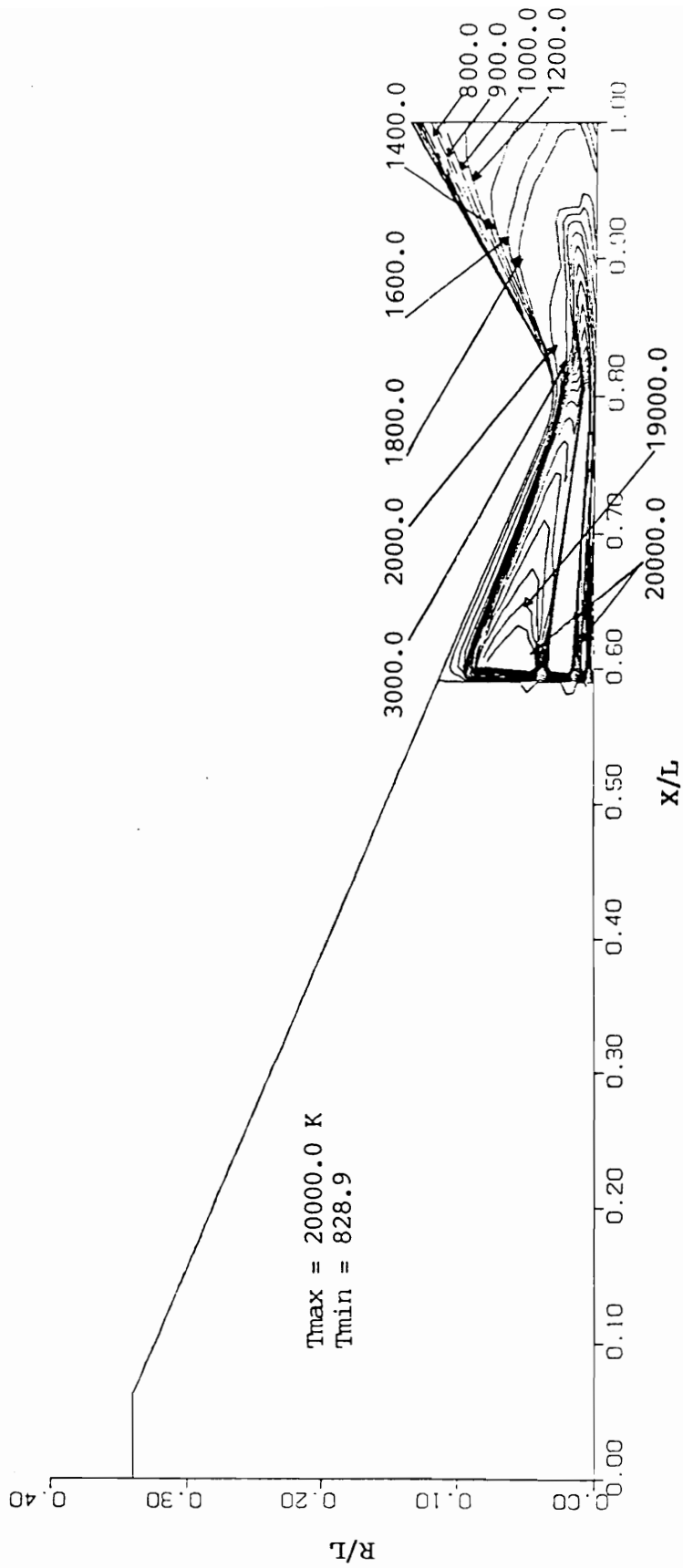

Figure 4.20. (a) Temperature contour, Case 18

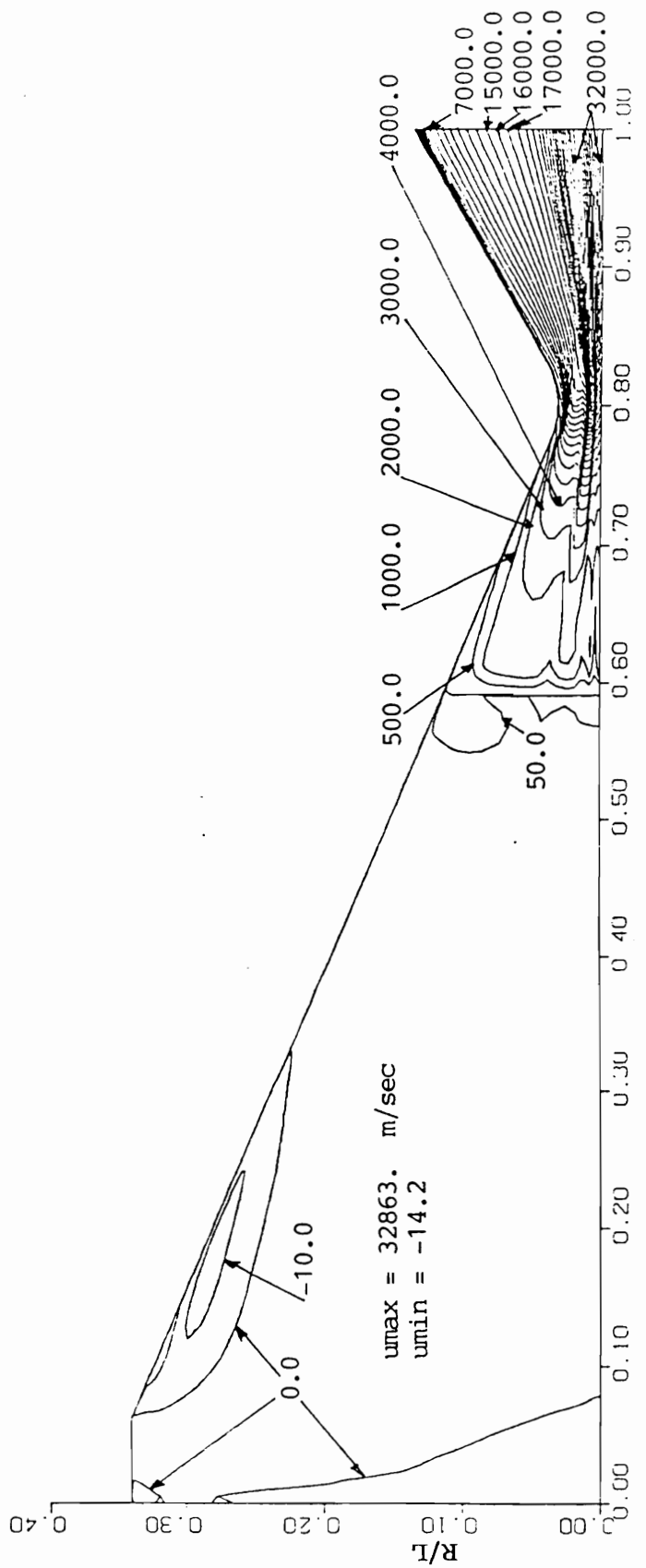

Figure 4.20. (b) u-velocity contour, Case 18

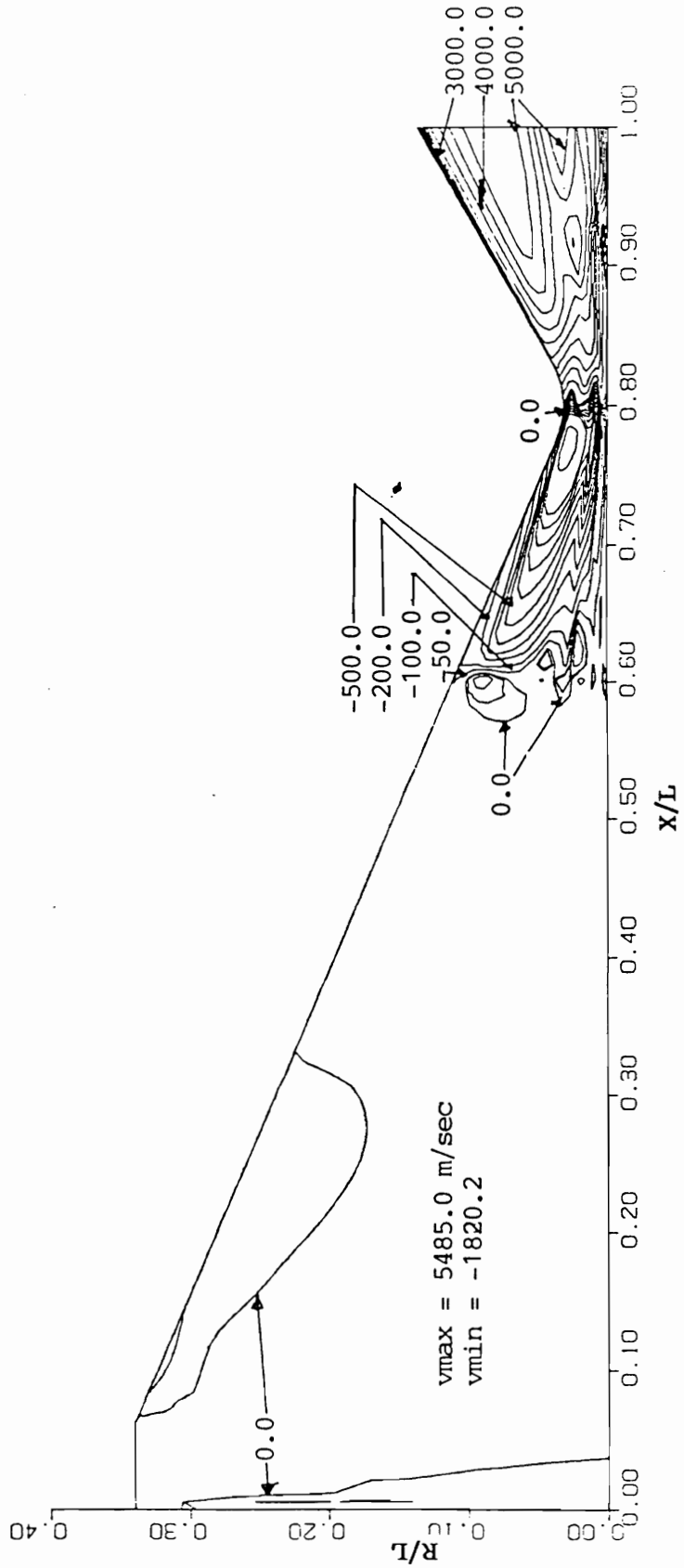

Figure 4.20. (c) v-velocity contour, Case 18

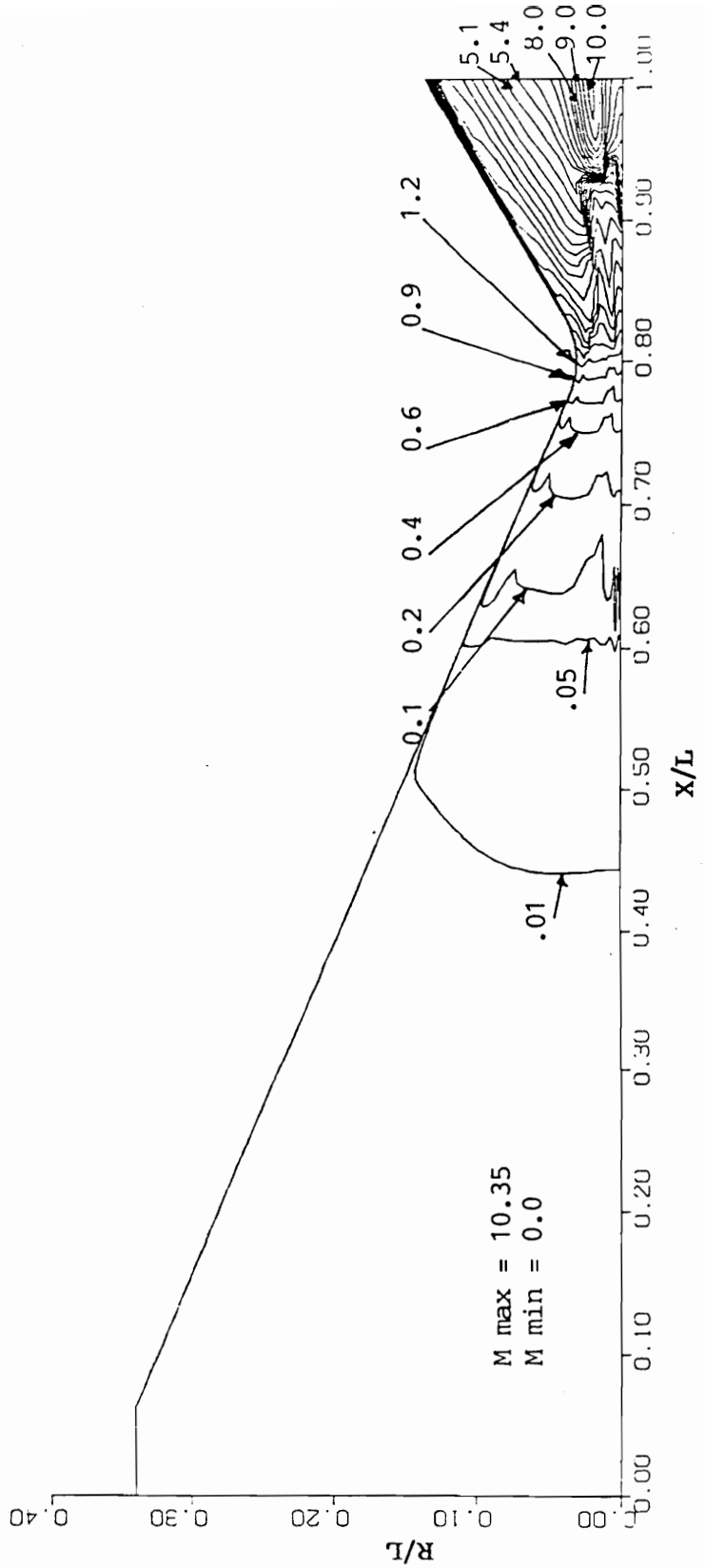

Figure 4.20. (d) Mach contour, Case 18

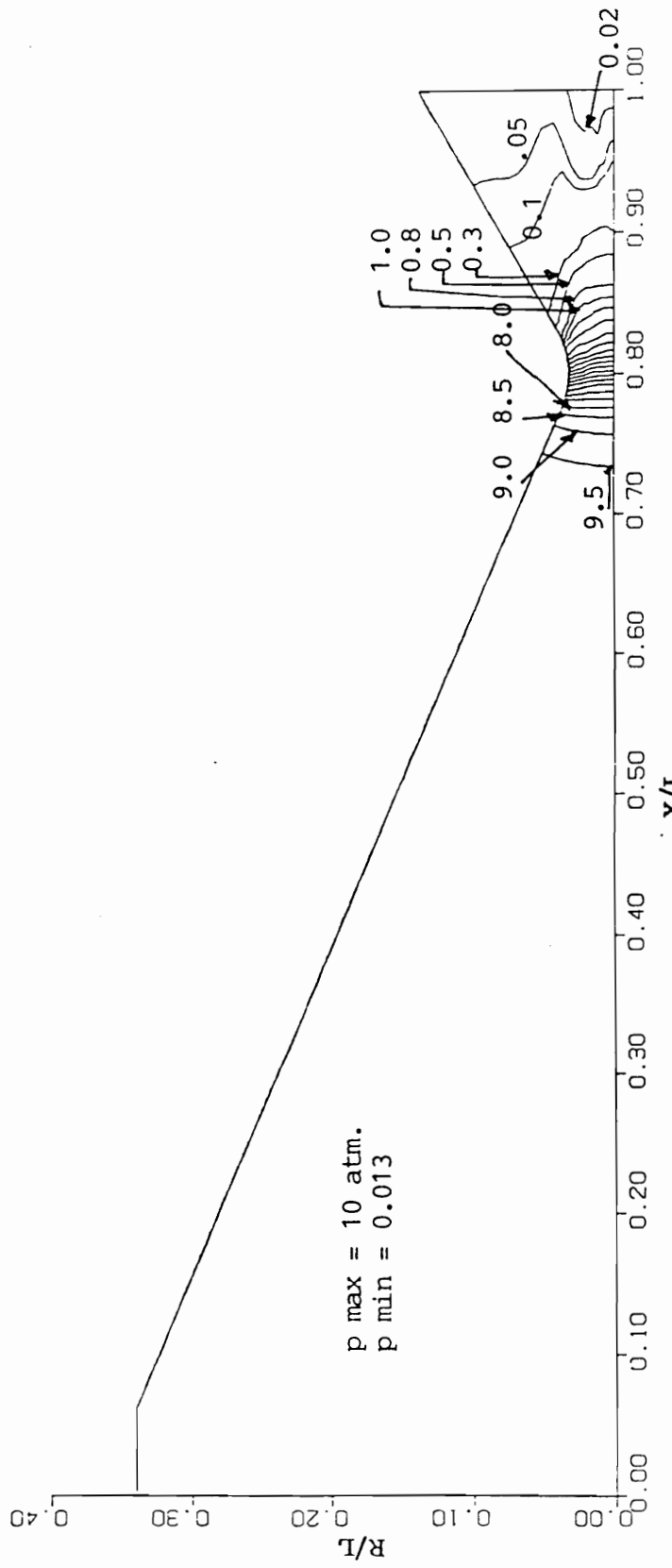

Figure 4.20. (e) Pressure contour, Case 18

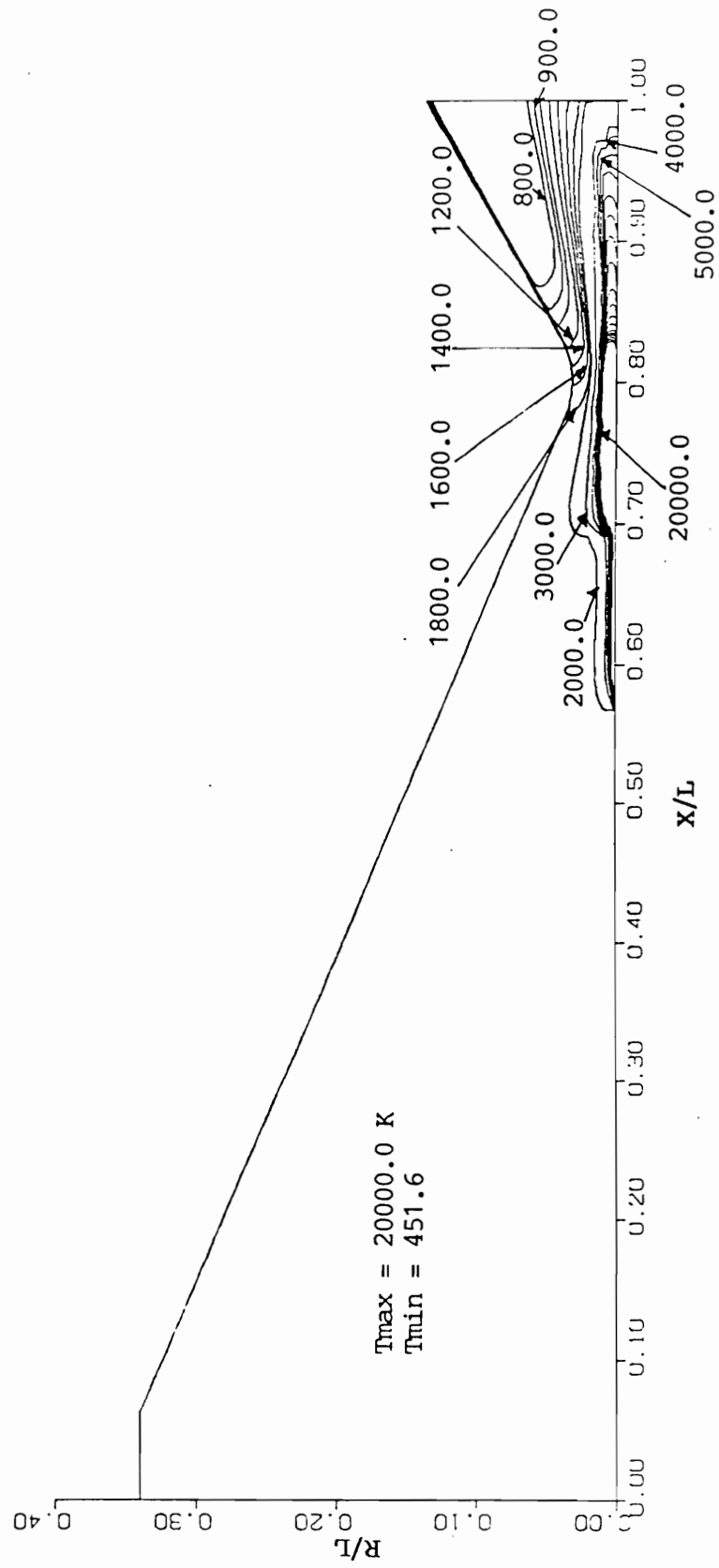

Figure 4.21. (a) Temperature contour, Case 19

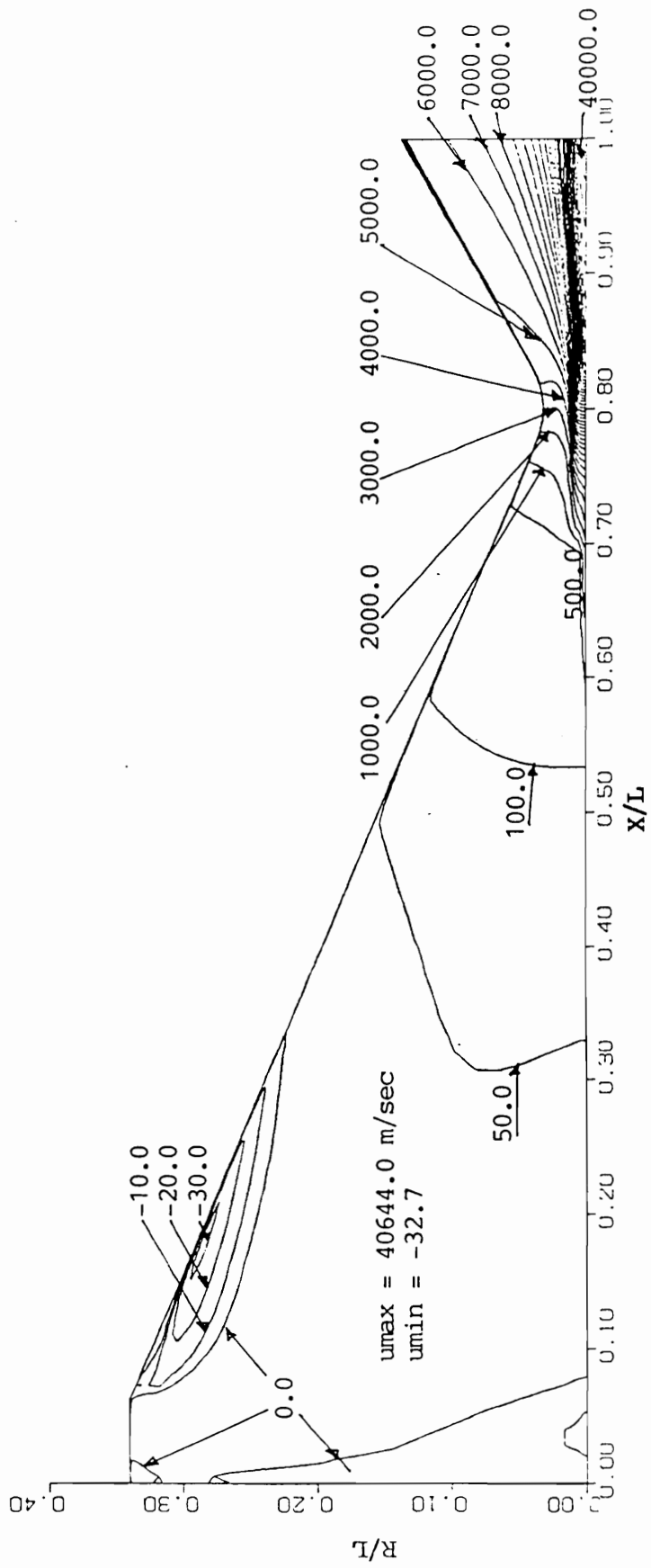

Figure 4.21. (b) u-velocity contour, Case 19

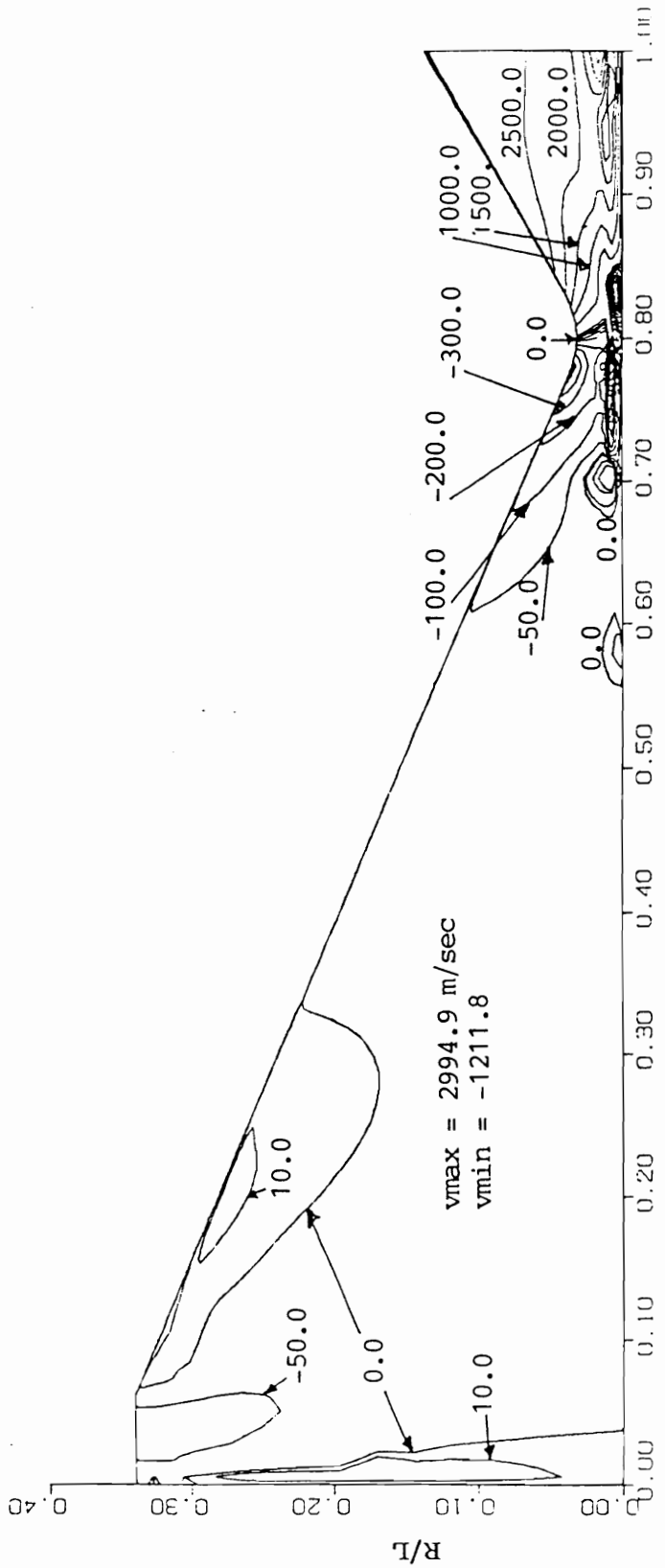

Figure 4.21. (c) *v*-velocity contour, Case 19

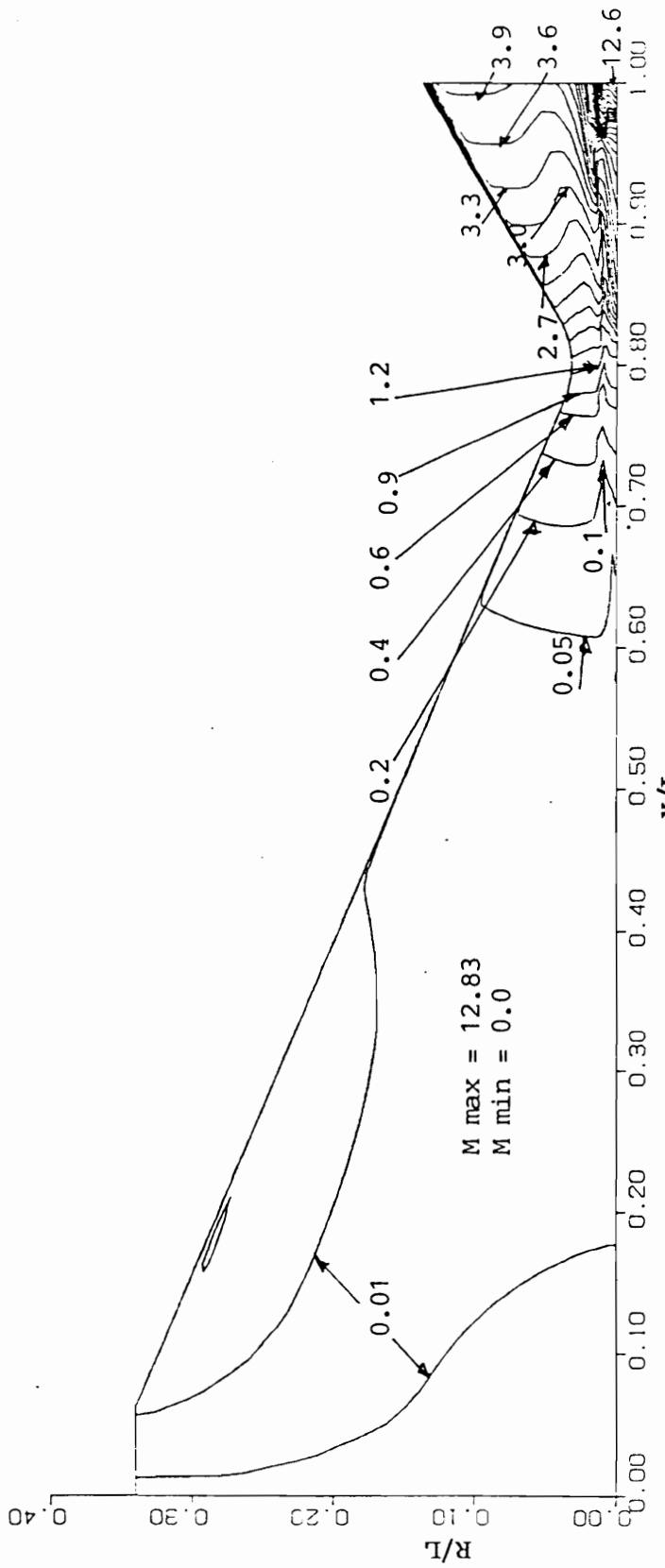

Figure 4.21. (d) Mach contour, Case 19

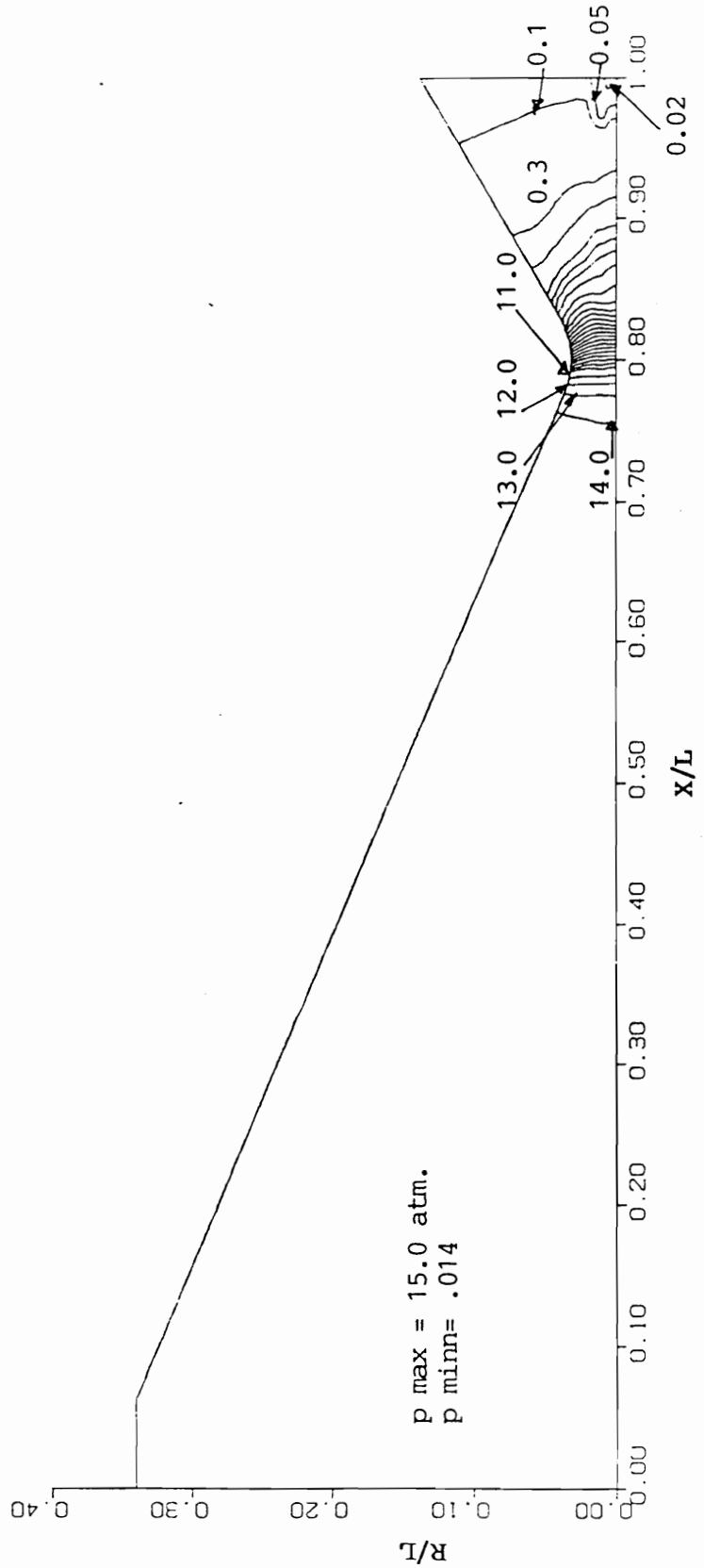

Figure 4.21. (e) Pressure contour, Case 19

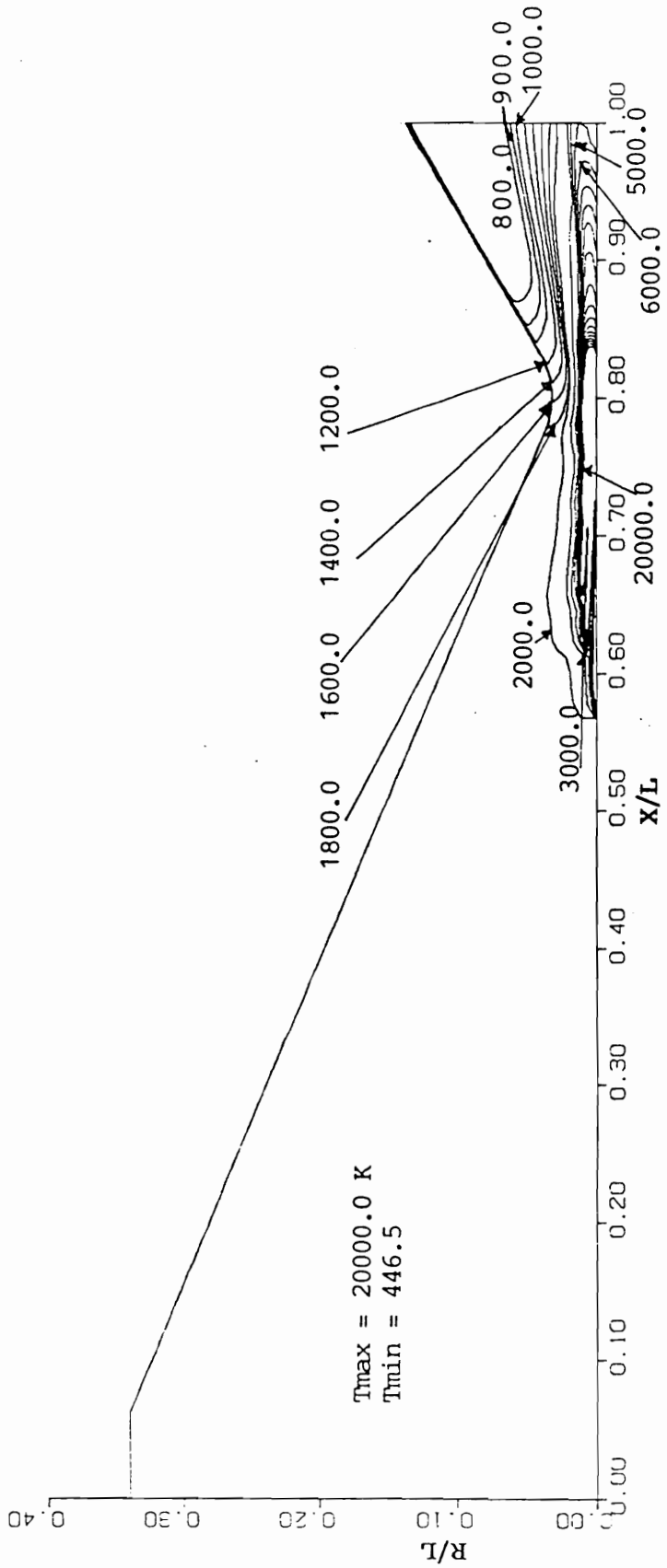

Figure 4.22. (a) Temperature contour, Case 20

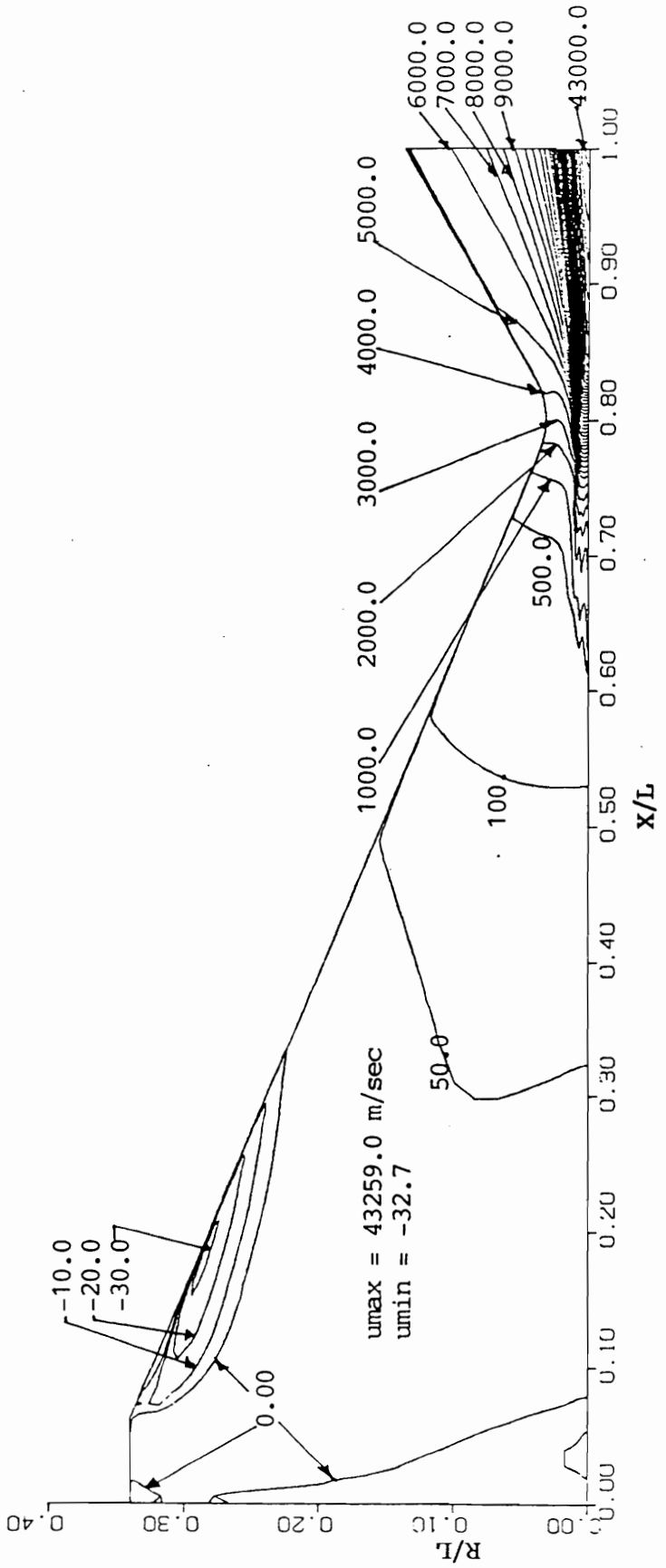

Figure 4.22. (b) u-velocity contour, Case 20

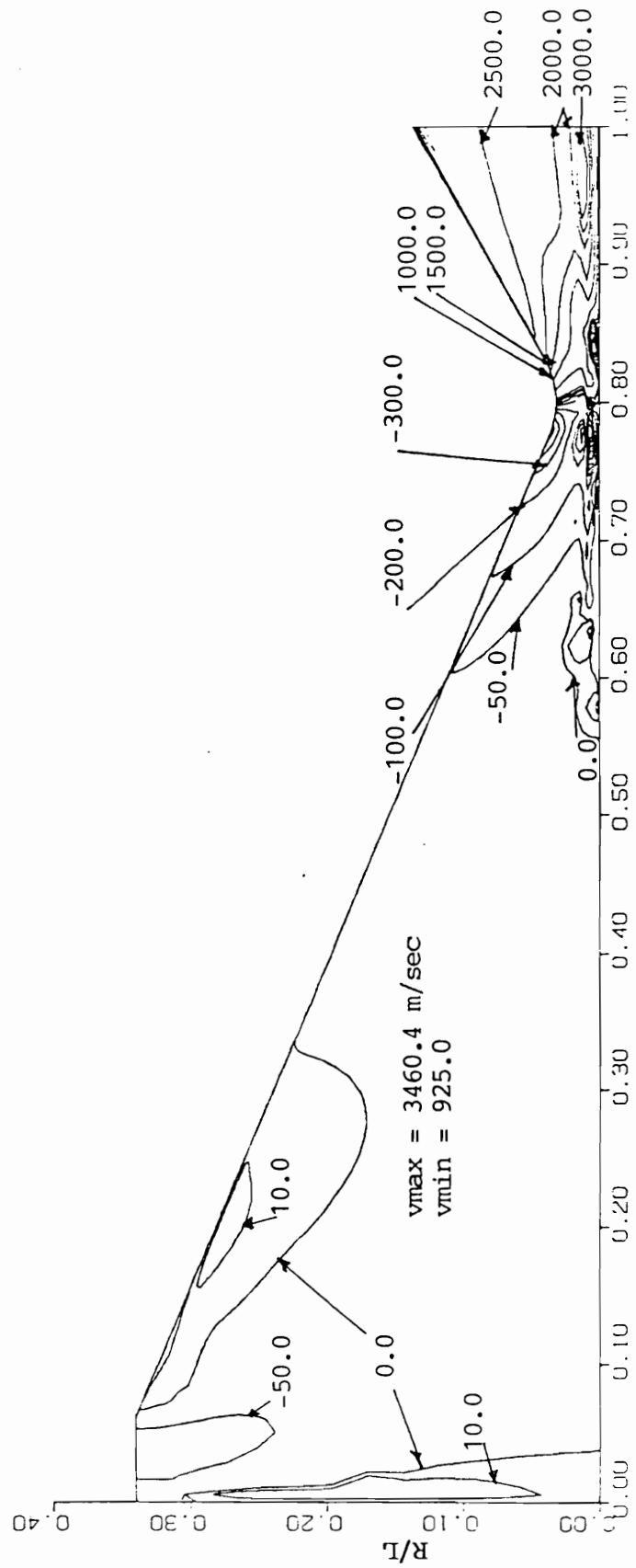

Figure 4.22. (c) v-velocity contour, Case 20

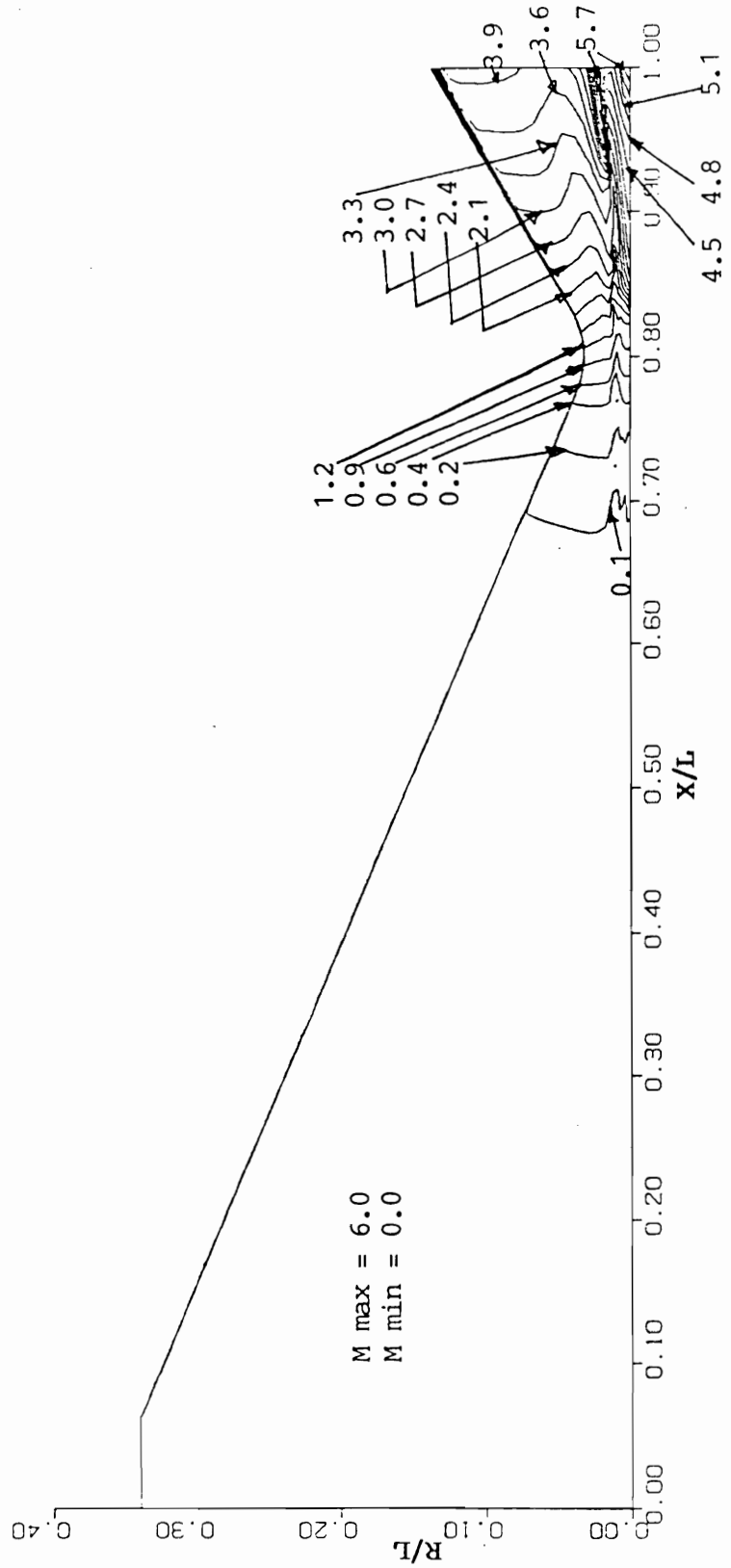

Figure 4.22. (d) Mach contour, Case 20

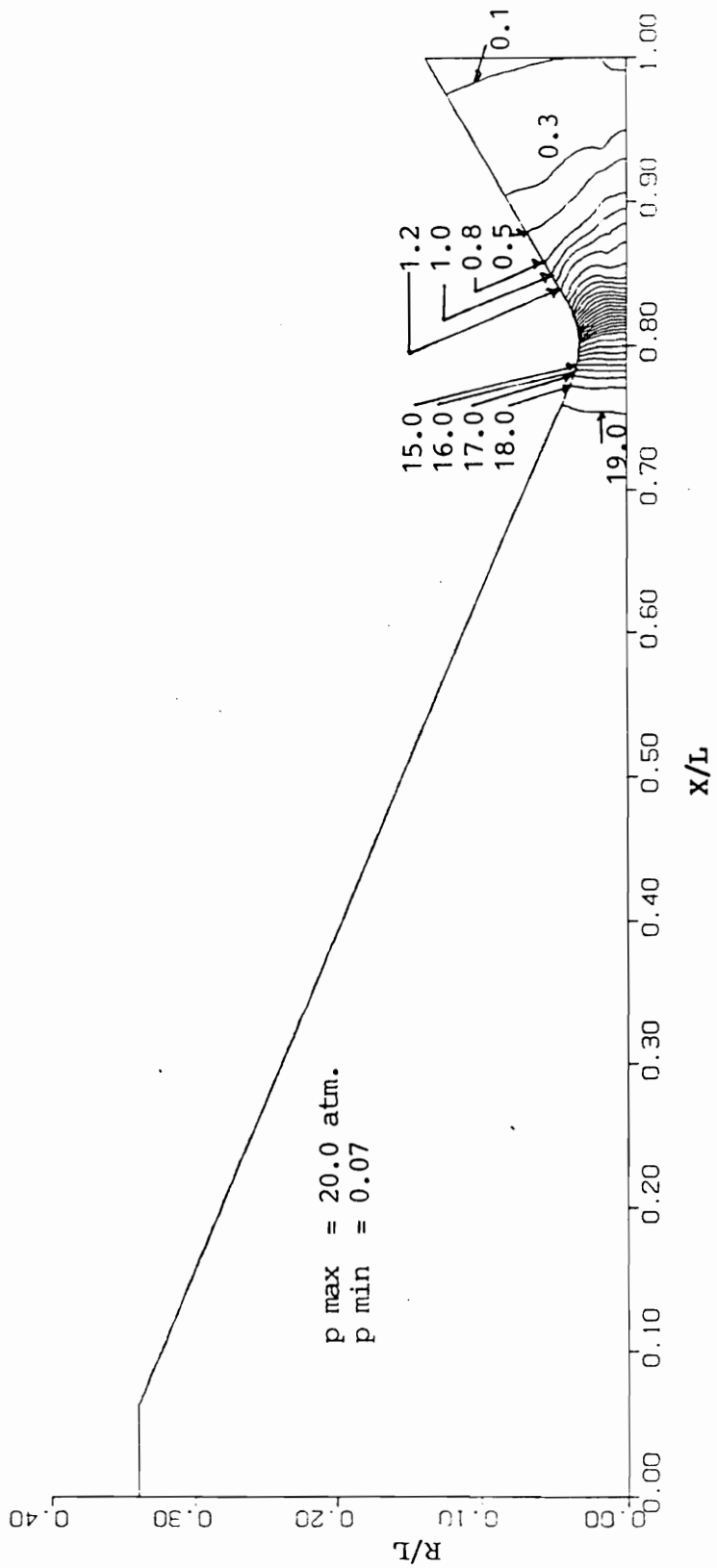

Figure 4.22. (e) Pressure contour, Case 20

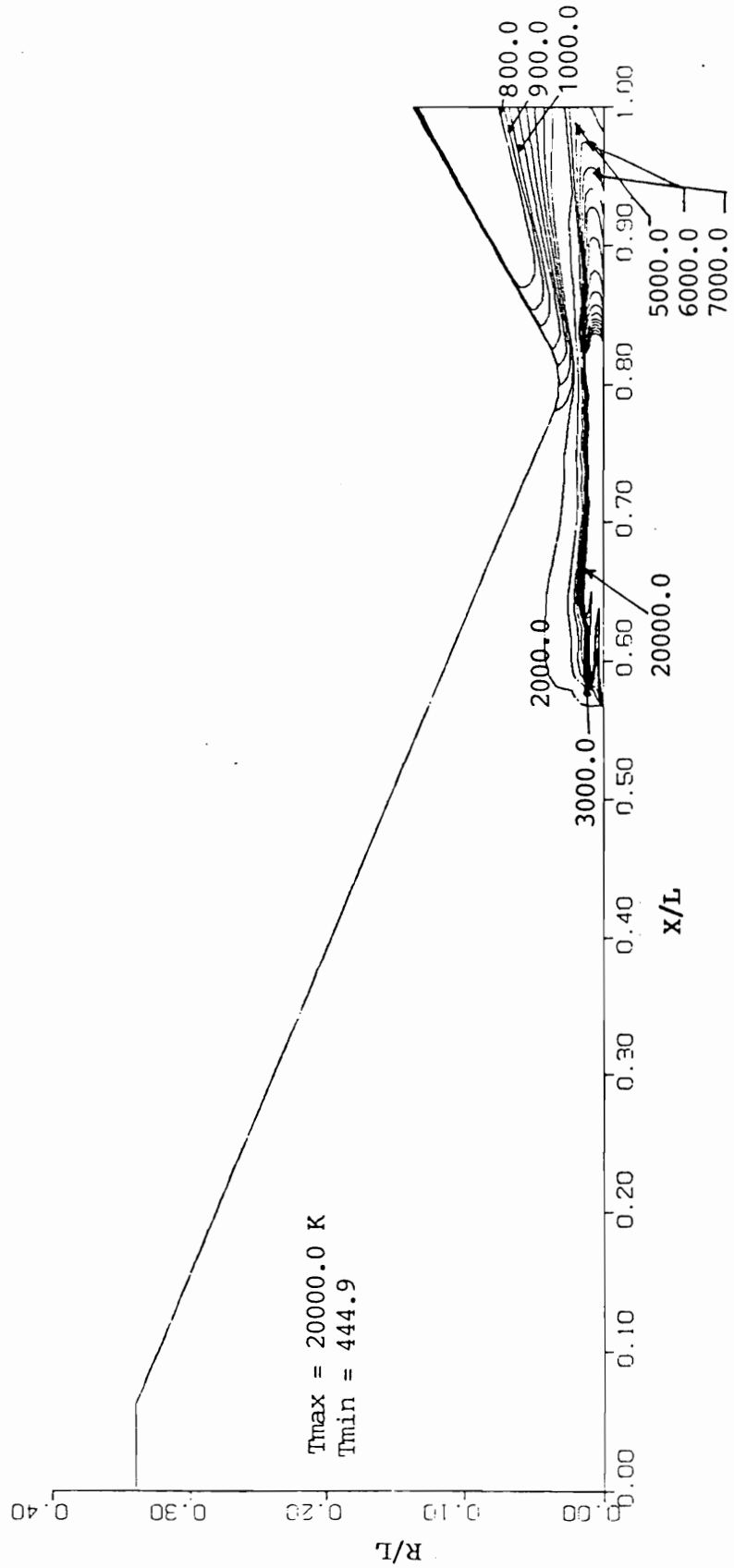

Figure 4.23. (a) Temperature contour, Case 21.

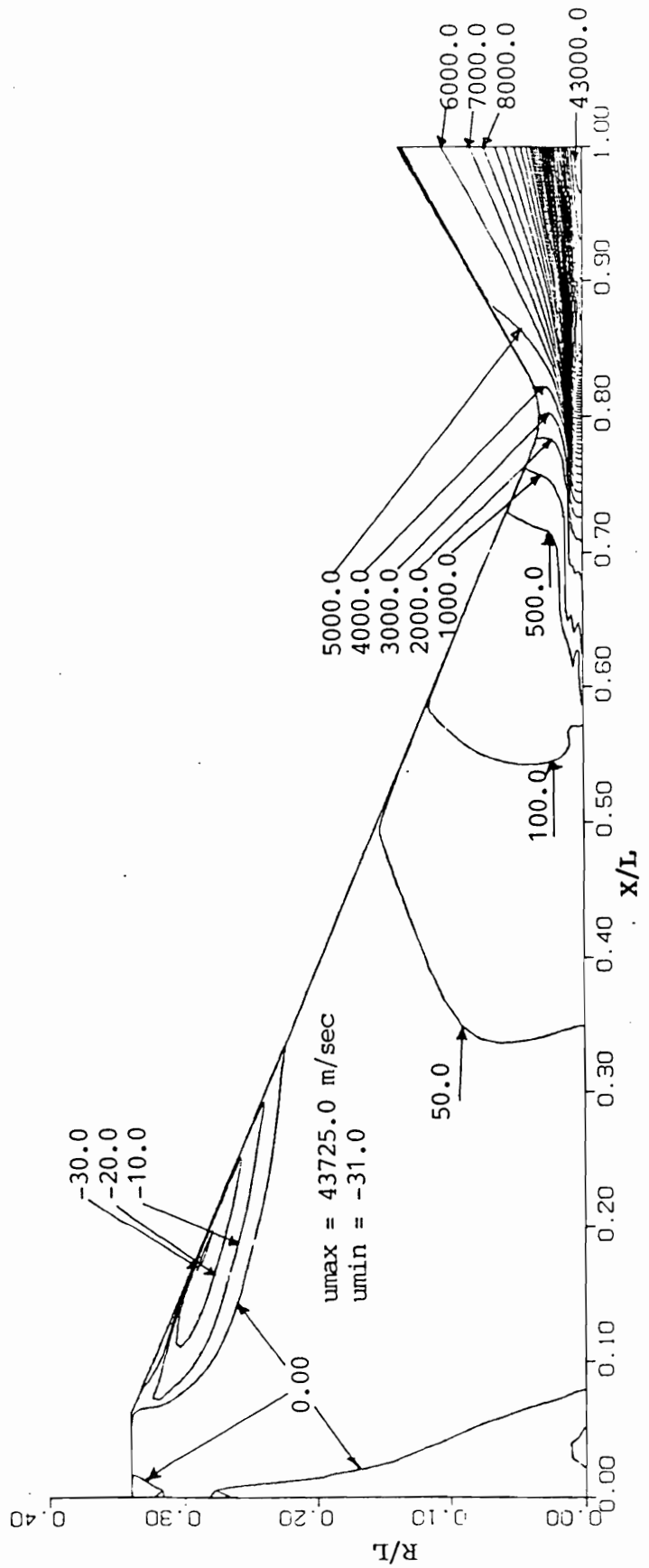

Figure 4.23. (b) u-velocity contour, Case 21

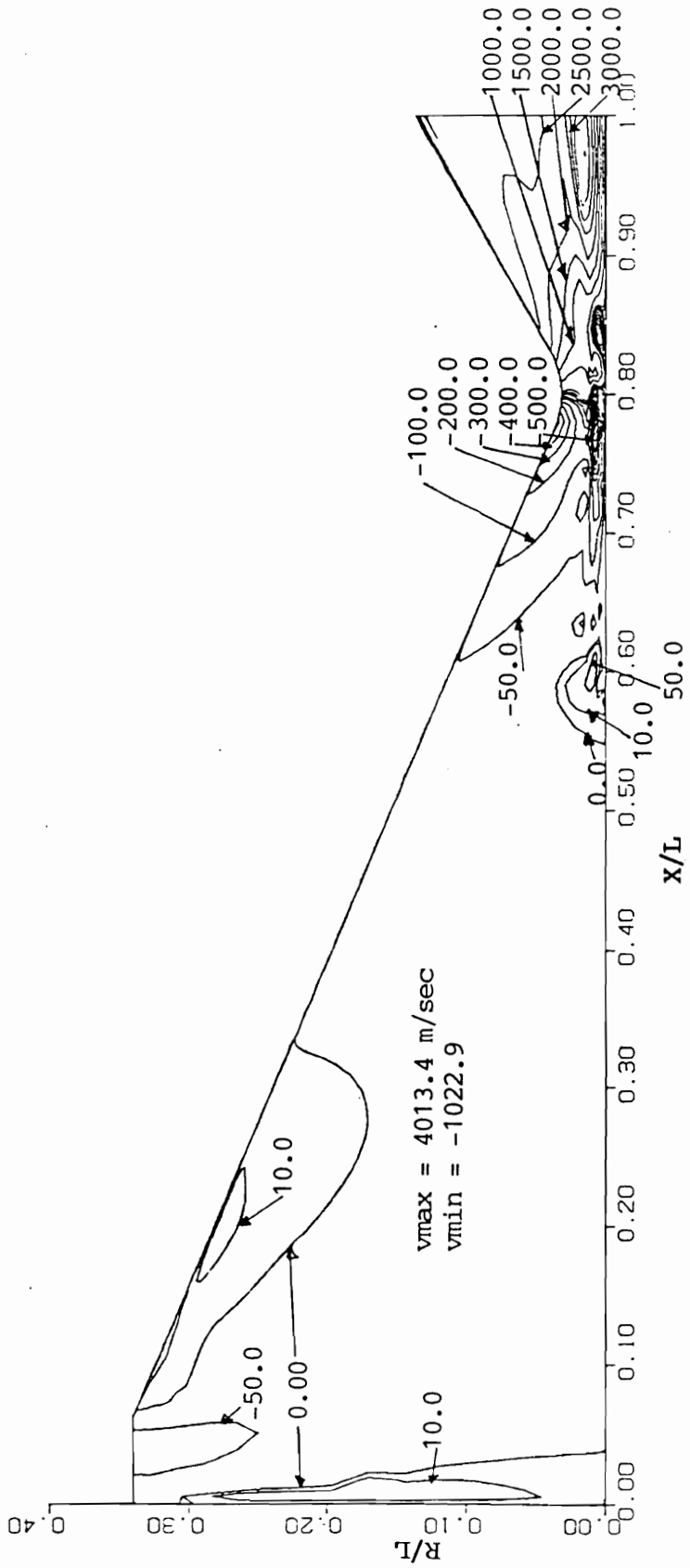

Figure 4.23. (c) v-velocity contour, Case 21

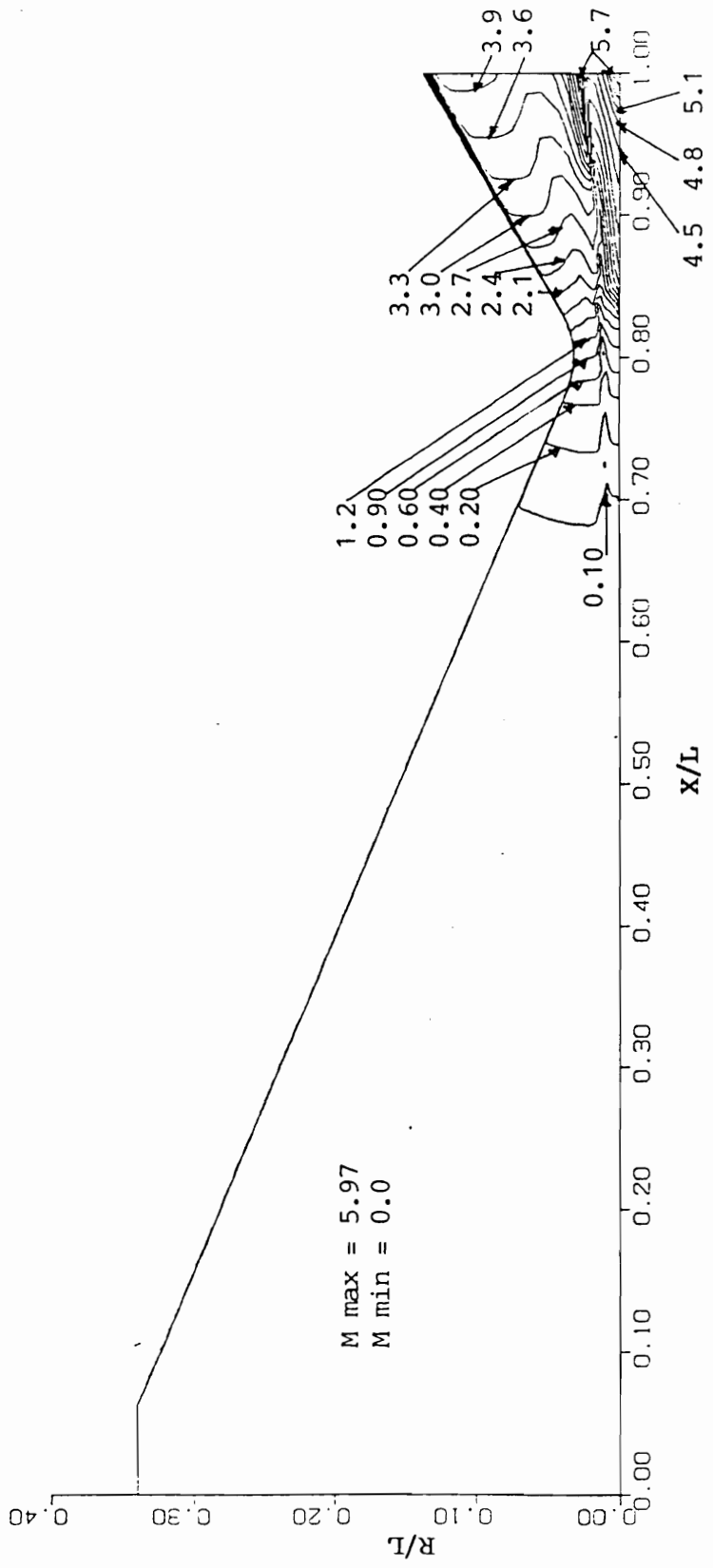

Figure 4.23. (d) Mach contour, Case 21

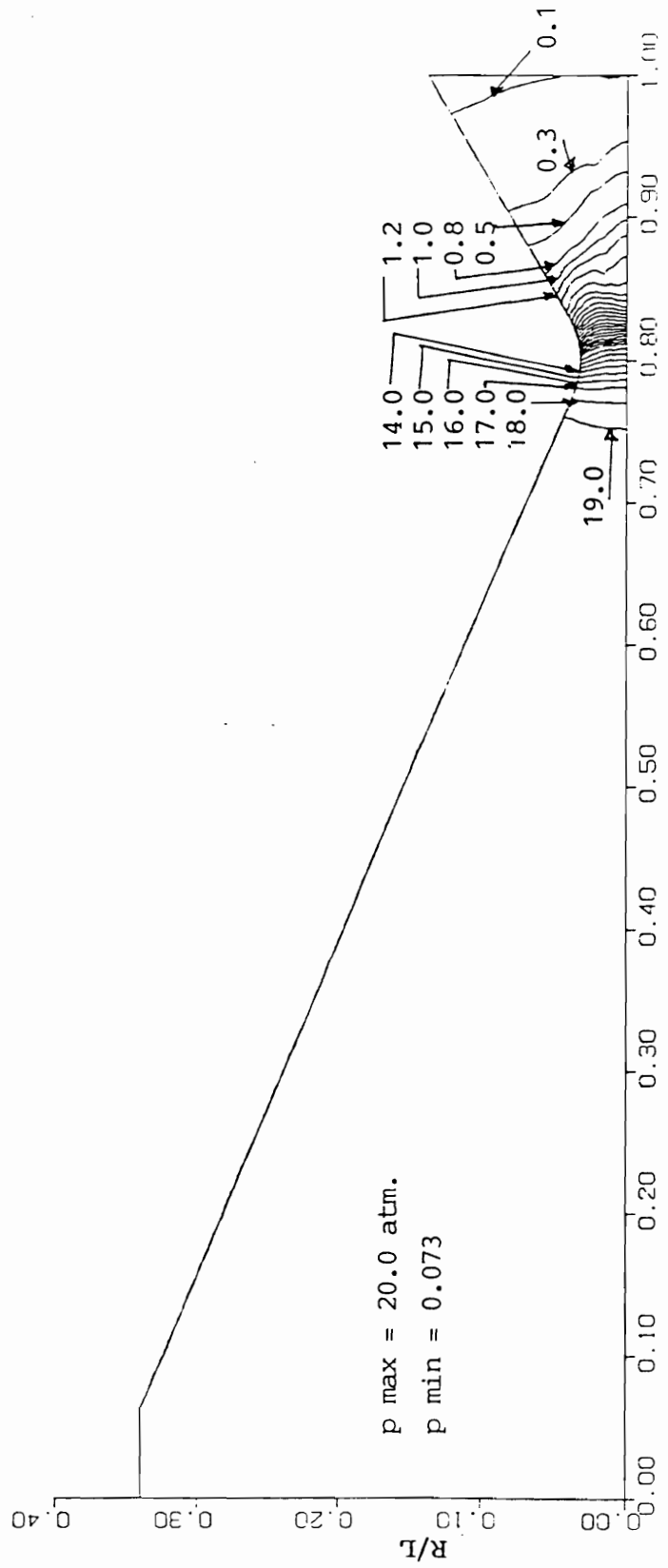

Figure 4.23. (c) Pressure contour, Case 21

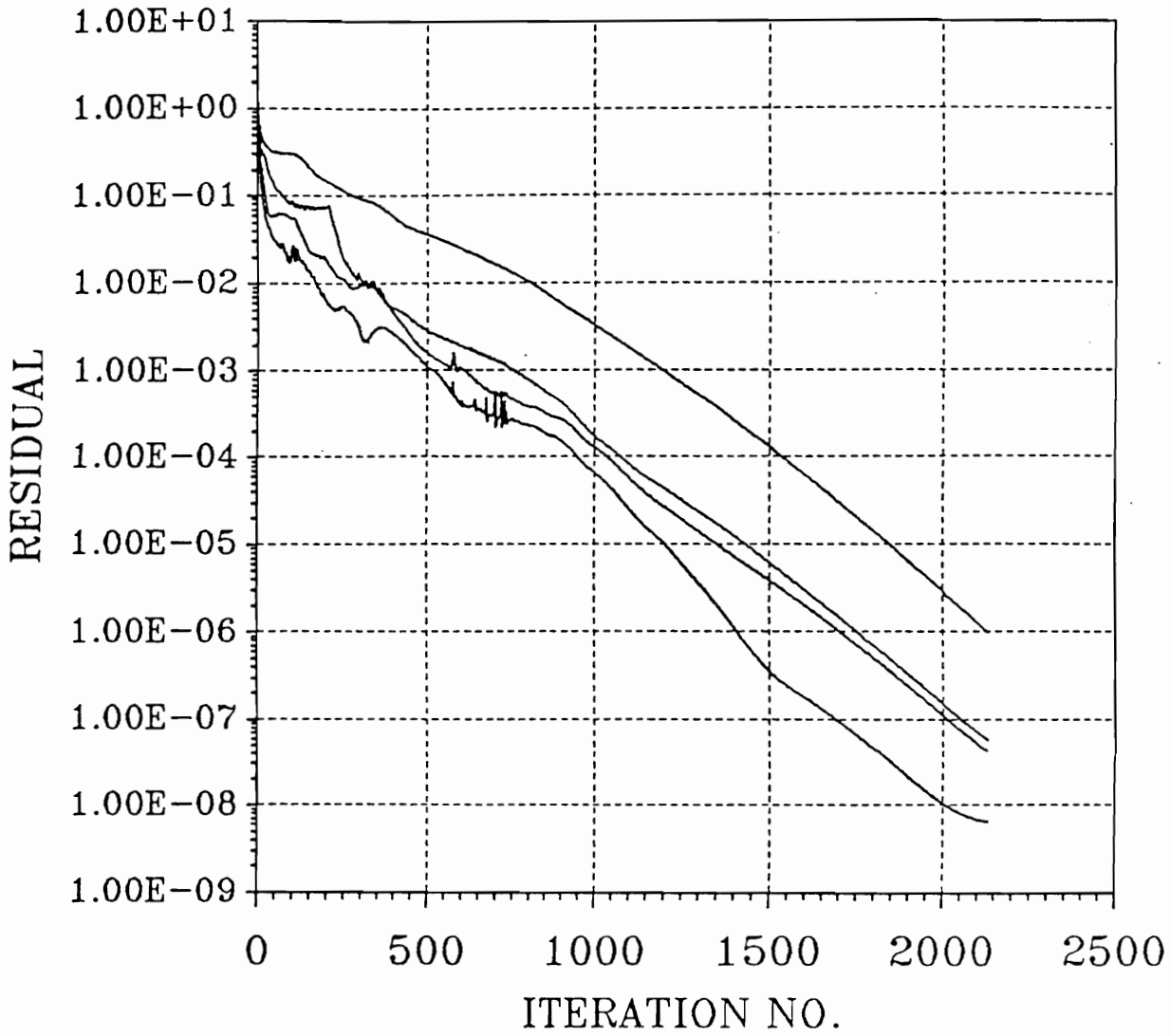

Figure 4.24. (a)Typical convergence history of the L_2 norm

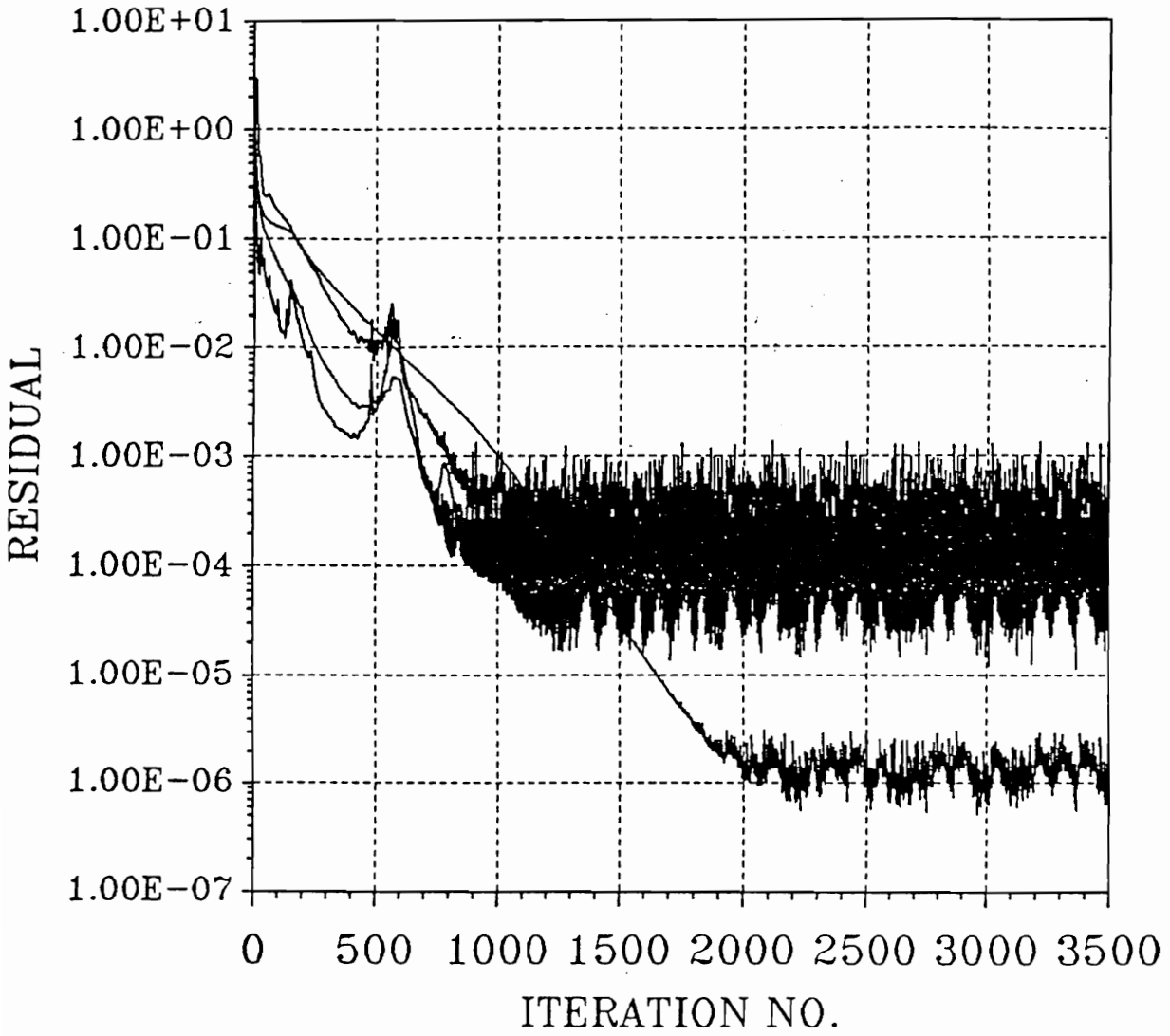

Figure 4.24. (b) Typical convergence history of the L_2 norm

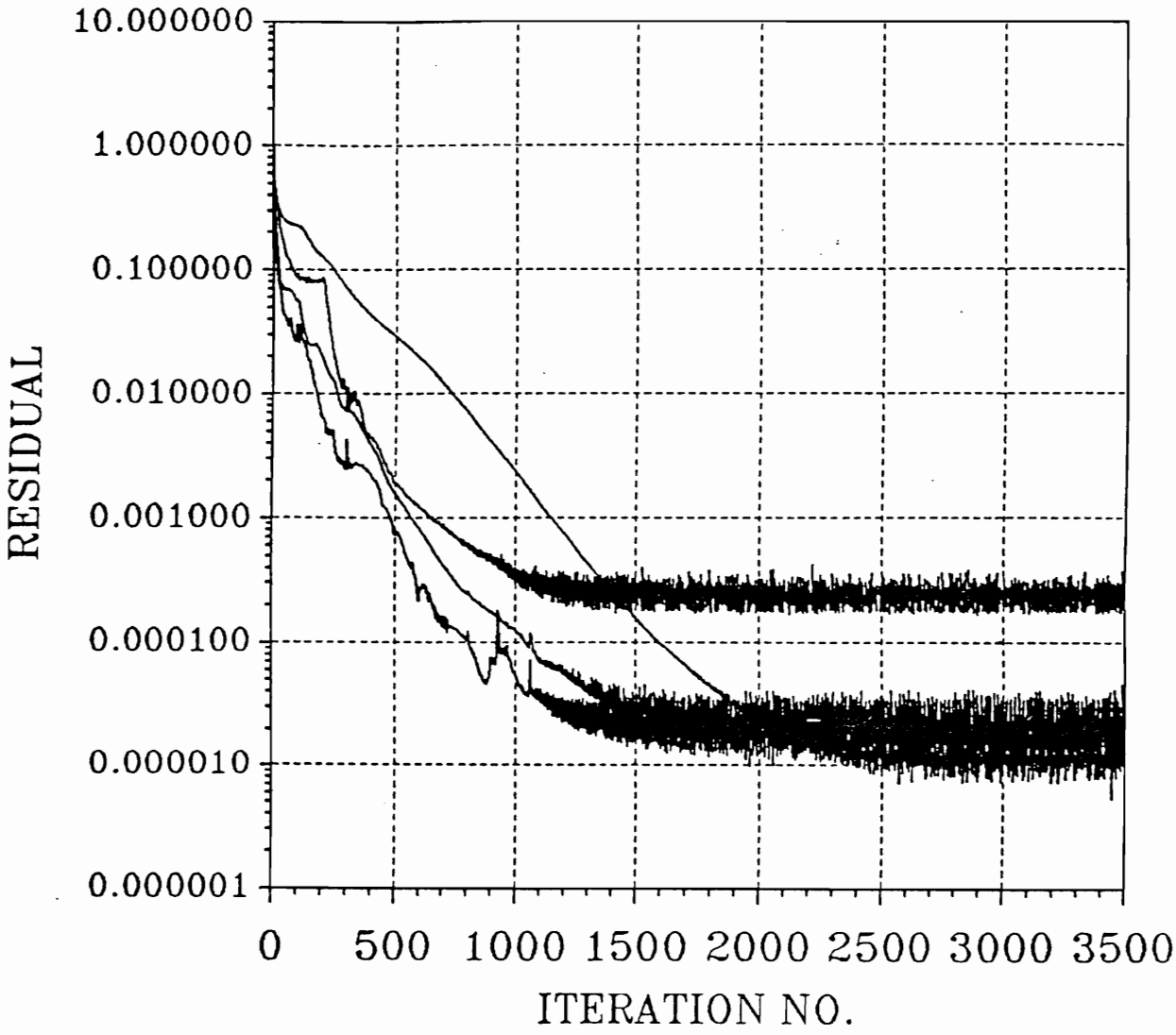

Figure 4.24. (c) Typical convergence history of the L_2 norm

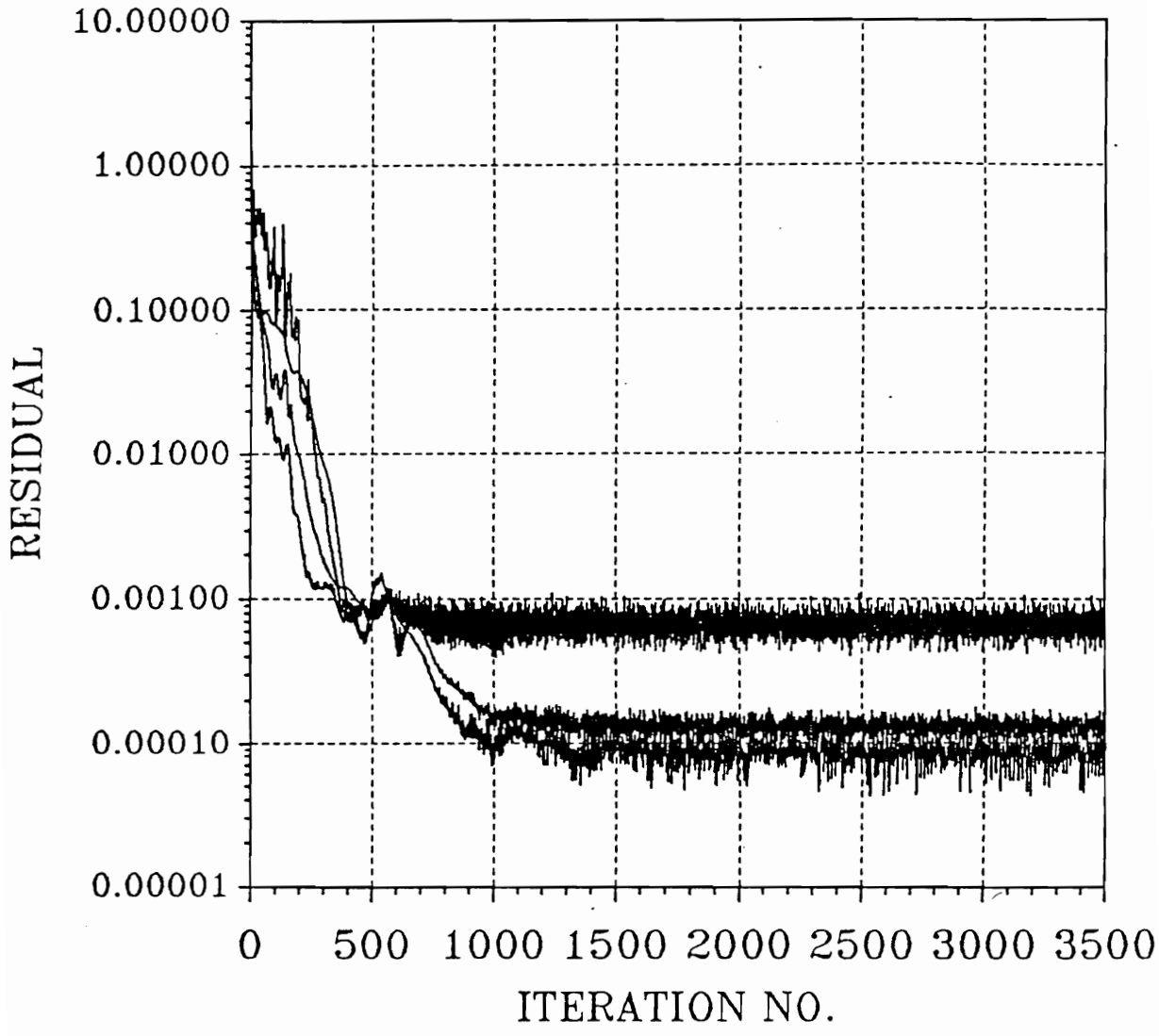

Figure 4.24. (d) Typical convergence history of the L_2 norm

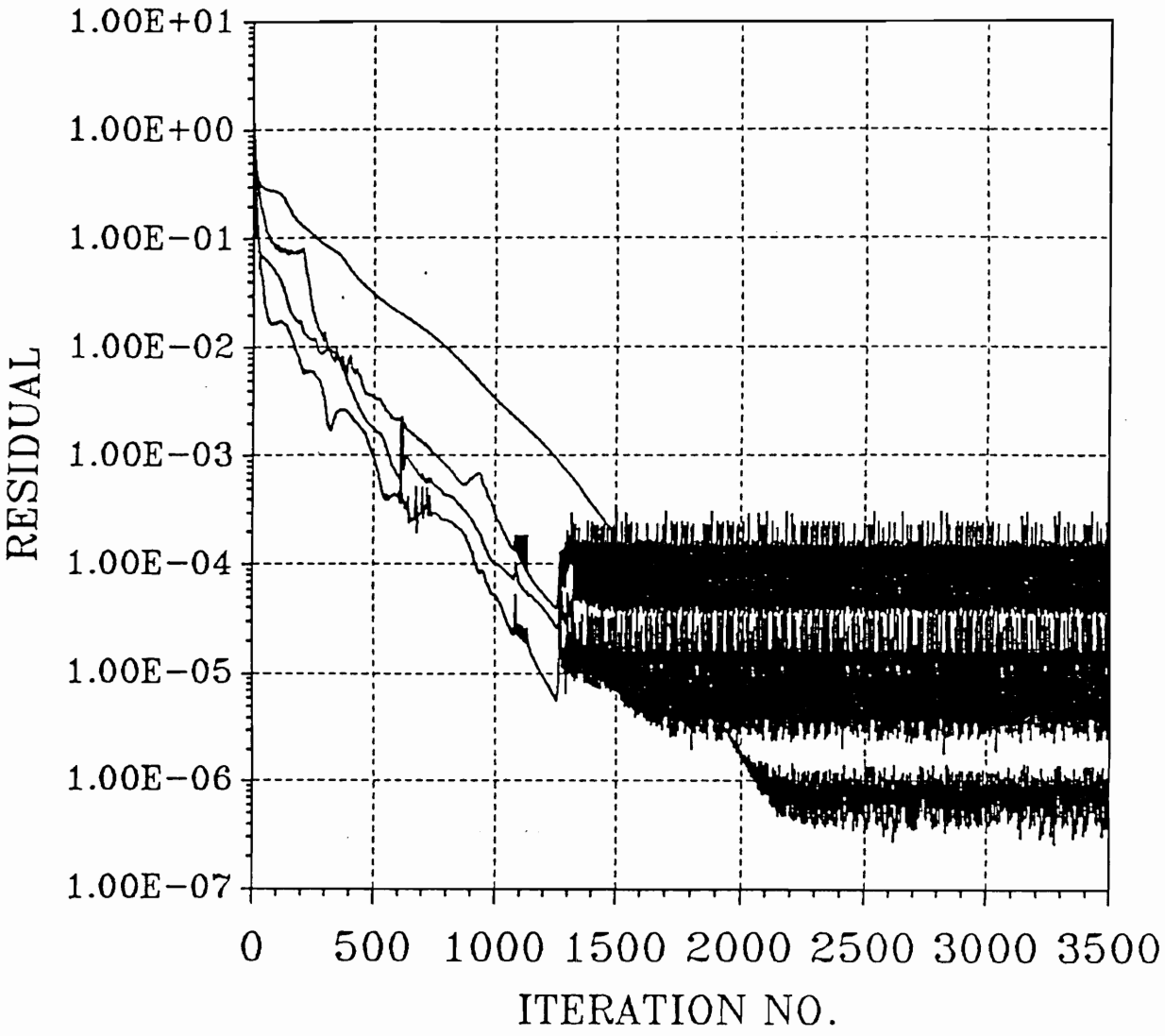

Figure 4.24. (e) Typical convergence history of the L_2 norm

Chapter V

CONCLUSIONS

5.1 Conclusions

A general calculation procedure for both incompressible and compressible flow in 2-D or axisymmetric geometries was introduced. The procedure utilized a primitive variables formulation on a non-staggered grid system. A pressure based Navier-Stokes solver (PBNS) was developed based on that procedure. The validation of the method was tested for a subsonic compressible flow over an insulated flat plate and for an axisymmetric converging- diverging nozzle. Test cases included equilibrium hydrogen as a flowing gas and different implementation of boundary conditions. The properties of hydrogen were calculated using the HPC code.

Next, the PBNS code was applied to analyze the laser-sustained plasma flow. Several numerical experiments were conducted using two basic thruster geometries with various dimensions, two laser types, and various laser power

levels and injection conditions. Based on the analysis of the computational results the following conclusions are drawn:

1. The pressure based algorithm is a flexible scheme capable of handling both incompressible and compressible flow problems in complex geometries with a non-staggered grid system.

2. The application of the PBNS solver to a subsonic compressible flow over an insulated flat plate successfully reproduced all of the essential flow features. The treatment of the boundary conditions is very important to the stability of the scheme. Special attention should be paid to the inlet flow. No difference was observed in the solution with Riemann invariant extrapolation, non-reflecting boundary or simple extrapolation of the velocity at a subsonic inlet.

3. The application of PBNS to an axisymmetric nozzle reproduced all the nozzle flow features include the recirculating region near the corner, and transition from subsonic flow to supersonic flow across the sonic line near the throat. Prediction of subsonic region near the wall at the exit plane must consider the behavior of the characteristics at the exit plane if an accurate simulation is required.

4. The inclusion of the equilibrium hydrogen code (HPC) and the laser beam into the nozzle flow analysis proved the ability of the PBNS code to handle

a complex laser-sustained plasma flow field. The application of PBNS to a laser thruster reproduced the key features of the flow field including laser power absorption, plasma formulation and radiation losses.

5. The PBNS calculations can be used for a preliminary selection of the laser engine configuration and design parameters.

6. The key element for achieving high performance for a laser engine is to guarantee good mixing between the hot core (20,000 K) and the cold gas off the center line of the engine.

7. The analysis of the injection conditions effects on the performance of laser engines showed that while the injection pressure has a great effect on the absorption process, the injection temperature has a negligible effect on the absorption of the laser power. As high as 100% absorption with a specific impulse of 1537 sec was calculated for a CO_2 laser at 10 atm. injection pressure in the thruster I. A pressure of 20 atm was needed for an iodide laser to produce about 40% absorption for a thruster having the same configuration. A specific impulse of 840 sec was calculated for this case.

8. Different laser types require different design considerations. An iodide laser beam produces slender plasmas and requires a longer nozzle with higher injection pressure than the CO_2 laser. The slender plasma reduces the radiation to the thruster walls.

9. As high as 7 MW radiation loss to the thruster walls was estimated for one of the test cases emphasizing the importance of wall cooling.

10. The predicted performance of the laser engines indicates that laser propulsion may become a strong candidate for certain propulsion missions. Its high specific impulse at different thrust levels can make a laser-OTV superior to a chemical-OTV.

5.2 Suggestions for Future Research

1. a. The PBNS code uses a power-law scheme for the discretization of the convective part in the Navier-Stokes equations. This scheme is first order upwind accurate for a Peclet number less than 10 and second order accurate for higher Peclet number. This implies that a diffusive part of the scheme will smear a shock wave. To have a better shock wave resolution, a Total Variation Diminishing (TVD) scheme could be applied for the discretization of the convective fluxes.

   b. To accelerate the convergence of the scheme a multi-grid technique can be implemented with the PBNS. This should cause a decay of short waves oscillations. Also, a conjugate-gradient solver can reduce the CPU time by eliminating the need for several Alternating Direction Implicit (ADI) sweeps that have been used in the PBNS.

c. An extension of PBNS to turbulent flow may be done by including a turbulent model such as a K- ε model. After solving the energy equation, the K and ε may be obtained by solving the appropriate equations for them. The new value of an eddy viscosity may then be estimated.

d. The extension of the PBNS solver to chemically reacting flow may be performed by including the conservation equations for the involved species. These equations can be solved using the same techniques used to solve the transport equation.

2. It has been suggested that the performance of the laser engines, may be improved by application of a multiplasma scheme shown in Fig. 6.1(a) [19], or a ring type plasma shown in Fig. 6.1(b). The performance of these engines can be analyzed by appropriately modified the laser energy solver in the PBNS code.

3. Theoretical predictions of the model presented here can be, perhaps significantly, improved by employing a more accurate model of the plasma radiation losses.

4. The presence of strong density gradients in the plasma core may cause strong refraction of the laser light rays. Incorporation of the refraction effects into the laser engine model will improve the theoretical predictions.

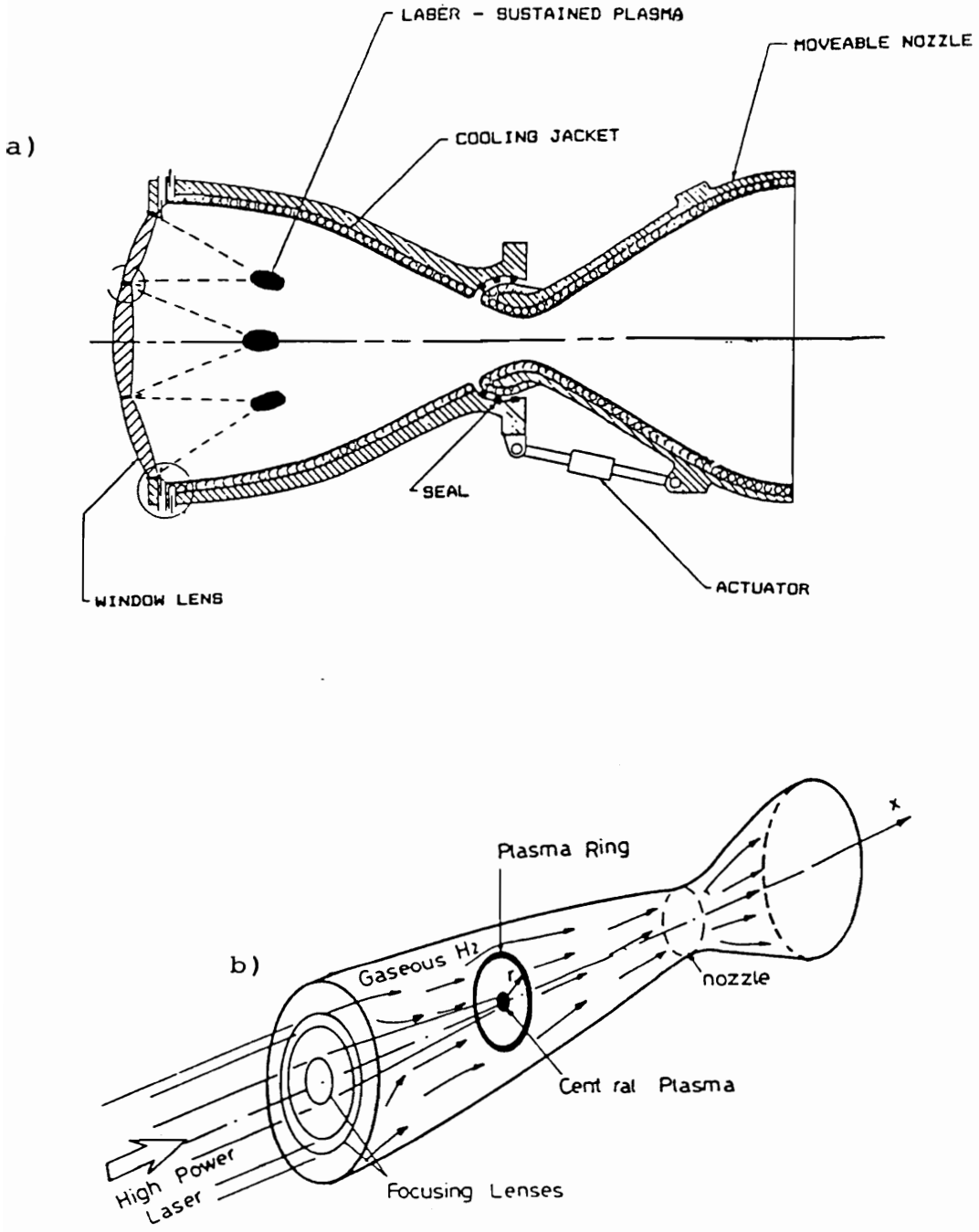

Figure 5.1. a)Multi-plasma configuration, b) Ring plasma configuration.

Appendix A. Thermodynamic Properties of Equilibrium Hydrogen

The thermodynamic properties of hydrogen (enthalpy, density, number densities and speed of sound) are calculated using the HPC code. The code is based on the model given by Kemp et al [41]. The main assumptions are:

1. Hydrogen is a mixture of perfect gases: hydrogen molecules, atoms, ions, and electrons, having the number densities of n_m , n_A , n_I and n_E , respectively. At the expected temperature ranges other species including multiple ionized atoms may be neglected. This implies that $n_I = n_E$.

2. Below a characteristic temperature(break down temperature) only atoms and molecules exist, above that temperature the gas is fully dissociated.

3. The hydrogen is in thermodynamic equilibrium.

A.1 Number density calculation

The fraction of dissociated molecules β and the fraction of ionized atoms α are given by

$$\beta = \frac{(n_A + n_I)/2}{n_M + (n_A + n_I)/2} \qquad \alpha = \frac{n_I}{n_A + n_I} \tag{A.1a,b}$$

The number densities of the species are given by

$$n_M = n_o(1 - \beta) \qquad n_A = 2n_o\beta(1 - \alpha) \qquad n_I = n_E = 2n_o\beta\alpha \tag{A.2a,b,c}$$

where $n_o = n_M + (n_A + n_I)/2$ is the original number of particles per unit volume. Using the assumption of perfect gas for each species, the partial pressure for species "i" is

$$P_i = n_i kT \tag{A.3}$$

where k is the Boltzmann constant. The partial mass density is expressed in terms of the particle masses m_i as follows

$$\rho_M = n_M m_M, \quad \rho_A = n_A m_A, \quad \rho_I = n_I m_I, \quad \rho_E = n_E m_E, \tag{A.4a,b,c,d}$$

The total number and mass density is

$$\sum n_i = n_o(1 + \beta(1 + 2\alpha)) \qquad \rho = n_o m_M \tag{A.5a,b}$$

Assume that $m_A = m_I = m_M/2$ is a good approximation for hydrogen atom. The equation of state for the mixture is

$$P = \sum P_i = \sum n_i kT = Zn_o kT \qquad (A.6)$$

where $Z = (1 + \beta(1 + 2\alpha))$ is the compressibility factor. Since $k = R_M m_M$, eq. (A.6) may be written as

$$P = Z\rho R_M T \qquad (A.7)$$

where R_M is the gas constant for the molecules.

Since we deal with thermodynamic equilibrium, the law of mass action can be used to estimate α and β . Two reactions have been used

Dissociation: $H_2 \rightleftarrows H + H$

Ionization: $H \rightleftarrows H^+ + E^-$

The relationship between the partial pressure ratio and the partition functions of the species involves the heat of reaction, and may be given as [42]

$$\frac{P_A^2}{P_M} = \left[\frac{\pi m_M}{H^2}\right]^{3/2} \frac{(kT)^{5/2} Q_{elA}^2}{Q_c Q_v Q_r Q_{elM}} \; e^{-h_D m_M/kT} \qquad (A.8a)$$

$$\frac{P_I P_E}{P_A} = \left[\frac{2\pi m_E}{H^2}\right]^{3/2} \frac{(kT)^{5/2} Q_{elI} Q_{elE}}{Q_{elA}} \; e^{-h_{IL} m_I/kT} \qquad (A.8b)$$

where; H is Planck's constant, Q_v and Q_r are the vibrational and rotational partition functions of H_2 , Q_c is the partition function for coupling the rotational and vibrational partition functions, Q_{eli} is the electronic partition function for species "i", h_D is the heat of dissociation of a molecule per unit mass, and h_{IL} is the heat of ionization of an atom per unit mass. From eq. (A.6) the partial pressure ratio is

$$\frac{P_A{}^2}{P_M} = \frac{4\beta^2(1-\alpha)^2}{1-\beta} \quad \frac{P}{Z} \tag{A.9a}$$

$$\frac{P_I P_E}{P_A} = \frac{2\beta\alpha^2}{1-\alpha} \quad \frac{P}{Z} \tag{A.9b}$$

The electronic partition function for the molecule can be given in term of its ground state statistical weight 1, since its first excited state lies very high (132,000 K). For the electron $Q_{elE} = 2$, because of the two electron spin states, and for the ion, there is no internal state, and $Q_{elI} = 1$. From the above values and the expression for the compressibility factor, the following relation may be derived

$$\frac{\beta^2(1-\alpha)^2}{(1-\beta)(1+\beta(1+2\alpha))} = \frac{f_d(T)}{P} \tag{A.10a}$$

$$\frac{\beta\alpha^2}{(1-\alpha)(1+\beta(1+2\alpha))} = \frac{f_I(T)}{P} \tag{A.10b}$$

where

$$f_D(T) = k\left[\frac{\pi m_A k}{H^2}\right]^{3/2} \frac{(T)^{5/2} Q_{elA}{}^2}{4 Q_c Q_v Q_r} \quad e^{-\theta_{D/T}} \qquad (A.11a)$$

$$f_I(T) = k\left[\frac{2\pi k m_E}{H^2}\right]^{3/2} \frac{(T)^{5/2}}{Q_{elA}} \quad e^{-\theta_{IL}/T} \qquad (A.11b)$$

$\theta_D = h_D m_M/k = 51970K$ is the characteristic temperature for dissociation, and $\theta_{IL} = h_{IL} m_I/k$ is the characteristic temperature for ionization. Equations (A.10) may be solved numerically for β and α. The hydrogen molecule dissociates almost completely before it ionizes significantly, thus the two reactions can be separated. Assume that α is small during the dissociation, while beta goes from 0 to 1, then β is near unity as α increases from near zero. The characteristic temperature is designated by T^* and is used to separate the two reactions. Its value may be obtained from table A.1.

The eq. (A.6) may be solved to give :

$$T \leq T^*: \quad \beta = (1 + P/f_D(T))^{-1/2}; \quad \alpha = \left[\frac{1+\beta}{\beta} \quad \frac{f_I(T)}{P}\right]^{1/2} \qquad (A.12a)$$

$$T > T^*: \quad \alpha = (1 + P/f_I(T))^{-1/2}$$
$$\beta = 1 - \left[\frac{(1-\alpha)^2}{1+\alpha} \quad \frac{P}{2f_D(T)}\right] \qquad (A.12b)$$

To complete the calculation of β and α, the partition function needs to be expressed in terms of temperature. The expressions for the partition functions may be obtained from spectroscopic data [41] . These expressions are lengthy and

need several iterations to be evaluated. Their evaluation had been embodied in the HPC code. After number densities of each species are estimated, the thermodynamic properties of the mixture may be evaluated.

A.2 Enthalpy, specific heat, and speed of sound

The enthalpy of the mixture is the sum of the species enthalpies weighted by their mass fractions and may given as

$$h = \sum_i h_i \rho_i / \rho \qquad (A.13a)$$

The transitional specific heats of atoms, ions and electrons are $5k/2$ per particle. For electrons and ions this is the total specific heat, thus

$$cp_I = 5k/2m_I \qquad cp_E = 5k/2m_E \qquad (A.14a,b)$$

We integrate the above expressions to obtain the enthalpies of ions and electrons. In addition, ions carry dissociation energy h_D , and ionization energy h_{IL} . Thus

$$h_I = (5k/2m_I)T + h_D + h_{IL} \qquad h_E = (5k/2m_E)T \qquad (A.15a,b)$$

The atoms have a transitional contributions of $5kT/2m_A$. They also carry dissociation energy and a contribution from the electronic state. The enthalpy of atoms is given by

$$h_A = (5k/2m_A)T + h_D + h_{IL}(1 - \frac{S_2}{S_1}) \qquad (A.16)$$

where

$$S_1 = \sum_{j=1}^{L} j^2 \exp(\theta_{IL}/TJ^2) \quad \text{and} \quad S_2 = \sum_{j=1}^{L} \exp(\theta_{IL}/TJ^2) \qquad (A.17a,b)$$

Here, L is the cut-off level, which may be obtained from Kemp et al [41]. The molecules have a transitional contribution of $5kt/2m_M$, rotational degrees of freedom, and vibrational contributions. Thus the enthalpy is given as

$$h_M = \frac{kT}{m_M}\left(\frac{7}{2} + \psi_v\right) \qquad (A.18)$$

$$\psi_v = \frac{\theta_v/T}{e^{\theta_v/T} - 1} \qquad (A.19)$$

The mass fraction may be obtained in terms of α and β

$$\frac{\rho_M}{\rho} = 1 - \beta \quad \frac{\rho_A}{\rho} = \beta(1-\alpha) \quad \frac{\rho_I}{\rho} = \beta\alpha \quad \frac{\rho_E}{\rho} = \beta\alpha(m_E/m_I) \qquad (A.19)$$

Substituting in eq. (A.13), the total enthalpy may be obtained. In low temperature regions, only atoms and molecules are considered. Thus for $T \leq T^*$, we may write

$$h = \frac{5kT}{2m_A}\left[(0.7 + 0.2\psi_v)(1-\beta) + \beta(1 + 0.2\theta_D/T)\right] \qquad (A.20)$$

In the higher temperature region, the molecules will be fully dissociated , i.e. , $\beta = 1$. Thus, for $T > T^*$

$$h = \frac{5kT}{2m_A}\left[1 + \alpha + \frac{0.2\theta_D}{T} + \frac{0.4\theta_I}{T}\left[1 - (1-\alpha)\frac{S_2}{S_1}\right]\right] \qquad (A.20)$$

The equilibrium's specific heat is obtained by a differentiation of the above expressions with respect to T at a constant pressure. The expressions for the specific heat may be found in [63].

The speed of sound may be obtained from the second law of thermodynamics as

$$a^2 = \left(\frac{\partial p}{\partial \rho}\right)_s = \left[\left(\frac{\partial \rho}{\partial p}\right)_T - \frac{1}{cpT}\left(\frac{\partial \rho}{\partial T}\right)_p^2\right]^{-1} \qquad (A.20)$$

Evaluation of the derivatives may be found in [41].

Determination of the shifting temperature is summarized in the following Table [41].

Table A.1. Shifting temperature of ionization for hydrogen

pressure (atm)	1	3	10	30	100
$T^*(10^3)$	7.3	8	9	10	11

The following curve fitting may be used [41]

$$T^* = 2000 \log(P(atm)) + 7000 \qquad (A.21)$$

The calculations discussed in this Appendix have been implemented in the HPC code. Figure A.1 shows the variation of the enthalpy with temperature for a pressure range of .1 atm to 30 atm, which is the operating range of the laser engine. Figures A.2 and A.3 represent results of the specific heat and speed of sound calculations. Comparison of the results with data obtain by Patch [63] shows good agreement. The code calculates accurately the thermodynamic properties of equilibrium hydrogen over wide ranges of temperature and pressure.

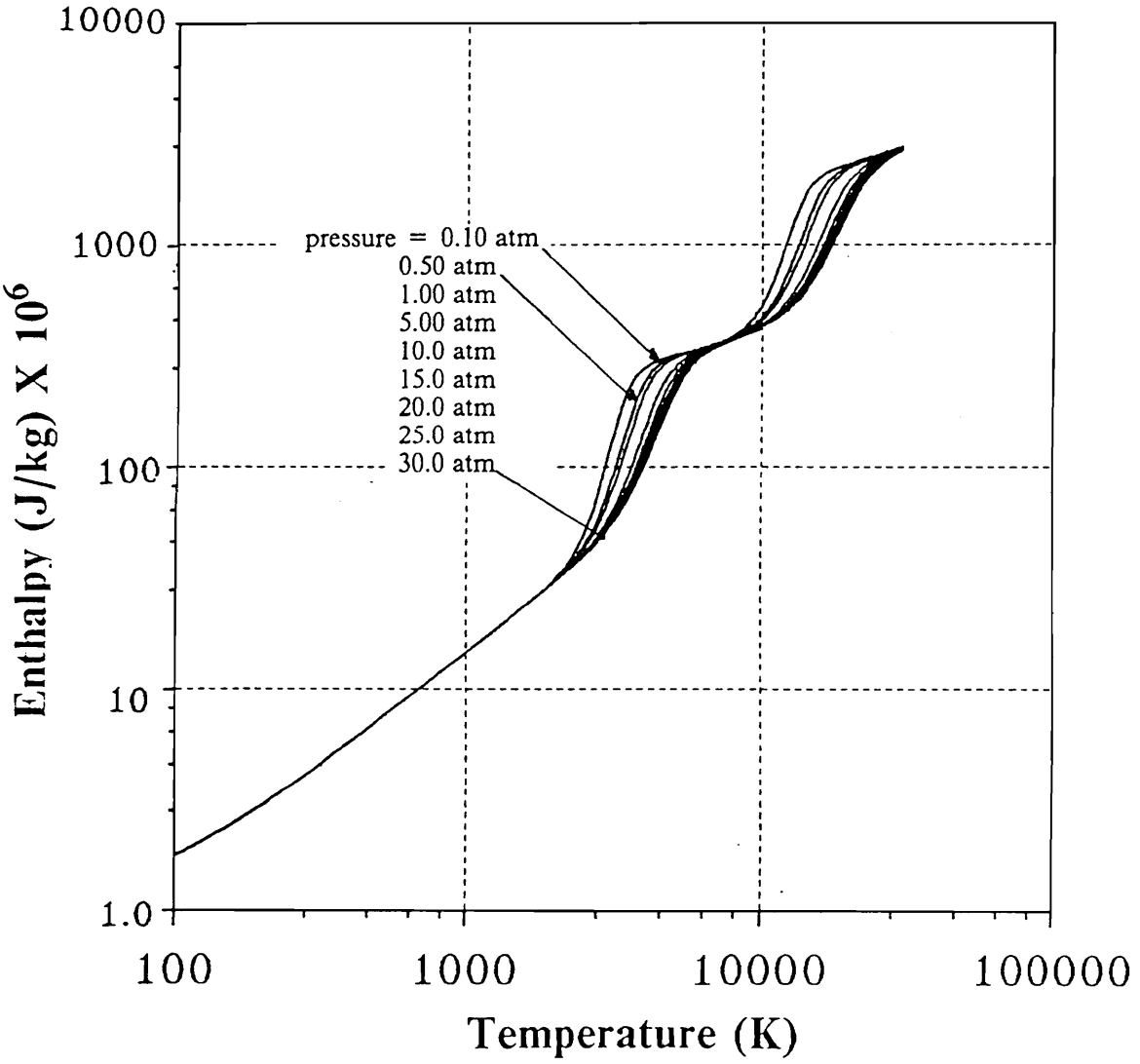

Figure A.1. Enthaply variation with temperature for different pressures.

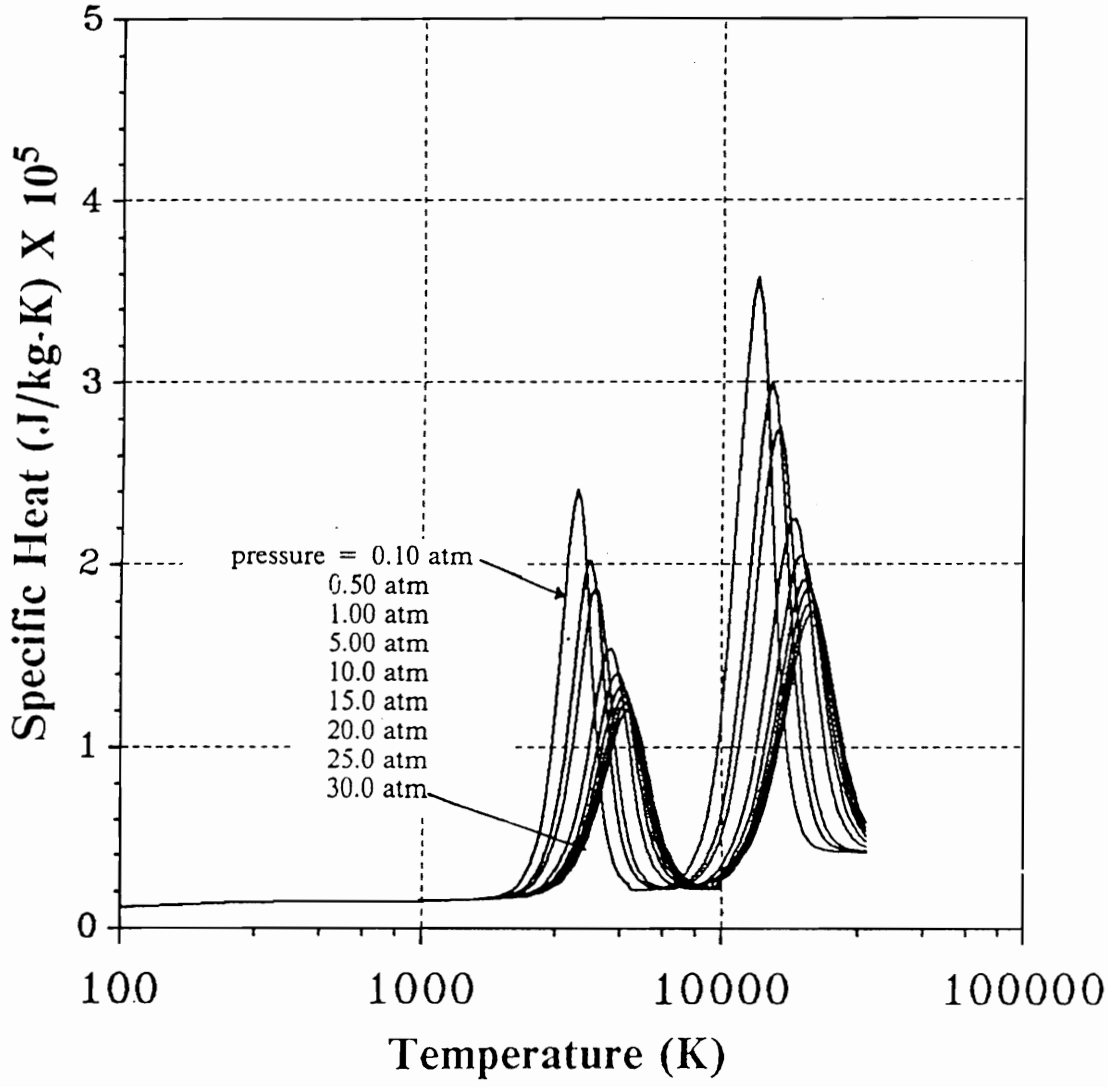

Figure A.2. Specific heat variation with temperature for different pressures.

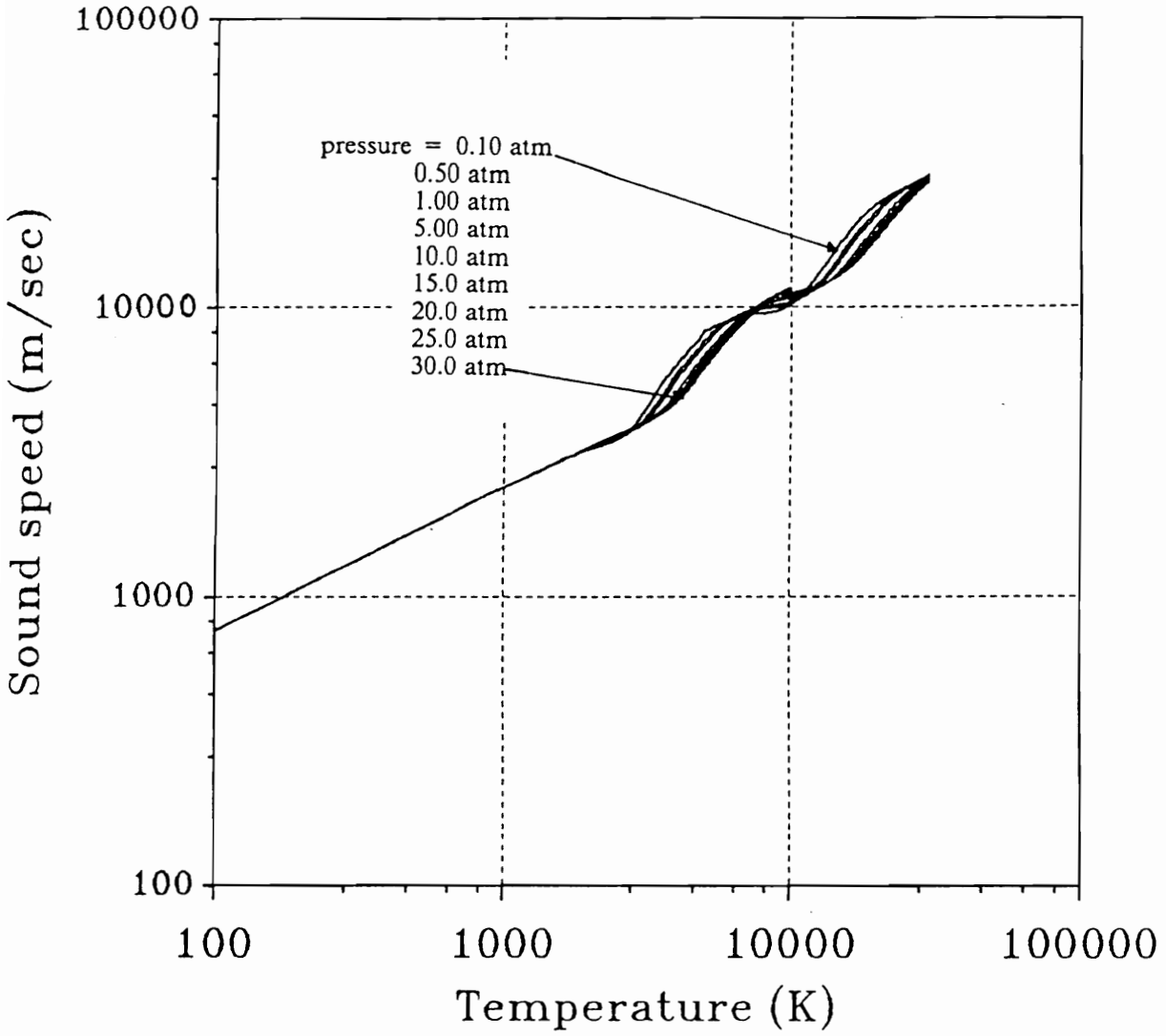

Figure A.3. Speed of sound variation with temperature for different pressures.

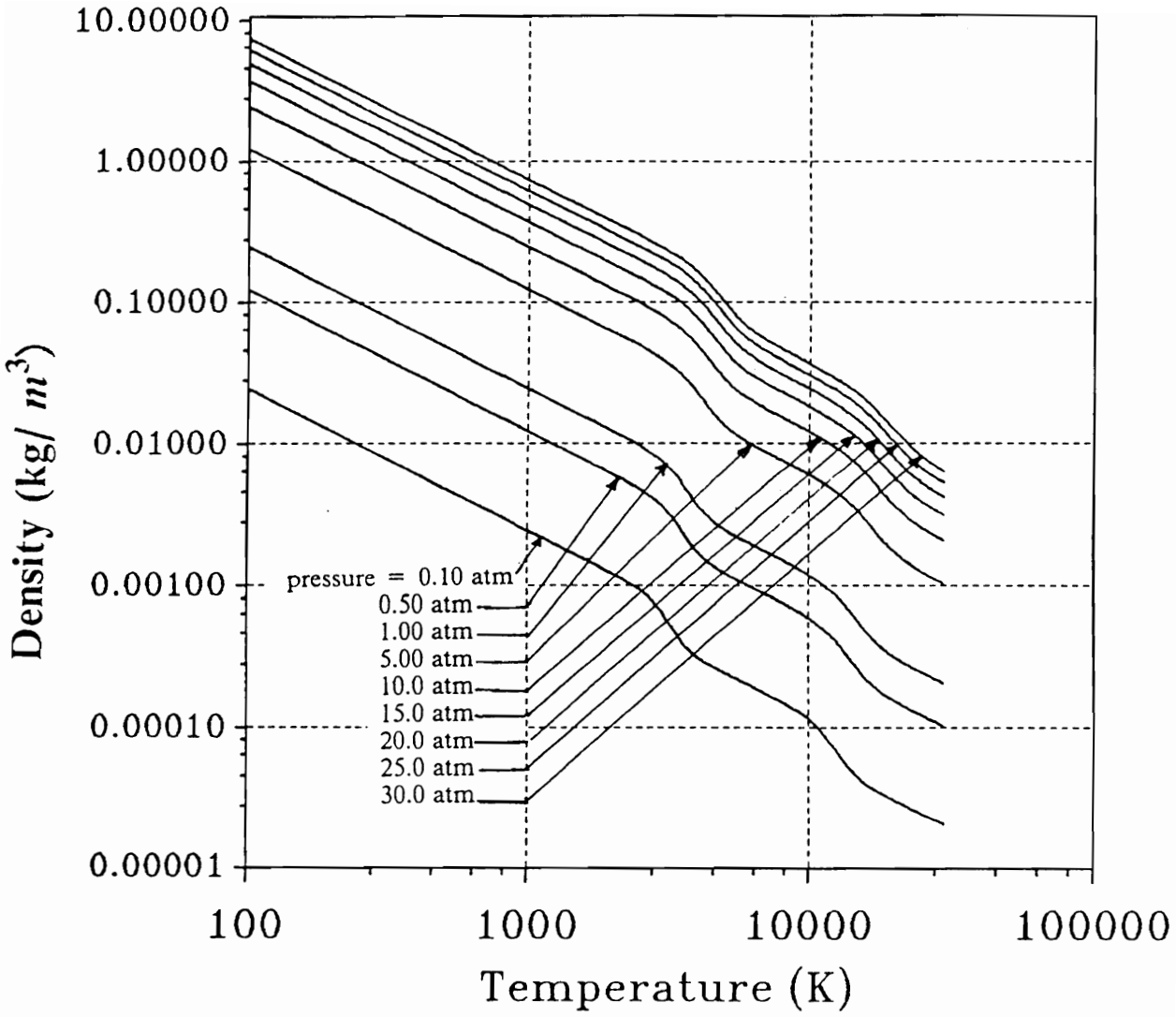

Figure A.4. Density variation with temperature for different pressures.

Appendix B. Absorption of Laser Energy

The main mechanism of the laser beam energy absorption in a laser engine is the inverse Bremsstrahlung involving both electron-ion and electron-neutral species, as discussed in Chapter I. The calculations of the absorption coefficient are based on a model given by Kemp et al [41].

The electron-ion absorption coefficient is given as

$$\alpha_{EI} = \sigma_{EI} n_E n_I [\exp(H\gamma/kT) - 1] \qquad (B.1)$$

where σ_{EI} is the electron-ion absorption cross- section, and γ is the laser wave frequency. Substituting for the value of σ_{EI}, the absorption coefficient for electron-ion becomes

$$\alpha_{EI} = \frac{36.96 \times 10^{-3}}{(\gamma^3/\sqrt{T})} n_E n_I (e^{47.98910^{-12}\gamma/T} - 1) \qquad (B.2)$$

Also, the electron-neutral absorption coefficient [41]

$$\alpha_{EN} = \sigma_{EN} n_E n_A (1 - \exp(H\gamma/kT)) \qquad (B.3)$$

where σ_{EN} is the electron-neutral absorption cross- section. Substituting for the value of σ_{EN}, we obtain

$$\alpha_{EN} = 1.275 \times 10^{-21} \frac{\sqrt{T}}{\gamma^2} \exp\left[-0.0122\sqrt{T}\,(1 - 5.28 \times 10^{-4}\sqrt{T}) \right] n_E n_A \qquad (B.4)$$

The total absorption is given as sum of eqs. (B.2) and (B.4)

$$\alpha' = \alpha_{EI} + \alpha_{EN} \qquad (B.5)$$

The n_E, n_I, n_A are the electron, ion and neutral number densities and are functions of pressure and temperature for equilibrium hydrogen and may be calculated as explained in Appendix A.

This study considered both the CO_2 laser ($10.16\mu m$) and iodide laser ($1.315\mu m$) as power source. Figure B.1 shows the values of the absorption coefficient for iodide laser at pressures of 5, 10, and 15 atm, and absorption coefficients for CO_2 laser at pressures of 0.5 and 1 atm. Comparing these values, we can see that, by significantly increasing the working pressure, the absorption of iodide laser beam energy can approach absorption values displayed by a CO_2 laser engine. for an iodide laser thruster. Figure B.2 shows the variation of the absorption coefficient for iodide laser for a pressure range from .1 atm to 30 atm. It is clear that almost no absorption occurs at temperatures below 10,000 K. The absorption reaches its maximum at a temperature of about 20,000 K.

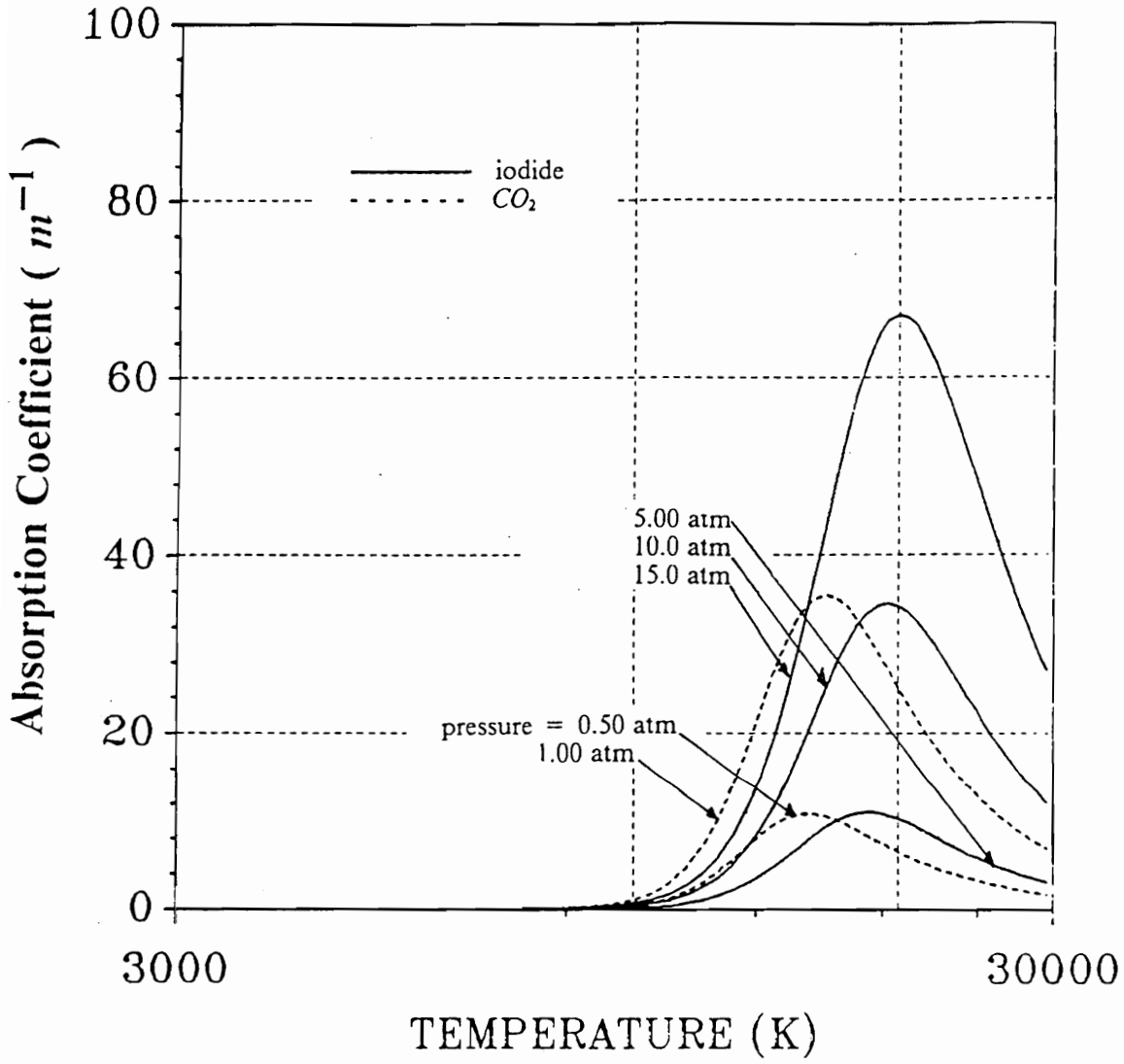

Figure B.1. Absorption coefficient for CO_2 and iodide laser.

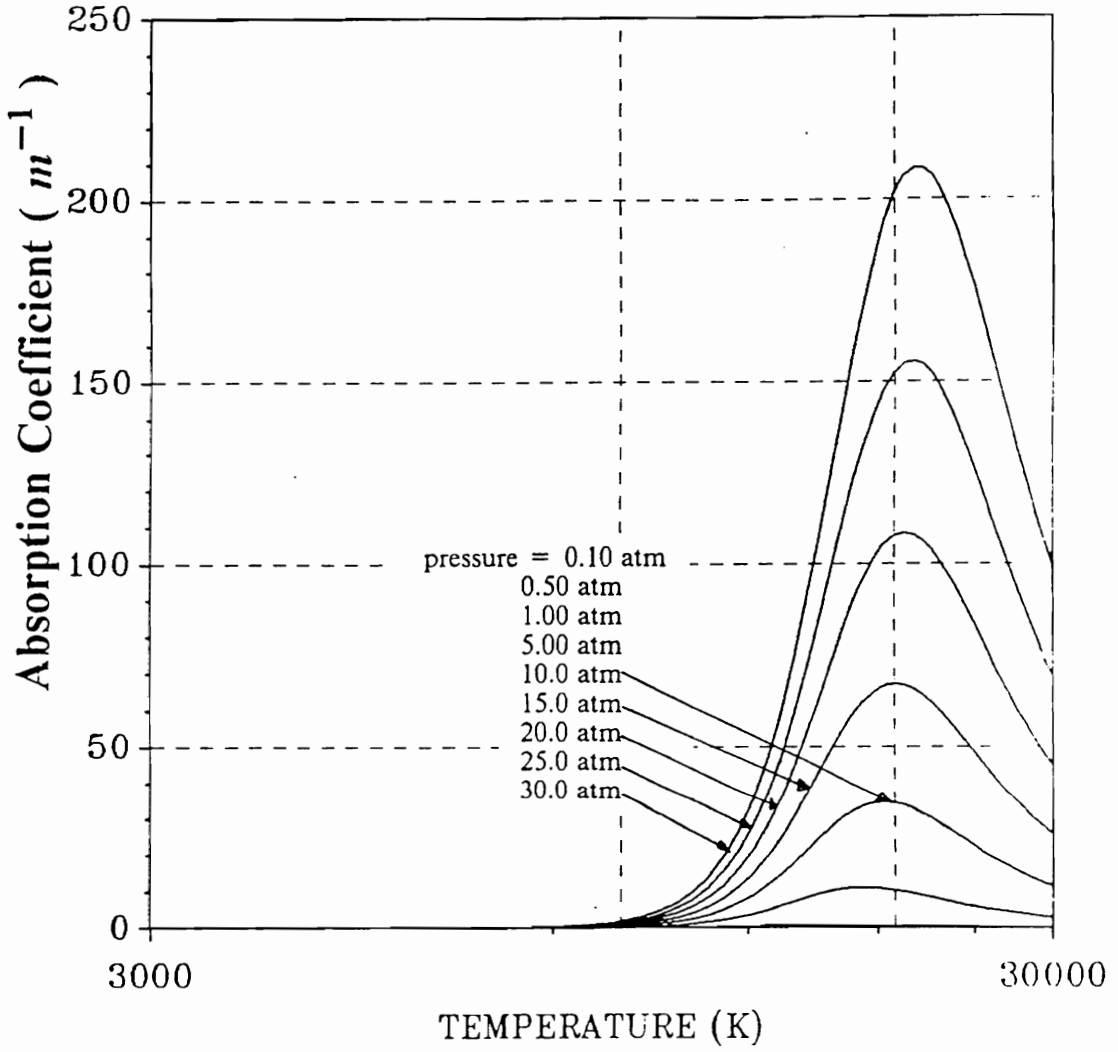

Figure B.2. Absorption coefficient variation with temperature at different pressures for iodide laser.

Appendix C. Radiative Model of the Hydrogen Plasma

The radiation loss from hot hydrogen has a very important effect on the formation of plasma and engine efficiency. This study follows closely the assumptions of Kemp's model [41]. The radiation is divided into two parts: the optically thin plasma where radiation escapes from the plasma and is considered as a loss in the energy equation, and the optically thick plasma where the heat is transferred to the cold gas diffusively.

C.1 Radiation loss from bulk plasma (optically thin)

The following radiation transitions are expected to occur in the operation range of a laser engine

1. Capture of free electron by an ion.

2. Bremsstrahlung involving electron-ion.

3. Bremsstrahlung involving electron-atom.

4. Radiative decay of an excited atom.

The first three types of transitions involve continuum emission which can be estimated using semiclassical theory correction for the quantum effect [41]. A line emission is more complex to determine and still under investigation. Kemp developed an expression for the power lost based on semiclassical theory. The results were fitted into an expression for power lost per unit volume for different chamber pressures and plasma radii. Estublier had studied the plasma radiation from elliposid shape plasma in a laser engine chamber [14]. He included the line radiation and obtained detailed estimates for radiation power from the hot plasma.

The HPC code adapted Kemp's model as its simplicity makes it an attractive approximation for the already complex model of the laser engine flowfield. The model was shown to give good agreement with some experimental data obtained for argon flow in laser engines. The total radiation loss per unit volume is given by [41]

$$q = 17.2 \times 10^{-}9(\frac{C_3 T}{\theta})(\frac{T}{\theta} + C_2)(\frac{n_A}{Q_{el}})e^{-\theta/T} \qquad (C.1)$$

where C_2 and C_3 are constants which depend on the pressure and the laser power and may be obtained from Ref. [41]. Q_{el} is the partition function for electron excitation as given in Appendix A.

Figure C.1 shows the radiation loss per unit volume, in W/m^3 for different pressures. It is interested to notice that the peak value occurs near the peak value of absorption.

C.2 Radiation transfer to cold gas (optically thick)

The hot hydrogen plasma emits radiative energy in the ultra-violet portion of the spectrum, and cool gas is expected to absorb this radiation. A model assuming that this radiation transport may be approximated by conductive radiation has been shown to give good results for plasma in air flow [41]. The model defines radiative conductivity coefficient as

$$K_r = \frac{0.775 \times 10^{30}}{T^2} \frac{Q_{ela}}{n_A} 7! \frac{e^{\frac{150865}{T}}}{(11605/T)^8} \sum_{k=1}^{7} \frac{(150865/T)^k}{k} \qquad (C.2)$$

Kemp modifies this coefficient to include radial conduction term for finite radius plasma. His modified formula has been employed in the HPC code for the calculation of the total thermal conductivity.

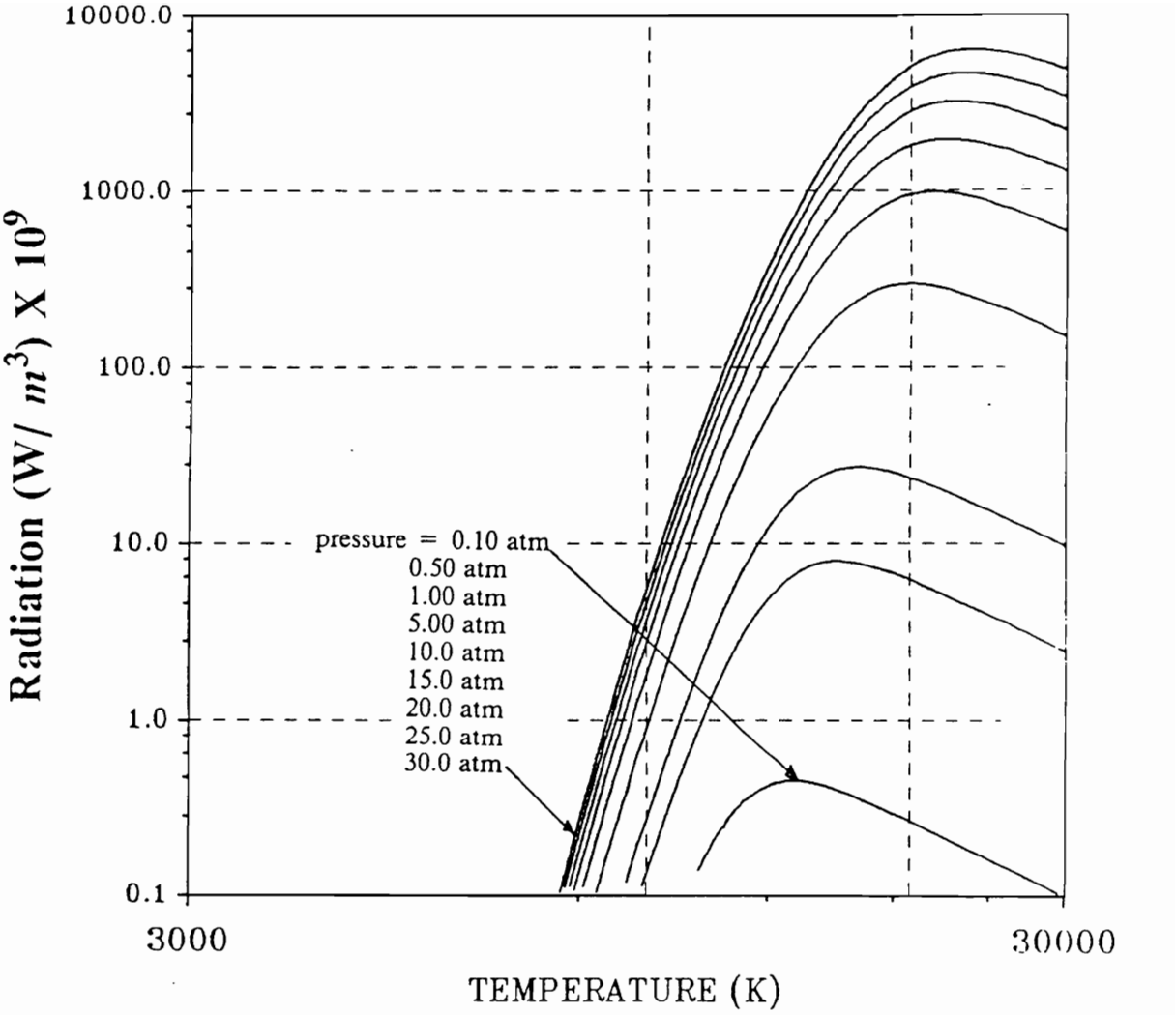

Figure C.1. Volumetric radiation variation with temperature for different pressures.

Appendix D. Hydrogen Transport Properties

Grier [22] has provided a theoretical model for both the viscosity and conductivity of hydrogen for a wide range of temperatures (5000 to 40000 K) and pressures (10^{-5} to 100 *atm.*). The HPC code uses these data to estimate the viscosity and conductivity and uses linear interpolation to find the intermediate values for a given pressure and temperature.

D.1.1 Viscosity

At temperatures below 5000 K, the viscosity is nearly independent of pressure and is calculated from data given in Reference [27]. For the temperatures above 5000 K, the dependency on both pressure and temperature is provided by the data of Grier [22] . Figure D.1 shows the results of these calculations.

D.1.2 Thermal conductivity

Data from reference [27] is used to calculate the thermal conductivity at temperatures below 1000 K. For temperature range of 1000 to 5000 K, data

provided by Yos [41] is used and the dependency on the pressure is included. Above 5000 K, Grier model [22] is used to calculate thermal conductivity. The intrinsic thermal conductivity obtained by these data must be modified to account for the absorption of radiation in the cold gases as in Appendix C. Thus we consider the effective conductivity as

$$K_{eff} = K_c + K_r \qquad (D.1)$$

where K_c is the intrinsic thermal conductivity obtained from Grier, and K_r is the radiative thermal conductivity given in Appendix C. Figure D.2 presents the values of the intrinsic conductivity.

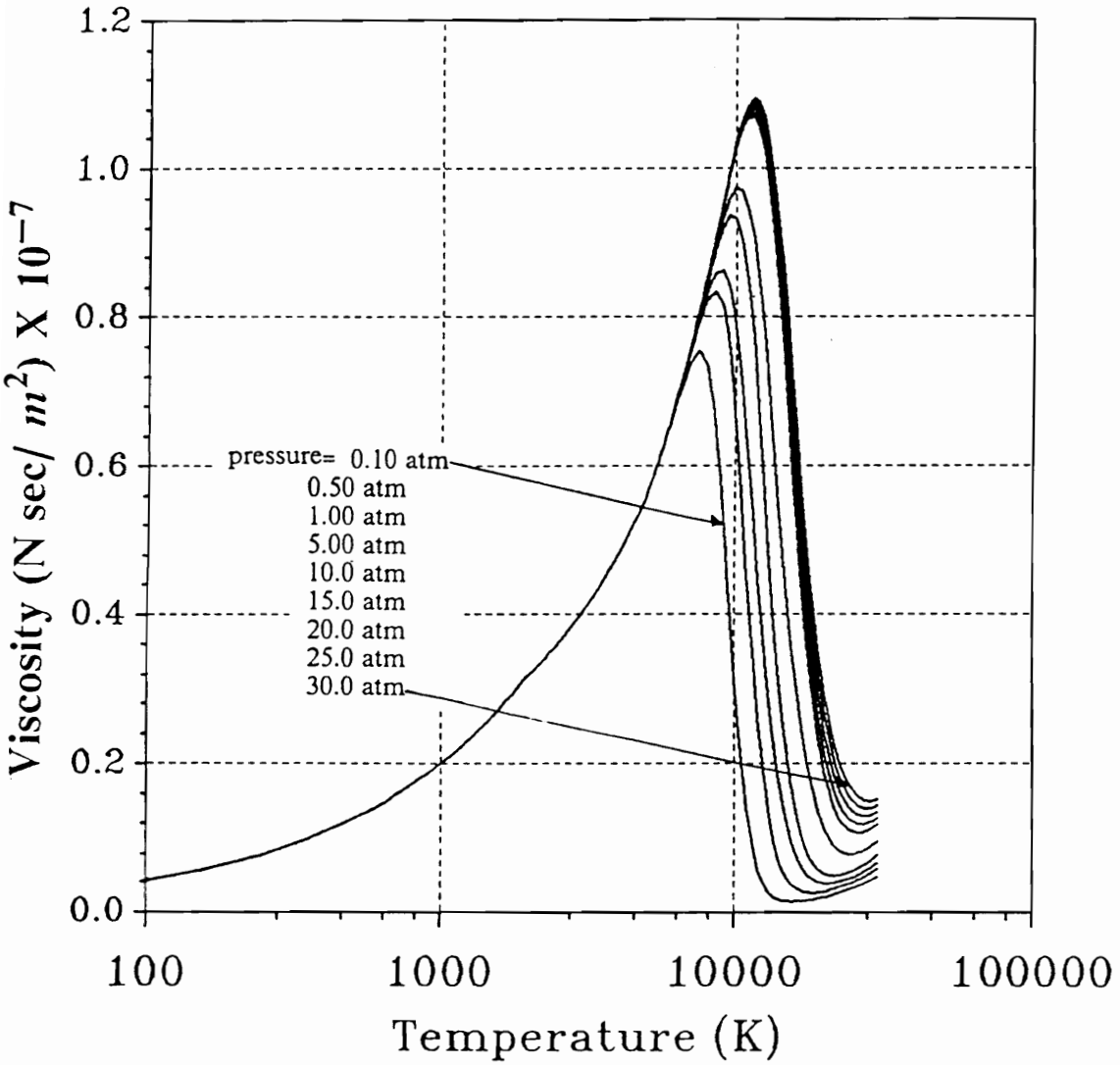

Figure D.1. Viscosity variation with temperature at different pressures.

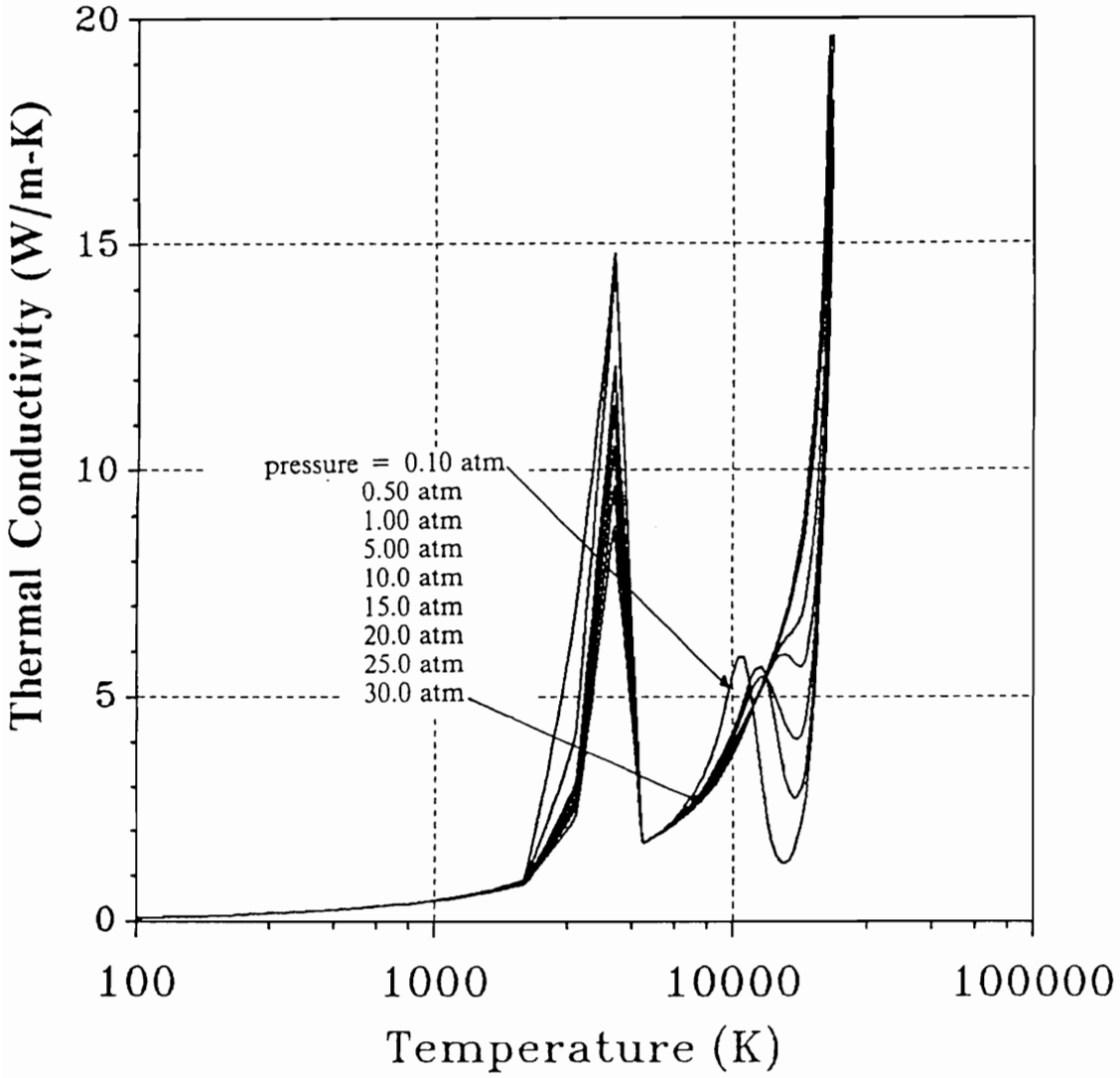

Figure D.2. Thermal conductivity variation at different pressures.

Appendix E. Grid Generation

A transformation from the physical domain to the computational domain is needed to obtain the solution of the Navier-Stokes equations. In this study, the integration of the governing equations is performed by finite volume method in the computational domain. The advantage of the transformation is that the body surface (nozzle wall) may be mapped as a selected boundary in the computational domain which results in a simple implementation of the surface boundary conditions. Also, the transformation to a uniform grid spacing in the computational domain reduces the complexity of using unequal spacing in the physical domain and allows us to use very dense grids in regions of expected large gradients in the flow. The details of grid generation problems may be found in Thompson et al [78] and Anderson et al [4]. Here, an outline of the transformation that has been used to create the grids for laser engine calculations is introduced.

E.1.1 Nozzle geometry

Two nozzle configurations have been used in this study. The first nozzle Fig. 4.1(b) consists of a short cylindrical duct followed by a converging-diverging nozzle using conical and circular throat region contours. The flow is injected radially through a slot in the duct section. The second nozzle Fig 4.1.(a) consists of a straight duct followed by a cosine curve. The dimensions used for the different test cases are given in Chapter IV.

E.1.2 Transformation to computational domain

The transformation from the physical to the computational domain is carried out using equally spaced points in the x-direction and a stretching grid in the r-direction. The stretching aims to produce dense grid in the region near the wall and near the axis of symmetry. Figures 4.2. (a,b) show a typical grid system for the the second nozzle configuration, together with the ray tracing used to solve the laser energy equation.

In this study, various grid systems were generated. Although the simple grid system shown in Chapter 4 was used to perform the calculations, the grid generation ability of our code is introduced below. A stretching in the x-axis may be used to produce a dense grid around the nozzle throat area. The following transformation may be used

$$\xi = B + \frac{1}{\tau}\sinh^{-1}\left[\left(\frac{x}{x_l} - 1\right)\sinh(\tau B)\right] \qquad (E.1a)$$

where

$$B = \frac{1}{2\tau} \ln\left[\frac{1 + (e^{\tau} - 1)(x_l/x_f)}{1 + (e^{-\tau} - 1)(x_l/x_f)} \right] \eta = \frac{y}{r(x)} \qquad (E.1b)$$

and τ is a stretching parameter to produce fine grid near the focal point x_l. A typical value of τ is 6.5.

To improve the smoothness of the grid system and obtain better orthogonality characteristics, elliptic PDE equations may be solved. The Laplace equation has been selected. It is given by

$$\nabla^2 \xi = 0 \qquad \nabla^2 \eta = 0 \qquad (E.1a,b)$$

transformation of the above equations gives

$$\alpha x_{\xi\xi} - 2\beta x_{\xi\eta} + \gamma x_{\eta\eta} = 0 \qquad (E.2a)$$

$$\alpha y_{\xi\xi} - 2\beta y_{\xi\eta} + \gamma y_{\eta\eta} = 0 \qquad (E.2b)$$

where

$$\begin{aligned} \alpha &= x_\eta^2 + y_\eta^2 \\ \beta &= x_\xi x_\eta + y_\xi y_\eta \\ \gamma &= x_\xi^2 + y_\xi^2 \end{aligned} \qquad (E.3a,b,c)$$

This system of equations may be discretized and solved numerically on a uniformly- spaced grid in the computational domain; the resulting grid system is shown in Fig. E.1. The grid includes stretching in the x-direction to produce a dense grid lines around the nozzle throat. It is noticed that the grid lines are not

orthogonal, at the symmetry axis. This is due to applications of Laplace PDE instead of Poisson's equations. Since in our study the orthognality of the grid lines at the symmetry axis is important, the Laplace's PDE equations have not been used for our calculations. Instead a stretched grid in y-direction only, Fig. 4.2. (a,b), was used.

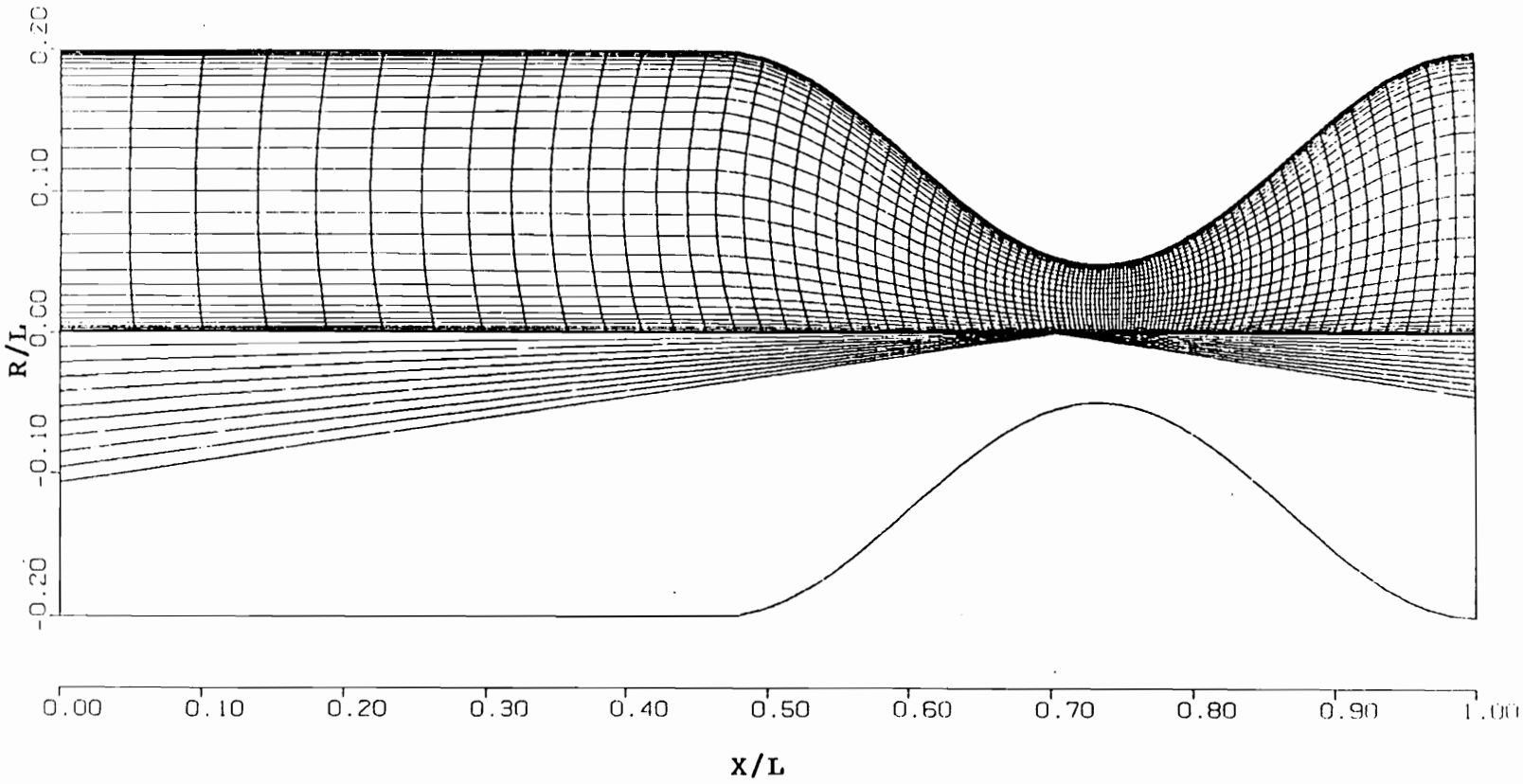

Figure E.2. Gridgeneration using elliptic differential equation.

Appendix F. Source Term Discretization in the Transport Equation

The source terms for the x-momentum, r-momentum, and the energy equations are given in nondimensionalized forms in Table 2.1., Chapter II.

F.1 Transformation to computational domain

The terms in Table 2.1 may be transformed to the computational domain (ξ, η) using the following transformation

$$\frac{\partial}{\partial x} = \frac{1}{J} \left(r_\eta \frac{\partial}{\partial \xi} - r_\xi \frac{\partial}{\partial \eta} \right) \qquad (F.1a)$$

$$\frac{\partial}{\partial r} = \frac{1}{J} \left(x_\xi \frac{\partial}{\partial \eta} - x_\eta \frac{\partial}{\partial \xi} \right) \qquad (F.1b)$$

where "J" is the Jacobian of the transformation, and is given as

$$J = \begin{vmatrix} x_\xi & x_\eta \\ r_\xi & r_\eta \end{vmatrix} \tag{F.2}$$

Applying this transformation to the source terms, the following equations may be written

- x-momentum

$$S^u(\xi,\eta) = -rr_\eta \frac{\partial p}{\partial \xi} + rr_\xi \frac{\partial p}{\partial \eta} + \frac{1}{R_e}\left[r_\eta \frac{\partial(\mu r U_x)}{\partial \xi} - r_\xi \frac{\partial(\mu r U_x)}{\partial \eta} + x_\xi \frac{\partial(\mu r V_x)}{\partial \eta} - x_\eta \frac{\partial(\mu r V_x)}{\partial \xi} - \frac{2}{3}\left[r_\eta \frac{\partial(\mu r(\nabla \overline{V}))}{\partial \xi} - r_\xi \frac{\partial(\mu r(\nabla \overline{V}))}{\partial \eta} \right]\right] \tag{F.3a}$$

- r-momentum

$$S^r(\xi,\eta) = -rx_\xi \frac{\partial p}{\partial \eta} + rx_\eta \frac{\partial p}{\partial \xi} + \frac{1}{R_e}\left[r_\eta \frac{\partial(\mu r U_r)}{\partial \xi} - r_\xi \frac{\partial(\mu r U_r)}{\partial \eta} + x_\xi \frac{\partial(\mu r V_r)}{\partial \eta} - x_\eta \frac{\partial(\mu r V_r)}{\partial \xi} - \frac{2}{3} r\left[x_\xi \frac{\partial(\mu(\nabla \overline{V}))}{\partial \eta} - x_\eta \frac{\partial(\mu(\nabla \overline{V}))}{\partial \xi} \right]\right] \tag{F.3b}$$

- Energy

$$S^h(\xi,\eta) = ru(r_\eta \frac{\partial p}{\partial \xi} - r_\xi \frac{\partial p}{\partial \eta}) + rv(x_\xi \frac{\partial p}{\partial \eta} - x_\eta \frac{\partial p}{\partial \xi}) + \frac{4\mu r J}{3R_e}\left[(U_x)^2 + (V_r)^2 + \frac{3}{4}\left[(V_x)^2 + (U_r)^2\right] + \frac{3}{2} U_r V_x - U_x V_r + \left(\frac{v}{r}\right)^2 - \left(\frac{v}{r}\right)[U_x + V_r]\right] \tag{F.3c}$$

where

$$(U, V)_x = \frac{1}{J}\left(r_\eta \frac{\partial(u,v)}{\partial\xi} - r_\xi \frac{\partial(u,v)}{\partial\eta}\right) \tag{F.4a}$$

$$(U, V)_r = \frac{1}{J}\left(x_\xi \frac{\partial(u,v)}{\partial\eta} - x_\eta \frac{\partial(u,v)}{\partial\xi}\right) \tag{F.4b}$$

$$\nabla\overline{V} = U_x + V_r + \frac{v}{r} \tag{F.4c}$$

F.2 Integration of the Source Terms

Equations F.3. a-c may be integrated over the control volume as shown in Fig. F.1. The integration should include rotation about the axis of symmetry, and the expressions are divided over 2 π. In Fig. F.1, e, w, s, and n refer to the points on the middle of the cell faces. After some calculus we obtain

- x-momentum:

$$\begin{aligned}\hat{S}^u(\xi,\eta) = &-(rr_\eta)_{i,j}\left[p_{i+1,j} - p_{i-1,j}\right] + (rr_\xi)_{i,j}\left[p_{i,j+1} - p_{i,j-1}\right] \\ &+ \frac{1}{R_e}\Big[(r_\eta)_{i,j}\left[(\mu r U_x)_e - (\mu r U_x)_w\right] - (r_\xi)_{i,j}\left[(\mu r U_x)_n - (\mu r U_x)_s\right] \\ &+ (x_\xi)_{i,j}\left[(\mu r V_x)_n - (\mu r V_x)_s\right] - (x_\eta)_{i,j}\left[(\mu r V_x)_e - (\mu r V_x)_w\right] \\ &- \frac{2}{3}\Big[(r_\eta)_{i,j}\left[(\mu r(\nabla\overline{V}))_e - (\mu r(\nabla\overline{V}))_w\right] - (r_\xi)_{i,j}\left[(\mu r(\nabla\overline{V}))_n - (\mu r(\nabla\overline{V}))_s\right]\Big]\Big]\end{aligned} \tag{F.5a}$$

- r-momentum

$$\hat{S}^{v}(\xi,\eta) = -(rx_{\xi})_{i,j}[p_{i,j+1} - p_{i,j-1}] + (rx_{\eta})_{i,j}[p_{i+1,j} - p_{i-1,j}]$$
$$+ \frac{1}{R_e}\Big[(r_{\eta})_{i,j}[(\mu r U_r)_e - (\mu r U_r)_w] - (r_{\xi})_{i,j}[(\mu r U_r)_n - (\mu r U_r)_s]$$
$$+ (x_{\xi})_{i,j}[(\mu r V_r)_n - (\mu r V_r)_s] - (x_{\eta})_{i,j}[(\mu r V_r)_e - (\mu r V_r)_w]$$
$$- \frac{2}{3} r_{i,j}\Big[(x_{\xi})_{i,j}[(\mu(\nabla\overline{V}))_n - (\mu(\nabla\overline{V}))_s] - (x_{\eta})_{i,j}[(\mu(\nabla\overline{V}))_e - (\mu(\nabla\overline{V}))_w]\Big]\Big] \qquad (F.5a)$$

- Energy

$$\hat{S}^{h}(\xi,\eta) = (rur_{\eta})_{i,j}[p_{i+1,j} - p_{i-1,j}] - (rur_{\xi})_{i,j}[p_{i,j+1} - p_{i,j-1}]$$
$$+ (rvx_{\xi})_{i,j}[p_{i,j+1} - p_{i,j-1}] - (rvx_{\eta})_{i,j}[p_{i+1,j} - p_{i-1,j}]$$
$$+ \left(\frac{4\mu r J}{3R_e}\right)_{i,j}\Big[(U_x)^2 + (V_r)^2 + \frac{3}{4}[(V_x)^2 + (U_r)^2]$$
$$+ \frac{3}{2} U_r V_x - U_x V_r + \left(\frac{v}{r}\right)^2 - \left(\frac{v}{r}\right)[U_x + V_r]\Big]_{i,j} \qquad (F.5c)$$

In the above discretization, a linear profile was assumed for the pressure field between the grid points. This will guarantee the accuracy of the scheme to second order accuracy, and will guarantee the coupling between the pressure and velocity fields. The above expressions include terms such as $(U_x)_e$,$(V_r)_e$, etc.... These terms must be evaluated at the cell faces. Here, the details are given for the east face "e". Similar expressions may be obtained for the other faces.

Equations F.4a-b written for U_x and V_r at the point e are

$$(U_x)_e = \left(\frac{1}{J_{i+1,j} + J_{ij}}\right)\Big[\left[(r_\eta)_{i+1,j} + (r_\eta)_{ij}\right]\left[u_{i+1,j} - u_{ij}\right] - \left[(r_\xi)_{i+1,j} + (r_\xi)_{ij}\right]\frac{\left[u_{i+1,j+1} - u_{i+1,j-1} + u_{ij+1} - u_{ij-1}\right]}{4}\Big] \quad (F.6a)$$

$$(V_x)_e = \left(\frac{1}{J_{i+1,j} + J_{ij}}\right)\Big[-\left[(x_\eta)_{i+1,j} + (x_\eta)_{ij}\right]\left[v_{i+1,j} - v_{ij}\right] + \left[(x_\xi)_{i+1,j} + (x_\xi)_{ij}\right]\frac{\left[v_{i+1,j+1} - v_{i+1,j-1} + v_{ij+1} - v_{ij-1}\right]}{4}\Big] \quad (F.6b)$$

After substituting all the expressions for the remaining faces into eqs. F.4. a-c the source terms can be evaluated. The scheme treats the above expressions as known from the previous step. This linearization was shown to give good results in the PBNS code.

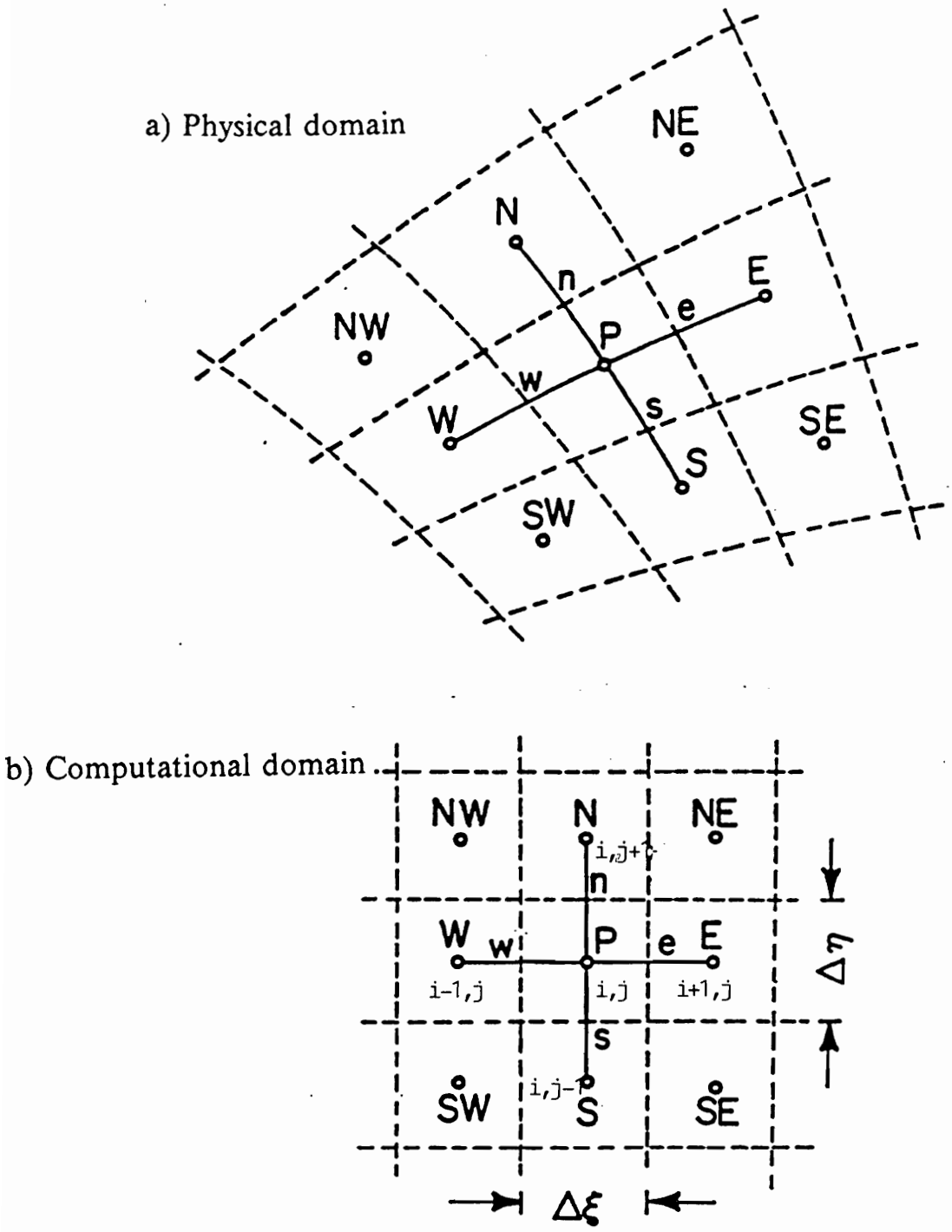

Figure F.1. Schematic of coordinate transformation.

Appendix G. Accelerating the Convergence of the Tridiagonal Solver

As it was explained in Chapter II, a tridiagonal solver was used to solve momentum, pressure correction and energy equations. This was achieved by performing successive sweep in both ξ and η directions. Rewriting eq.2.52 for the grid point i,j (as it is shown in Fig. F.1.) gives

$$a_{i,j}\phi_{i,j} = b_{i+1,j}\phi_{i+1,j} + c_{i-1,j}\phi_{i-1,j} + d_{i,j+1}\phi_{i,j+1} + e_{i,j-1}\phi_{i,j-1} + \hat{S}_{i,j} \qquad (G.1)$$

Two schemes, discussed below, may be used to accelerate the convergence of the solver.

G.1 Relaxation parameter scheme

The scheme devised by Van Doormal [79] introduced a relaxation parameter, Ω, that produces a better estimate of the off-line terms in the sweep pass. The

details are given here for the sweep in ξ direction. Similar expression may be obtained for the sweep in η direction. For a sweep in ξ direction, eq. G.1 may be written as

$$-e_{i,j-1}\phi_{i,j-1}\, a_{i,j}\phi_{i,j} \; - d_{i,j+1}\phi_{i,j+1} = b_{i+1,j}\phi_{i+1,j} + c_{i-1,j}\phi_{i-1,j} + \hat{S}_{i,j} \qquad (G.2)$$

During the computation, $\phi_{i-1,j}$ is evaluated using the most recent values from the line i-1. The value at i+1 line is only known from the previous iteration. To improve the convergence rate, the following relaxation factor may be used

$$\phi_{i+1,j} = \phi^{*}_{i+1,j} + (\Omega - 1)(\phi_{i,j} - \phi^{*}_{i,j}) \qquad (G.3)$$

where the "*" refers to the previous iteration. Substituting in eq. G.2, we obtain

$$\begin{aligned} -e_{i,j-1}\phi_{i,j-1}\,[a_{i,j} - b_{i+1,j}(\Omega - 1)]\,\phi_{i,j} \; - d_{i,j-1}\phi_{i,j-1} \; = \\ b_{i+1,j}\phi_{i+1,j} + c_{i-1,j}\phi_{i-1,j} - [b_{i+1,j}(\Omega - 1)]\phi^{*}_{i,j} + \hat{S}_{i,j} \end{aligned} \qquad (G.4)$$

Van et al [79] suggested a value of Ω of less than 2.

G.2 Block Correction Scheme

The main idea of the block correction method [62] is that the unconverged field $\phi^{*}_{i,j}$ obtained from prior iterations is corrected by adding uniform correction $\overline{\phi}_i$ along lines of constant i for a sweep in the ξ direction. Thus

$$\phi_{i,j} = \phi^{*}_{i,j} + \overline{\phi}_i \qquad (G.5)$$

The corrections $\overline{\phi}_i$ are chosen such that the integral conservation over the control volume blocks defined by each constant i line is exactly satisfied. Substituting of eq. G.6 into eq. G.1 and summing over j for j=2,my-1, the following equation can be written

$$-C_i\overline{\phi}_{i-1} + A_i\overline{\phi}_i - B_i\overline{\phi}_{i+1} = D_i \qquad (G.6)$$

where

$$A_i = \sum_{j=2}^{j=my-1} (a_{i,j} - e_{i,j} - d_{i,j}) \quad B_i = \sum_{j=2}^{j=my-1} b_{i,j} \quad C_i = \sum_{j=2}^{j=my-1} c_{i,j} \qquad (G.7a,b,c)$$

$$D_i = \sum_{j=2}^{j=my-1} (b_{i,j}\phi^*_{i+1,j} + c_{i,j}\phi^*_{i-1,j} + d_{i,j}\phi^*_{i,j+1} + e_{i,j-1}\phi^*_{i,j-1} + S_{i,j} - a_{i,j}\phi^*_{i,j}) \qquad (G.7a,b,c)$$

A similar equations may be written for i=2,mx-1. These equations may be solved by a tridiagonal solver to find the correct field.

The scheme in general consists of the following steps:

- Solve eq. G.1 by sweeping in ξ for all the grid points i,j.
- Solve eq. G.6 to find $\overline{\phi}_i$, then update the field using eq. G.5.
- Repeat the steps by sweeping in η direction followed by block correction along the j lines.

In this study, the block correction scheme was found to be more robust and faster for achieving convergence. Several steps may be performed before the residual reaches the convergence level.

Appendix H. Non-reflecting Boundary Condition for Subsonic Inlet

In this treatment of subsonic inlet, it is assumed that the flow is isentropic at the boundary. Thus, the stagnation density and pressure are given by

$$p_o = p(1 + \frac{\gamma - 1}{2} M^2)^{\frac{\gamma}{\gamma - 1}} \qquad \rho_o = \rho(1 + \frac{\gamma - 1}{2} M^2)^{\frac{1}{\gamma - 1}} \qquad (H.1a,b)$$

Since for an axial injection flow, the v-velocity component is zero

$$M^2 = \frac{\rho u^2}{\gamma p} \qquad (H.1c)$$

The characteristic variable Δw_3 is given by

$$\Delta w_3 = (\Delta u - \frac{\Delta p}{\rho c}) \qquad (H.2)$$

Using small perturbations in eq. H.1 a-c and eq. H.2, the following equation may be written

$$\begin{bmatrix} 1-\Theta & \Theta & 2\Theta \\ -\Theta & \gamma+\Theta & 2\Theta \\ -\dfrac{p}{\rho c} & 0 & u \end{bmatrix} \begin{bmatrix} \dfrac{\Delta p}{p} \\ \dfrac{\Delta \rho}{\rho} \\ \dfrac{\Delta u}{u} \end{bmatrix} = \begin{bmatrix} \dfrac{\Delta p_o}{p_o} \\ \dfrac{\Delta \rho_o}{\rho_o} \\ \Delta W_3 \end{bmatrix} \qquad (H.3)$$

The above system may be solved for $\frac{\Delta p}{p}$, $\frac{\Delta \rho}{\rho}$ and $\frac{\Delta u}{u}$. For subsonic inlet, Δp_o and $\Delta \rho_o$ are zero. This may be used in the right hand side of the eq. H.3. The characteristic variable is considered as a numerical boundary condition. It can be extrapolated from the interior solution at the new step by second or first order extrapolation scheme.

The above boundary condition at the inlet was tested for the flat plate problem and the axisymmetric nozzle.

REFERENCES

1. Acharya, S. and Moukalled, F.H. **"Improvements To Incompressible Flow Calculation On Nonstaggered Curvilinear Grid, "** Numerical Heat Transfer, Vol. 15, pp. 131-152, 1989.

2. Aksoy, H. and Chen, C.J., **"Numerical Solution Of Navier-Stokes Equations With Nonstaggered Grids Using Finite Analytical Methods,"** Numerical Heat Transfer, Part B, Vol. 21, pp. 287-306, 1992.

3. Andreson, D.A., Tannehill, J.C., Pletcher, R.H., **"Computational Fluid Mechanics And Heat Transfer, "** hemisphere Publishing Corporation, 1984.

4. Anderson, J.D., **"Modern Compressible Flow, "** McGraw-Hill Book Company, 1982.

5. Ashok, U.C., and Turan, A. **" Improved Pressure-Velocity Coupling Algorithm Based On Minimization Of Global Residual Norm, "** Numerical Heat Transfer, Part B, Vol. 20, pp. 115-123, 1991.

6. Batteh, J.H. and Keefer, D.R., **"Two Dimension Generalization Of Raizer's For The Subsonic Propagation Of Laser Sparks, "** IEEE Transactions on plasma science, Vol.PS-2, September 1974.

7. Birkan, M.A. **"Laser Propulsion: Research Status and Needs"** Journal of Propulsion and Power, Vol. 8, March-April, 1992.

8. Biringen, S. and Cook, C. **"On Pressure Boundary Conditions For The Incompressible Navier-Stokes Equations Using Nonstaggered Grids, "** Numerical Heat Transfer, Vol. 13, pp. 241-252, 1987.

9. Blank, D.A. and Shih, T.M., **"Hypergolic Combustion Model For Four Storke Heat-Barrier Piston Engines, "** Numerical Heat Transfer, Vol. 17, pp. 1- 20, 1990.

10. Boeing/NASA, **"Advanced Propulsion Systems Concepts For Orbital Transfer, "** Boeing Report, December, 1982.

11. Chima, R.V., **"Invisicd and Viscous Flows in Cascades with an Explicit Multiple-Grid Algorithm,"** AIAA journal, Vol. 23, No. 10, October 1985.

12. Chiu, C.P. and Wu, T.S., **"Study Of Air Motion In Reciprocating Engine Using An Algebraic Grid Generation Technique,"** Numerical Heat Transfer, Vol. 17, pp. 309-327, 1990.

13. Cornelisse, J.W., Schoyer, H.F.R. and Wakker, K.F., **"Rocket Propulsion and Spaceflight Dynamics,"** Pitman Publishing Limited, 1979.

14. Estublier, D.L., **"Radiation Emission and Absorption in a Hydrogen Plasma of a Laser Engine,"** Master of Scince, Virginia Tech, May 1990.

15. Fletcher,C.A.J., **"Computational Techniques For Fluid Dynamics,"** Springer-Verlag, 1988.

16. Frisbee, R.H., Horvath, J.C. And Sercel, J.C. **"Laser Propulsion For The Orbital Transfer Mission,"** AIAA-85-1224, 21th Joint Propulsion Conference, July, 1985.

17. Galpin, P.F. and Raithby, G.D., **"Numerical Solution Of Problems In Incompressible Fluid Flow: Treatment Of Temperature-Velocity Coupling,"** Numerical Heat Transfer, Vol. 17, pp. 105-129, 1990.

18. Glumb, R.J., **"Laser Propulsion For Earth-Moon Transportation Systems,"** Lunar Bases & Space Activities In The 21st Century, LBS-88-086, 1988.

19. Glumb, R.J. and Krier, H., **"Concepts And Status Of Laser-Supported Rocket Propulsion,"** Journal of Spacecraft and Rockets, Vol. 21, No. 1, Jan-Feb. 1984.

20. Glumb, R.J. and krier, H., **"Two-Dimensional Model Of Laser-Sustained Plasmas In Axisymmertic Flowfields,"** AIAA paper 85-1533,1985.

21. Gosman, A.D., Khalil, E.E. and Whitelaw, J.H. **"The Calculation Of Two-Dimensional Turbulent Recirculating Flows,"** Symposium on Turbulent Shear Flows, April 1977.

22. Grier, N.T. , **"Calculation Of Transport Properties Of Ionizing Atomic Hydrogen,"** NASA TN D-3186, 1966.

23. Hah, C., **"A Navier-Stokes Analysis Of Three-Dimensional Turbulent Floes Inside Turbine Blade Rows At Design and Off-Design Conditions,"** Journal of Engineering For Gas Turbine And Power, Vol. 106, April 1984.

24. Han, S.M. **"A Generalized Implicit Finite Difference Method For Transient Analysis Of Compressible And Incompressible Fluid Flows,"** Numerical Methods for fluid Transient Analysis, presented at Applied Mechanics, Bioengineering, and Fluids Conference, ASME, Texas, June, 1983.

25. Hasen, G.A., **"Navier-Stokes Solutions For An Axisymmetric Nozzle, "** AIAA-81-1474, 17th Joint Propulsion Conference, July 1981.

26. Hirsch, C., **"Numerical Computation Of Internal And External Flows, "** John Wiley & Sons, 1991.

27. Incropera, F.P. and Dewitt, D.P., **"Fundamentals Of Heat And Mass Transfer,"** John Wile & Sons, 1985.

28. Issa, R.I. and Lockwood, F.C. **"On The Prediction Of Two-Dimensional Supersonic Viscous Interactions Near Walls, "** AIAA Journal, Vol. 15, No. 2, Febrary 1977.

29. Issa, R.I. **"Solution Of The Implicitly Discretised Fluid Flow Equations By Operator-Splitting, "** Journal of Computational Pyysics, Vol. 62, 1986.

30. Jackson, J.P., **" Role Of Radiative Transport In The Propagation Of Laser Supported Combustion Waves, "** AIAA Journal, Vol. 12, No. 11, November 1974.

31. Jang, D.S., Jetli, R. and Acharya, S., **" Comparison Of The Piso, Simpler , And Simplec Algorithms For The Treatment Of The Pressure-Velocity Coupling In Steady Flow Problems, "** Numerical Heat Transfer, Vol. 10, pp. 209-228, 1986.

32. Jeng, S.M. and Keefer, D.R., **"Numerical Study Of Laser-Sustained Hydrogen Plasmas In A Forced Convective Flow, "** AIAA-86-1524, 22nd Joint Propulsion Conference, June 1986.

33. Jeng, S.M., Keefer, D.R., Welle, R. and Peters, C., **"Numerical Study Of Laser-Sustained Argon Plasmas In A Forced Convective Flow, "** AIAA-86-1078, 4th Fluid Mechanics, Plasma Dynamics and Lasers Conference , May 1986.

34. Jeng, S.M. and Keefer, D., **"A Theoretical Investigation Of Laser-Sustained Plasma Thruster, "** AIAA-87-0383, 25th Aerospace Sciences Meeting, 1987.

35. Jeng, S.M. , Litchford, R. and Keefer, D. **"Computational Design Of An Experimental Laser-Powered Thruster,"** Final Report, NAS8-36220 , March, 1988.

36. Kantrowitz, A. **"Propulsion to Orbit by Ground-Based Lasers, "** Astronautics & Aeronautics, May 1972.

37. Karki, K.C. and Patankar, S.V. **"Pressure Based Calculation Procedure For Viscous Flows At All Speeds In Arbitrary Configurations,"** AIAA Journal, Vol.27, No. 9, September, 1989.

38. Keefer, D.R., Crowder, H., Elkins, R. and Eskridge, R., **"Laser Heated Rocket Analytical And Experimental Support, "** SM80C1160F, July 1981.

39. Keefer, D., Welle, R. and Peters, C. **"Power Absorption In Laser-Sustained Argon Plasmas, "** AIAA paper 85-1552, 18th Fluid Dynamics, Plasmadynamics and Laser, July 1985.

40. Keefer, D.R., Crowder, H. and Peters, C., **"A RE-examination Of Laser-Supported Combustion Wave, "** AIAA Journal, Vol. 23, No. 8, August 1985.

41. Kemp, N.H. and Root, R.G. **" Analytical Study Of Laser-Supported Combustion Waves In Hydrogen, "** NASA CR-135349, PSI TR-97, August 1977.

42. Kemp, N.H. and Root, R.G. **" Analytical Study Of Laser-Supported Combustion Waves In Hydrogen, "** Journal Of Energy, Vol.3, No. 1, Jan-Feb. 1979.

43. Kobayashi, M.H. and Pereira, J.C.F., **"Calculation Of Incompressible Laminar Flows On Nonstaggered, Nonorthogonal Grid, "** Numerical Heat Transfer, Part B, Vol. 19, pp. 243-262, 1991.

44. Kobayashi, M.H. and Pereira, J.C.F. **"Predictions Of Compressible Viscous Flows At All Mach Number Using Pressure Correction, Collocated Primitive Variables and Non-Orthogonal Meshes,"** ,AIAA 92-0426.

45. Krier, H., Mazumder, J., Rockstroh, T.J., Bender, T.D. and Glumb, R.J., **"Continuous Wave Laser Gas Heating By Sustained Plasmas In Flowing Argon, "** AIAA Journal, Vol. 24, No. 10, October 1986. 275-296.

46. Lee, D. and Chiu, J.J. **"Covariant Velocity Calculation Procedure With Nonstaggered Grids For Computation Of Pulstatile Flows , "** Numerical Heat Transfer, Part B, Vol. 21, pp. 269-286, 1992.

47. Lockheed Missiles & Space Company, **"Laser Rocket System Analysis, "** NASA CR-159521, September 1978.

48. Majumdar, S. **"Role Of Underrelaxation in Momentum Interpolation For Calculation Of Flow With Nonstaggered Grids, "** Numerical Heat Transfer, Vol. 14, pp. 125-132, 1988.

49. Mazumder, J., Rockstroh, T.J. and Krier, H. **" Spectroscopic Studies Of Plasma During CW Laser Gas Heating In Flowing Argon, "** Journal of applied physics, Vol. 62, No. 12, December 1987.

50. McCay, T.D., **"Chemical Kinetic Performance Losses For A Hydrogen Laser Thermal Thruster, "** Journal Of Spacecraft And Rockets, Vol. 24, No. 2, August 1987.

51. McMillin, B.K., Zerkle, D.K., Glumb, R.J., Krier, H. and Mazumder, J. , **"Energy Conservation In Laser Sustained Argon Plasmas For Application To**

Rocket Propulsion," AIAA-87-1459, 19th Fluid Dynamics, Plasmadynamics and Laser Conference, June 1987.

52. Melaaen, M.C. **"Calculation Of Fluid Flows With Staggered And Nonstaggered Curvilinear Nonorthogonal Grids-The Theory ,"** Numerical Heat Transfer, Part B, Vol. 21, pp. 1-19, 1992.

53. Melaaen, M.C. **"Calculation Of Fluid Flows With Staggered And Nonstaggered Curvilinear Nonorthogonal Grids-A Comparison ,"** Numerical Heat Transfer, Part B, Vol. 21, pp. 21-39, 1992.

54. Merkle, C.L. **"Prediction Of the Flowfield In Laser Propulsion Devices,"** AIAA Journal, Vol. 22, No. 8, August 1984.

55. Merkle, C.L., Gulati, A.and Choi, Y.H., **"The Effect Of Strong Heat Addition On The Convergence Of Implicit Schemes,"** AIAA Journal, Vol. 23, No. 6, June 1985.

56. Merkle, C.L., Molvik, G.A. and Shaw, E.J., **"Numerical Solution Of Strong Radiation Gasdynamic Interactions In A Hydrogen-Seedant Mixture,"** Journal of Propulsion, Vol. 2, No. 5, Sept-Oct. 1986.

57. Merkle, C.L., Venkateeswaran, S. and Buelow, P.E., **"The Relationship Between Pressure-Based And Density-Based Algorithms,"** , AIAA-92-5432, 1992.

58. Miller, T.F. and Schmidt, F.W. **"Use Of Pressure-Weighted Interpolation Method For The Solution Of The Incompressible Navier- Stokes Equations On NonoStaggered Grid System,"** Numerical Heat Transfer, Vol. 14, pp. 213-233, 1988.

59. Minovitch, M.A., **"Performance Analysis Of A Laser Propelled Interorbital Transfer Vehicle,"** NASA CR-134966, February 1976.

60. Molvik, G.A., Choi, D. and Merkle, C.L., **"A Two-Dimensional Analysis Of Laser Heat Addition In A Constant Absoptivity Gas,"** AIAA Journal, Vol. 23, July 1985.

61. Patankar, S.V. And Spalding, D.B., **"A Calculation Procedure For Heat, Mass And Momentum Transfer In Three-Dimensional Parabolic Flows,"** Int. J. Heat And Mass Transfer Vol. 15, pp. 1787-1806, 1972. 443-454.

62. Patankar, S.V. **"Numerical Heat Transfer And Fluid Flow,"** McGraw-Hill Book Company, 1980.

63. Patch, **"Thermodynamic Properties And Theoretical Rocket Performance Of Hydrogen To 100000 K and 1.01325X10 sup 8 N/m sup2 ,"** NASA SP-3069, Feb 1972.

64. Peric, M. and Kessller, R. and Scheuerer, G. **"Comparison Of Finite-Volume Numerical Mehtods With Staggered And Collocated Grids,"** Computers and Fluids, Vol.16, No. 4, pp. 389-403, 1988.

65. Peterson, P.F., **"A Method For Predicting And Minimizing Numerical Diffusion,"** Numerical Heat Transfer, Part B, Vol. 21, pp. 343-366, 1992.

66. Raithby, G.D. and Schneider, G.E., **"Numerical Solution Of Problems In Incompressible Fluid Flow: Treatment Of The Velocity-Pressure Coupling,"** Numerical Heat Transfer, Vol. 2, no. 2, pp. 417-440, 1979.

67. Raizer, Yu. P. **"Optical Discharges,"** Soviet Physics, Usp. 23(11), November 1980.

68. Reggio, M. and Camarero, R., **" Numerical Solution Procedure For Viscous Incompressible Flows,"** Numerical Heat Transfer, Vol. 10, pp. 131-146, 1986.

69. Rihe, C.M. and Chow,W.L., **"Numerical Study Of Turbulent Flow Past An Airfoil With Trailing Edge Separation,"** AIAA Journal, Vol. 21, No. 11, November 1983.

70. Rihe, C.M., **"A Pressure Based Navier-Stokes Solver Using The Multigrid Method,"** AIAA-86-0207, 24th Aerospace Sciences Meeting, January, 1986/Reno.

71. Rockstroh, T.J. and Mazumder, J. **"Characterization Laser Induced Plasmas And Temperature Measurment During Surface Treatment,"** NATO Conference, September 1985.

72. Rocketdyne Design Group, **"Laser-Heated Rocket Thruster "** NASA-Lerc, 1984.

73. Schwartz, S., Mertogul, A., Eguiguren, J., Zerkle, D., Chen, X., Krier, H. and Mazumder, J. **"Laser-Sustained Gas Plasmas For Application To Rocket Propulsion,"** AIAA-89-2631, 25th joint propulsion conference, July 1989.

74. Shamroth, S.J., McDonald, H. and Briley, W.R., **"Prediction Of Cascade Flow Fields Using The Averaged Navier-Stokes Equations,"** Journal of Engineering For Gas Turbine And Power, Vol. 106, April 1984.

75. Shih, T.M. and Ren, A.L., **"Primitive-Variable Formulations Using Nonstaggered Grids,"** Numerical Heat Transfer, Vol. 7, pp. 413-428, 1984.

76. Shyy, W., Chen, M.H. and Sun, C.S., **"A Pressure-Based FMG/FAS Algorithm For Flow At All Speed,"** AIAA-92-0548, 1992.

77. Stone, H., **" Iterative Solution Of Implicit Approximations Of Multidimensional Partial Differential Equations,"** Journal Of Numerical Analysis, Vol. 5, No.3, September 1968.

78. Thompson, J.F., Warsi, Z.U.A. and Mastin, C.W., **"Numerical Grid Generation; Foundation And Applications,"** 1985.

79. Van Hove, W. **"Calculation Of Three-Dimensional, Inviscid, Rotational Flow In Axial Turbine Blade Row,"** Journal of Engineering For Gas Turbine And Power, Vol. 106, April 1984.

80. Young, R.J., Walker, G.H., Williams, M.D., Schuster, G.L. and Conway, E.J. **"Preliminary Design And Cost Of A 1-Megawatt Solar-Pumped Iodide Laser Space-To-Space Transmission Station,"** NASA Technical Memorandum 4002, 1987.

Vita

The author was born on January 15, 1960, in Alexandria, Egypt. He earned a B.S. from Marine Engineering and Naval Architecture department at Alexandria University, with Offshore Structures as his major. In 1983, he was appointed as instructor at the same department, where he taught courses in machine design, thermodynamics and structures. He obtained his M.S. from Alexandria University, in 1986, with a thesis titled "Design Considerations of Jack-up Platforms ". During that period he was involved in a consultant maritime office as a technical consultant for many projects. In 1987 he joined the Aerospace and Ocean Engineering department at Virginia Polytechnic Institute and State University, as a doctoral candidate. In 1988, he shifted his major from structures to computational fluid dynamics and propulsion. During his doctoral study, he worked as research assistant on several senior design projects funded by NASA/USRA advanced design program.